

MOLECULAR PRECURSOR DERIVED SIBCN/CNT AND SIOC/CNT COMPOSITE  
NANOWIRES FOR ENERGY BASED APPLICATIONS

by

ROMIL BHANDAVAT

B.E., Nirma Institute of Technology, Gujarat, India, 2004  
M.S., Lawrence Technological University, MI, USA, 2008

AN ABSTRACT OF A DISSERTATION

submitted in partial fulfillment of the requirements for the degree

DOCTOR OF PHILOSOPHY

Department of Mechanical & Nuclear Engineering  
College of Engineering

KANSAS STATE UNIVERSITY  
Manhattan, Kansas

2013

## Abstract

Molecular precursor derived ceramics (also known as polymer-derived ceramics or PDCs) are high temperature glasses that have been studied for applications involving operation at elevated temperatures. Prepared from controlled thermal degradation of liquid-phase organosilicon precursors, these ceramics offer remarkable engineering properties such as resistance to crystallization up to 1400 °C, semiconductor behavior at high temperatures and intense photoluminescence. These properties are a direct result of their covalent bonded amorphous network and free ( $-sp^2$ ) carbon along with mixed Si/B/C/N/O bonds, which otherwise can not be obtained through conventional ceramic processing techniques.

This thesis demonstrates synthesis of a unique core/shell type nanowire structure involving either siliconboroncarbonitride (SiBCN) or siliconoxycarbide (SiOC) as the shell with carbon nanotube (CNT) acting as the core. This was made possible by liquid phase functionalization of CNT surfaces with respective polymeric precursor (e.g., home-made boron-modified polyureamethylvinylsilazane for SiBCN/CNT and commercially obtained polysiloxane for SiOC/CNT), followed by controlled pyrolysis in inert conditions. This unique architecture has several benefits such as high temperature oxidation resistance (provided by the ceramic shell), improved electrical conductivity and mechanical toughness (attributed to the CNT core) that allowed us to explore its use in energy conversion and storage devices.

The first application involved use of SiBCN/CNT composite as a high temperature radiation absorbant material for laser thermal calorimeter. SiBCN/CNT spray coatings on copper substrate were exposed to high energy laser beams (continuous wave at 10.6  $\mu\text{m}$ , 2.5 kW CO<sub>2</sub> laser, 10 seconds) and resulting change in its microstructure was studied ex-situ. With the aid of multiple

techniques we ascertained the thermal damage resistance to be  $15 \text{ kWcm}^{-2}$  with optical absorbance exceeding 97 %. This represents one order of magnitude improvement over bare CNTs ( $1.4 \text{ kWcm}^{-2}$ ) coatings and two orders of magnitude over the conventional carbon paint ( $0.1 \text{ kWcm}^{-2}$ ) currently in use.

The second application involved use of SiBCN/CNT and SiOC/CNT composite coatings as energy storage (anode) material in a Li-ion rechargeable battery. Anode coatings ( $\sim 1 \text{ mgcm}^{-2}$ ) prepared using SiBCN/CNT synthesized at  $1100 \text{ }^\circ\text{C}$  exhibited high reversible (useable) capacity of  $412 \text{ mAhg}^{-1}$  even after 30 cycles. Further improvement in reversible capacity was obtained for SiOC/CNT coatings with  $686 \text{ mAhg}^{-1}$  at 40 cycles and approximately 99.6 % cyclic efficiency. Further, post cycling imaging of disassembled cells indicated good mechanical stability of these anodes and formation of a stable passivating layer necessary for long term cycling of the cell. This improved performance was collectively attributed to the amorphous ceramic shell that offered Li storage sites and the CNT core that provided the required mechanical strength against volume changes associated with repeated Li-cycling.

This novel approach for synthesis of PDC nanocomposites and its application based testing offers a starting point to carry out further research with a variety of PDC chemistries at both fundamental and applied levels.

MOLECULAR PRECURSOR DERIVED SIBCN/CNT AND SIOC/CNT COMPOSITE  
NANOWIRES FOR ENERGY BASED APPLICATIONS

by

ROMIL BHANDEVAT

B.E., Nirma Institute of Technology, Gujarat, India, 2004  
M.S., Lawrence Technological University, MI, USA, 2008

A DISSERTATION

submitted in partial fulfillment of the requirements for the degree

DOCTOR OF PHILOSOPHY

Department of Mechanical & Nuclear Engineering  
College of Engineering

KANSAS STATE UNIVERSITY  
Manhattan, Kansas

2013

Approved by:

Major Professor  
Dr. Gurpreet Singh

## Abstract

Molecular precursor derived ceramics (also known as polymer-derived ceramics or PDCs) are high temperature glasses that have been studied for applications involving operation at elevated temperatures. Prepared from controlled thermal degradation of liquid-phase organosilicon precursors, these ceramics offer remarkable engineering properties such as resistance to crystallization up to 1400 °C, semiconductor behavior at high temperatures and intense photoluminescence. These properties are a direct result of their covalent bonded amorphous network and free ( $-sp^2$ ) carbon along with mixed Si/B/C/N/O bonds, which otherwise can not be obtained through conventional ceramic processing techniques.

This thesis demonstrates synthesis of a unique core/shell type nanowire structure involving either siliconboroncarbonitride (SiBCN) or siliconoxycarbide (SiOC) as the shell with carbon nanotube (CNT) acting as the core. This was made possible by liquid phase functionalization of CNT surfaces with respective polymeric precursor (e.g., home-made boron-modified polyureamethylvinylsilazane for SiBCN/CNT and commercially obtained polysiloxane for SiOC/CNT), followed by controlled pyrolysis in inert conditions. This unique architecture has several benefits such as high temperature oxidation resistance (provided by the ceramic shell), improved electrical conductivity and mechanical toughness (attributed to the CNT core) that allowed us to explore its use in energy conversion and storage devices.

The first application involved use of SiBCN/CNT composite as a high temperature radiation absorbant material for laser thermal calorimeter. SiBCN/CNT spray coatings on copper substrate were exposed to high energy laser beams (continuous wave at 10.6  $\mu\text{m}$ , 2.5 kW CO<sub>2</sub> laser, 10 seconds) and resulting change in its microstructure was studied ex-situ. With the aid of multiple

techniques we ascertained the thermal damage resistance to be  $15 \text{ kWcm}^{-2}$  with optical absorbance exceeding 97 %. This represents one order of magnitude improvement over bare CNTs ( $1.4 \text{ kWcm}^{-2}$ ) coatings and two orders of magnitude over the conventional carbon paint ( $0.1 \text{ kWcm}^{-2}$ ) currently in use.

The second application involved use of SiBCN/CNT and SiOC/CNT composite coatings as energy storage (anode) material in a Li-ion rechargeable battery. Anode coatings ( $\sim 1 \text{ mgcm}^{-2}$ ) prepared using SiBCN/CNT synthesized at  $1100 \text{ }^\circ\text{C}$  exhibited high reversible (useable) capacity of  $412 \text{ mAhg}^{-1}$  even after 30 cycles. Further improvement in reversible capacity was obtained for SiOC/CNT coatings with  $686 \text{ mAhg}^{-1}$  at 40 cycles and approximately 99.6 % cyclic efficiency. Further, post cycling imaging of disassembled cells indicated good mechanical stability of these anodes and formation of a stable passivating layer necessary for long term cycling of the cell. This improved performance was collectively attributed to the amorphous ceramic shell that offered Li storage sites and the CNT core that provided the required mechanical strength against volume changes associated with repeated Li-cycling.

This novel approach for synthesis of PDC nanocomposites and its application based testing offers a starting point to carry out further research with a variety of PDC chemistries at both fundamental and applied levels.

# Table of Contents

List of Figures .....	x
List of Tables .....	xxi
Acknowledgements .....	xxiii
Dedication .....	xxv
Chapter 1 - Introduction .....	1
1.1 POLYMER-DERIVED CERAMICS .....	1
1.1.1 Polymer Synthesis .....	2
1.1.2 Polymer to ceramic conversion .....	3
1.1.3 Polymer Derived Ceramic Structure .....	8
1.1.4 Tunable Engineering Properties .....	9
1.2 CARBON NANOTUBES .....	15
1.2.1 Engineering Properties .....	15
1.2.2 Engineering Applications .....	16
1.3 POLYMER-DERIVED CERAMIC-CARBON NANOTUBE COMPOSITE .....	17
1.3.1 Application 1: Laser Thermal Detector Coatings .....	20
1.3.2 Application 2: Lithium Ion Battery .....	25
1.4 OVERVIEW OF DISSERTATION .....	43
1.5 REFERENCES .....	45
Chapter 2 - Synthesis, Characterization and High Temperature Stability of Si(B)CN Coated Carbon Nanotubes Using a Boron-modified Poly(ureamethylvinyl)silazane Chemistry .....	63
2.1 INTRODUCTION .....	64
2.2 EXPERIMENTAL PROCEDURE .....	66
2.2.1 Sample preparation .....	66
2.2.2 Characterization .....	66
2.3 RESULTS AND DISCUSSION .....	68
2.4 CONCLUSION .....	83
2.5 REFERENCES .....	85

Chapter 3 - Synthesis of Polymer-derived Ceramic Si(B)CN-Carbon Nanotube Composite by Microwave Induced Interfacial Polarization.....	92
3.1 INTRODUCTION .....	93
3.2 EXPERIMENTAL PROCEDURE.....	94
3.2.1 Materials and Methods.....	94
3.2.2 Dielectric Measurement Setup.....	96
3.3 RESULTS AND DISCUSSION.....	98
3.3.1 Irradiation experiments and carbon nanotube functionalization mechanism .....	98
3.3.2 Material Characterization.....	99
3.4 DIELECTRIC MEASUREMENTS .....	107
3.5 CONCLUSION.....	111
3.6 REFERENCES .....	113
Chapter 4 - Very High Laser-Damage Threshold of Polymer-derived Si(B)CN- Carbon Nanotube Composite Coatings .....	117
4.1 INTRODUCTION .....	118
4.2 EXPERIMENTAL PROCEDURE.....	119
4.2.1 Composite material and coating preparation .....	119
4.2.2 Tape test for measuring the composite coating adhesion on the copper substrate .	121
4.2.3 Experimental Setup.....	124
4.3 RESULTS AND DISCUSSION.....	125
4.4 CONCLUSION.....	136
4.5 REFERENCES .....	137
Chapter 5 - Improved Electrochemical Capacity of Precursor-Derived Si(B)CN-Carbon Nanotube Composite as Li-ion Battery Anode.....	141
5.1 INTRODUCTION .....	142
5.2 EXPERIMENTAL PROCEDURE.....	144
5.2.1 Material Preparation.....	144
5.2.2 Instrumentation .....	145
5.2.3 Half-cell assembly and testing.....	145
5.3 RESULTS AND DISCUSSION.....	146



5.3.1	Electrochemical cycling results .....	146
5.3.2	Post-electrochemical cycling characterization.....	156
5.4	CONCLUSION.....	160
5.5	REFERENCES .....	161
Chapter 6 - Stable and Efficient Li-ion Battery Anodes Prepared From Polymer-Derived Silicon Oxycarbide-Carbon Nanotube Shell/Core Composites .....		
		166
6.1	INTRODUCTION .....	167
6.2	EXPERIMENTAL PROCEDURE.....	168
6.2.1	Material Preparation.....	168
6.2.2	Instrumentation .....	170
6.2.3	Half-cell assembly and testing.....	171
6.3	RESULTS AND DISCUSSION.....	171
6.4	CONCLUSION.....	185
6.5	REFERENCES .....	186
Chapter 7-Conclusion and Future Work .....		191

## List of Figures

<b>Figure 1-1:</b> Timeline of the most important inventions and findings of PDCs. ....	3
<b>Figure 1-2 :</b> Stepwise synthesis of amorphous ceramic from liquid polymer precursor (shown: polysilazane). ....	4
<b>Figure 1-3:</b> (a) Weight change and densification of PDCs during the thermal decomposition as a function of ceramic processing temperatures and (b) analysis of the gases evolved corresponding to the processing temperatures for a polysilazane polymer. ....	7
<b>Figure 1-4:</b> (a) Predicted nanodomain structure of polymer-derived SiOC ceramic and (b) SiCN ceramic prepared from pyrolysis of polysilylcarbodiimide precursor. Presence of graphitic carbon and nanovoids in these amorphous ceramics provide ample sites for Li-ion intercalation. (c) and (d) High-resolution TEM images of SiOC and SiCN specimens pyrolyzed at 1000 °C. These ceramics are featureless in both X-ray and TEM up to at least 1300 °C. ....	9
<b>Figure 1-5:</b> High temperature thermal stability comparison of Si <sub>3</sub> N <sub>4</sub> with PDC-SiCN and SiBCN ceramics with tunable behavior. ....	10
<b>Figure 1-6:</b> Application of PDCs in (a) SMP-10 (polycarbosilane) used to repair heat shield in a space shuttle, (b) CMC (C/SiC) brake rotor of motorbike, (c) Micro glow plug, (d) linear rolling bearings, (e-1) BN and (e-2) SiBCN ceramic fibers.....	14
<b>Figure 1-7:</b> (a-b) TEM images of Si-C nanoparticles interfaced with CNT, (c) SEM micrograph of Al <sub>2</sub> O <sub>3</sub> -CNT nanocomposites fracture surface, (d-e) SEM image of fracture surface of SiCN/CNT composite with 10 and 5 vol % CNT respectively, (f) SEM image of SiCN/MWCNT composite nanowires.....	18

**Figure 1-8:** (a) Single walled carbon nanotube model showing the sites (ends, sidewalls and bends) for chemical group functionalizing (b-f) SEM and TEM micrographs of PDC-MWCNT core shell structures synthesized at different processing conditions. .... 19

**Figure 1-9:** Cutaway diagram of the flowing-water thermal detector, illustrating the absorbing cavity and the water-flow channel on the outer surface of the cavity. .... 20

**Figure 1-10:** (a) Sectional side view of the thermal detector illustrating the actual systems used (b) Photograph of an actual copper cone used for laser calibration (inset: actual cone has its inner surface coated with CNTs)..... 21

**Figure 1-11:** (a) Spectral responsivity of four identical pyroelectric detectors comparing the thermal absorber coating performance. (b) Photographic image of a laser induced damaged area for MWCNT-sodium silicate coating with the beam size of ~2 mm (c) & (d) Comparison of damage threshold for the sprayed coatings upon irradiance at 1.06  $\mu\text{m}$  and 10.6  $\mu\text{m}$  respectively ..... 23

**Figure 1-12:** The properties of various black coating types highlighting the advantage of PDCs and CNTs for high power laser radiometry. A PDC-CNT composite is likely to exhibit both high laser damage threshold in air. .... 24

**Figure 1-13:** Comparison of specific power and energy of the LIB with other commonly used commercial batteries and super capacitors ..... 26

**Figure 1-14:** Schematic representation of a Li-ion battery full cell. Positive electrode in a commercial battery is a layered oxide of lithium (e.g.  $\text{LiCoO}_2$ ) and the negative electrode is carbon (e.g. graphite) ..... 28

**Figure 1-15:** Summary of possible cause, effect and prevention of battery operational issues in anode materials. .... 31

**Figure 1-16:** (a): Highlighted (shaded) area in the Si-O-C compositional triangle, represents the specimen with mixed bonds tetrahedra and (b) Initial electrochemical cycling data of three representative SiOC anodes that lie in the shaded region of the composition diagram ..... 33

**Figure 1-17:** (a) The oxygen-rich SiCNO ceramic shows higher reversible capacity than the nitrogen rich counterpart and (b) First charge/discharge cycles for SiCNO anodes prepared from nitrogen-rich (N/O= 61) and nitrogen deficient (N/O=0) specimen..... 35

**Figure 1-18:** (a) and (b) Electrochemical cycling of SiOC thin film anodes with thickness 0.5 and 500 micrometers respectively. Both cells were cycled at 100 mA.g<sup>-1</sup>. (c) and (d) Post electrochemical SEM surface of 0.5 and 500 micrometers thick anodes, respectively..... 36

**Figure 1-19:** (a) <sup>29</sup>Si Solid-state NMR data showing emergence of various Si chemical states when SiOC anode is at full-charged and discharged states (b) Comparison of cyclic voltammograms of SiOC anodes with commercial amorphous Si and SiO<sub>2</sub> ..... 37

**Figure 1-20:** (a) Comparison of electrochemical performance of SiCN specimens pyrolyzed at increasing temperatures. (b) First cycle charge/discharge capacities and coulombic efficiency comparison of various SiCN anodes specimens. First cycle loss in excess of (30 to 40) % is typical of polymer-derived SiCN ceramics, which makes them unsuitable for practical applications. .... 39

**Figure 1-21:** Step by step comparison of the effect of lithium intercalation and deintercalation in the silicon particle electrode with and without carbon nanotubes as conducting agents..... 40

**Figure 2-1:** Proposed reaction mechanism for molecular level interfacing of boron with poly(ureamethylvinyl)silazane liquid polymer. .... 69

**Figure 2-2:** (a) FTIR spectra of poly(ureamethylvinyl)silazane and boron-modified poly(ureamethylvinyl)silazane. (b and c) Experimental <sup>11</sup>B and <sup>29</sup>Si liquid NMR spectra of liquid

boron-modified polymer precursor collected at room temperature, respectively. The sample consisted of liquid precursor in  $C_6D_6$  solvent. .... 70

**Figure 2-3:** (a to d) SEM images of Si(B)CN coated MWCNTs pyrolyzed at 800, 1100, 1300, 1500 °C respectively. Arrows in (d) point at the ultra-long rod like structures..... 71

**Figure 2-4:** TEM images of nanowires pyrolyzed at (a) 800 °C, (b) 1000 °C, (c) 1000 °C (high resolution), (d) 1200 °C (e) Energy dispersive spectroscopy plot for 1200 °C specimen, and (f) 1300 °C. .... 72

**Figure 2-5:** (a) TEM image of one of the ultra-long rod structures that were observed for specimen processed at 1500 C. Inset: Select Area Electron Diffraction (SAED) pattern. .... 73

**Figure 2-6:** X-ray Diffraction plots for selected nanowire (powders) specimen. Si(B)CN shell is amorphous up to 1300 °C, crystallization is observed for specimen processed at 1500 °C..... 74

**Figure 2-7:** (a to f) Core level elemental XPS spectra of Si(B)CN-MWCNT synthesized 800 °C, 1100 °C, 1200 °C, 1300 °C, 1400 °C and 1500 °C respectively. .... 75

**Figure 2-8:** (a) Comparative experimental  $^{11}B$  SS-NMR spectra of the samples pyrolysed at 1000 °C, 1200 °C and 1400 °C shows the B-N type bond formation (preferred at higher temperatures) than B-O at lower processing temperatures. These spectra were collected by finely crushing the sample using mortar and pestle. .... 76

**Figure 2-9:** (a-g) Diffuse Reflectance Infrared Fourier Transform (DRIFT) spectra of samples pyrolyzed at 800, 1000, 1100, 1200, 1300, 1400 and 1500 °C. ( $\nu$ : stretching vibration mode and  $\delta$ : bending vibration mode)..... 77

**Figure 2-10:** (a) TGA plots showing the weight loss (%) and oxidation temperature (°C) for Si(B)CN, MWCNTs, Si(B)CN-MWCNTs and SiCN-MWCNTs performed in flowing air. (b) and (c) TEM micrographs showing residual TGA Si(B)CN-MWCNT and SiCN-MWCNT

respectively. MWCNTs could be seen in the Si(B)CN-MWCNTs TGA residual while for SiCN-MWCNTs, the material turned white indicating severe oxidation and burning of the CNT core. 78

**Figure 2-11:** Comparison of bulk SiCN/CNT and Si(B)CN/CNT nanowires heated in air up to (a) 1000 °C (b) 1340 °C in air..... 79

**Figure 2-12:** Raman spectra for various specimens prepared in this study. Raman plot of Si(B)CN-MWCNT TGA residual confirms presence of D (~1350 cm<sup>-1</sup>) and G (~1600 cm<sup>-1</sup>) bands (peaks) that are characteristic of CNT similar to that observed in “as-obtained” MWCNTs specimen. As expected, SiCN-MWCNT TGA residual did not show distinct D and G peaks indicating burning of MWCNTs in this specimen (correlating TEM observations in Fig. 2-10). 81

**Figure 2-13:** (a) Digital photograph of the pellets prepared at different pyrolysis conditions (1100, 1300 °C) and oxidation times (10, 25, 50 and 100 hours) (b) Corresponding powder XRD spectra of the as-prepared, 1100 °C-10 h, 1300 °C-25 h, 1300 °C-50 h, 1300 °C-100 h pellet specimens (c) Square of specific weight change versus oxidation time to determine the oxidation rate constant ( $K_p$ ) for the 1000 °C and the 1300 °C pellet specimens..... 82

**Figure 2-14:** Proposed structural evolution of Si(B)CN ceramic from polyborosilazane polymer precursor via cross-linked infusible mass..... 83

**Figure 3-1:** Experimental procedure for the synthesis of polymer-derived ceramic coated MWCNTs by (1) conventional heating method and (2) proposed method. .... 95

**Figure 3-2:** Block diagram of the experimental setup used for measuring the impedance at different resonant frequencies and the expanded view of field lines in the TEM mode in the coaxial connector with specimen sandwiched between conductors. .... 97

**Figure 3-3:** Symbolic illustration explaining the mechanism of non-covalent exohedral sequential sidewall functionalization of MWCNT with: (a) solvent (toluene), (b) boron-modified

polysilazane polymeric precursor and (c) pyrolyzed Si(B)CN ceramic following microwave irradiation..... 99

**Figure 3-4:** (a) and (b) are TEM images showing untreated polymer-MWCNT mix. (c) and (d) are the conventional TEM and high angle annular dark field (HAADF) images of Si(B)CN-MWCNTs synthesized by microwave irradiation, respectively. Note that elements with higher atomic weight (i.e., Si) appears bright in HAADF mode. .... 100

**Figure 3-5:** Core level elemental XPS spectra of Si(B)CN-MWCNT processed (a) at 800 °C for 4 hours and (b) exposed to microwave for 10 min. .... 101

**Figure 3-6:** Diffuse reflectance spectrum of Si(B)CN-MWCNT microwave (MW) specimen, Si(B)CN-MWCNT specimen pyrolyzed at 800 °C and the starting polymeric precursor ( $\nu$ : stretching vibration mode and  $\delta$ : bending vibration mode). .... 104

**Figure 3-7:** (a) TGA plots showing the comparative weight loss (%) for Si(B)CN-MWCNT composites synthesized by 10 minute microwave irradiation (black) and conventional pyrolysis at 800 °C (red). Labels indicate respective residual weight percentages. Weight loss for ‘as obtained’ MWCNTs (blue) and ‘untreated’ polymer-MWCNT mix (green) has also been included for comparison. TGA was performed in flowing air @ 25 mL/min. (b)-(d) TEM micrographs of TGA residual corresponding to Si(B)CN-MWCNT composite synthesized by microwave irradiation. .... 106

**Figure 3-8:** Dielectric properties calculated from impedance measurements: (a) Real permittivity quantifies the electrical energy the dielectric can retain; (b) imaginary permittivity determines the effectiveness to absorb microwave energy; and (c) loss tangent represents the ability to effectively convert the electromagnetic energy into heat energy, and (d) return loss is a measure of effectiveness of the power delivered from the transmission line to the load for the dispersed

MWCNT in polymer and agglomerated MWCNT specimens measured in the microwave frequency range from 100 MHz to 3 GHz. .... 110

**Figure 4-1:** Schematic representation of the spray coating process (Inset is the TEM image showing shell/core structure of the Si(B)CN-MWCNT composite). Uniformly dispersed Si(B)CN-MWCNT nanowires in toluene solution were spray coated using an air brush technique. The coated specimen were then baked overnight at 100 °C for curing..... 120

**Figure 4-2:** Digital image of the (a) bare copper test slide, (b) copper test slide coated with Si(B)CN-CNT composite, (c)-(d) copper test slide with incisions made on coating, (e)-(f) results of the Tape test using 3MTM Removable Repositionable 665 Clear Tape, and (g)-(h) Results of the Tape test using Scotch® General Purpose Masking Tape 234. .... 122

**Figure 4-3:** Table classifying the adhesion test results and highlighted class ‘4B’ (in red) corresponds to the flaking undergone by the composite coating when tested with Tape 2 ..... 123  
"Reprinted, with permission, from ASTM D3359-09<sup>e2</sup> Standard Test Methods for Measuring Adhesion by Tape Test, copyright ASTM International, 100 Barr Harbor Drive, West Conshohocken, PA 19428." ..... 123

**Figure 4-4:** Normalized Raman spectra of Si(B)CN MWCNT coatings exposed to laser irradiance at (a) 0 kWcm<sup>-2</sup> (unexposed), (b) 4 kWcm<sup>-2</sup>, (c) 8 kWcm<sup>-2</sup>, (d) 12 kWcm<sup>-2</sup>, and (e) 15 kWcm<sup>-2</sup> for 10 seconds respectively, along with the corresponding SEM micrographs. Scale bar (image b to e) is 1 mm. Insert (top left) is the digital camera image of the specimen..... 126

**Figure 4-5:** (a)-(b) SEM images of the ‘as-prepared’ coating on copper disk specimen. While (c) through (f) are SEM images from the coating area irradiated at 4, 8, 12, and 15 kWcm<sup>-2</sup> for 10 seconds, respectively. Image (d) seems out of focus because of the coating height difference. Scale bar is 5 micrometer in all images. .... 128



**Figure 4-6:** Normalized Raman spectra of Si(B)CN-MWCNT coatings exposed to laser irradiance at (a) 0 kWcm<sup>-2</sup> (unexposed), (b) 4 kWcm<sup>-2</sup>, (c) 8 kWcm<sup>-2</sup>, (d) 12 kWcm<sup>-2</sup>, and (e) 15 kWcm<sup>-2</sup> for 2 seconds, respectively with the corresponding low-magnification SEM micrographs. Scale bar (image b to e) is 1 mm. Insert (top left) is the digital camera image of the plate specimen. .... 129

**Figure 4-7:** SEM micrographs showing laser-irradiated areas of the coating for copper plate specimen at (a) 4 kWcm<sup>-2</sup>, (b) 8 kWcm<sup>-2</sup>, (c) 12 kWcm<sup>-2</sup>, and (d) 15 kWcm<sup>-2</sup> for 2 seconds exposure. Scale bar is 5 micrometer in all images..... 131

**Figure 4-8:** (a) Measured reflected power profiles for the incident laser of 1.137 W at 10.6 μm wavelength from various irradiated areas on the coating for the copper disk specimen. Peak power measurements made with less than 0.5% variance. (b) Mid-IR range spectral absorption response of Si(B)CN-MWCNT coating before and after irradiation at 15 kWcm<sup>-2</sup> for 10 seconds. .... 132

**Figure 4-9:** Elemental X-ray photoelectron spectra of Si(B)CN-MWCNT coatings on copper plate specimen exposed to laser irradiance at (a) 0 kWcm<sup>-2</sup> (unexposed), (b) 4 kWcm<sup>-2</sup>, (c) 8 kWcm<sup>-2</sup>, (d) 12 kWcm<sup>-2</sup>, and (e) 15 kWcm<sup>-2</sup> for 2 seconds, respectively..... 134

**Figure 5-1:** High-resolution TEM images of the Si(B)CN-CNT-1100 composite showing the shell/core morphology. .... 144

**Figure 5-2:** First and second electrochemical intercalation and deintercalation cycles and corresponding dQ/dV plots for (a)-(b) SiCN-1100, (c)-(d) Si(B)CN-1100, and (e)-(f) Si(B)CN-CNT-1100. .... 148

**Figure 5-3:** First two electrochemical voltage profiles and corresponding differentiated capacity with respect to the voltage for (a-b) Si(B)CN-CNT-800, (c-d) Si(B)CN-CNT-1500. Comparison

of charge (reversible) capacity versus the cycle number for: (e) for SiCN-1100, Si(B)CN-1100 and Si(B)CN-CNT-1100 anodes, and (f) various Si(B)CN anodes showing the effect of pyrolysis temperature (20 cycles only)..... 150

**Figure 5-4:** (a) First and second charge/discharge cycles for the MWCNT anode, cycled at 100 mA/g, and (b) Charge capacity for the first 30 cycles for MWCNT anode..... 152

**Figure 5-5:** GITT Data: (a) Charge and discharge cycles with 15 min of current pulse at 100 mA/g followed by 4 h of relaxation for Si(B)CN-CNT- 1100 specimen and (b) calculated diffusion coefficient based on the relaxation steps at the corresponding voltages. .... 153

**Figure 5-6:** 4-point resistivity measurement test setup..... 154

**Figure 5-7:** X-ray diffraction data for various Si(B)CN and SiCN pellet specimen, confirming the amorphous nature of the precursor-derived Si(B)CN ceramic for temperatures below 1500 °C. .... 156

**Figure 5-8:** Comparison of SEM images of “as-prepared” anodes with the cycled anodes (disassembled in delithiated state) for (a, b) SiCN-1100 (after 30 cycles), (c, d) Si(B)CN-1100 (after 30 cycles), (e, f) Si(B)CN-CNT-800 (after 20 cycles), (g, h) Si(B)CN-CNT-1100 (after 30 cycles), and (i, j) Si(B)CN-CNT-1500 (after 30 cycles)..... 157

**Figure 5-9:** (a) Elemental survey (top) and (b) high-resolution scan (bottom) for SiCN-1100, Si(B)CN-1100, and Si(B)CN-CNT cycled anode specimens. .... 159

**Figure 6-1:** Schematic displaying the stepwise procedure for synthesis of SiOC (shell)-CNT (core) composite. TTCS is the polymeric precursor for SiOC ceramic..... 169

**Figure 6-2:** SEM, TEM image and Histogram (size distribution) of various SiOC/CNT composites prepared in this study: (a, b, c) SiOC/CNT-5, (d, e, f) SiOC/CNT-8 and (g, h, i)

SiOC/CNT-10, respectively. Thicker composite nanowires were observed for composites with lower CNT loading. .... 172

**Figure 6-3:** (a) Schematic representation of the molecular level interfacing of TTCS polymeric precursor with CNT sidewalls and resulting transformation to SiOC ceramic shell up on pyrolysis (the schematic is Not To Scale). (b) XRD data confirming the amorphous nature of polymer-derived SiOC ceramic (hallmark of these materials) and survival of carbon nanotubes in SiOC-CNT composites (peak at 26 degrees). (c) FTIR spectra showing chemical bond evolution for MWCNTs, cross-linked TTCS polymer, SiOC ceramic and various SiOC-CNT composite specimens. Polymer to ceramic conversion generally involves breaking of Si-H and Si-CH<sub>3</sub> bonds with release of hydrogen and other volatile species such as CO<sub>2</sub>, CH<sub>4</sub>, H<sub>2</sub>O etc., and (d) TGA data for determination of weight percent of CNTs in final composite. .... 175

**Figure 6-4:** Electrochemical data for various SiOC anodes used in this study: (a, c, e, g, i) first and second charge/discharge profiles for SiOC, MWCNT, SiOC/CNT-5, SiOC/CNT-8, and SiOC/CNT-10, respectively. (b, d, f, h, j) differentiated capacity versus voltage plot for SiOC, MWCNT, SiOC/CNT-5, SiOC/CNT-8, and SiOC/CNT-10, respectively. .... 177

**Figure 6-5:** (a) Specific discharge capacity and efficiency of the SiOC particles and MWCNTs cycled for 40 cycles. (b) Specific discharge capacity and efficiency of SiOC/CNT anode specimens cycled for 40 cycles at ~C/10. .... 178

**Figure 6-6:** SEM micrographs (Left: low mag and Right: high mag) of various disassembled anode specimen after testing for 40 cycles, (a, b) SiOC (active anode weight :1.4 mg), (c, d) SiOC-CNT-5 (active anode weight : 1.4 mg), (e, f) SiOC-CNT-8 (active anode weight : 1.5 mg), and (g, h) SiOC-CNT-10 (active anode weight : 1.6 mg). All anodes were approximately 127 μm thick..... 181

**Figure 6-7:** Rate capability test data for SiOC, SiOC-CNT-5, SiOC-CNT-8 and SiOC-CNT-10 anode specimens showing specific discharge capacity and columbic efficiency. All SiOC-CNT anodes showed stable performance with SiOC-CNT-5 showing best overall cycleability. .... 182

**Figure 6-8:** Rate capability test data for SiOC, SiOC-CNT-2.5 and SiOC-CNT-5 anode specimens showing specific discharge capacity and columbic efficiency..... 183

**Figure 6-9:** (a) 15 min of current pulse at 100 mA/g for SiOC/CNT-5 anode specimen (b) Cell voltage response during the current pulse and relaxation for SiOC/CNT-5 anode specimen (c)-(d) calculated diffusion coefficient based on the pulse and relaxation steps at the corresponding voltages during lithitation and delithiation. .... 184

## List of Tables

<b>Table 1-1:</b> Summary of the organosilicon polymers and corresponding ceramics derived using conventional pyrolysis. ....	6
<b>Table 1-2:</b> Summary of various physical properties of polymer derived SiCN and SiOC ceramics and comparison with conventional SiC and Si <sub>3</sub> N <sub>4</sub> ceramics. ....	13
<b>Table 1-3:</b> Summary of the experimental results of the electrochemical cycling of PDC and their nanocomposites. ....	42
<b>Table 2-1:</b> XPS Chemical composition of SiBCN-MWCNT nanowires for varying pyrolysis temperatures ( $T_{\text{pyrolysis}}$ ). Hydrogen content is assumed to be less than 1 wt % and is neglected in analysis. ....	76
<b>Table 3-1:</b> XPS elemental and phase analysis comparison of the specimen synthesized by microwave exposure for 10 min and pyrolysis at 800 °C for 4 hours. ....	102
<b>Table 3-2:</b> Summary of oxidation temperatures and residual weight obtained from TGA analysis of various specimens used in this study. ....	107
<b>Table 4-1:</b> Dependence of D-peak position and $I_D/I_G$ (Intensity ratio of D and G peak) as observed in the Raman spectra for the disk specimen, on the incident laser irradiation power density. ....	127
<b>Table 4-2:</b> Dependence of D-peak position and $I_D/I_G$ as observed in the Raman spectra for the plate specimen, on the incident laser irradiation power density. ....	130
<b>Table 4-3:</b> Atomic composition of Si(B)CN-MWCNT coating for unexposed and irradiated coating areas (2 seconds exposure) for copper plate specimen obtained through XPS. ....	135
<b>Table 5-1:</b> Summary of electrochemical cycling data for various specimens. Error in the measurements is $\pm 0.1$ %. ....	147

**Table 5-2:** Summary of surface elemental composition of various specimen (atomic percent) used in this study all atomic percentage measurements are accurate up to approximately 15% 158

**Table 6-1:** Summary of the TGA data. Weight percent of CNTs in SiOC is calculated based on the residual weight. All weight values in the table are accurate up to 0.1 %. ..... 174

**Table 6-2:** Summary of the electrochemical data and comparison with results from literature. (\*2nd cycle onwards)..... 179

## Acknowledgements

I would like to thank my Advisor, Dr. Gurpreet Singh for his useful suggestions and comments that helped me improve the quality of my work. I am grateful for his mentorship and inspiration. In addition, I would also like to acknowledge the Mechanical and Nuclear Engineering Department at Kansas State University for financial support.

Thanks are also due to Dr. John Lehman, Dr. Chris Cromer, Dr. Elisabeth Mansfield and Ari Feldman (NIST-Boulder) for the help with Laser irradiation experiments. I would also like to thank Professor Rishi Raj (University of Colorado), Dr. Yigal Blum (SRI International) and Prof. Gian Soraru (University of Trento) for helpful suggestions related to processing of polymer-derived ceramics. Prof. Bill Kuhn (KSU) for the help with dielectric measurements. I would also like to thank my PhD thesis committee members Prof. Mary Rezac, Prof. Kristan Corwin and Prof. Terry Beck for reading my thesis and providing useful suggestions.

I would like to express my gratitude to the following people for providing training on/access to various characterization instruments: Prof. Vikas Berry, Dr. Daniel Boyle, Dr. Leila Maurmann, Dr. Dewey Barich (KU), Dr. Charles Ye (KU), Dr. Jerry Hunter (Virginia Tech), Prof. Jun Li, Myles Ikenberry, Abhijit Sinha, Dr. Deon van der Merwe, Dr. John Desper, Dr. Hongwang Wang and Yen Ting Kuo.

I am extremely thankful to my colleagues Lamuel David, Uriel Barerra and Alex Wu for their assistance with various experiments. I would also like to thank Prof. Z. J. Pei, Prof. Mark Hollingsworth, Prof. Takashi Ito, Kabeer Jasuja, Nihar Mohanty, Tashfin Hussain, Prashant Chopade, Lateef Syed, Mausam Kalita, Sreeram Cingarapu, Ibrahim Saleh, Jim Hodgson, Ron Jackson and Steve Booth and for their helpful suggestions.

For rechargeable batteries, I would like to thank Marco Cologna, Kalvis Terauds, Issac Scott, Steve Klankowski and Professor Palani Balaya for sharing their knowledge.

I am thankful to my parents, parents-in-law and brother for their love and support. I am grateful to Nana (Shri Mannalal Baid) for his unconditional love and blessings. I also thank Abhinav Singhal, Dr. Rahul Singhvi and Dr. Keyur Patel for their motivation. I made some very good friends during past few years. A big thank you goes to Naanu, Jeri, Arka, Nabaneeta, Siddharth, Abhinav, Uma, Shantanu, Jhinook, Mandeep, Neha, Foram, Duane, Nivas and Manu.

Last and most importantly, I would like to thank Aditi for loving & supporting me during all times.



# **Dedication**

To my mother and my wife

# Chapter 1 - Introduction

## 1.1 Polymer-derived ceramics

Polymer-derived ceramics (PDCs) are advanced engineering ceramics synthesized by thermal decomposition of certain high molecular weight organometallic polymers. PDCs were first synthesized in early 1960s as binary systems and were proposed for making micrometer sized SiC/Si<sub>3</sub>N<sub>4</sub> fibers for high temperature applications [1-3]. They were then suggested as a potential replacement for contemporary carbon fibers. Interest in PDCs further grew with time with the development of desired polymer precursor chemistries and various nanocharacterization tools that allowed the study of these materials in greater detail (Fig. 1-1).

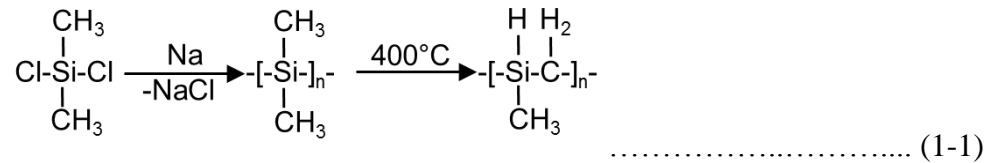
PDCs are generally classified based on the number of constituent elements or phases in the synthesized final ceramic. Binary systems like SiC, Si<sub>3</sub>N<sub>4</sub>, BN, BC and B<sub>2</sub>O<sub>3</sub>, tertiary systems like SiCN, SiBC, SiCO and BCN and quaternary systems like SiBCN, SiBCO, SiAlCO and SiCNO are popular and have been mainly investigated. A unique feature observed in these ceramics (tertiary and higher order systems) is their amorphous structure when synthesized in the temperature range of (800 to 1400) °C with silicon forming mixed bonds with both carbon and nitrogen/oxygen. This unique molecular level bonding of carbon with other elements in the ceramics is a distinct feature of PDCs, which is also responsible for their multifunctional properties.

PDCs differ from other conventional ceramics in several ways. Unique features such as process flexibility to attain near net shape of the desired structure, controlled molecular structure of the final ceramic based on precursor chemistry, ease of synthesizing a composite, low processing temperatures and elemental doping are generally not possible for other ceramics.

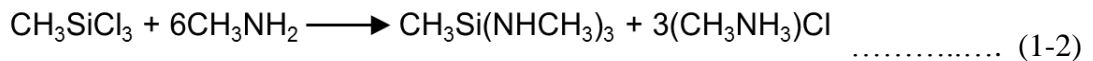
### 1.1.1 Polymer Synthesis

Si-based preceramic polymers are composed of long repetitive chains of silicon based monomers (-Si-C-, -Si-N-, -Si-O-) in the backbone and organic groups on its branches. Thermolysis of polymer precursors in controlled conditions (inert atmosphere) results in formation of amorphous/crystalline ceramic depending on processing temperatures and precursor's chemical structure (Table 1-1).

The synthesis of polymer precursor for the binary system was first demonstrated in 1970s by Yajima and coworkers, where dimethyldichlorosilane was used to form polycarbosilane, which on thermolysis yielded SiC ceramic fibers as shown in equation 1-1[4].



Verbeek in 1974, synthesized N-methyl polysilazane by reacting (ammonolysis of) trichloromethylsilane with methylamine as shown in equation 1-2 [3].



Synthesis of quaternary PDC was first investigated in 1984 by Takamizawa *et al.* using single source polymer precursor [5]. By decomposition and polycondensation of polydimethylsilane with B-trimethyl-N-triphenylborazine they synthesized Si-B-C-N ceramic [5]. But co-condensation of constituting molecules for synthesizing polymers was the most commonly used method [6-9]. Alternatively, synthesis of polyborosilazane or polyborocarbosilazane by hydroboration of single source precursor (chlorine substituents) and nitrogen containing (methyl amine) compounds as crosslinking agent followed by condensation and deamination reactions is also a very popular method [10]. The major issue with this process was the formation of

ammonium chloride salt, which had to be washed out using liquid ammonia or by sublimation. To overcome this, use of a less reactive hexamethyl disilazane as a crosslinking agent instead of ammonia to avoid the formation of  $\text{NH}_4\text{Cl}$  was proposed as shown in equation 1-3. Hence, the use of a single source precursor involved multiple steps and was a lengthy process.

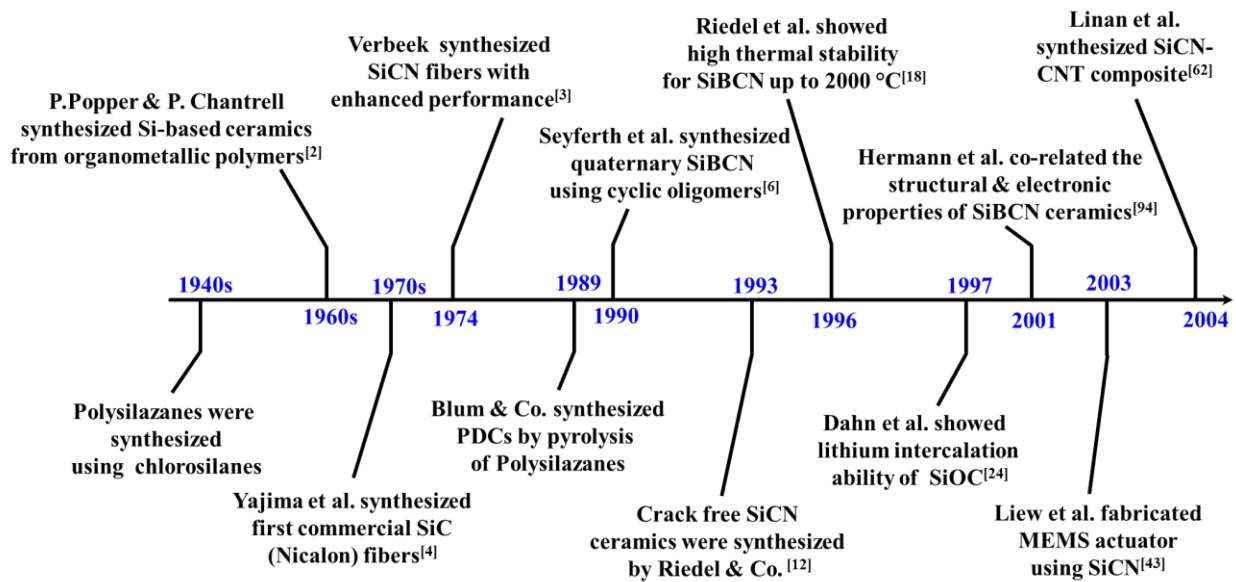
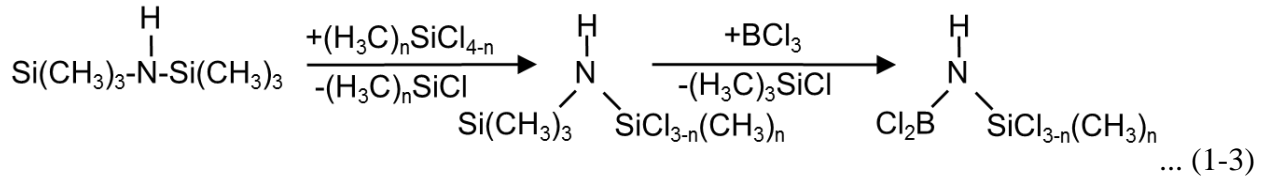


**Figure 1-1:** Timeline of the most important inventions and findings of PDCs.

### 1.1.2 Polymer to ceramic conversion

Polymeric precursors are designed depending on the desired chemical composition of the final ceramic by following the appropriate processes, discussed earlier (Table 1-1). The discussion in this work is limited to polysilazane, polysiloxane and polyborosilazane precursors, which results in the formation of SiCN, SiOC and SiBCN PDCs, respectively.

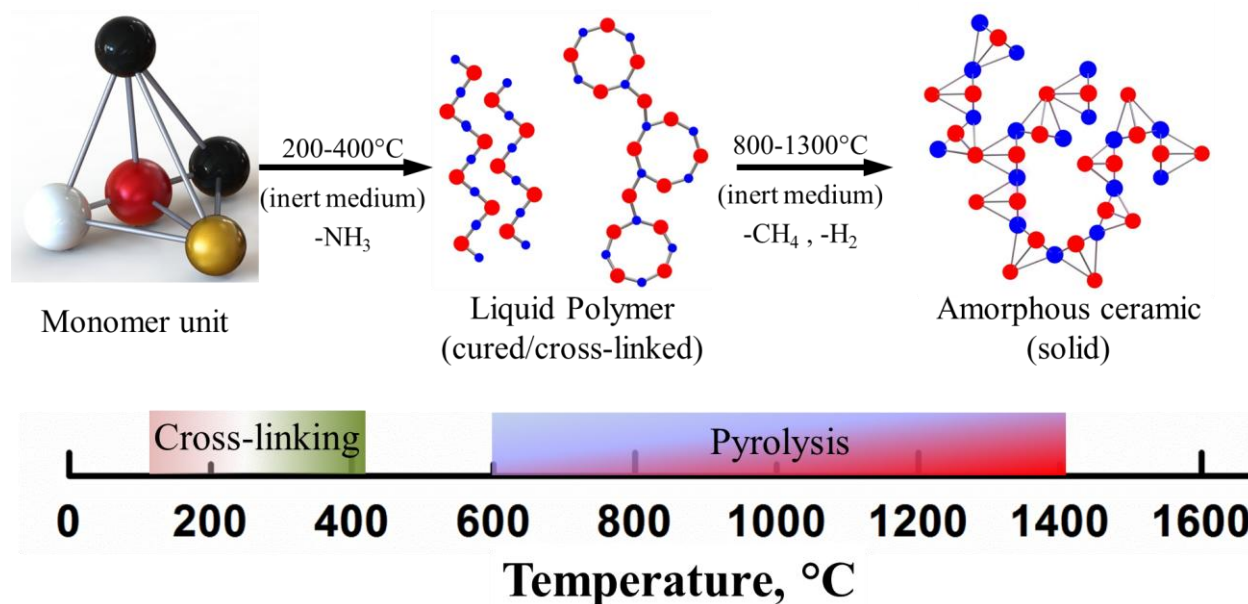
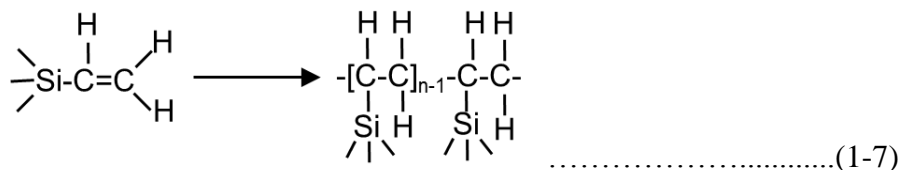
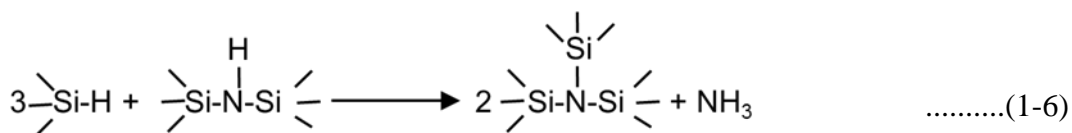
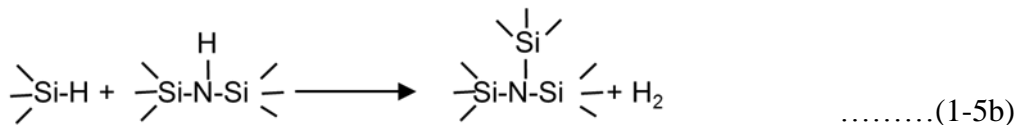
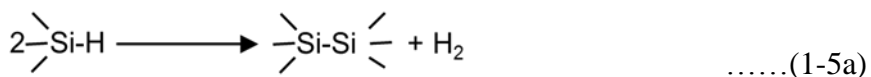
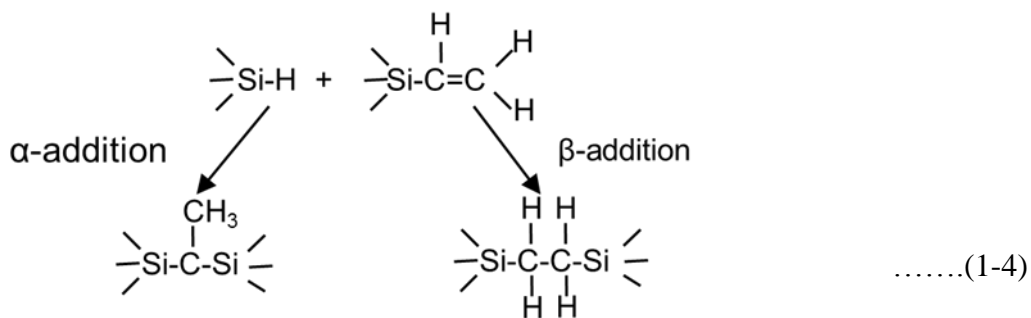


**Figure 1-2 :** Stepwise synthesis of amorphous ceramic from liquid polymer precursor (shown: polysilazane) [11,12].

Polymer to ceramic conversion can be accomplished by two main synthesis routes i.e. monomer route or polymer route. The complete conversion of polymer to ceramic is mainly a two-staged process (Fig. 1-2). The first stage carried out at low temperature ( $\sim 400$  °C) in inert medium is known as the cross-linking of polymer. Cross-linking results in increased bonding between the elements of the precursor leading to highly interconnected backbone (Si-N, Si-C, Si-O, etc.), reducing the volatility of the crosslinked product and increasing the ceramic yield. Crosslinking can be carried out by either a thermal or a chemical route. In thermal crosslinking, the liquid ceramic precursor is heated at low temperatures for a predetermined time in the presence of inert gases, whereas in chemical route, catalysts like peroxides are used along with heating. In thermal cross-linking vinyl or silyl functional groups are intentionally added to the polymer precursor for effective cross-linking. Thermal cross-linking is preferred over chemical route as the possibility of chemical contamination is less. Four main thermal cross-linking routes (for polysilazanes) are hydrosilylation of the vinyl group, dehydrocoupling of Si-H and N-H groups, transamination by

trisilylating nitrogen atoms and vinyl polymerization reaction shown in equations (1-4) to (1-7), respectively.



Experimental evidence for the increased cross-linking of polymer precursor was shown to depend on the amount of vinyl or Si-H groups instead of N-H or methyl groups. Moreover, highest cross-linking was observed for the hydrosilylation followed by dehydrocoupling, transamination and vinyl group polymerization. The mono- or oligomer precursor compound can thus be pre-cured and molded or drawn in the desired structure.

**Table 1-1:** Summary of the organosilicon polymers and corresponding ceramics derived using conventional pyrolysis.

Liquid organosilicon polymer precursor	Ceramic	Reference
Polycarbosilanes	Si-C	4
Polysilsesquioxanes	Si-O-C	13
Polycarbosiloxanes	Si-O-C	14
Polysiloxanes	Si-O-C	15
Polysilazanes, Polysilylcarbodiimides, Polysilsesquicarbodiimides	Si-C-N	16
Polysilsesquicarbodiimides	Si-C-N	16
Polyvinylsilazane	Si-C-N	6
Polysilsesquioxanes	Si-C-N	17
Polyborosilazanes	Si-B-C-N	18
Polyborosiloxanes	Si-B-C-O	19

Followed by crosslinking, is pyrolysis carried out at 800-1400 °C under inert conditions. During pyrolysis, thermal induced decomposition of cross-linked polymer releases oligomer, hydrocarbons and other volatile compounds and consolidates to amorphous ceramic. More hydrogen is retained at lower processing temperatures (~800 °C). Annealing (beyond 1400°C) results in nucleation and growth of nano-sized crystalline phases in the ceramic. Meanwhile, depending on the polymer chemical structure and composition, precipitation of free sp<sup>2</sup> bonded carbon occurs during the polymer to ceramic conversion. The chemical composition of the final

ceramic depends on the polymer precursor chemistry, presence of reactive groups, degree of crosslinking, heating rate and pyrolysis environment. The density of the final ceramic is generally higher (1.8 to 2.3) g/cc than the polymer precursor (~1 g/cc) resulting in linear and volumetric shrinkages due to the synthesis process. This structural transformation results in formation of defects like cracks and pores within the ceramic.

Several alternative methods have been suggested to reduce these defects in ceramics. Lcke *et al.* showed that the ‘branched polymer’ precursor resulted in higher ceramic yield (51-77%) as compared to the unbranched precursors (~15%). Branching is believed to increase the molecular weight of the crosslinked polymer and reduce the polymer volatility. Crosslinked polymer’s heating rate is also a critical aspect as higher rate results in formation of cracks and pores whereas slower rate can cause the volatile elements to evaporate.

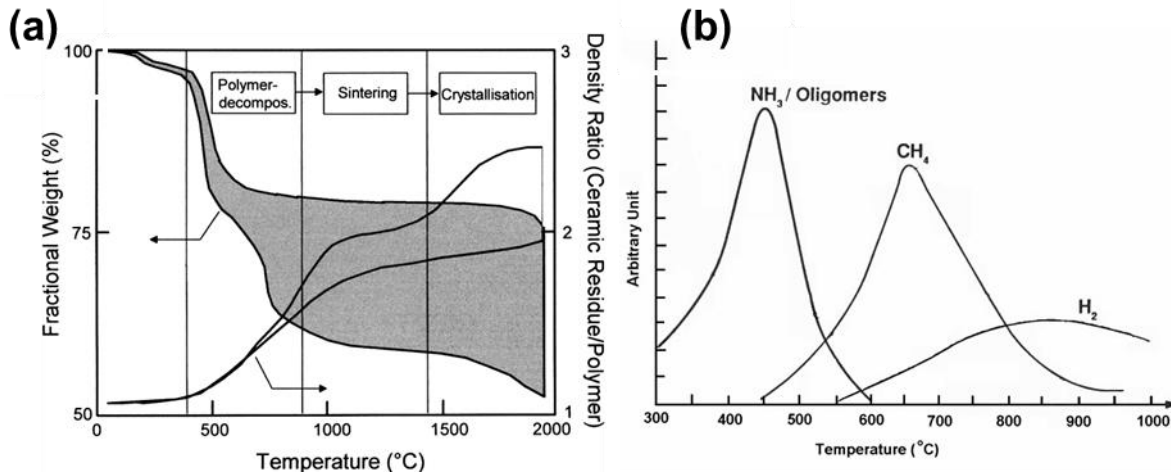


**Figure 1-3:** (a) Weight change and densification of PDCs during the thermal decomposition as a function of ceramic processing temperatures and (b) analysis of the gases evolved corresponding to the processing temperatures for a polysilazane polymer [11,20].

During the complete conversion of polymer (shown: polysilazane) to ceramic the weight loss due to released gases at different temperatures is shown in Fig. 1-3. Initial weight loss at lower temperatures (<500 °C) is due to the evaporation of oligomers due to hydrosilylation and



ammonia gas due to transamination reaction. At higher temperatures of up to 800 °C, hydrocarbons and hydrogen release results in further weight loss.

The temperature, at which the weight loss occurs, is largely governed by the polymer precursor chemistry and heating rates.

During the conversion of polymer to ceramic, carbon present in the precursor is either released at about 600-800 °C or is retained in the form of free turbostratic carbon and other carbon bound to parent silicon atoms. The presence and distribution of carbon in PDCs is critical as it influences the engineering properties (thermal stability, electrical conductivity, etc) of PDCs.

### **1.1.3 Polymer Derived Ceramic Structure**

PDC are covalently bonded ceramics, generally synthesized through controlled thermal decomposition of certain organosilicon polymers like polysilazane, polysiloxanes, polycarbosilanes and polyborosilanes in inert atmosphere. PDCs have been shown to exhibit numerous functional properties including high electrical conductivity, high temperature stability, chemical resistance, creep resistance and mechanical strength. The ability to engineer the functional properties of PDCs by programming the synthesis conditions is an important feature of these materials.

These properties are mainly attributed to their temperature dependent microstructure which consists of  $-sp^2$  bonded carbon network along with nanodomains of silicon mixed bond tetrahedra that resists crystallization up to approx. (1300 to 1500) °C (Fig. 1-4).

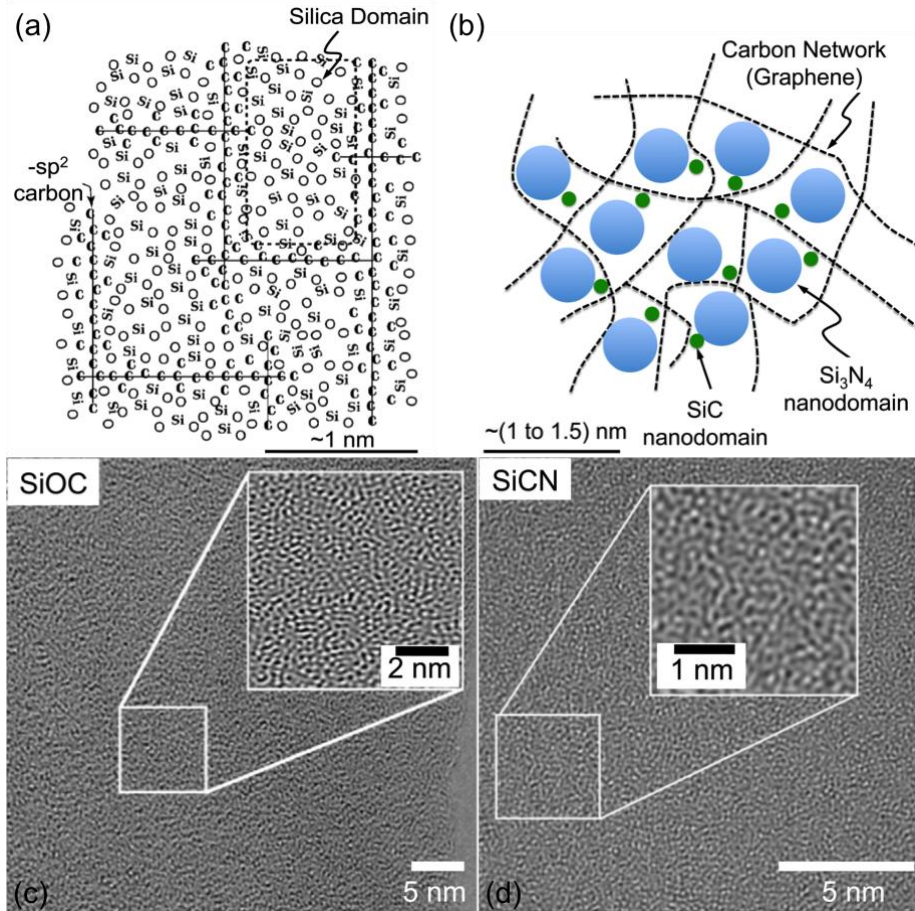


**Figure 1-4:** (a) Predicted nanodomain structure of polymer-derived SiOC ceramic [21] and (b) SiCN ceramic prepared from pyrolysis of polysilylcarbodiimide precursor [22]. Presence of graphitic carbon and nanovoids in these amorphous ceramics provide ample sites for Li-ion intercalation. (c) and (d) High-resolution TEM images of SiOC [23] and SiCN specimens [24] pyrolyzed at 1000 °C. These ceramics are featureless in both X-ray and TEM up to at least 1300 °C.

#### 1.1.4 Tunable Engineering Properties

As discussed earlier, the chemical composition of the polymer precursor and the processing conditions mainly govern the structure of the final ceramic that determines the PDC's properties.

Thus PDC's properties are tunable based on synthesis conditions (Table 1-2). Some of the important properties are discussed below.

(a) Thermodynamic stability: PDCs such as SiOC and SiCN are thermodynamically more stable than their crystalline binary forms (such as SiO<sub>2</sub>, SiC and Si<sub>3</sub>N<sub>4</sub>) primarily because of the presence of Si mixed bond tetrahedra and excess free-carbon that limits atomic mobility in the ceramic resisting crystallization up to very high temperatures.

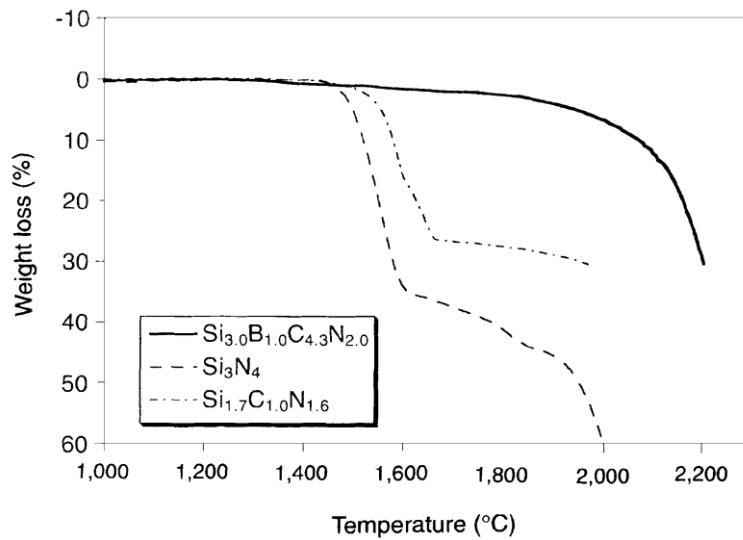


**Figure 1-5:** High temperature thermal stability comparison of Si<sub>3</sub>N<sub>4</sub> with PDC-SiCN and SiBCN ceramics with tunable behavior [18].

Generally, it is the carbon-rich PDCs that show higher resistance to crystallization than carbon deficient PDCs. In case of SiCN, it is believed that graphene like carbon wraps (seals) around Si<sub>3</sub>N<sub>4</sub> domains and thereby limits outward diffusion of nitrogen atoms. Addition of elements like B, Zr and Hf has been shown to further improve resistance to crystallization and decomposition of SiCN at high temperatures [25]. Boron is known to form a turbostratic B-C-N phase with carbon resulting in a diffusion barrier in Si-B-C-N ceramics, further improving their thermal stability (Fig. 1-5) [26]. Hence, thermodynamic stability in these materials can be tailored by

either elemental doping (ternary to quaternary systems) or by controlling the processing conditions.

Generally silicon based ceramics undergo oxidation when exposed to high temperatures. Oxidation of these ceramics results in the formation of an oxide scale which acts as a protective covering on the ceramic at the surface and prevents further oxidation. The quality of the passivating layer depends on the amount of silicon present on the surface [27].

(b) Electrical conductivity: PDC can be made semi-conducting or insulating depending upon the pyrolysis temperature, which in turn determines the microstructure and amount of electron conducting phases in the final ceramic. In general, electronic conductivity increases with increasing pyrolysis temperatures, which also coincides with increasing free-carbon phase. For PDCs synthesized at low temperatures (600 to 800) °C, D.C. conductivities in the range of ( $10^{-10}$  to  $10^{-8}$ ) S/cm have been reported [28-30]. While semiconducting or even metallic conductivities have been observed for PDCs synthesized between (1000 to 1400) °C, which is usually attributed to the formation of a carbon percolation network. Even higher electronic conductivities for PDCs synthesized above 1400 °C were understood to be due to the percolation of nano-crystalline phases formed. Further increase in electrical conductivity can also be achieved by means of doping.

(c) Chemical stability: SiOC have been shown to possess better chemical stability than conventional SiO<sub>2</sub>, due to the presence of free carbon, stable Si-C bonds and overall disordered ceramic structure. The chemical stability of SiOC tends to depend on the formation and separation of Si-C and SiO<sub>2</sub> phases (increase in phase formation reduces its chemical stability). The presence of Si-C bond (resists the nucleophilic reactions) and the graphene like carbon network suppresses chemical diffusion into these ceramics [31]. Similarly, chemical stability of

polymer-derived SiCN and Si(B)CN have also been shown to be higher than crystalline Si-N or SiC.

(d) Mechanical properties: Mechanical properties of PDCs have majorly been investigated in the form of fibers. Most PDCs show tensile strength (up to 3 GPa) and elastic modulus (50 to 150) GPa, which is slightly lower as compared to the conventional ceramics [32]. The elasticity of PDCs depends on the atomic arrangement and their covalent bonding. For SiOC ceramics, carbon provides the rigidity, which is balanced by flexibility of oxygen in the silicon tetrahedral. Bulk density ( $1.8$  to  $2.3 \text{ g/cm}^3$ ) increases with increasing pyrolysis temperature due to lesser hydrogen in the ceramic and has a positive influence on mechanical strength and elastic modulus.

(e) Processability: PDCs can be synthesized using traditional processing techniques such as hot and cold pressing, extrusion and injection molding. Further, the direct polymer-to-ceramic processing route makes these ceramics suitable for making complex structures at micro and nanometer scales including fibers [32, 34], thin films [35] and shell/core nano-composites [36, 37-41]. In addition, the polymer-to-ceramic route also allows homogenous distribution of constituent elements at the molecular level with controlled microstructure.

It is also possible to control the porosity in these ceramics. Colombo *et al.* have demonstrated porous PDCs with volumetric porosity ranging between (55 to 90) %, cell size ranging from (1 to 2000)  $\mu\text{m}$  and resulting surface area ranging from (150 to 700)  $\text{m}^2.\text{g}^{-1}$  [42].

**Table 1-2:** Summary of various physical properties of polymer derived SiCN and SiOC ceramics and comparison with conventional SiC and Si<sub>3</sub>N<sub>4</sub> ceramics [33,42].

Properties	PDC-SiCN	PDC-SiOC	SiC	Si <sub>3</sub> N <sub>4</sub>
Appearance	Dark Brown-Black	Dark Brown-Black	colorless, green, yellow	Dark grey
Density (g/cm <sup>3</sup> )	1.85-2.35	1.85-2.35	3.17	3.19
Δ Young's modulus (GPa)	90-150	57-113	400	320
Poisson's Ratio	0.21-0.24	0.11	0.14	0.24
#Strength (MPa)	~1000	250	420	700
Vickers Hardness (GPa)	≈ 8-15	≈ 5-9	30	28
Fiber's Tensile Strength (GPa)	1.3	3	2.5	6.2
Fracture toughness (MPa•m <sup>0.5</sup> )	≈ 0.56-3	--	4.6	6.1
Shear Viscosity (Pa•s)	2 x 10 <sup>13</sup>	3 x 10 <sup>13</sup> -10 <sup>17</sup>	--	--
Electrical Conductivity (S/cm)	10 <sup>-15</sup> -10 <sup>0</sup>	10 <sup>-13</sup> -10 <sup>-1</sup>	10 <sup>-6</sup> -10 <sup>-2</sup>	10 <sup>-14</sup> -10 <sup>-12</sup>
Oxidation resistance (°C)	1400	1200	1400-1600	1000
Thermal Shock = (#) / (*.Δ)	~300	--	350	880
Thermal Conductivity (W/m•K)	0.3-0.7	--	120	30
*Coefficient of thermal expansion (x10 <sup>-6</sup> /K)	3	--	3.8	2.5

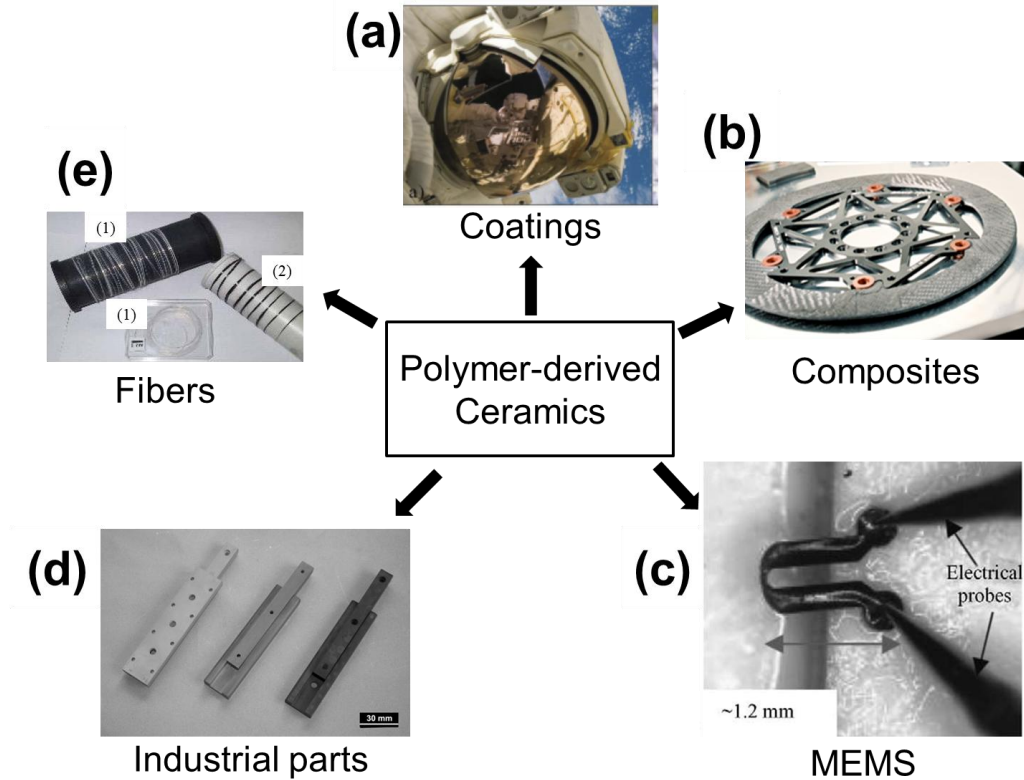


**Figure 1-6:** Application of PDCs in (a) SMP-10 (polycarbosilane) used to repair heat shield in a space shuttle [47], (b) CMC (C/SiC) brake rotor of motorbike [47], (c) Micro glow plug [46], (d) linear rolling bearings [48], (e-1) BN and (e-2) SiBCN ceramic fibers [45].

(f) Optical properties: Black color of PDC is ascribed to the presence of free  $sp^2$  carbon present in the ceramic network structure. Molecular tailoring of SiCNO ceramics demonstrated controlled luminescence when tested from 500 -800 nm [43]. Lower temperature (500-600 °C) synthesized specimen exhibits intense luminescence whereas high temperature specimens are more absorbing.

In another investigation, Karakuscu *et al.* studied the effect of incremental synthesis temperature on luminescence of SiCO thin films. Specimens synthesized at low pyrolysis temperature (800-1000 °C) showed UV-blue luminescence, whereas high-temperature specimens emitted green–yellow luminescence. For Si-rich SiCO films, intense white luminescence was observed with a

broad emission from 430 to 900 nm while for C-rich SiCO films no measurable luminescence was observed due to absorption by carbon clusters [44]. Increasing challenges and rising expectations for ceramics used in engineering applications have driven the rapid development of PDC ceramics (Fig. 1-6).

## **1.2 Carbon Nanotubes**

$sp^2$  hybridized elemental carbon have been shown to exhibit a well-defined nanostructured form. Among these nanostructures  $C_{60}$  (buckyball), carbon nanotube and graphene sheets are most popularly investigated since last two decades. These nanostructures are either synthesized by bottom-up methods (atom to nanostructure) or by top-down approach (bulk to nanostructures), depending on the application requirements [49-52]. Carbon nanotubes (CNT) generally exist as single walled or concentrically arranged multi-walled tubular (MWCNT) structures. In MWCNT each tube is concentrically separated by a fixed distance (carbon to carbon spacing of  $\sim 0.34$  nm). Under normal conditions the nanotubes are weakly bonded by van der Waals forces with each other. Their diameter typically ranges from 1-50 nm and length from few  $\mu m$  to mm. MWCNTs are mainly synthesized using arc-discharge, laser-ablation and catalytic growth methods and are characterized using electron microscopy (SEM, TEM, STEM, etc.) and spectroscopy techniques like Raman and other optical methods [49-52].

### **1.2.1 Engineering Properties**

CNTs are structurally classified based on their diameter and chirality which governs their physical properties. SWCNTs can be either semiconductor or quasi-metallic. Band gaps varying from  $\sim 0.5$  eV to 10 meV have been reported for tubes with identical ( $\sim 1.5$  nm) diameters depending on their chirality. MWCNTs on the other hand usually exhibit semiconducting behavior [53].



Mechanical properties of CNTs in the bundled form or with a few structural defects are mainly investigated by the use of HRTEM, STEM or AFM. Based on the previous results that showed graphite in-plane modulus (1.06 TPa), C-C bond properties (130 GPa) and whiskers (20 GPa), CNTs were expected to exhibit similar magnitude of strength and stiffness [54-56]. Uniquely, CNTs possess high flexibility and high strength along with high stiffness. Young's modulus measured for individual arc-grown MWCNTs (26-76 nm diameter) using AFM were measured to be  $1.28 \pm 0.59$  GPa [57]. Bending strength of MWCNTs were measured to be  $14.2 \pm 0.8$  GPa. For the composites prepared using CNTs, load transfer from the matrix to CNTs is considered as the most important factor. Hence the adhesion between the matrix material and CNTs needs strong without inducing greater defects in the CNTs.

For MWCNT, high thermal conductivity of about 3000 W/mK at room temperature which is twice as high as that of diamond at 1000 W/mK and 10 times that of copper have also been demonstrated [54].

### **1.2.2 Engineering Applications**

Owing to their physical properties discussed above, MWCNTs have been shown to exhibit enhanced performance in several engineering applications. The enhanced mechanical properties (Young's modulus, tensile strength) of MWCNTs provide the promise for being used in composite synthesis. Owing to their nanosize, well defined morphology and structure, high electrical conductivity and chemical stability, they were demonstrated to be used in flat panel displays. CNTs have demonstrated high and reversible hydrogen storage ability and can be used as a hydrogen storage medium. Unlike PDCs, MWCNTs are not quite extensively used in commercial applications. However several potential applications are under investigation. Recently, MWCNTs have been shown to exhibit Li-intercalation ability with high capacity and

cycling for hundreds of cycles. High cyclability of CNT is attributed to the amount of Li-ions that can be intercalated between the concentric nanotubes. High electrical conductivity in CNTs results in faster cycling of the electrodes and so CNTs are being extensively investigated as a filler material for anodes in Li-ion batteries. Use of CNTs in Li-ion battery anodes results in both high specific capacity and high power density. Additionally CNTs have been proposed for use as field effect transistors, single electron transistors diodes, gas sensors, water purification and biomedical applications [50].

### **1.3 Polymer-derived Ceramic-Carbon Nanotube Composite**

Polymers, ceramics or other structural and functional materials can be blended with CNTs with the aim to achieve enhanced multifunctional properties possessed by both participating materials. Unfortunately, the as-synthesized nanotubes tend to self-assemble into agglomerated bundles due to van der Waals bonding between the carbon atoms. Hence for composite synthesis, uniform distribution of nanotubes is necessary in order to have homogenous properties of the composites. Dispersion of the CNT bundles directly using sonication in solvents (organic/aqueous) is possible but it does not result in a stable suspension. Stable suspension of CNTs in the solution form is reliably formed by use of particular polymers species, polynuclear aromatic compounds, surfactants and biomolecules. The functionalization of CNTs is broadly classified into two types (1) exohedral attachment of functional groups or compounds (a) by covalent functionalization onto  $\pi$ -conjugated CNT surface (b) non-covalent bonding or wrapping of functional groups and (2) endohedral filling of molecules at the empty sites [52].

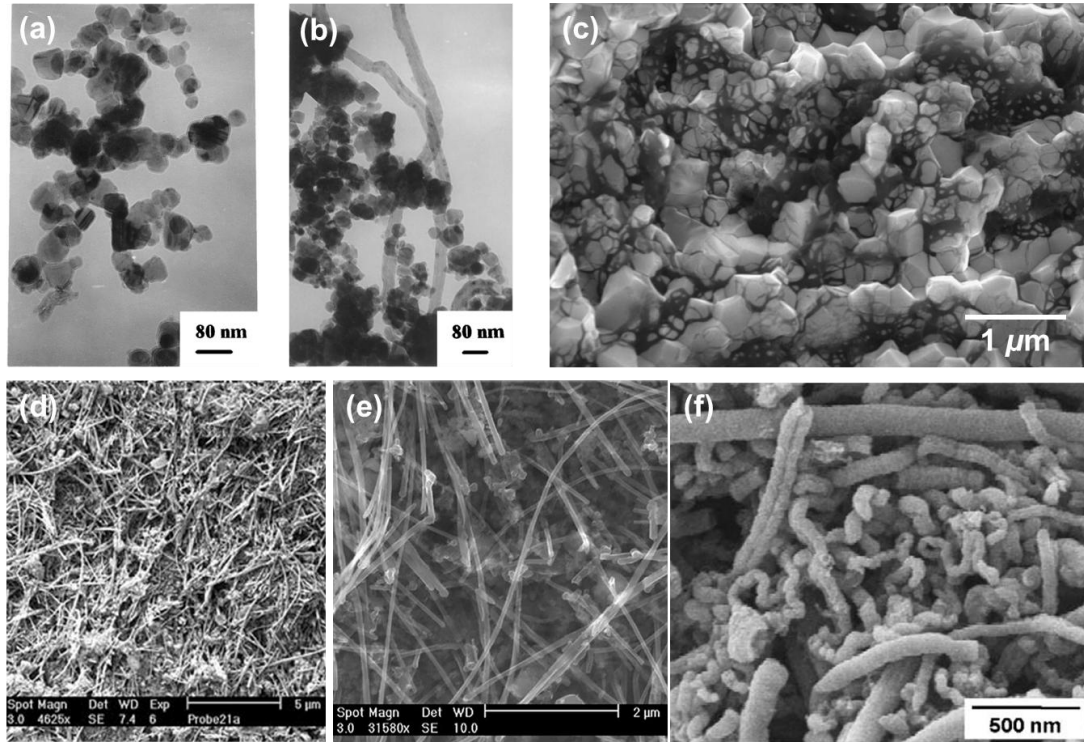


**Figure 1-7:** (a-b) TEM images of Si-C nanoparticles interfaced with CNT [55], (c) SEM micrograph of  $\text{Al}_2\text{O}_3$ -CNT nanocomposites fracture surface, (d-e) SEM image of fracture surface of SiCN/CNT composite with 10 and 5 vol % CNT respectively [60,61], (f) SEM image of SiCN/MWCNT composite nanowires [62].

Composites using CNT and ceramic ( $\text{SiC}$ ,  $\text{Al}_2\text{O}_3$ ) were initially explored by several groups (Fig. 1-7). These approaches had minimal molecular interaction between CNT and ceramics and hence exhibited slight improvement in the functional properties [58,59,63,64]. In a novel approach by Duan *et al.*, PDC and CNT were interfaced in liquid phase for synthesizing amorphous SiCNO nanowires [64]. Later on, a similar approach of adding dispersed CNTs in polymer, followed by pyrolysis to yield ceramic coated CNT, was used to synthesize SiCN-CNT [62,65,66] and SiOC/CNT [67-69] composites. In separate works their engineering properties were investigated in detail [60,62, 66, 70-74].

Silicon-based polymers are known to non-covalently functionalize CNTs sidewalls (Fig. 1-8). This mode of chemical interaction is particularly desired because it offers the possibility of attaching functional groups and compounds without resulting in a greater alteration in physical or electronic properties of CNTs. The polymer coated CNTs overcomes the van der Waals force due to steric repulsion between each other and results in a stable de-agglomerated suspension [75].

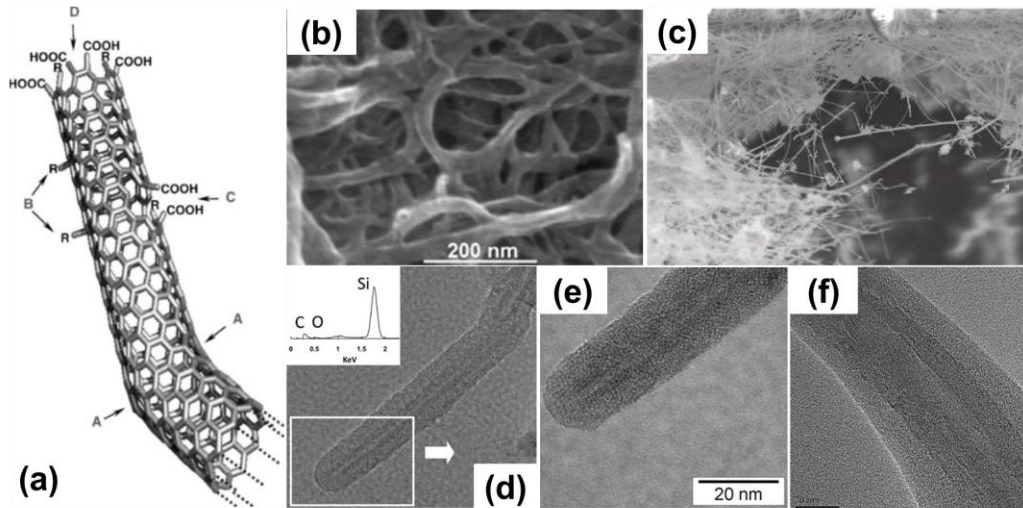


**Figure 1-8:** (a) Single walled carbon nanotube model showing the sites (ends, sidewalls and bends) for chemical group functionalizing (b-f) SEM and TEM micrographs of PDC-MWCNT core shell structures synthesized at different processing conditions [37, 67].

Mechanical properties (mainly elasticity) investigated by Linan *et al.* for SiCN-CNT using indentation test revealed that addition of CNTs results in increased stiffness of the composite [65]. While Shah *et al.* measured the actuation voltage and strain response under application of external load. Their SiCN/CNT specimens exhibited both higher sensitivity and linear response to the input load [66]. Katsuda *et al.* studied the reinforcement to the SiCN/CNT composite via fracture toughness behavior, which remained uniform with increasing crack length [62].

Several engineering applications, demand high performance and multifunctional properties from the material. In this dissertation, composites using PDCs and CNTs are synthesized and their performance, when used in two advanced energy based engineering applications, has been evaluated.

### 1.3.1 Application 1: Laser Thermal Detector Coatings

For the purpose of precise calibration of high power lasers (upto 10 kW or greater), organizations such as National Institute of Standards and Technology (NIST) at Boulder in Colorado maintains a customized setup. These setups use calorimetric methods based on heat conduction for laser power calibration. Here the incident optical laser energy is converted into heat on the surface of radiation absorbing cavity with a black coating. This heat is absorbed by the continuously flowing water jacket outside the cavity.

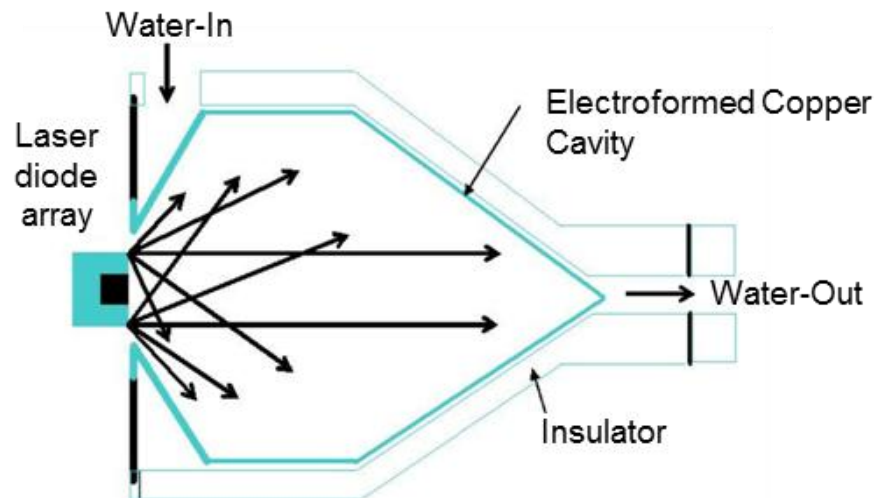


**Figure 1-9:** Cutaway diagram of the flowing-water thermal detector, illustrating the absorbing cavity and the water-flow channel on the outer surface of the cavity. [76]

Under steady state conditions, measurement of mass flow rate of water, increase in temperature and specific heat determines the power absorbed by the black coating (Equation 1-8). The reflected laser power at a given wavelength from the black coating can be measured in a separate

set of experiment by using a power meter and low laser power. Thus the laser power can be precisely determined. The cutaway diagram of the flowing-water thermal detector is shown in Fig. 1-9.

$$P_{Laser} = \dot{m} \cdot C_p \cdot \Delta T \dots\dots\dots(1-8)$$

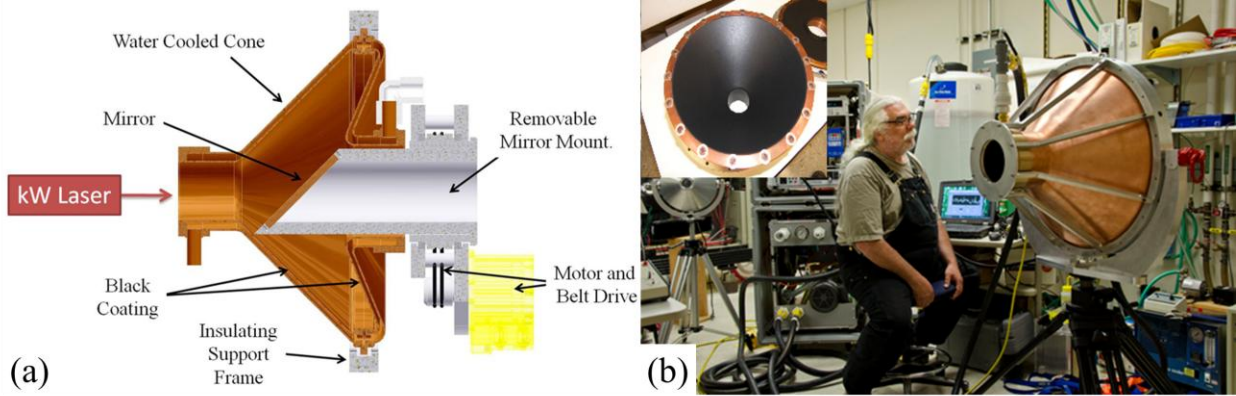


**Figure 1-10:** (a) Sectional side view of the thermal detector illustrating the actual systems used (b) Photograph of an actual copper cone used for laser calibration (inset: actual cone has its inner surface coated with CNTs) [77].

An optimal coating material is desired to possess several functional properties for accuracy and proper working of the detector, which includes: (a) high thermal conductivity for effective transmission of absorbed heat to the substrate, (b) absolute zero reflectivity in the visible to infrared spectrum for accurate response and to prevent coating damage due to radiation attenuation, (c) low thermal mass of the coating for higher responsivity, and (d) high visual damage threshold (mainly for high power lasers). Additionally, physical properties such as (a) forming a uniform and optimum coating thickness on the desired surface, (b) adhering and forming a stable coating against adverse handling and test conditions, and (c) morphology that

allows maximum surface area contact with the substrate are also desired. The actual CNT coated copper cone is shown in Fig. 1-10.

*Performance Comparison: Black absorbing coatings*

Typical coating materials for laser thermal detector consists of carbon-based paints, diffuse metal (gold black, silver black), oxidized metals (anodized aluminum), etc., because of absorption over a broad wavelength range (up to 40 micrometers) (Fig. 1-11) [82-87]. In spite of having low thermal mass, these coating materials are not suitable for high-power laser radiometry because of their poor laser damage threshold (or low oxidation resistance) (Fig. 1-12) [92-93]. In addition, these materials exhibit non-uniform spectral response with reflectance reaching as high as (10 to 20) % [88].

Better performance using single and multiwalled carbon nanotubes (MWCNTs) coatings has been previously demonstrated [80,81,88-92]. MWCNTs are most promising, because of their broad and uniform spectral absorbance from visible to IR wavelengths, high thermal conductivity and a laser damage threshold of approximately  $15 \text{ kWcm}^{-2}$  at  $1.06 \mu\text{m}$  exposure ( $7.1 \text{ kWcm}^{-2}$  for SWCNTs) [80]. However, MWCNT coatings experienced greater damage at  $10.6 \mu\text{m}$  exposure with a reduced damaged threshold value of  $1.4 \text{ kWcm}^{-2}$  and 76 % absorption efficiency [80].

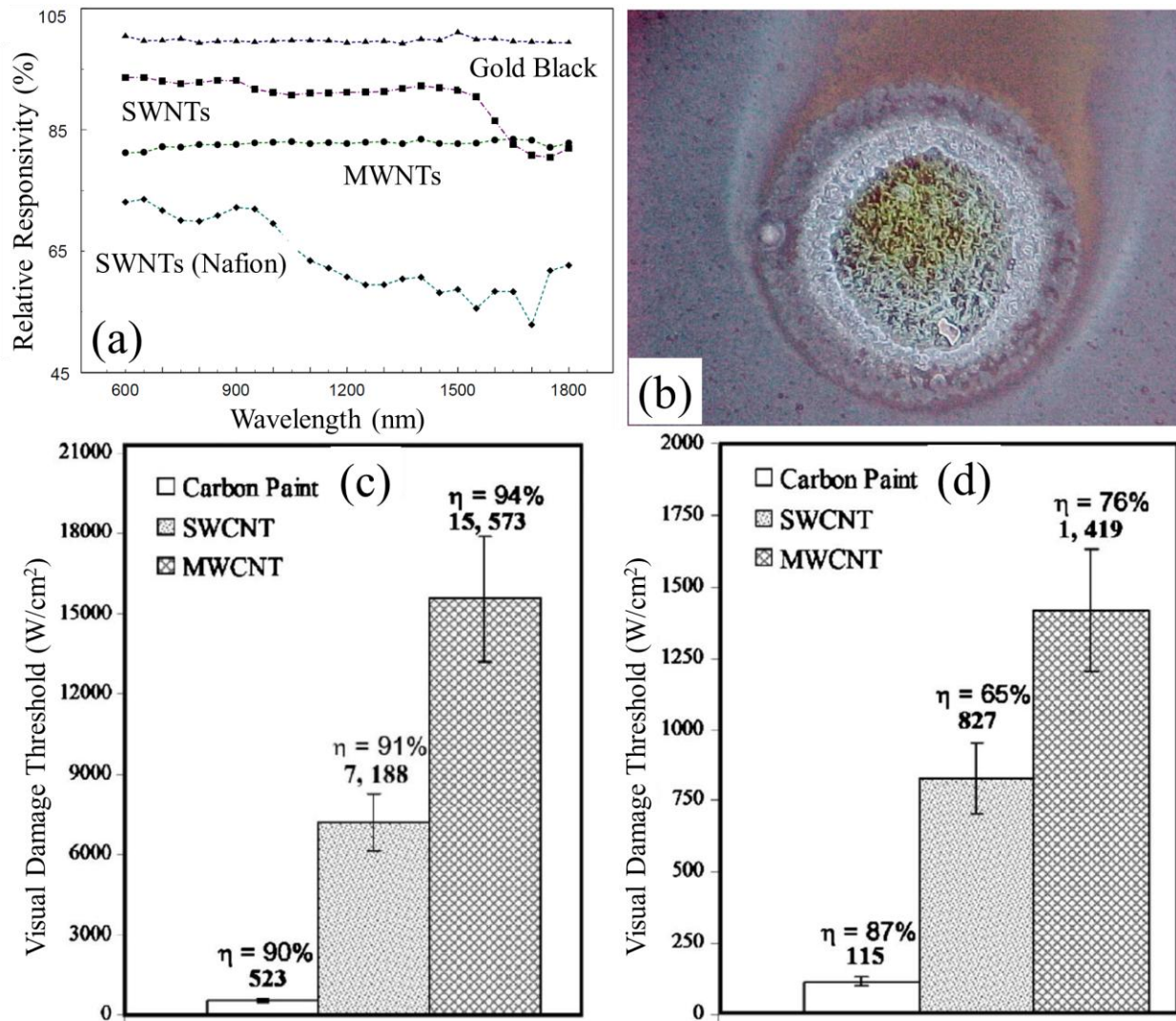


**Figure 1-11:** (a) Spectral responsivity of four identical pyroelectric detectors comparing the thermal absorber coating performance [78]. (b) Photographic image of a laser induced damaged area for MWCNT-sodium silicate coating with the beam size of  $\sim 2$  mm [79] (c) & (d) Comparison of damage threshold for the sprayed coatings upon irradiance at  $1.06 \mu\text{m}$  and  $10.6 \mu\text{m}$  respectively [80].



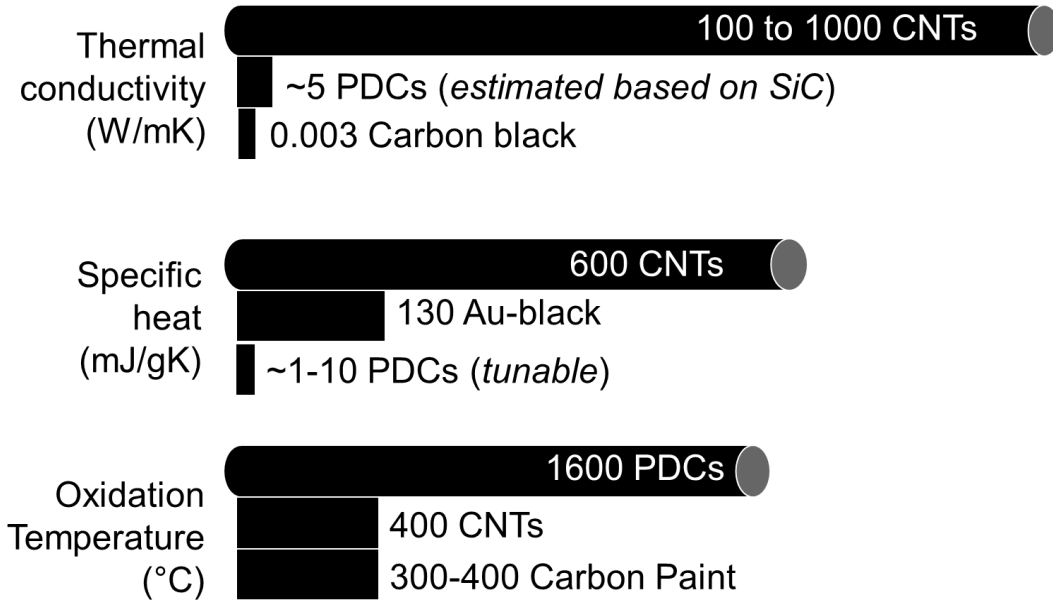


**Figure 1-12:** The properties of various black coating types highlighting the advantage of PDCs and CNTs for high power laser radiometry. A PDC-CNT composite is likely to exhibit both high laser damage threshold in air.

### ***PDC-CNT advantage as a coating material***

One way to improve the laser damage resistance of MWCNTs (at 10.6  $\mu\text{m}$  exposure) would be to functionalize their surfaces with high oxidation resistant PDC materials. PDCs which are produced by controlled thermal decomposition of liquid polymer precursors are chemically stable up to as high as 1400°C [93,94]. In addition to improved oxidation resistance, the core/shell composite is likely to exhibit high thermal conductivity and optical absorbance contributed by both the nanotube core and graphene like carbon inherently present in PDC shell [95-99]. Also, the one pot-synthesis of PDC-CNT composite will make it relatively easy to be prepared in large quantities (gram levels), which makes it feasible for laminating any desired substrate of large area using simple spray coating techniques, including the surface of a laser thermal detector. More details on this topic are presented in Chapter 4 of this thesis.

### 1.3.2 Application 2: Lithium Ion Battery

Limited availability and rising cost of fossil fuels and widespread use of multifunctional portable devices are continuously pushing the performance demands for highly efficient energy storage devices. Research in rechargeable lithium-ion battery (LIB) has gained momentum since the introduction of graphite and  $\text{LiCoO}_2$  in 1970's and its commercialization in 1991. Development of efficient and durable LIB mainly includes designing and testing, electrode and electrolyte materials which possess desired energy storage properties and synchronized performance. LIBs have several advantages over other traditional rechargeable batteries as they exhibit high cell voltage, high energy density, long cycle life, no memory effect and longer shelf life [100,101].

Gravimetric energy and power density of LIB are compared with other battery technologies in Fig. 1-13. Use of non-aqueous liquid polymer electrolyte with larger electrochemical window has made it possible for LIBs to operate in a larger voltage range, thereby exhibiting higher power density.

---

Reprinted with permission from (R. Bhandavat, Z. J. Pei, G. Singh, Polymer-derived ceramics as anode material for rechargeable Li-ion batteries: a review, *Nanomaterials and Energy*, **1**, 6, 324-337). Copyright (2012) ICE Publishing Ltd.

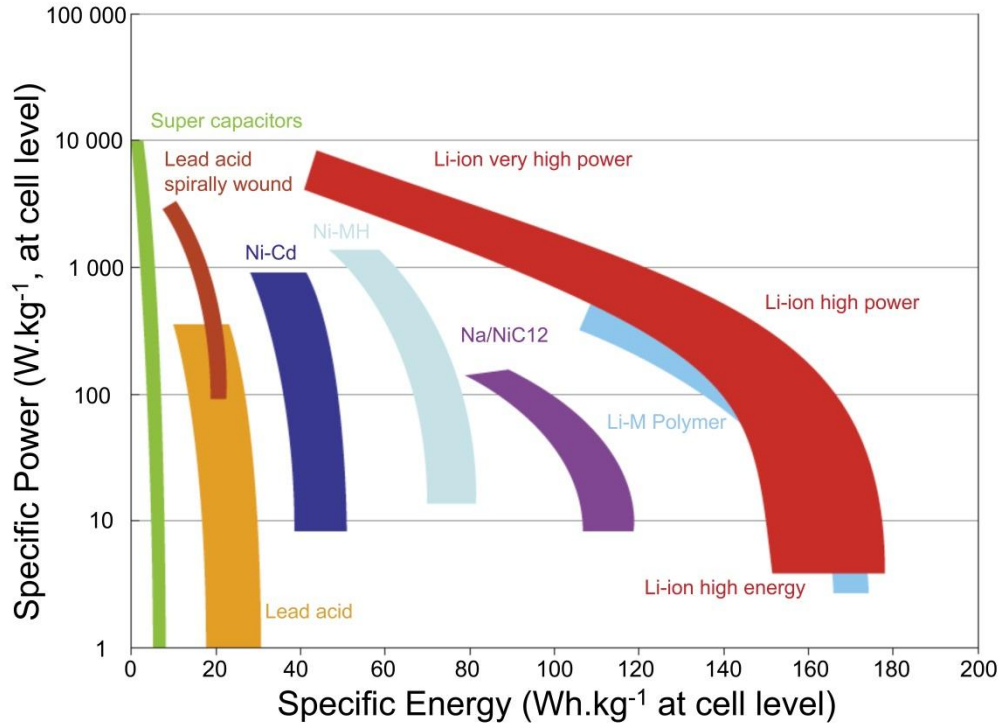


**Figure 1-13:** Comparison of specific power and energy of the LIB with other commonly used commercial batteries and super capacitors [102].

LIB consists of several electrochemical cells connected in series and/or in parallel to provide the desired voltage and capacity, respectively. The schematic of one such electrochemical cell is shown in Fig. 1-14. The cell mainly consists of a positive (cathode) and a negative (anode) electrode partitioned by a polymeric membrane and all these elements floats in lithium salt doped polymeric electrolyte. Simultaneously, redox reactions occur in the electrodes liberating Li-ions in the electrolyte and electrons in the external circuit when the cell is plugged into an external supply. During LIB discharge, cathode oxidizes releasing Li-ions that travel through the electrolyte and intercalate the anode microstructure. Meanwhile under the influence of external energy, the electrons travel through the external circuit and neutralize the Li-ion in the anode, resulting in its reduction. During LIB charge half cycle, Li-ion deintercalate the anode and travel

back to the cathode. Simultaneously, the electrons do the useful work by passing through the external circuit

A LIB is an electrochemical cell employing a combined system of dissimilar materials undergoing oxidation-reduction reactions at the electrodes in tandem to store and retrieve energy as desired.

The main parameters for performance evaluation of an electrode material can be broadly classified into the following four categories namely (a) energy density, (b) rate capability, (c) cycleability and (d) thermodynamic stability. For a full LIB, gravimetric energy density is defined as the product of its average operating potential (V) and the total amount of charge transfer (Ah) for the unit weight (g) of active electrode material under test, is commonly expressed in Wh.g<sup>-1</sup> (VAh.g<sup>-1</sup>). It is alternatively expressed in Wh/L as desired by an application. Charge transfer quantifies the amount of ions moving between the electrodes via electrolyte and same number of electrons in the connecting external circuit. As the ionic conductivity of Li-ions in the electrolyte and electrode is smaller than that of electron conductivity in an external circuit, the electrodes need to possess larger interaction area.

In general, it is desired that the electrode material undergo fast charge and discharge while maintaining the high energy density. Specifically, it is the ability of the anode material's structure to allow faster Li-ions diffusion in and out of the electrode material under the influence of external energy [103, 104]. The ability of the anode material to reversibly cycle Li-ions with sustained energy density and least IRC is the cycleability of the anode material. The repeated diffusion of Li-ions in and out of anode material can disrupt (volume expansion, pulverization, delamination) its morphology. To reinstate or prevent the possible change in anode structure,

addition of external matrix material or similar chemical modifications are desired. Recent review articles by Tarascon and Scrosati discuss these challenges in greater detail [105,106].

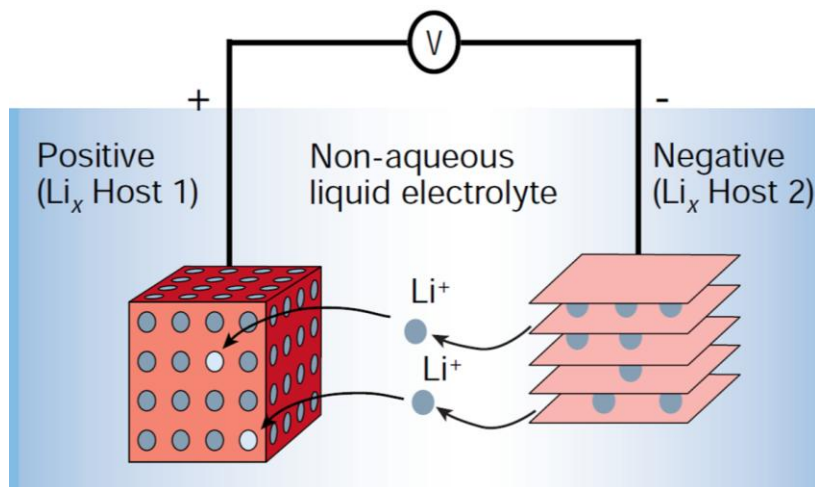


**Figure 1-14:** Schematic representation of a Li-ion battery full cell. Positive electrode in a commercial battery is a layered oxide of lithium (e.g.  $\text{LiCoO}_2$ ) and the negative electrode is carbon (e.g. graphite) [105].

Polymer-derived ceramics (PDCs) are known for their high thermodynamic and chemical stability, tunable electrical conductivity, high mechanical strength, and tunable porosity, which make them a viable candidate for LIB anode material. Additionally, PDCs can be conveniently molded into any desired shape, size, structure or morphology as demanded by the application. Contemporary materials may only possess one or few of the desired properties, which makes it difficult to obtain a high performing anode from a single material system. PDCs with tailored properties can be independently used as battery anodes.

### ***Anode material-dependent operational issues***

As a battery system consists of several different elements or materials that work in synchronous, each operational issue could originate from one or more different battery elements. In this thesis, we restrict our discussion to the issues involving anode materials only.

#### ***Irreversible capacity (IRC)***

During Li-ion intercalation in the anode, formation of solid electrolyte interphase (SEI) layer on anode's surface results in consumption of lithium (dissociating lithium salt from the electrolyte). This phase transformation of lithium is an irreversible reaction. Moreover, during the intercalation, Li-ions can form stable compounds either with the active material or at the defect such as surfaces, interfaces and grain boundaries. These trapped ions cannot be de-intercalated during the second half cycle. Due to the active material volume change during cycling, loss of electrical connection between the current collector, and conducting additive or the active material can result in the anode's increased internal resistance and reduce charge transfer. These phenomena can result in a capacity difference between two half cycles (discharge and charge), which is referred to as the irreversible capacity (IRC) or the first cycle loss (ICL). Primarily consisting of lithium carbonate, fluorides and oxides SEI is formed out of reduced electrolyte on electrode surfaces. Fortunately, the formation of this passivation layer is important as it prevents further decomposition of the electrolyte but allows Li-ion diffusion through itself. For the first few cycles, the SEI layer breaks and repairs itself to accommodate volume changes associated with Li-ion diffusion. After few initial cycles, the SEI stabilizes and prevents further reduction of electrolyte on the anode surface, prolonging anode cycle life [107-109].

IRC is a measure of the chemical and structural stability of the electrode with electrochemical electrode cycling. For longer electrode life it is thus desired to reduce the IRC and maximize the

coulombic efficiency. To this end, prelithiation of anode can compensate for the lithium lost in initial irreversible reactions until stable SEI has formed. Inclusion of additives in the electrolyte, which can enhance SEI layer formation or coating a SEI inhibiting layer, can also help reduce IRC. Formation of an artificial layer on the active material surface to inhibit the SEI formation, before cycling can further reduce the IRC.

### *Voltage hysteresis*

The difference of the average operating potential of the Li-ion intercalation and deintercalation cycle for a given electrode is termed as hysteresis. Physically the polarization in the electrode material can be observed as a shift in average operating voltages of charge and discharge cycles [110-112]. Reduction in particle size of the active material, reduced anode film thickness, operating the cell at slower charge/discharge rates during initial cycles have been known to reduce the cyclic hysteresis. In general, these methods reduce the electrode over-potential either by reducing the cycling rate or by decreasing the impedance resulting from charge transport. Even though these factors can decrease the hysteresis, it cannot be eliminated completely due to its thermodynamic origin [113]. Inclusion of non-conducting binder further induces the polarization in the anode and hence the reduction or elimination of the binder can also reduce the hysteresis.

### *Capacity decay/fading*

During electrochemical cycling, several reactions including dissociation of Li-ions from the positive electrode, their transport in electrolyte through separator, ionic diffusion in anode during charge and electrolyte-electrode interfacial reactions can result in instabilities in overall cell performance and can cause its specific capacity to fade. The decay in the cyclic capacity of the

anodes can effectively be studied by measuring the internal resistance of the electrode. Correlating the physical phenomenon contributing to the increased impedance can help address the capacity decay issue. Increase in internal resistance can also be caused due to the loss of physical connection between the active particle and the conducting medium, phase change, etc. [114].

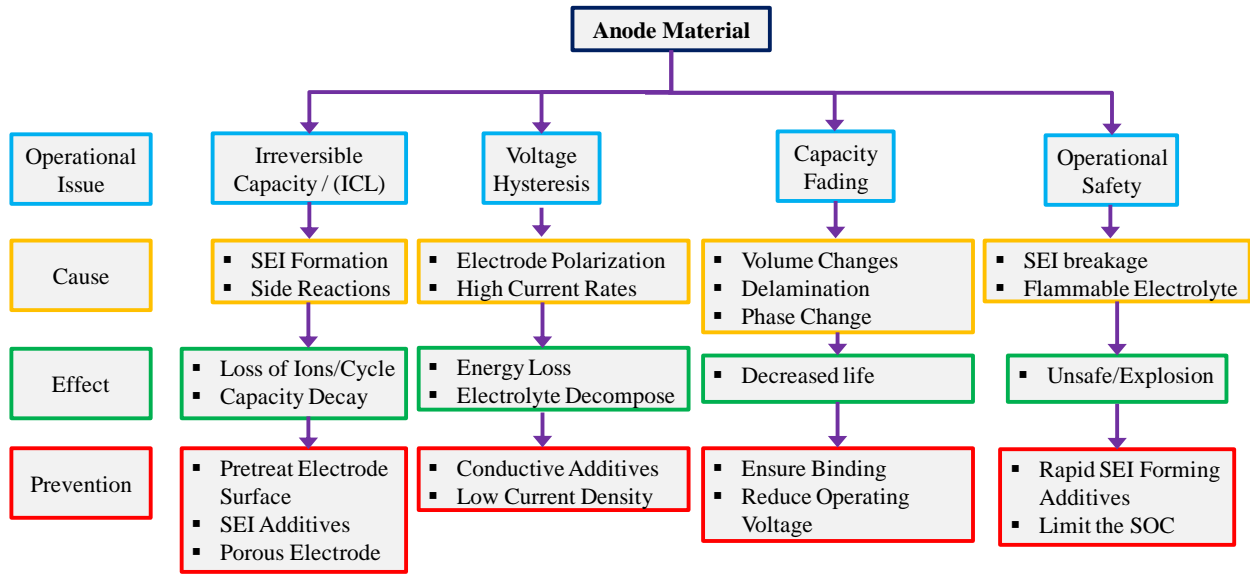


**Figure 1-15:** Summary of possible cause, effect and prevention of battery operational issues in anode materials.

### *Operational safety*

When operating at low voltages, in the absence of or due to discontinuous SEI layer on the electrode surfaces, reduction of Li-ion at the electrode surface can result in the formation of dendrites. Prolonged accumulation of lithium can further result in increased size of dendrites, puncturing the separator and there-by short circuiting the cell. As the electrolyte used in LIBs is a mix of organic compounds, severe explosion can result. Lithium plating on the electrodes can be prevented by limiting the state of charge or inclusion of an additive material in the electrolyte



that assists in rapid formation of amorphous SEI layer during charging [115]. The major material issues can thus be summarized in Fig. 1-15.

### ***Experimental Results***

Silicon based nanostructures are being explored aggressively as potential battery anode materials, because of silicon's high Li alloyability with theoretical capacity exceeding 4000 mAh.g<sup>-1</sup> (an order of magnitude higher than graphite anodes used in commercially available Li-ion batteries) and its low discharge potential [116-119]. But silicon's high electrochemical capacity comes at the cost of increased volume changes (up to 400 %) that occur upon lithiation and delithiation causing several operational issues including pulverization and poor capacity retention especially for large-size battery anodes (active material loading >2 mg) making them commercially unviable. Although several solutions have been suggested, convincing results are yet to be seen.

To this end, silicon-based amorphous PDC anodes have demonstrated promising results. Recent studies show that PDCs can store lithium reversibly in the voltage range of 0 to 3 V with electrochemical capacities as high as 900 mAh.g<sup>-1</sup> with coulombic efficiencies exceeding 99%. Other advantages include, high thermodynamic stability, open amorphous structure and processing flexibility. While major concerns include their first cycle loss (27 to 50 % depending upon the chemical composition) and voltage hysteresis (0.8 to 1.2 V). It is believed that these issues can be addressed by altering the chemical structure of the starting polymer (and hence the final ceramic), increasing surface area (by inducing porosity, surface etching) or by addition of electrically conducting nano-fillers with favorable chemical composition.

Much of the work involving PDC anodes have been performed on polysilazane derived SiCN and polysiloxane derived SiOC systems. The ease of availability and well established processing

methods for these PDCs are the main reasons for their popularity. Experimental results obtained using these two tertiary PDC systems are reviewed in the following section and are summarized in Table 1-3.

### The Si-C-O System

Because of the limitations associated with crystalline silicon-based anodes, there was an obvious interest in exploring other similar materials that can offer high electrochemical capacity and remain mechanically and chemically stable for large number of cycles.

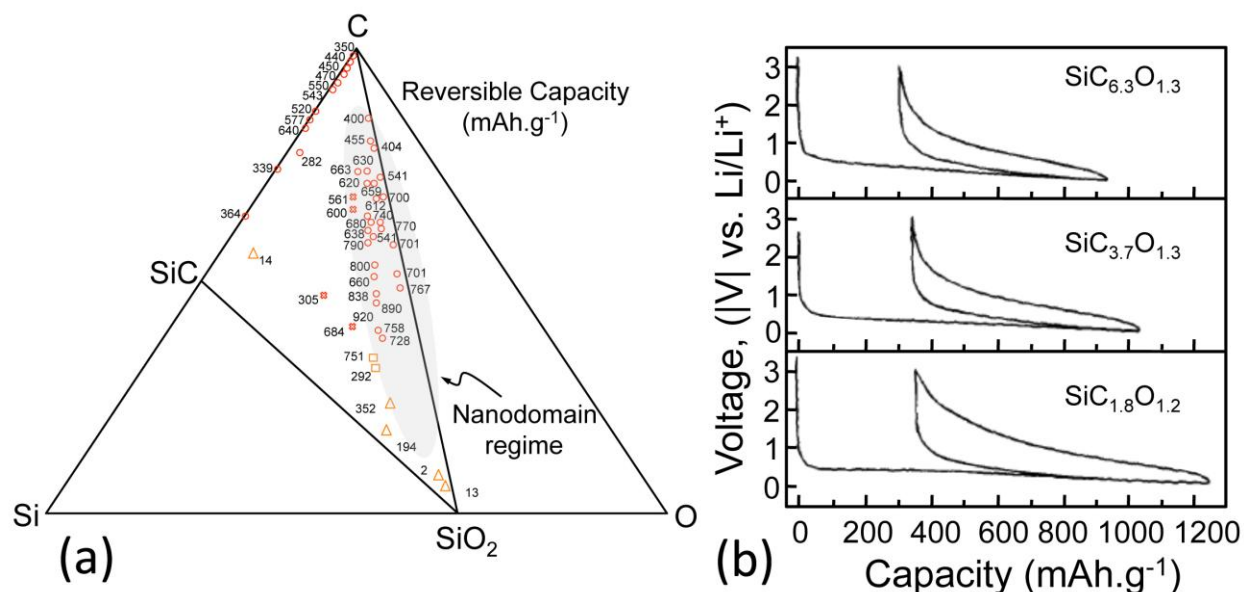


**Figure 1-16:** (a): Highlighted (shaded) area in the Si-O-C compositional triangle, represents the specimen with mixed bonds tetrahedra [120,121] and (b) Initial electrochemical cycling data of three representative SiOC anodes that lie in the shaded region of the composition diagram [120].

The cyclic performance of polymer-derived SiOC was first investigated by Wilson *et al.* [122,123], in which they showed SiOC's ability to reversibly intercalate Li-ions under 1 V with a capacity of approx. 600 mAh.g<sup>-1</sup>. Later, they studied the effect of processing temperature on

SiOC's lithium cycleability, which revealed least first cycle loss and highest reversible capacity for specimen processed at 1000 °C [122]. Further, Xing *et al.* performed a parametric study involving sixty different SiOC anode specimens with varying chemical composition. Their results showed best performance for SiOC ceramic with 14 % Si and 80 % C (Fig. 1-16) [120]. The SiOC ceramic with equal concentrations of Si, O and C performed better than either the crystalline graphite or SiC or SiO<sub>2</sub> individually.

Later, Sanchez-Jiminez *et al.* [121] concluded that the best performing anodes specimens lie in the nanodomain regime in the Si-O-C composition triangle as shown in Fig. 1-16. The specimens inside (above) the SiC-SiO<sub>2</sub> tie-line will have Si mixed bonds with O or C (nanodomain model in Figure 3) whereas those outside this region will possess Si clusters or other agglomerated phases. Therefore, when mixed bonds (either O-rich or C-rich) in silicon tetrahedral were co-related to the specific reversible capacity, about 0.75 Li-atom were estimated to intercalate in 1 mixed bond of Si-tetrahedra. However, exact mechanism or site of Li-ion intercalation in SiOC was not explained.

Further, Ahn *et al.* studied hysteresis in SiOC ceramics by means of coulometric titration experiments and determined the origin of hysteresis as polarization (250 to 500 mV) that occurs at anode-electrolyte interface and observed to be proportional to the cycling rate [124]. Application of a non-active atomic layer deposition (ALD) coating of Al<sub>2</sub>O<sub>3</sub> on SiOC marginally decreased the hysteresis to 0.4 V. Hence, the hysteresis is believed to be a combined effect of thermodynamic and kinetic factors that mainly originated during the deintercalation half of the cycle.

Ahn *et al.* further varied the ceramic precursor chemistry to synthesize a range of Si-C-N-O ceramics with varying N/O ratio [125]. Results from these specimens showed that the SiOC

structure was more desirable than SiCN processed under similar conditions (Fig. 1-17). They concluded that the higher covalence in Si-N bond localizes electron density and is less effective in Li-ion binding than Si-O bonds. In the same work they also studied cyclic stability of SiOC as a function of their pyrolyzed temperature. Specimens pyrolyzed at 800 and 1000 °C showed approx. 100 % capacity retention after 60 cycles while those prepared at 1200 and 1400 °C showed a continuous drop [125]. Similarly, other groups have also shown improved electrochemical performance for SiOC specimen processed at 1100 and 1300 °C [126,127].

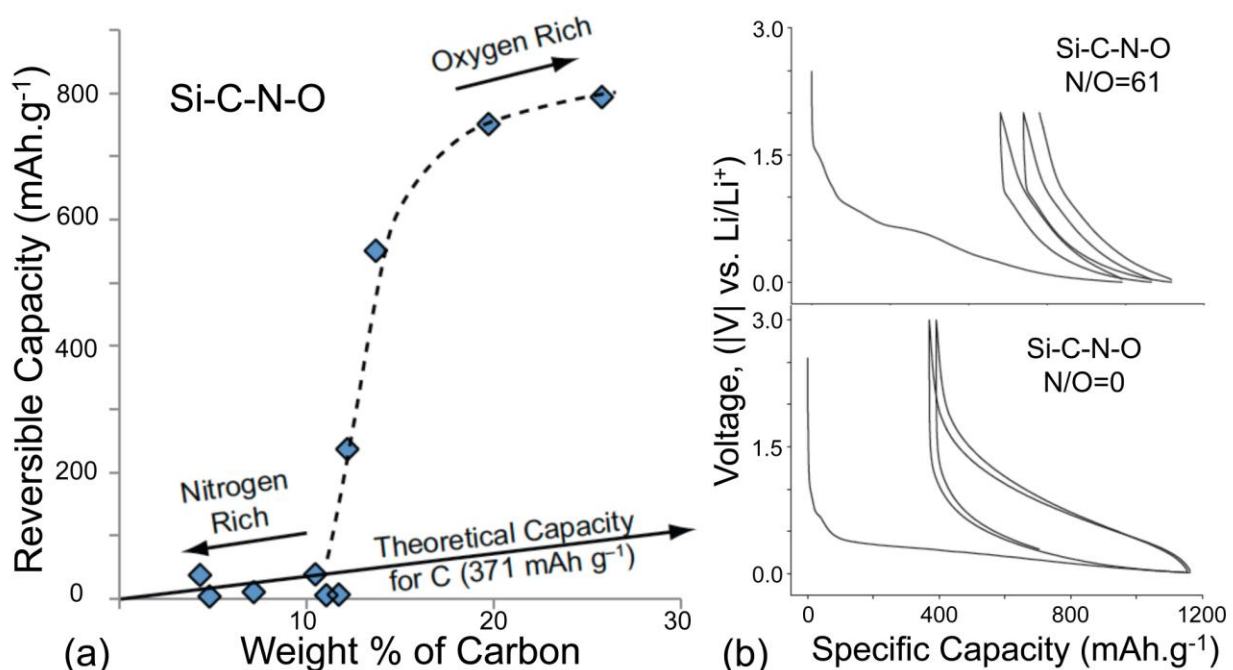


**Figure 1-17:** (a) The oxygen-rich SiCNO ceramic shows higher reversible capacity than the nitrogen rich counterpart and (b) First charge/discharge cycles for SiCNO anodes prepared from nitrogen-rich (N/O= 61) and nitrogen deficient (N/O=0) specimen [125].

Further work on SiOC was carried out by Liu *et al.* [128], who found that changing the pyrolysis medium from argon to hydrogen increased carbon content in SiOC ceramic resulting in better reversible capacity. Addition of external carbon source like divinyl benzene further resulted in capacity improvement, but a slight increase in hysteresis was also observed [128].

The processing flexibility of PDCs has also allowed synthesis of SiOC thin film based anodes. Experiments involving (0.5 to 5)  $\mu\text{m}$  thick SiOC films showed improved electrochemical performance over the bulk SiOC specimens. Unlike the conventional anodes that have conducting agents and binders added in them, these films were exclusively made from SiOC (thereby reducing the battery weight). As shown in Fig. 1-18, the SiOC films exhibited low first cycle loss (27 %), high cyclic efficiency ( $\sim 99\%$ ) and sustained capacity ( $\sim 1100\text{ mAh.g}^{-1}$ ) [129]. With increasing cycle number, the films formed segments and the lithium diffusion was suggested to depend on segment size rather than its thickness.

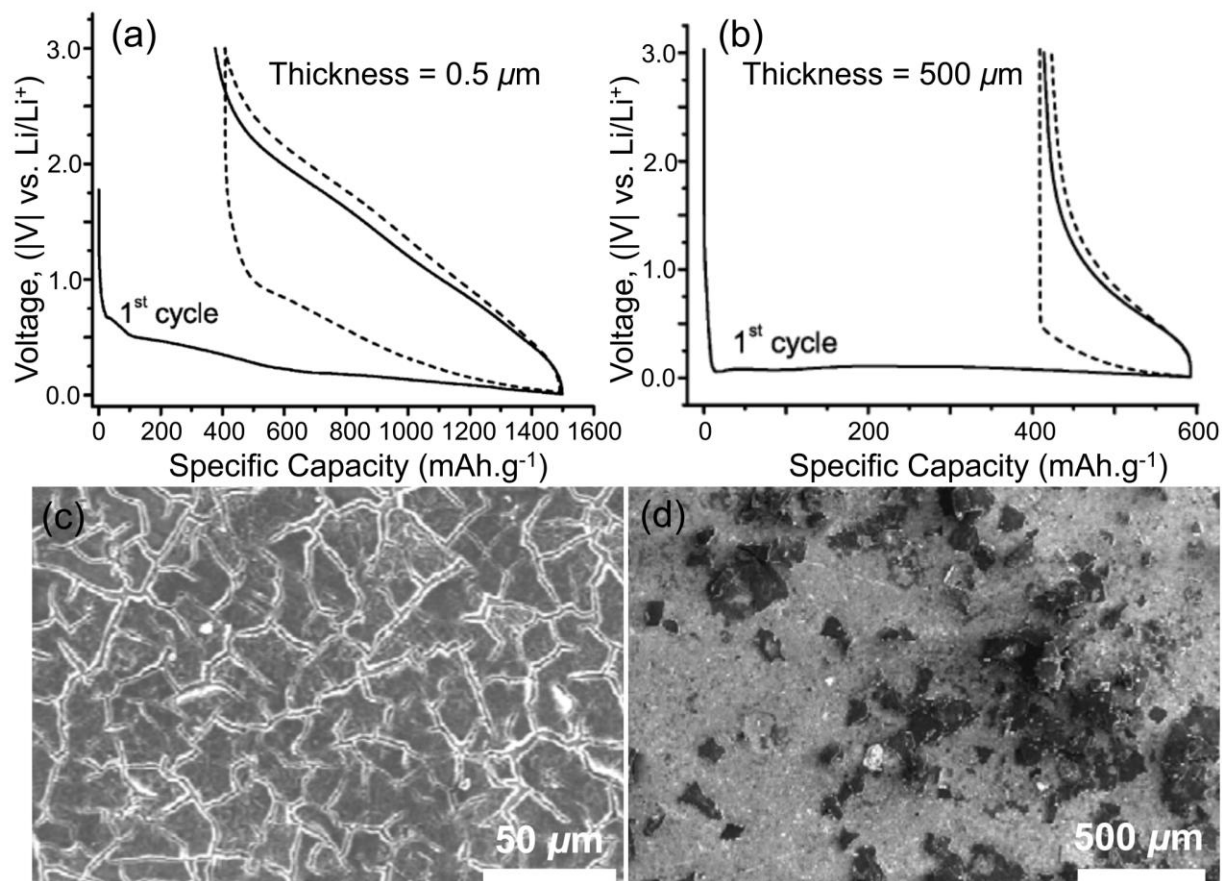


**Figure 1-18:** (a) and (b) Electrochemical cycling of SiOC thin film anodes with thickness 0.5 and 500 micrometers respectively. Both cells were cycled at  $100\text{ mA.g}^{-1}$ . (c) and (d) Post electrochemical SEM surface of 0.5 and 500 micrometers thick anodes, respectively [129].

Recently, Fukui *et al.* advanced the SiOC study by inducing porosity and increased exposed surface area that was expected to increase the capacity and cycle life. Porous specimens were synthesized by blending branched polysilanes and polystyrene with pore size and surface area of  $\sim 2$  nm and  $\sim 14$   $\text{m}^2\cdot\text{g}^{-1}$ , respectively. The best performance obtained for  $\text{SiO}_{0.4}\text{C}_{0.8}$  was 565  $\text{mAh}\cdot\text{g}^{-1}$  reversible capacity with 73 % efficiency [130,131]. Although the Si-29 NMR suggested cleavage of Si-Si bonds, the  $^7\text{Li}$ -NMR suggested multiple sites for Li-ion intercalation and no evidence of Si-Li bond formation was observed [132]. In another interesting work, Fukui *et al.* [133] used a microelectrode technique to cycle a 13  $\mu\text{m}$  SiOC particle at 100 nA current (80 C-rate). A 98% efficiency was observed for a pristine SiOC particle (without electrode additives exhibits) highlighting intrinsic rate capability of these PDC materials.

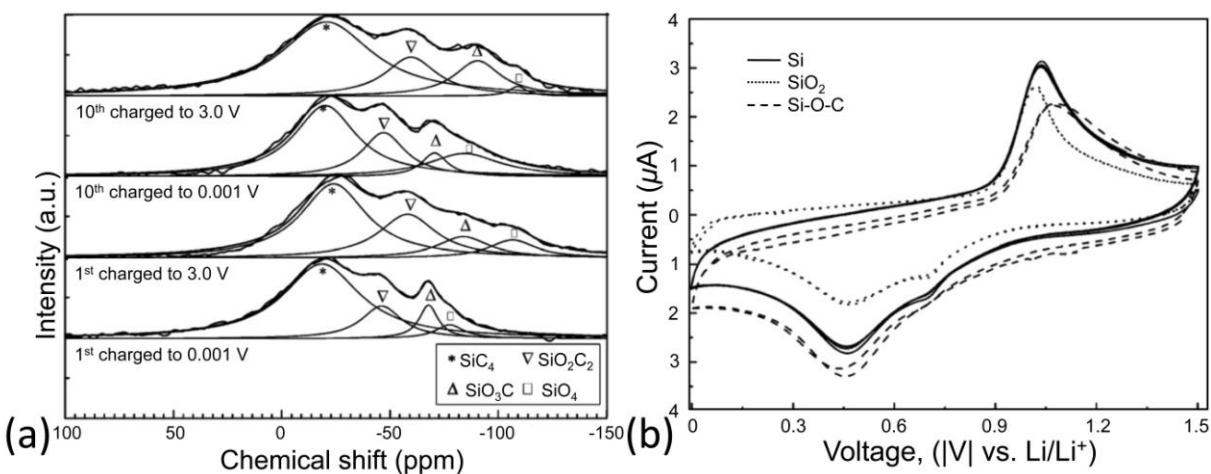


**Figure 1-19:** (a)  $^{29}\text{Si}$  Solid-state NMR data showing emergence of various Si chemical states when SiOC anode is at full-charged and discharged states (b) Comparison of cyclic voltammograms of SiOC anodes with commercial amorphous Si and  $\text{SiO}_2$  [134].

More recently, Liu *et al.* studied Li-ion intercalation mechanisms in SiOC anode specimens [134]. They utilized a combination of C-V, NMR and XPS techniques to compare the performance of SiOC anode with amorphous  $\text{SiO}_2$  and Si (Fig. 1-19). Their analysis showed that

some Si species in SiOC were in fact active toward electrochemical binding with Li while the majority of the capacity was due to the amorphous SiOC matrix. Of the co-existing  $\text{SiO}_2\text{C}_3$ ,  $\text{SiO}_3\text{C}$  and  $\text{SiO}_4$  phases, the active  $\text{SiO}_4$  phase formed  $\text{Li}_2\text{SiO}_3$  upon intercalation, while the inactive part formed  $\text{Li}_4\text{SiO}_4$ . Additionally, their XPS results showed that the  $\text{SiOC}_3$  phases were completely irreversible and converted to  $\text{SiC}_4$  upon first discharge (contributing to the ICL). The CV measurements could not distinguish between Li-intercalation in SiOC with amorphous  $\text{SiO}_2$  and Si.

### *The Si-C-N System*

Liebau *et al.* were among the first ones to propose PDC SiCN based electrode material for LIB applications [135]. Although no electrochemical cycling tests were performed, their work showed formation and lithium bonding both C and N in SiCN ceramic upon pyrolysis at  $1100^\circ\text{C}$ . Later, the effect of pyrolysis temperature (600 to  $1500^\circ\text{C}$ ) on electrochemical performance of SiCN ceramics was studied by Su *et al.* [136]. Their results showed strong correlation between ceramic's pyrolysis temperature and their electrochemical capacity; as shown in Fig. 1-20, specimens pyrolyzed in (1000 to  $1300^\circ\text{C}$ ) temperature range showed higher discharge capacity than others. Further, Kaspar *et al.* studied the performance of carbon rich SiCN based anodes prepared from pyrolysis of polydiphenylsilyl carbodimide in a range of temperatures ( $1100$ ,  $1300$  and  $1700^\circ\text{C}$ ) [137,138]. Among these (binder free) anodes, the  $1100^\circ\text{C}$  SiCN exhibited best performance with 47 % cycling efficiency and  $254 \text{ mAh.g}^{-1}$  reversible capacity. Electrochemical behavior of microporous SiCN anodes have also been documented in a recent study by Fukui *et al.*; these specimens, prepared by blending polystyrene and polysilane pyrolyzed at  $600^\circ\text{C}$ , showed improved reversible capacity ( $565 \text{ mAh.g}^{-1}$ ) and are believed to accommodate volume

changes associated with continuous Li-cycling [139]. More than 95 % of the first cycle capacity was retained after 40 cycles for these specimens.

The effect of heat treatment on SiCN ceramics has also been investigated recently; Feng *et al.* have shown that heat treatment of  $\text{SiN}_{0.31}\text{C}_{0.97}\text{H}_{0.31}\text{O}_{0.05}$  at 1000 °C in argon can lead to the formation of  $\text{SiN}_{0.18}\text{C}_{0.41}\text{H}_{0.91}\text{O}_{0.1}$  ceramic with improved coulombic efficiency and reversible capacity at higher current densities [140]. This improvement was collectively attributed to the decreased N and increased O content in the heat-treated ceramic [125].

In conclusion, the lithium intercalation capacity in the SiCN system is largely attributed to the presence of free carbon and nanovoids in the amorphous structure. Due to their high first cycle loss, voltage hysteresis and average intercalation capacity, it is highly unlikely that PDC SiCN will make a commercially viable anode for LIBs.

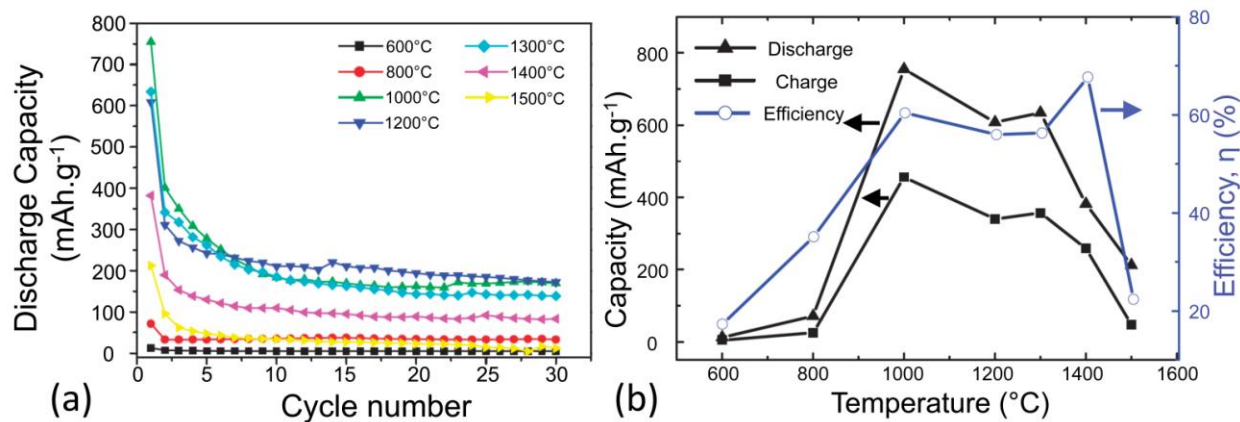


**Figure 1-20:** (a) Comparison of electrochemical performance of SiCN specimens pyrolyzed at increasing temperatures [136]. (b) First cycle charge/discharge capacities and coulombic efficiency comparison of various SiCN anodes specimens [136]. First cycle loss in excess of (30 to 40) % is typical of polymer-derived SiCN ceramics, which makes them unsuitable for practical applications.



*PDC carbon nano-material composites*

Experimental data on bulk PDC based anodes has highlighted some drawbacks in these materials: first cycle loss, capacity degradation, and voltage hysteresis. Recent work on PDC-based anode has been focused on addressing these issues by means of introducing carbon nano-materials such as CNTs and graphene [141-143]. These nano-materials offer several interesting properties like high aspect ratio (that translates to high flexibility), high electronic mobility, reduced ionic diffusion length, lighter weight and mechanical strength. Shown in Figure 1-21 is an instance where lithium cycling results in volume changes causing the loss of contact between the active anode particles. This eventually results in capacity decay with increasing cycles. Addition of CNTs in the active material can suppress the loss of electrical and ionic conductivity due to volume changes, thereby putting a check on capacity fading.

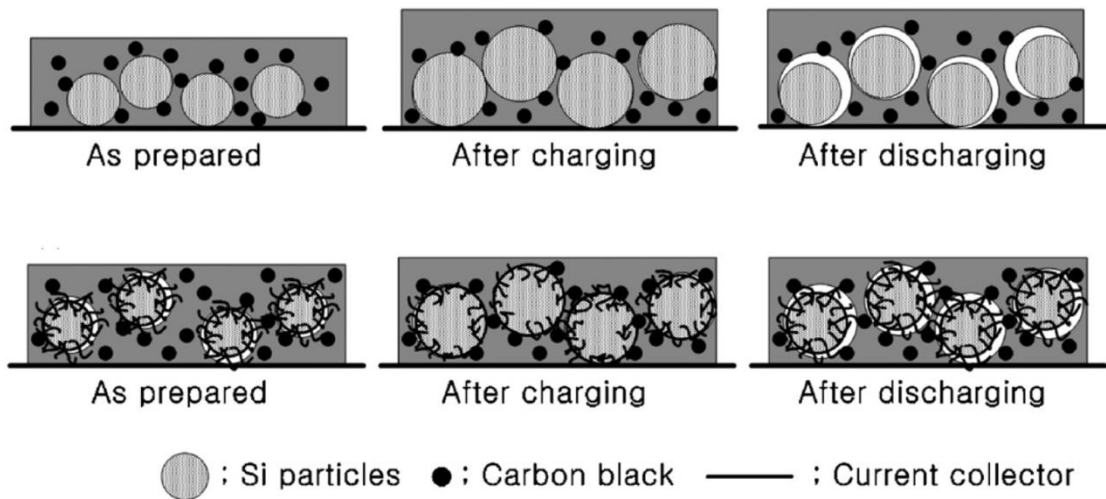


**Figure 1-21:** Step by step comparison of the effect of lithium intercalation and deintercalation in the silicon particle electrode with and without carbon nanotubes as conducting agents [141].

To this end, Konno *et al.* have demonstrated functionalization of graphite with polysiloxane precursors, which on pyrolysis resulted in SiOC-graphite ( $\text{SiOC}_{1.1}$ ) composite. A reversible capacity of  $625 \text{ mAh.g}^{-1}$  was observed for these composites, which remained stable up to 15 cycles at  $100 \text{ mA.g}^{-1}$  current density with first cycle loss of 40 %. Following a similar approach, Ji *et al.* [144] showed a reversible discharge capacity of  $357 \text{ mAh.g}^{-1}$  for a composite anode consisting of 25 wt. % graphene in SiOC. Following a slightly different approach, Kolb *et al.* [145] synthesized SiCN-graphite composites, by mixing 25% cross-linked polysilazane in graphite followed by pyrolysis at  $1000 \text{ }^\circ\text{C}$ . These composite anodes showed electrochemical capacity of  $474 \text{ mAh.g}^{-1}$  when operated at a current density of  $0.06 \text{ mA.cm}^{-2}$ . This improvement in the capacity was attributed to the increased Li-ion intercalation sites in the SiCN: graphite composite sheets [145]. Later, using a similar approach Graczyk *et al.* [146] synthesized SiCN-graphite composite and showed that more than 80 % of the capacity could be retrieved under 1 V. Of the three specimens prepared at  $950 \text{ }^\circ\text{C}$ ,  $1100 \text{ }^\circ\text{C}$  and  $1300 \text{ }^\circ\text{C}$ , the  $950 \text{ }^\circ\text{C}$  specimen exhibited best performance of  $376 \text{ mAh.g}^{-1}$  reversible capacity and 72.3 % first cycle efficiency [146]. Ahn and co-workers have also demonstrated improvements with SiOC-graphene composites; their approach has involved liquid phase mixing of graphene oxide in liquid polysiloxane precursor which upon pyrolysis yields a SiOC-graphene composite with uniform composition [147]. Battery anodes prepared from these nano-composites have shown tremendous potential; electrochemical capacity in excess of  $800 \text{ mAh.g}^{-1}$  has been reported for up to 500 cycles. In another work, they have also demonstrated improved high C-rate performance of SiOC/CNT composites prepared by mixing deagglomerated CNTs with SiOC powder, followed by heating to  $1000 \text{ }^\circ\text{C}$  [148].

**Table 1-3:** Summary of the experimental results of the electrochemical cycling of PDC and their nanocomposites.

Specimen (current density)	First reversible capacity (mAhg <sup>-1</sup> )	First cycle loss (%)	Reversible capacity (mAhg <sup>-1</sup> ) after n cycles	Reference
<b>SiOC (polysiloxane derived)</b>				
SiC <sub>1.83</sub> O <sub>1.23</sub>	920	25	–	117
SiOC-800°C (100 mA <sub>g</sub> <sup>-1</sup> )	906	33	700 (60)	120
SiOC-1000°C (100 mA <sub>g</sub> <sup>-1</sup> )	958	23	650 (60)	120
SiC <sub>0.70</sub> O <sub>0.01</sub> N <sub>0.61</sub>	38	60	–	120
SiOC-1100°C (37 mA <sub>g</sub> <sup>-1</sup> )	532	38	521 (10)	121
SiOC-800°C (18 mA <sub>g</sub> <sup>-1</sup> )	700	6	–	122
SiOC-1100°C (18.6 mA <sub>g</sub> <sup>-1</sup> )	719	42	–	123
SiOC-800°C, H <sub>2</sub> (50 mA <sub>g</sub> <sup>-1</sup> )	965	42	660 (40)	123
SiOC thin film (100 mA <sub>g</sub> <sup>-1</sup> )	1100	27	975 (40)	124
<b>SiOC (polysilane/polysilycarbodiimide derived)</b>				
SiOC-1000°C (37.2 mA <sub>g</sub> <sup>-1</sup> )	608	31	571 (50)	125
SiOC-1000°C (37.2 mA <sub>g</sub> <sup>-1</sup> )	580	32	540 (40)	126
SiOC (37.2 mA <sub>g</sub> <sup>-1</sup> )	573	30	–	127
SiOC:polystyrene (37.2 mA <sub>g</sub> <sup>-1</sup> )	608	30	577 (40)	134
<b>SiCN (polysilazane derived)</b>				
SiCN-1000°C (40 mA <sub>g</sub> <sup>-1</sup> )	456	40	171 (30)	131
SiCN-1100°C (18 mA <sub>g</sub> <sup>-1</sup> )	254	53	–	132
SiCN-1300°C (18 mA <sub>g</sub> <sup>-1</sup> )	383	31	–	132
SiCN-1700°C (18 mA <sub>g</sub> <sup>-1</sup> )	120	67	–	132
SiCN-1100°C (18 mA <sub>g</sub> <sup>-1</sup> )	263	57	175 (10)	133
Heat treated SiCN (40 mA <sub>g</sub> <sup>-1</sup> )	546	34	371 (30)	135
<b>PDC nanocomposites</b>				
SiOC:GNS (7:3) (40 mA <sub>g</sub> <sup>-1</sup> )	357	68	–	140
SiCN:graphite (1:3) (0.06 mA <sub>g</sub> <sup>-1</sup> )	474	35	440 (50)	141
SiCN:G 1300 °C (18 mA <sub>g</sub> <sup>-1</sup> )	312	24	–	142
SiOC:GO (100 mA <sub>g</sub> <sup>-1</sup> )	440	37	400 (75)	143
SiOC-CNT (100 mA <sub>g</sub> <sup>-1</sup> )	948	35	846 (40)	144
SiOC-exfoliated graphite	625	40	650 (15)	139

The enhanced cyclic performance for SiOC/CNT composite ( $515 \text{ mAh.g}^{-1}$  at  $8.5 \text{ A.g}^{-1}$ ) was primarily attributed to the increased electrical conductivity achieved by the addition of CNTs. Studies involving solid state mixing of MWCNT in SiCN ceramic particles have also been encouraging; a 14 % improvement over SiCN was observed with a reversible capacity of  $\sim 750$  ( $1^{\text{st}}$  cycle) and  $400 \text{ mAh.g}^{-1}$  ( $30^{\text{th}}$  cycle) for these composites [149].

## 1.4 Overview of Dissertation

Chapter 1, introduces polymer-derived ceramics and explains the need for a PDC-CNT composite with multifunctional properties. It also introduces two different energy based engineering applications and currently existing material related challenges in these applications.

In Chapter 2, we show the preparation of a boron modified organo-silicon polymer precursor, its chemical structure determination and its use in synthesis of Si(B)CN-MWCNT core-shell composite nanowires by ab-initio mixing and pyrolysis. The physical and chemical structure, oxidation resistance and thermal stability of the nanowires are also studied.

Chapter 3, details about an alternative method of synthesizing Si(B)CN-MWCNT composite nanowires by using kitchen microwaves operating at 2.45 GHz. Dielectric measurements are also presented, which were used to quantify the extent of microwave–CNT interaction and the degree of selective heating available at the CNT-polymer interface.

In Chapter 4, we studied the high-power laser irradiance behavior and resulting structural evolution of Si(B)CN-MWCNT coatings. Detailed electron microscopy and chemical spectroscopy further analyzes the irradiated coatings.

Chapter 5, presents the electrochemical cycling test results of Si(B)CN-MWCNT composite nanowire coatings as a lithium-ion battery anode. Performance of SiCN, boron doped Si(B)CN

and Si(B)CN-MWCNT specimens are compared and further post cycling microscopy and chemical analysis of the anodes is studied.

Chapter 6, is a modified approach wherein SiOC/CNT composite nanowires are synthesized and their electrochemical cycling is studied. The change in the chemistry results in improvement of various cycling performance parameters of Li-ion battery anode. Preliminary studies measuring the diffusion coefficient, which explains the enhanced performance are also presented.

Chapter 7, concludes the thesis and lays out a plan for the future work related to composite nanowires for energy based applications.

## 1.5 References

1. F.W. Ainger and J.M. Herbert . pp. 168-181 in The preparation of Phosphorous-Nitrogen Compounds as Non-Porous Solids. Anonymous Academic Press, NY, 1960.
2. Chantrel.Pg and P. Popper. "Anorganische Polymere Und Keramik," Chemie Ingenieur Technik, **37**, (1965).
3. Verbeek, W. U.S. Patent 3,853,867, 1974.
4. S. Yajima, J. Hayashi and M. Omori. "Continuous Silicon-Carbide Fiber of High-Tensile Strength," Chemistry Letters, 12, 1209-1212 (1975).
5. Takamizawa, M.; Kobayashi, T.; Hayashida, A.; Takeda, Y. U.S. Patent 4604367, 1986.
6. D. Seyferth and H. Plenio. "Borasilazane Polymeric Precursors for Borosilicon Nitride," Journal of American Ceramic Society, **73**, 2131-2133 (1990).
7. M. Weinmann, R. Haug, J. Bill, F. Aldinger, J. Schuhmacher and K. Muller. "Boron-containing polysilylcarbodi-imides: a new class of molecular precursors for Si-B-C-N ceramics," Journal of Organometallic Chemistry, **541**, 345-353 (1997).
8. M. Weinmann, R. Haug, J. Bill, M. de Guire and F. Aldinger. "Boron-modified polysilylcarbodi-imides as precursors for Si-B-C-N ceramics: Synthesis, plastic-forming and high-temperature behavior," Applied Organometallic Chemistry, **12**, 725-734 (1998).
9. O. Funayama, T. Kato, Y. Tashiro and T. Isoda. "Synthesis of a Polyborosilazane and its Conversion into Inorganic-Compounds," Journal of American Ceramic Society, **76**, 717-723 (1993).
10. Jungermann, H.; Jansen, M. EP 0973781A1, 1998.
11. P. Greil, "Polymer derived engineering ceramics," Advanced Engineering Materials, **2**, 339-348 (2000).

12. R. Riedel, G. Mera, R. Hauser and A. Klonczynski. "Silicon-based polymer-derived ceramics: Synthesis properties and applications - A review," *Journal of the Ceramic Society of Japan*, **114**, 425-444 (2006).
13. F.I. Hurwitz, P. Heimann, S.C. Farmer and D.M. Hembree. "Characterization of the Pyrolytic Conversion of Polysilsesquioxanes to Silicon Oxycarbides," *Journal of Material Science*, **28**, 6622-6630 (1993).
14. Gelest Inc., Polymers, company document.
15. B.V.M. Kumar and Y. Kim. "Processing of polysiloxane-derived porous ceramics: a review," *Science and Technology of Advanced Materials*, **11**, 044303 (2010).
16. J. Lipowitz, J.A. Rabe and T.M. Carr. "NMR Characterization of Polymethyldisilylazane Polymer - a Precursor to Si-C-N-O Ceramics," *Abstracts of Papers of the American Chemical Society*, **193**, 46 (1987).
17. D.A. Loy and K.J. Shea. "Bridged Polysilsesquioxanes - Highly Porous Hybrid Organic-Inorganic Materials," *Chemical Review*, **95**, 1431-1442 (1995).
18. R. Riedel, A. Kienzle, W. Dressler, L. Ruwisch, J. Bill and F. Aldinger. "A silicoboron carbonitride ceramic stable to 2,000 degrees C," *Nature*, **382**, 796-798 (1996).
19. H.W. Bai, G. Wen, X.X. Huang, Z. X. Han, B. Zhong, Z.H. Hu, Z.D. Zhang. "Synthesis and structural characterization of SiBOC ceramic fibers derived from single-source polyborosiloxane," *Journal of the European Ceramic Society*, **31**, 931-940, (2011).
20. Clariant Kion Corp. KiON Polysilazanes, company document.
21. A. Saha, R. Raj, D. Williamson, "A model for the nanodomains in polymer-derived SiCO." *Journal of the American Ceramic Society*, **89**, 2188-2195 (2006).

22. R. M. Morcos, G. Mera, A. Navrotsky, T. Varga, R. Riedel, F. Poli, K. Müller, "Enthalpy of formation of carbon-rich polymer-derived amorphous SiCN ceramics." *Journal of the American Ceramic Society*, **91**, 3349–3354 (2008).
23. G. Mera, R. Riedel, F. Poli, K. Müller, "Carbon rich SiCN ceramics derived from phenyl-containing poly(silylcarbodiimides)." *Journal of the European Ceramic Society*, **29**, 2873–2883 (2009).
24. H. Störmer, H. J. Kleebe, G. Ziegler, "Metastable SiCN glass matrices studied by energy-filtered electron diffraction pattern analysis." *Journal of Non-Crystalline Solids*, **353**, 2867–2877 (2007).
25. M.M. Guron, M.J. Kim and L.G. Sneddon. "A simple polymeric precursor strategy for the syntheses of complex zirconium and hafnium-based ultra high-temperature silicon-carbide composite ceramics," *Journal of American Ceramic Society*, **91**, 1412-1415 (2008).
26. A. Jalowiecki, J. Bill, F. Aldinger and J. Mayer. "Interface characterization of nanosized B-doped Si<sub>3</sub>N<sub>4</sub>/SiC ceramics," *Composites Part A-Applied Science and Manufacturing*, **27**, 717-721 (1996).
27. S. R. Shah, "High Temperature Mechanical and Oxidation Behavior of Amorphous Silicon Carbonitride Processed via Chemical Nanoprecursor Route", Thesis, University of Colorado, Boulder, Boulder, **2000**.
28. J. Cordelair and P. Greil. "Electrical conductivity measurements as a microprobe for structure transitions in polysiloxane derived Si-O-C ceramics," *Journal of the European Ceramic Society*, **20**, 1947-1957 (2000).



29. C. Haluschka, C. Engel and R. Riedel. "Silicon carbonitride ceramics derived from polysilazanes Part II. Investigation of electrical properties," *Journal of the European Ceramic Society*, **20**, 1365-1374 (2000).
30. P. Kroll, "Modelling and simulation of amorphous silicon oxycarbide," *Journal of Materials Chemistry*, **13**, 1657-1668 (2003).
31. G.D. Soraru, S. Modena, E. Guadagnino, P. Colombo, J. Egan and C. Pantano. "Chemical durability of silicon oxycarbide glasses," *Journal of American Ceramic Society*, **85**, 1529-1536 (2002).
32. S. Yajima, J. Hayashi, M. Omori and K. Okamura. "Development of a Silicon-Carbide Fiber with High-Tensile Strength," *Nature*, **261**, 683-685 (1976).
33. T. J. Cross, "Mechanical Properties of Polymer-Derived Ceramics constituted from Si-C-O-N and Their Tribological Behavior in Dry and Humid Environment, " Thesis, University of Colorado, Boulder, Boulder, **2006**.
34. P. Baldus, M. Jansen and D. Sporn. "Ceramic fibers for matrix composites in high-temperature engine applications," *Science*, **285**, 699-703 (1999).
35. T.J. Cross, R. Raj, T.J. Cross, S.V. Prasad and D.R. Tallant. "Synthesis and tribological behavior of silicon oxycarbonitride thin films derived from poly(urea)methyl vinyl silazane," *International Journal of Applied Ceramic Technology*, **3**, 113-126 (2006).
36. J. Bill and D. Heimann. "Polymer-derived ceramic coatings on C/C-SiC composites," *Journal of the European Ceramic Society*, **16**, 1115-20 (1996).
37. J. H. Lehman, K. E. Hurst, G. Singh, E. Mansfield, J. D. Perkins, C. L. Cromer, "Core-shell composite of SiCN and multiwalled carbon nanotubes from toluene dispersion." *Journal of Materials Science*, **45**, 4251-4254 (2010).

38. G. Singh, S. Priya, M. Hossu, S. R. Shah, S. Grover, A. R. Koymen, R. L. Mahajan, "Synthesis, electrical and magnetic characterization of core-shell carbon nanotube – SiCN nanowires." *Materials Letters*, **63**, 2435–2438 (2009).
39. V. Bedekar, G. Singh, R. L. Mahajan, S. Priya. "Synthesis and microstructural characterization of Barium Titanate nanoparticles decorated SiCN-MWCNT nanotubes – “nanoNecklace.”" *Ferroelectrics Letters Section*, **36**, 133–140 (2009).
40. R. Bhandavat, G. Singh, "Synthesis, characterization, and high temperature stability of Si(B)CN-coated carbon nanotubes using a boron-modified poly(ureamethylvinyl)silazane chemistry." *Journal of the American Ceramic Society*, **95**, 1536–1543 (2012).
41. R. Bhandavat, W. Kuhn, E. Mansfield, J. Lehman, G. Singh, "Synthesis of polymer-derived ceramic Si(B)CN-carbon nanotube composite by microwave-induced interfacial polarization." *ACS Applied Materials & Interfaces*, **4**, 11–16 (2012).
42. P. Colombo, G. Mera, R. Riedel and G.D. Soraru. "Polymer-Derived Ceramics: 40 Years of Research and Innovation in Advanced Ceramics," *Journal of American Ceramic Society*, **93**, 1805-1837 (2010).
43. L. Ferraioli, D. Ahn, A. Saha, L. Pavesi and R. Raj. "Intensely photoluminescent pseudo-amorphous SiliconOxyCarboNitride polymer-ceramic hybrids," *Journal of American Ceramic Society*, **91**, 2422-2424 (2008).
44. A. Karakuscu, R. Guider, L. Pavesi and G.D. Soraru. "White Luminescence from Sol-Gel-Derived SiOC Thin Films," *Journal of American Ceramic Society*, **92**, 2969-2974 (2009).

45. P. Miele, S. Bernard, D. Cornu and B. Toury. "Recent developments in polymer-derived ceramic fibers (PDCFs): Preparation, properties and applications - A review," *Soft Materials*, **4**, 249-286 (2006).
46. L.A. Liew, V.M. Bright and R. Raj. "A novel micro glow plug fabricated from polymer-derived ceramics: in situ measurement of high-temperature properties and application to ultrahigh-temperature ignition," *Sensors and Actuators A-Physical*, **104**, 246-262 (2003).
47. Starfire Inc., Polymer-to-Ceramic™ Technology for Friction Applications, company document.
48. M. Steinau, N. Travitzky, J. Gegner, J. Hofmann, and P. Greil, P. , "Polymer-Derived Ceramics for Advanced Bearing Applications, " *Advanced Engineering Materials*, **10**, 1141-1146 (2008).
49. S. Banerjee, T. Hemraj-Benny and S.S. Wong. "Covalent surface chemistry of single-walled carbon nanotubes," *Advanced Materials*, **17**, 17-29 (2005).
50. V.N. Popov, "Carbon nanotubes: properties and application," *Materials Science & Engineering R-Reports*, **43**, 61-102 (2004).
51. Y.P. Sun, K.F. Fu, Y. Lin and W.J. Huang. "Functionalized carbon nanotubes: Properties and applications," *Accounts of Chemical Research*, **35**, 1096-1104 (2002).
52. D. Tasis, N. Tagmatarchis, A. Bianco and M. Prato. "Chemistry of carbon nanotubes," *Chemical Reviews*, **106**, 1105-1136 (2006).
53. A. Javey, R. Tu, D.B. Farmer, J. Guo, R.G. Gordon and H.J. Dai. "High performance n-type carbon nanotube field-effect transistors with chemically doped contacts," *Nano Letters*, **5**, 345-348 (2005).
54. Kelly, B. T., Ed.; *Physics of Graphite*; Applied Science Publishers: London., 1981

55. Kelly, A.; Macmillan, N.H. *Strong solids*; Oxford University Press: 1986
56. R. Bacon, "Growth, Structure, and Properties of Graphite Whiskers," *Journal of Applied Physics*, **31**, 283-290 (1960).
57. E.W. Wong, P.E. Sheehan and C.M. Lieber. "Nanobeam mechanics: Elasticity, strength, and toughness of nanorods and nanotubes," *Science*, **277**, 1971-1975 (1997).
58. S. Berber, Y.K. Kwon and D. Tomanek. "Unusually high thermal conductivity of carbon nanotubes," *Physics Review Letters*, **84**, 4613-4616 (2000).
59. R.Z. Ma, J. Wu, B.Q. Wei, J. Liang and D.H. Wu. "Processing and properties of carbon nanotubes-nano-SiC ceramic," *Journal of Material Science*, **33**, 5243-5246 (1998).
60. E. Ionescu, A. Francis and R. Riedel. "Dispersion assessment and studies on AC percolative conductivity in polymer-derived Si-C-N/CNT ceramic nanocomposites," *Journal of Material Science*, **44**, 2055-2062 (2009).
61. A. Francis and R. Riedel. "Unusual magnetic behavior of SiCN/multiwalled carbon nanotubes nanocomposites," *Journal of Applied Physics*, **105**, 07A318 (2009).
62. Y. Katsuda, P. Gerstel, N. Janakiraman, J. Bill and F. Aldinger. "Reinforcement of precursor-derived Si-C-N ceramics with carbon nanotubes," *Journal of the European Ceramic Society*, **26**, 3399-3405 (2006).
63. G.D. Zhan, J.D. Kuntz, J.L. Wan and A.K. Mukherjee. "Single-wall carbon nanotubes as attractive toughening agents in alumina-based nanocomposites," *Nature Materials*, **2**, 38-42, (2003).
64. R.G. Duan and A.K. Mukherjee. "Synthesis of SiCNO nanowires through heat-treatment of polymer-functionalized single-walled carbon nanotubes," *Advanced Materials*, **16**, 1106-1109 (2004).

65. L.N. An, W.X. Xu, S. Rajagopalan, et al. "Carbon-nanotube-reinforced polymer-derived ceramic composites," *Advanced Materials*, **16**, 2036-2040 (2004).
66. S.R. Shah and R. Raj. "Nanodevices that explore the synergies between PDCs and carbon nanotubes," *Journal of the European Ceramic Society*, **25**, 243-249 (2005).
67. M. Luo, Y. Li, S. Jin, S. Sang and L. Zhao. "Oxidation resistance of multi-walled carbon nanotubes coated with polycarbosilane-derived SiC<sub>x</sub>O<sub>y</sub> ceramic," *Ceramics International*, **37**, 3055-3062 (2011).
68. M. Pashchanka, J. Engstler, J.J. Schneider, et al. "Polymer-Derived SiOC Nanotubes and Nanorods via a Template Approach," *European Journal of Inorganic Chemistry*, **23**, 3496-3506 (2009).
69. Y. Wang, Z. Iqbal and S. Mitra. "Rapid, low temperature microwave synthesis of novel carbon nano tube-silicon carbide composite," *Carbon*, **44**, 2804-2808 (2006).
70. H. Wang, X. Li, J. Ma, G. Li, T. Hu. "Multi-walled carbon nanotube-reinforced silicon carbide fibers prepared by polymer-derived ceramic route," *Composites Part A-Applied Science and Manufacturing*, **43**, 3, 317-324 (2012).
71. J. Cho, A.R. Boccaccini and M.S.P. Shaffer. "Ceramic matrix composites containing carbon nanotubes," *Journal of Material Science*, **44**, 1934-1951 (2009).
72. D. Shopova-Gospodinova, Z. Burghard, T. Dufaux, M. Burghard and J. Bill. "Mechanical and electrical properties of polymer-derived Si-C-N ceramics reinforced by octadecylamine - Modified single-wall carbon nanotubes," *Composites Science and Technology*, **71**, 931-937 (2011).

73. J. Honga, J. Lee, D. Jung and S. Shima. "Thermal and electrical conduction behavior of alumina and multiwalled carbon nanotube incorporated poly(dimethyl siloxane)," *Thermochimica Acta*, **512**, 34-39 (2010).
74. S. Kokott, L. Heymann and G. Motz. "Rheology and processability of multi-walled carbon nanotubes-ABSE polycarbosilazane composites," *Journal of European Ceramic Society*, **28**, 1015-1021 (2008).
75. R. Shvartzman-Cohen, Y. Levi-Kalisman, E. Nativ-Roth and R. Yerushalmi-Rozen. "Generic approach for dispersing single-walled carbon nanotubes: The strength of a weak interaction," *Langmuir*, **20**, 6085-6088 (2004).
76. K. Ramadurai, " Carbon Nanostructures For Thermal Applications: Synthesis And Characterization", Thesis, University of Colorado, Boulder, Boulder, **2007**.
77. [http://www.nist.gov/pml/div686/laser\\_power\\_meter.cfm](http://www.nist.gov/pml/div686/laser_power_meter.cfm)
78. J. Lehman, N. Varaksa, T. Theocharous and A. Dillon, "Carbon Nanotube-Based Coatings For Laser Power And Energy Measurements," *Laser Microfabrication Conference Proceedings*, 344-348 (2005).
79. C.L. Cromer, K.E. Hurst, X. Li and J.H. Lehman. "Black optical coating for high-power laser measurements from carbon nanotubes and silicate," *Optics Letters*, **34**, 193-195 (2009).
80. K. Ramadurai, C.L. Cromer, L.A. Lewis, K.E. Hurst, A.C. Dillon, R.L. Mahajan and J. H. Lehman, "High-performance carbon nanotube coatings for high-power laser radiometry," *Journal of Applied Physics*, **103**, 013103 (2008).

81. J. Lehman, and A. Sanders. "Very Black Infrared Detector from Vertically Aligned Carbon Nanotubes and Electric-Field Poling of Lithium Tantalate," *Nano Letters*, **10**, 3261-3266 (2010).
82. D.J. Advena, V.T. Bly and J.T. Cox. "Deposition and Characterization of Far-Infrared Absorbing Gold Black Films," *Applied Optics*, **32**, 1136-1144 (1993).
83. W.R. Blevin and J. Geist. "Infrared Reflectometry with a Cavity-Shaped Pyroelectric Detector," *Applied Optics*, **13**, 2212-2217 (1974).
84. W.R. Blevin and J. Geist. "Influence of Black Coatings on Pyroelectric Detectors," *Applied Optics*, **13**, 1171-1178 (1974).
85. J. Lehman, E. Theocharous, G. Eppeldauer and C. Pannell. "Gold-black coatings for freestanding pyroelectric detectors," *Measurement Science and Technology*, **14**, 916-922 (2003).
86. D.B. Betts, F.J.J. Clarke, L.J. Cox and J.A. Larkin. "Infrared Reflection Properties of 5 Types of Black Coating for Radiometric Detectors," *Journal of Physics E-Scientific Instruments*, **18**, 689-696 (1985).
87. N. Nelms and J. Dowson. "Goldblack coating for thermal infrared detectors," *Sensors and Actuators A-Physical*, **120**, 403-407 (2005).
88. J.H. Lehman, K.E. Hurst, L.K. Roberson, K. Nield and J.D. Hamlin. "Inverted spectra of single-wall carbon nanotube films," *Journal of Physical Chemistry C*, **112**, 11776-11778 (2008).
89. C. J. Chunnillall, J. H. Lehman, E. Theocharous and A. Sanders, "Infrared hemispherical reflectance of carbon nanotube mats and arrays in the 5–50  $\mu\text{m}$  wavelength region," *Carbon*, **50**, 14, 5348-5350, (2012).

90. K.E. Hurst, A.C. Dillon, S. Yang and J.H. Lehman. "Purification of Single Wall Carbon Nanotubes As a Function of UV Wavelength, Atmosphere, and Temperature," *Journal of Physical Chemistry C*, **112**, 16296-16300 (2008).
91. K. Ramadurai, C.L. Cromer, X. Li, R.L. Mahajan and J.H. Lehman. "Foam-based optical absorber for high-power laser radiometry," *Applied Optics*, **46**, 8268-8271 (2007).
92. K. Ramadurai, C.L. Cromer, A.C. Dillon, R.L. Mahajan and J.H. Lehman. "Raman and electron microscopy analysis of carbon nanotubes exposed to high power laser irradiance," *Journal of Applied Physics*, **105**, 093106 (2009).
93. H.L. Kleebe, "Microstructure and Stability of Polymer-Derived Ceramics; the Si-C-N System," *Physica Status Solidi (a)* **166**, 297 (1998).
94. Z.C. Wang, F. Aldinger and R. Riedel. "Novel silicon-boron-carbon-nitrogen materials thermally stable up to 2200 degrees C," *Journal of American Ceramic Society*, **84**, 2179-2183 (2001).
95. A. Göbel, F. Hemberger, H.P. Ebert, M. Jansen, J. Wilfert. " Thermophysical properties of an amorphous polymer-derived Si/B/N/C ceramic," *Thermochimica Acta*, **520**, 20-24 (2011).
96. A. Star, J. F. Stoddart, D. Steuerman, M. Diehl, A. Boukai, E. W. Wong, X. Yang, S. W. Chung, H. Choi, J. R. Heath, "Preparation and Properties of Polymer-Wrapped Single-Walled Carbon Nanotubes," *Angewandte Chemie International Edition* **40**, 9 (2001).
97. E. Ionescu, H.J. Kleebe and R. Riedel. "Silicon-containing polymer-derived ceramic nanocomposites (PDC-NCs): preparative approaches and properties," *Chemical Society Review*, *Journal of European Ceramic Society*, **41**, 5032-5052 (2011).



98. J. Bill and F. Aldinger. "Precursor-Derived Covalent Ceramics," *Advanced Material*, **7**, 775-787 (1995).
99. B. Papendorf, K. Nonnenmacher, E. Ionescu, H. Kleebe and R. Riedel. "Strong Influence of Polymer Architecture on the Microstructural Evolution of Hafnium-Alkoxide-Modified Silazanes upon Ceramization," *Small*, **7**, 970-978 (2011).
100. R. Marom, S.F. Amalraj, N. Leifer, D. Jacob, D. Aurbach, "A review of advanced and practical lithium battery materials, " *Journal of Material Chemistry*, **21**, 9938-9954, (2011).
101. A. Patil, V. Patil, D.W. Shin, J. Choi, D. Paik, S. Yoon, "Issue and challenges facing rechargeable thin film lithium batteries, " *Materials Research Bulletin*, **43**, 1913-1942 (2008).
102. [http://www.iea.org: EV\\_PHEV\\_Roadmap.pdf](http://www.iea.org: EV_PHEV_Roadmap.pdf)
103. B.J. Landi, M.J. Ganter, C.D. Cress, R.A. DiLeo, R.P. Raffaele, "Carbon nanotubes for lithium ion batteries, " *Energy & Environmental Science*, **2**, 638-654 (2009).
104. J.B. Goodenough, Y. Kim. "Challenges for Rechargeable Li Batteries," *Chemistry of Materials*, **22**, 587-603 (2010).
105. J.M. Tarascon, M. Armand, "Issues and challenges facing rechargeable lithium batteries," *Nature*, **414**, 359-367 (2001).
106. B. Scrosati, J. Garche, "Lithium batteries: Status, prospects and future," *Journal of Power Sources*, **195**, 2419-2430 (2010).
107. W. Zhang, "Lithium insertion/extraction mechanism in alloy anodes for lithium-ion batteries," *Journal of Power Sources*, **196**, 877-885 (2011).

108. D. Aurbach, Y. Talyosef, B. Markovsky, E. Markevich, E. Zinigrad, L. Asraf, J.S. Gnanaraj, H.J. Kim, "Design of electrolyte solutions for Li and Li-ion batteries: a review," *Electrochimica Acta*, **50**, 247-254 (2004).
109. V. Etacheri, R. Marom, R. Elazari, G. Salitra, D. Aurbach, "Challenges in the development of advanced Li-ion batteries: a review," *Energy & Environmental Science*, **4**, 3243-3262 (2011).
110. N. Takami, A. Satoh, T. Ohsaki, M. Kanda, "Lithium insertion and extraction for high-capacity disordered carbons with large hysteresis." *Electrochim. Acta*, **42**, 2537-2543 (1997).
111. N. Takami, A. Satoh, T. Ohsaki, M. Kanda, "Large hysteresis during lithium insertion into and extraction from high-capacity disordered carbons," *Journal of Electrochemical Society*, **145**, 478-482 (1998).
112. T. Zheng, W.R. McKinnon, J.R. Dahn, "Hysteresis during lithium insertion in hydrogen-containing carbons," *Journal of Electrochemical Society*, **143**, 2137-2145 (1996).
113. W. Dreyer, J. Jamnik, C. Gohlke, R. Huth, J. Moskon, M. Gaberscek, "The thermodynamic origin of hysteresis in insertion batteries," *Nature Materials*, **9**, 448-453 (2010).
114. L.S. Kanevskii, V.S. Dubasova, "Degradation of lithium-ion batteries and how to fight it: A review." *Russian Journal of Electrochemistry*, **41**, 1-16 (2005).
115. F. Cheng, J. Liang, Z. Tao, J. Chen, "Functional Materials for Rechargeable Batteries." *Advanced Materials*, **23**, 1695-1715 (2011).
116. J.R. Dahn, T. Zheng, Y.H. Liu, J.S. Xue, "Mechanisms for Lithium Insertion in Carbonaceous Materials." *Science*, **270**, 590-593 (1995).

117. M. Winter, J.O. Besenhard, M.E. Spahr, P. Novak, "Insertion electrode materials for rechargeable lithium batteries." *Advanced Materials*, **10**, 725-763 (1998).
118. W. Zhang, "A review of the electrochemical performance of alloy anodes for lithium-ion batteries." *Journal of Power Sources*, **196**, 13-24 (2011).
119. J. Saint, M. Morcrette, D. Larcher, L. Laffont, S. Beattie, J. Peres, "Towards a fundamental understanding of the improved electrochemical performance of silicon-carbon composites." *Advanced Functional Materials*, **17**, 1765-1774 (2007).
120. W.B. Xing, A.M. Wilson, K Eguchi, G. Zank, J.R. Dahn, "Pyrolyzed polysiloxanes for use as anode materials in lithium-ion batteries." *J Journal of Electrochemical Society*, **144**, 2410-2416 (1997).
121. P.E. Sanchez-Jimenez, R. Raj, "Lithium Insertion in Polymer-Derived Silicon Oxycarbide Ceramics." *Journal of American Ceramic Society*, **93**, 1127-1135 (2010).
122. A.M. Wilson, J.N. Reimers, E.W. Fuller, J.R. Dahn, "Lithium Insertion in Pyrolyzed Siloxane Polymers." *Solid State Ionics*, **74**, 249-254 (1994).
123. A.M. Wilson, W.B. Xing, G. Zank, B. Yates, J.R. Dahn, "Pyrolysed pitch-polysilane blends for use as anode materials in lithium ion batteries-2, the effect of oxygen." *Solid State Ionics*, **100**, 259-266 (1997).
124. D. Ahn, R. Raj, "Thermodynamic measurements pertaining to the hysteretic intercalation of lithium in polymer-derived silicon oxycarbide." *Journal of Power Sources*, **195**, 3900-3906 (2010).
125. D. Ahn, R. Raj, "Cyclic stability and C-rate performance of amorphous silicon and carbon based anodes for electrochemical storage of lithium." *Journal of Power Sources*, **196**, 2179-2186 (2011).

126. J. Kaspar, M. Graczyk-Zajac, R. Riedel, "Carbon-rich SiOC anodes for lithium-ion batteries: Part II. Role of thermal cross-linking." *Solid State Ionics*, **225**, 527–531 (2012).
127. M. Graczyk-Zajac, L. Toma, C. Fasel, R. Riedel, "Carbon-rich SiOC anodes for lithium-ion batteries: Part I. Influence of material UV-pre-treatment on high power properties." *Solid State Ionics*, **225**, 522–526 (2012).
128. X. Liu, M. Zheng, K. Xie, J. Liu, "The relationship between the electrochemical performance and the composition of Si-O-C materials prepared from a phenyl-substituted polysiloxane utilizing various processing methods." *Electrochimica Acta*, **59**, 304-309 (2012).
129. J. Shen, R. Raj, "Silicon-oxycarbide based thin film anodes for lithium ion batteries." *Journal of Power Sources*, **196**, 5945-5950 (2011).
130. H. Fukui, H. Ohsuka, T. Hino, K. Kanamura, "Preparation of Microporous Si-O-C Composite Material and Its Lithium Storage Capability." *Chemistry Letters*, **38**, 86-87 (2009).
131. H. Fukui, H. Ohsuka, T. Hino, K. Kanamura, "Polysilane/Acenaphthylene Blends Toward Si-O-C Composite Anodes for Rechargeable Lithium-Ion Batteries." *Journal of Electrochemical Society*, **158**, A550-A555 (2011).
132. H. Fukui, H. Ohsuka, T. Hino, K. Kanamura, "A Si-O-C Composite Anode: High Capability and Proposed Mechanism of Lithium Storage Associated with Microstructural Characteristics." *ACS Applied Materials and Interfaces*, **2**, 998-1008 (2010).
133. H. Fukui, N. Nakata, K. Dokko, B. Takemura, H. Ohsuka, T. Hino, K. Kanamura, "Lithiation and Delithiation of Silicon Oxycarbide Single Particles with a Unique Microstructure." *ACS Applied Materials and Interfaces*, **3**, 2318-2322 (2011).

134. X. Liu, M. Zheng, K. Xie, "Mechanism of lithium storage in Si-O-C composite anodes." *Journal of Power Sources*, **196**, 10667-10672 (2011).
135. V. Liebau-Kunzmann, C. Fasel, R. Kolb, R. Riedel, "Lithium containing silazanes as precursors for SiCN: Li ceramics - A potential material for electrochemical applications." *Journal of The European Ceramic Society*, **26**, 3897-3901 (2006).
136. D. Su, Y. Li, Y. Feng, J. Jin "Electrochemical Properties of Polymer-Derived SiCN Materials as the Anode in Lithium Ion Batteries." *Journal of American Ceramic Society*, **92**, 2962-2968 (2009).
137. J. Kaspar, G. Mera, A.P. Nowak, M. Graczyk-Zajac, R. Riedel, "Electrochemical study of lithium insertion into carbon-rich polymer-derived silicon carbonitride ceramics." *Electrochimica Acta*, **56**, 174-182 (2010).
138. M. Graczyk-Zajac, G. Mera, J. Kaspar, R. Riedel, "Electrochemical studies of carbon-rich polymer-derived SiCN ceramics as anode materials for lithium-ion batteries." *Journal of The European Ceramic Society*, **30**, 3235-3243 (2010).
139. H. Fukui, H. Ohsuka, T. Hino, K. Kanamura, "Influence of polystyrene/phenyl substituents in precursors on microstructures of Si-O-C composite anodes for lithium-ion batteries." *Journal of Power Sources*, **196**, 371-378 (2011).
140. Y. Feng, "Electrochemical properties of heat-treated polymer-derived SiCN anode for lithium ion batteries." *Electrochimica Acta*, **55**, 5860-5866 (2010).
141. T. Kim, Y.H. Mo, K.S. Nahm, S.M. Oh, "Carbon nanotubes (CNTs) as a buffer layer in silicon/CNTs composite electrodes for lithium secondary batteries." *Journal of Power Sources*, **162**, 1275-1281 (2006).

142. B.J. Landi, R.A. Dileo, C.M. Schauerman, C.D. Cress, M.J. Ganter, R.P. Raffaele, "Multi-Walled Carbon Nanotube Paper Anodes for Lithium Ion Batteries." *Journal of Nanoscience and Nanotechnology*, **9**, 3406-3410 (2009).
143. X. Liu, Z.D. Huang, S.W. Oh, B. Zhang, P. Ma, M.M.F. Yuen, J.K. Kim, "Carbon nanotube (CNT)-based composites as electrode material for rechargeable Li-ion batteries: A review." *Composites Science and Technology*, **72**, 121-144 (2012).
144. F. Ji, Y. Li, J Feng, D. Su, Y. Wen, Y. Feng, "Electrochemical performance of graphene nanosheets and ceramic composites as anodes for lithium batteries." *Journal of Material Chemistry*, **19**, 9063-9067 (2009).
145. R. Kolb, C. Fasel, V. Liebau-Kunzmann, R. Riedel, "SiCN/C-ceramic composite as anode material for lithium ion batteries." *Journal of The European Ceramic Society*, **26**, 3903-3908 (2006).
146. M. Graczyk-Zajac, C. Fasel, R. Riedel, "Polymer-derived-SiCN ceramic/graphite composite as anode material with enhanced rate capability for lithium ion batteries." *Journal of Power Sources*, **196**, 6412-6418 (2011).
147. D. Ahn, M. Lee, S.R. Shah, "Electrode Material, Lithium-ion Battery and Method Thereof." US Patent 291 438, Nov. 2010.
148. J. Shen, D. Ahn, R. Raj, "C-rate performance of silicon oxycarbide anodes for Li plus batteries enhanced by carbon nanotubes." *Journal of Power Sources*, **196**, 2875-2878 (2011).
149. L.J. Ning, Y.P. Wu, L.Z. Wang, S.B. Fang, R. Holze, "Carbon anode materials from polysiloxanes for lithium ion batteries." *Journal of Solid State Electrochemistry*, **9**, 520-523 (2005).

150. P. Dibandjo, M. Graczyk-Zajac, R. Riedel, V.S. Pradeepa, G.D. Soraru, "Lithium insertion into dense and porous carbon-rich polymer-derived SiOC ceramics." *Journal of The European Ceramic Society*, **32**, 2495–2503 (2012)
151. Y. Chen, C. Li, Y. Wang, Q. Zhang, C. Xu, B. Wei, L. An "Self-assembled carbon-silicon carbonitride nanocomposites: high performance anode materials for lithium-ion batteries. " *Journal of Material Chemistry*, **21**, 18186-18190 (2011).
152. H. Tamai, H. Sugahara, H. Yasuda, "Preparation of carbons from pitch containing polysilane and their anode properties for lithium-ion batteries." *Journal of Material Science Letters*, **19**, 53-56 (2000).
153. H. Konno, T. Morishita, S. Sato, H. Habazaki, M. Inagaki, "High-capacity negative electrode materials composed of Si-C-O glass-like compounds and exfoliated graphite for lithium ion battery." *Carbon*, **43**, 1111-1114 (2005).
154. Y. Feng, G. Du, X. Zhao, E. Yang, "Preparation and electrochemical performance of SiCN-CNTs composite anode material for lithium ion batteries." *Journal of Applied Electrochemistry*, **41**, 999-1002 (2011).
155. W.B. Xing, A.M. Wilson, G. Zank, J.R. Dahn, "Pyrolysed pitch-polysilane blends for use as anode materials in lithium ion batteries." *Solid State Ionics*, **93**, 239-244 (1997).
156. J.S. Xue, K. Myrtle, J.R. Dahn, "An Epoxy-Silane Approach to Prepare Anode Materials for Rechargeable Lithium Ion Batteries." *Journal of Electrochemical Society*, **142**, 2927-2935 (1995).

## **Chapter 2 - Synthesis, Characterization and High Temperature Stability of Si(B)CN Coated Carbon Nanotubes Using a Boron-modified Poly(ureamethylvinyl)silazane Chemistry**

### **Abstract**

Carbon nanotubes (CNT) and polymer-derived ceramics (PDCs) are of interest due to their unique multifunctional properties. CNTs, however, tend to lose their well-defined structure and geometry at about 400 °C in air. PDCs on the other hand are structureless in X-ray diffraction but show high chemical and thermal stability in air (up to ~1400 °C). Here, we demonstrate synthesis of a composite nanowire structure consisting of polymer-derived silicon boron-carbonitride (Si-B-C-N) shell with a multiwalled carbon nanotube core. This was achieved through a novel process involving preparation of a boron-modified liquid polymeric precursor through a reaction of trimethyl borate and poly(ureamethylvinyl)silazane under normal conditions; followed by conversion of polymer to ceramic on carbon nanotube surfaces through controlled heating. Electron microscopy and X-ray diffraction confirm presence of amorphous Si(B)CN coating on individual nanotubes for all specimen processed below 1400 °C. Thermogravimetric analysis, followed by Raman spectroscopy and transmission electron microscopy (TEM) revealed high temperature stability of the carbon nanotube core in flowing air up to 1000 °C.

---

Reprinted with permission from (R. Bhandavat, and G. Singh, “Synthesis, Characterization and High Temperature Stability of Si(B)CN Coated Carbon Nanotubes Using a Boron-modified Poly(ureamethylvinyl)silazane Chemistry,” *Journal of American Ceramic Society*, **95**, 5, 1536-1543). Copyright (2012) The American Ceramic Society.



## 2.1 Introduction

Superior functional properties of pristine single/multiwalled carbon nanotubes (MWCNT) including their high thermal conductivity, mechanical strength, and optical properties are now well documented in the literature [1-4]. Unfortunately, carbon nanotubes which are sp<sup>2</sup> bonded carbon structures tend to lose their well-defined structure and geometry due to oxidation at temperatures around 400 °C in air [5]. Polymer-derived ceramics (PDC) on the other hand are featureless in X-ray and TEM and yet possess some very remarkable physical properties [6-10]. Bulk PDCs belonging to Si/B/C/N/O families have been shown to possess extremely high oxidation resistance [6, 7], high temperature piezoresistivity [8], high mechanical strength [10, 11], and photoluminescence [14] among other properties [12, 13, 15, 16]. PDC precursor is a polymer in liquid state that allows the final ceramic to take any desired shape upon thermal curing [10, 15]. Hence, considering the unique properties and structure of both these materials, a composite nanowire in the core-shell configuration with Si-B-C-N forming the shell and carbon nanotube as a core is desired for the development of building blocks with much desired functional properties namely, flexibility with high temperature stability, piezoresistivity, electrochemical and optical properties. This also makes Si(B)CN-MWCNT composite an ideal coating material for copper cone type laser thermal detectors (that require high thermal stability and optical absorbance) and a robust anode material for Li-ion rechargeable batteries (high thermodynamic stability and electronic conductivity), which has been the focus of our research. Initial work involving introduction of carbon nanotubes in PDC composites was performed by Duan *et al.* [17], Linan *et al.* [18] and Shah *et al.* [19]. They reported enhancement in electrical, electrochemical and mechanical properties for these composites. More recently, SiCN-CNT bulk composite coatings were reported for high power laser thermal detectors based applications [20]. We anticipate that the Si(B)CN nanowires may have advantages over SiCN such as better

thermal stability, resistance to crystallization and hence greater oxidation resistance. In case of bulk ceramics, these properties of quaternary boron-containing ceramics have been attributed to the formation of turbostratic BN that can act as a barrier for the diffusing atoms, possibly slowing down related decomposition reactions. While various classes of polymer precursors have been utilized for synthesis of Si(B)CN ceramics, chlorosilanes, chloroborosilanes and polyborosilazanes remain the most popular [21-26]. Early work on boron-modified SiCN and SiOC ceramics was performed by European researchers, in which boron was introduced into silazanes typically by aminolysis of chloroborosilanes with methyl amine or by ammonolysis of single-source precursor ( $B[C_2H_4Si(CH_3)Cl_2]_3$ ) [21]. Hydroboration of new dopant ( $HBCl_2 \cdot SMe_2$ ) further enhanced the boron to silicon molar content in precursor to 1:2 with 56 % yield [23]. Alternatively, dehydrogenative coupling reactions of hydrosilanes have also been utilized to synthesize polysilazanes or polycarbosilazanes polymer precursors. As a further simplification, hydroboration of vinyl-substituted polysilazanes was performed after ammonolysis of chlorosilanes, to eliminate the by-product salt formed in the polymer. In almost all of these methods developed for Si(B)CN synthesis, preparation of polymeric precursor required several intermediate steps involving exclusive synthesis setup and special handling of hazardous chemicals (borane dimethyl sulfide, chlorosilanes) and their by-products (ammonium chloride). Even the most recently reported work on Si(B)CN polymeric precursor involved coammonolysis of chlorosilanes with boron trichloride resulting in a very low boron retention in final ceramic [27].

Here, we report a relatively novel, single-step process for molecular level interfacing of boron with polyureamethylvinylsilazane liquid polymeric precursor and utilize it for synthesis of Si(B)CN-MWCNT composite. In addition, ceramic shell's structural evolution has been

investigated and their high temperature stability has been highlighted by use of thermogravimetric analysis (TGA) and TEM. The XPS boron to silicon ratio in the final ceramic was 1:1 or higher for all specimen processed in (800 to 1500) °C temperature range.

## **2.2 Experimental Procedure**

### **2.2.1 Sample preparation**

1-gram MWCNTs (Bayer AG) were dispersed in 125 mL Toluene (grade: ACS 99.5 %) and sonicated for approximately 30 minutes (Branson 2510). Polymeric precursor, Poly(ureamethylvinyl)silazane (commercial name: Ceraset<sup>TM</sup>) and boron precursor, trimethyl borate (Sigma Aldrich<sup>TM</sup>) were then added at a very slow rate of approximately 1 mL/min to assist thorough and uniform polymer adhesion on nanotube surface while the mixture was being stirred at 300 rpm for about 24 hours. Attempt was made to achieve a homogenous dispersion of ~10 wt % of MWCNTs in the solution. The mixture was slowly dried in an inert atmosphere at 80 °C. Slow drying also facilitates evaporation of the byproducts (methanol) formed during the reaction. The dried powder was then cross-linked at 400 °C for 90 minutes and pyrolyzed at 800 °C for 4 hours, under nitrogen flowing at approximately 25 mL/min. The heating rate for crosslinking and pyrolysis was 10 °C/min. For the samples prepared at higher pyrolysis temperatures (1000 °C, 1100 °C, 1200 °C, 1300 °C, 1400 °C and 1500 °C), same material composition, heating/cooling rate and dwell times were used.

### **2.2.2 Characterization**

Electron Microscopy: SEM was performed using Carl Zeiss EVO Low-Vacuum SEM and FEI Nova NanoSEM 430. TEM was performed using Philips CM 100 (100 KeV) and FEI Tecnai F20 XT (200 KeV) for high-resolution imaging.

NMR:  $^{11}\text{B}$  and  $^{29}\text{Si}$  NMR Spectroscopy: Liquid State: Experiments were carried out on a Varian INOVA 400 (9.7 T) with 4 Nuclei Auto switchable probe operating at the resonance frequency of 128.33 MHz for  $^{11}\text{B}$  and 79.46 MHz for  $^{29}\text{Si}$ . The spectra  $^{11}\text{B}$  and  $^{29}\text{Si}$  were collected with sample rotating at 20 Hz with single pulse excitation. The high power  $90^\circ$  decoupling RF pulse of  $26\ \mu\text{m}$  @36 dB for  $^{29}\text{Si}$  and  $41\ \mu\text{m}$ @36 dB for  $^{11}\text{B}$  was applied and the recycle delay of 4 seconds for  $^{11}\text{B}$  and 3 seconds for  $^{29}\text{Si}$  was used.  $\text{C}_6\text{D}_6$  was used as a solvent and external standard diethyletherate of trifluoroborane  $(\text{C}_2\text{H}_5)_2\text{O}\cdot\text{BF}_3$  was used as a reference ( $\delta=0$  ppm) for  $^{11}\text{B}$  and Tetramethylsilane  $(\text{CH}_3)_4\text{Si}$  ( $\delta=0$  ppm) for  $^{29}\text{Si}$ .

Solid State NMR: Experiments were carried out on a Bruker Avance II 300 spectrometer operating at a static magnetic field of 7.05 T. A 4 mm MAS static H-X double-resonance probe at room temperature was used for collecting  $^{11}\text{B}$  and  $^{29}\text{Si}$  spectra. The solid-state experiments were conducted at the resonance frequencies of 96.26 MHz for  $^{11}\text{B}$  and 59.60 MHz for  $^{29}\text{Si}$ . The  $^{29}\text{Si}$  and  $^{11}\text{B}$  chemical shifts were expressed relative to 100 % external reference compound [Sodium 3-Trimethylsilyl Propionate, TMSP 2, 2, 3, 3-d4] signaled at  $\delta = 0$  ppm.

XPS: The surface chemistry of the nanowires was studied by X-ray photoelectron spectroscopy (PHI Quantera SXM) using monochromatic Al  $K\alpha$  X-radiation (beam size <9 micrometers). The overall scan was followed by a 15-minute high-resolution element scan for each sample.

FTIR: The FTIR spectra were collected on Thermo-Nicolet Nexus 870FT-IR spectrometer. FTIR samples were prepared by mixing approximately 1 wt % of the finely powdered sample with FTIR grade KBr powder.

XRD: The phase evolution in Si(B)CN-MWCNTs were characterized by Bruker powder X-ray diffractometer operating at room temperature, with Cu  $K\alpha$  radiation and nickel filter. The

pyrolyzed samples were finely crushed with mortar and pestle and laid on the palette for analysis.

TGA: Thermogravimetric analysis was performed using Shimadzu 50 TGA (limited to 1000 °C). Sample weighing, approximately 5 mg, was heated in a platinum pan at a rate of 10 °C/min in air flowing at 20 mL/min.

Raman Spectroscopy: Thermo Scientific DXR Raman microscope with an air-cooled green Nd:YAG laser ( $\lambda = 532$  nm) of 5 mW power was used as excitation source for all the specimens. Spectra were collected on the instrument operating with 3.1  $\mu\text{m}$  confocal hole size, 50  $\mu\text{m}$  wide entrance slit, 900 grating lines/mm and 10X MPlan objective Olympus lens. Data processing was performed using Thermo Scientific's Omnic software for microRaman. The samples were mounted on a manually controlled x-y stage.

### **2.3 Results and Discussion**

The addition of tri-methyl borate in ceraset resulted in formation of boron-modified poly(ureamethylvinyl)silazane by substitution reaction as shown in Fig. 2-1. In this reaction, a dative covalent bond was formed between the electron pair donor nitrogen and electron deficient boron. The methoxy ion from tri-methyl borate combined with weakly bonded hydrogen in Si-N polymer backbone, releasing methanol as a by-product. The characterization of polyborosilazane was performed using FT-IR (Fig. 2-2a), and liquid  $^{11}\text{B}$  and  $^{29}\text{Si}$  NMR (Fig. 2-2b and c). When compared with SiCN precursor (ceraset), the emergence of peaks at 1340, 1153 and 1080  $\text{cm}^{-1}$  in FTIR spectra of polyborosilazane shows the formation of new B-N and B-O bonds.

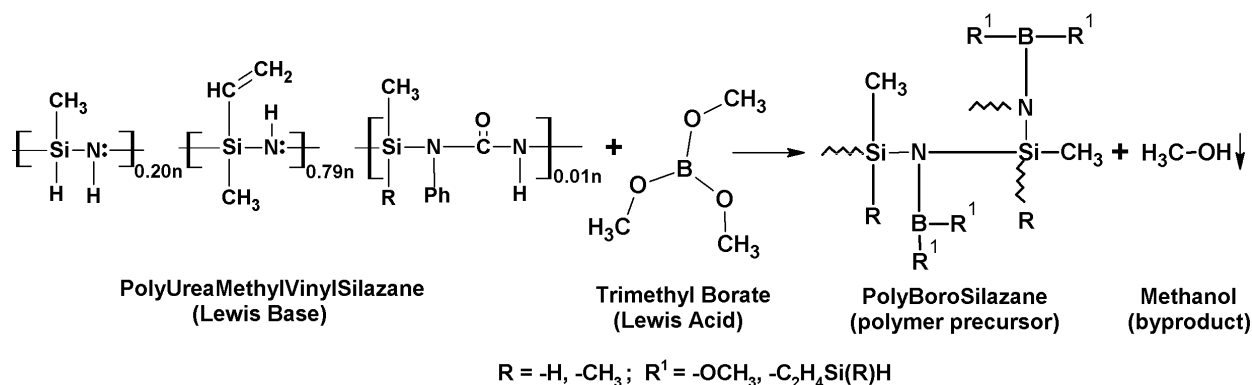


**Figure 2-1:** Proposed reaction mechanism for molecular level interfacing of boron with poly(ureamethylvinyl)silazane liquid polymer.

$^{11}\text{B}$  NMR spectrum showed a strong signal at 18.27 ppm and a weak signal at 22.12 ppm. As shown in Fig. 2(b), the 18.27 ppm is due to the electronegative methoxy functional group present in the reactant compound trimethyl borate with  $\text{sp}^2$ -bonded boron [28-31]. Whereas higher electronegativity of the dimethyl amine functional group in tertiary boron compounds resulted in electron deshielding at the boron nucleus and resulted in a peak downfield at 22.12 ppm [31-37]. It signifies B-O bond cleavage, which was replaced by B-N bonds, formed as a result of trimethyl borate reacting with ceraset.  $^{29}\text{Si}$  exhibited a strong and broad peak centered at -23 ppm, which were resolved in four peaks at -21, -22.27, -22.77, and -23.52 ppm due to the C-Si-H type magnetic environment present in the reacting ceraset, as shown in Fig. 2-2(c) [38]. A strong and sharp peak at -8.53 ppm and weak peak at -12.4 and -14.87 ppm signifies C-Si-N type bonds that arise from the environment present around the silicon in ceraset, similar to previous studies [29, 38, 39]. These sharp peaks were not observed in  $^{29}\text{Si}$  NMR of liquid ceraset (prior to the addition of trimethyl borate), implying an obvious change in Si magnetic surrounding caused by long range coupling, possibly caused by boron based functional group forming either B-C or B-N type chemical bonds.

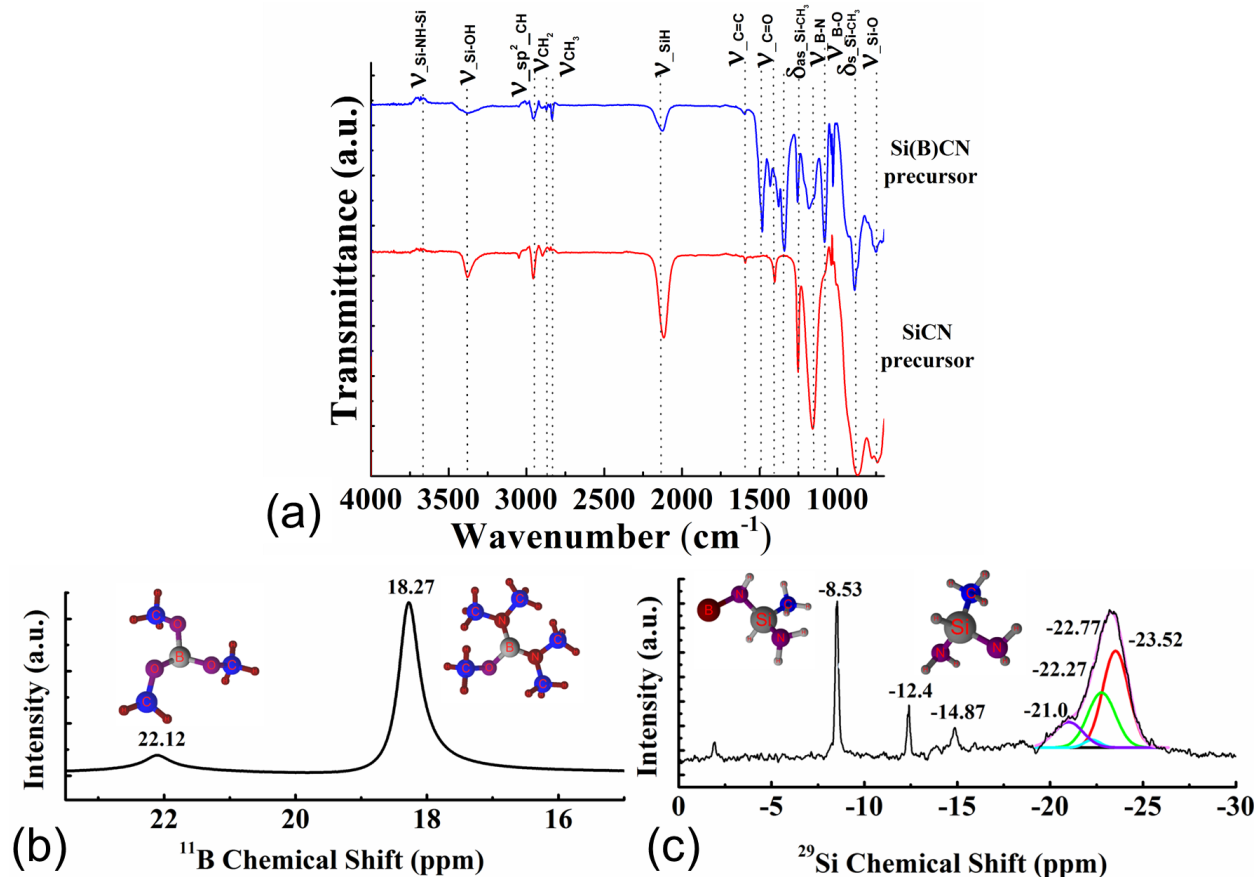


**Figure 2-2:** (a) FTIR spectra of poly(ureamethylvinyl)silazane and boron-modified poly(ureamethylvinyl)silazane. (b and c) Experimental <sup>11</sup>B and <sup>29</sup>Si liquid NMR spectra of liquid boron-modified polymer precursor collected at room temperature, respectively. The sample consisted of liquid precursor in C<sub>6</sub>D<sub>6</sub> solvent.

SEM and TEM analysis of specimen processed at various pyrolysis temperatures confirmed formation of composite nanowires consisting of Si(B)CN shell on MWCNT core. Majority of the nanowires remained isolated from each other while some ceramic “clusters” with embedded nanotubes were also observed. The ceramic coating on nanotubes was observed to be anywhere between (5 to 15) nm as revealed through HR-TEM. Fig. 2-3 and 2-4 are the SEM and TEM micrographs of nanowires pyrolyzed in (800 to 1500) °C range respectively. TEM, selected area

electron diffraction (SAED) of individual nanowires and XRD analysis of nanowire powder confirmed the typical pseudo-amorphous nature of Si-B-C-N ceramic. However, for samples processed at 1500 °C, a few ultra long (~ 50  $\mu\text{m}$  to 100  $\mu\text{m}$ ) crystalline rods were also observed, these were estimated to be about (1 to 5) % of the total content (Fig. 2-5). The formation of crystalline nanorods at 1500 °C is similar to that observed by Duan *et al.* [17] where the amorphous SiCN and  $\text{NH}_3$  (released during pyrolysis) reacted on CNT surfaces to form SiCNO nanowires.

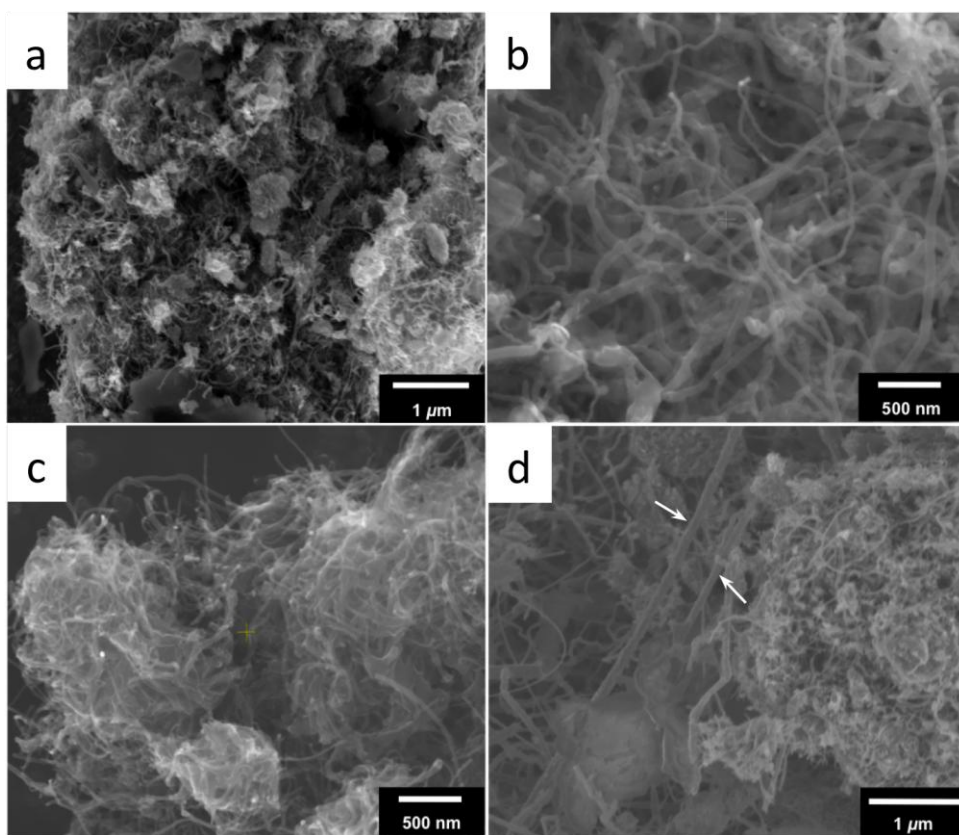


**Figure 2-3:** (a to d) SEM images of Si(B)CN coated MWCNTs pyrolyzed at 800, 1100, 1300, 1500 °C respectively. Arrows in (d) point at the ultra-long rod like structures.



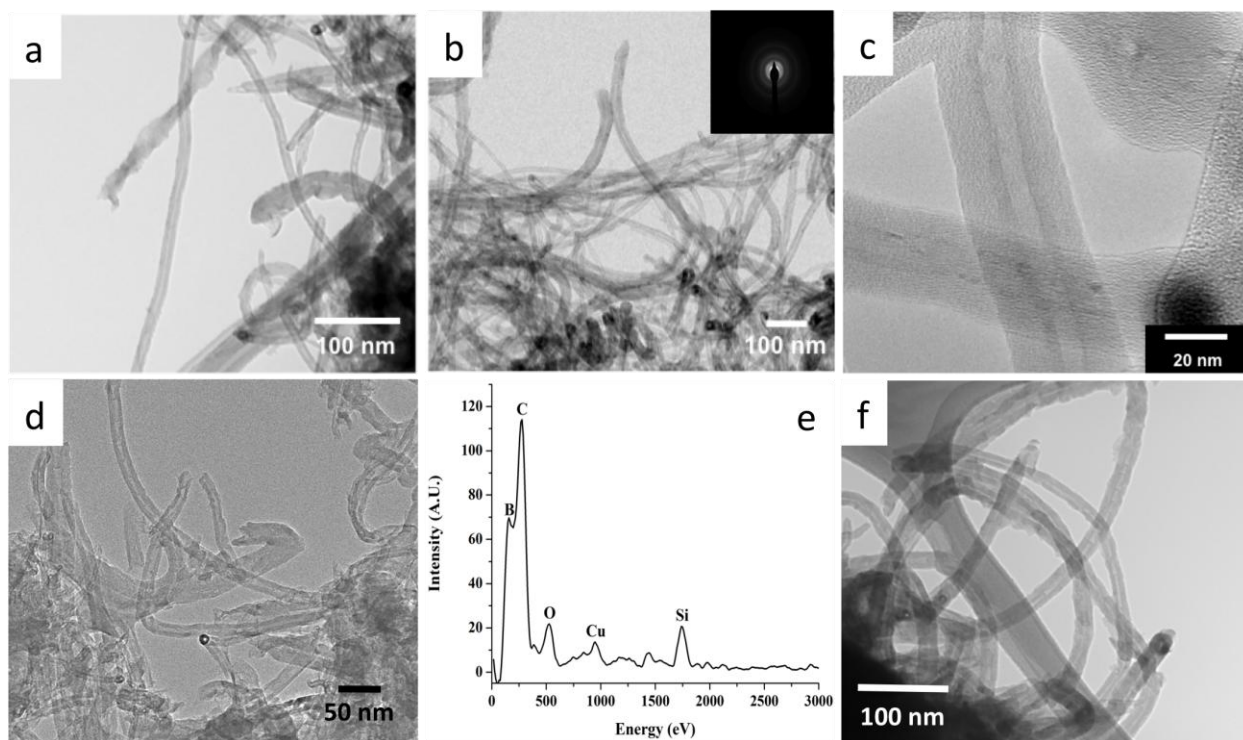


**Figure 2-4:** TEM images of nanowires pyrolyzed at (a) 800 °C, (b) 1000 °C, (c) 1000 °C (high resolution), (d) 1200 °C (e) Energy dispersive spectroscopy plot for 1200 °C specimen, and (f) 1300 °C.

Fig. 2-6 shows the XRD patterns of the specimen processed at 1200 °C, 1300 °C and 1500 °C. The analysis shows broad and featureless diffraction spectra for samples processed at lower temperatures suggesting amorphous nature of the ceramic, further implying that the structural transformation was retarded up to 1500 °C. Small peaks observed in the ceramic processed at 1500 °C suggests transition into partial crystallization. These small peaks could become more distinct and intense at even higher processing temperatures. Peaks at  $2\theta = 26.05^\circ$  and  $41.65^\circ$  were assigned to BN, while  $2\theta = 35.55^\circ$ ,  $41.65^\circ$ ,  $60^\circ$ ,  $71.75^\circ$  and  $77.9^\circ$  to  $\beta$ -SiC and at  $2\theta = 19.85^\circ$  and  $26.05^\circ$  are from the graphitic carbon in CNT [21].

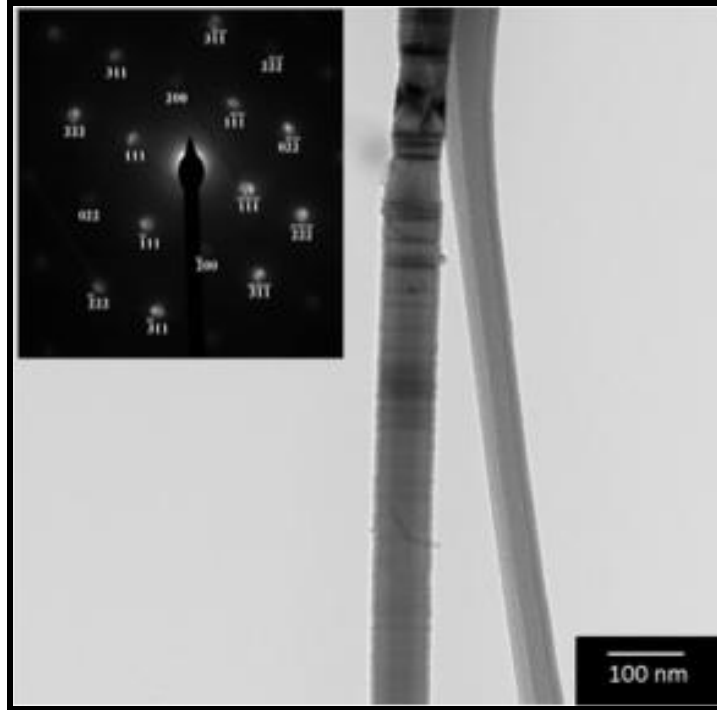


**Figure 2-5:** (a) TEM image of one of the ultra-long rod structures that were observed for specimen processed at 1500 °C. Inset: Select Area Electron Diffraction (SAED) pattern.

The XPS analysis involved curve fitting for the core and valence band peaks using non-linear least squares Gaussian-Lorentzian (70:30) mix function. As anticipated the Si, B, C, N and O peaks were consistently observed in all the samples. Since the XPS signal originates from the top few angstroms of the sample surface only, it was assumed that the carbon photoelectrons detected were emitted mostly from the ceramic and not MWCNT core.

Fig. 2-7 compares XPS data from nanowire specimens prepared at varying pyrolysis temperatures. The silicon band (for Si 2p photoelectrons) indicated peaks at 100.4 eV and 102.0 eV corresponding to SiC and Si<sub>3</sub>N<sub>4</sub> phases respectively [40, 41]. They emerge out into two distinct peaks with increasing pyrolysis temperatures. Whereas a higher energy peak of smaller magnitude interpreted at 103.3 eV indicates Si-O bonds (mostly SiO<sub>2</sub>). The higher energy peaks

at 188.7 eV and 190 eV indicate B-N bonds (as in  $\text{BN}_x\text{O}$ ) while the lower intensity peaks at a greater binding energy shift of 2 eV at 192 eV are due to B-O type bonds (in  $\text{B}_2\text{O}_3$ ).

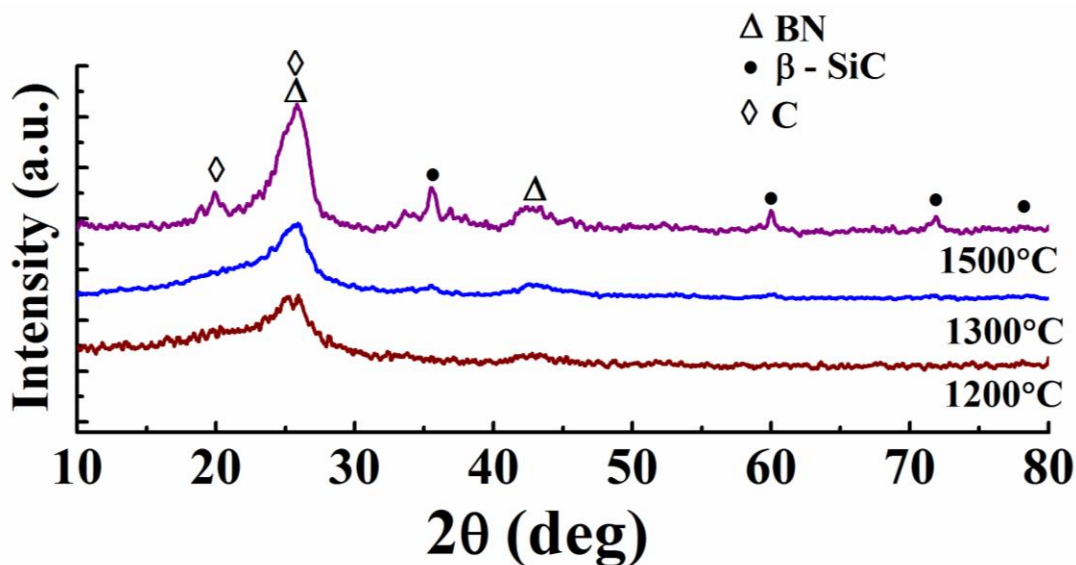


**Figure 2-6:** X-ray Diffraction plots for selected nanowire (powders) specimen. Si(B)CN shell is amorphous up to 1300 °C, crystallization is observed for specimen processed at 1500 °C.

Progressively increasing intensity of the B-N peak and simultaneously decreasing B-O peak implies the transition from one bond type to another observed with samples processed at higher temperatures i.e., above 1200 °C. The binding energy of C1s photoelectrons at 282.9 eV confirms the Si-C bond assignment. Whereas the aliphatic carbon is responsible for peaks at 284.18 eV due to  $\text{sp}^2$  bonded carbon atoms and peak at 285.18 eV is due to  $\text{sp}^3$  bonded carbon atoms [43]. Few instances that showed the shake-up satellite peaks typically observed beyond 290 eV were ignored. The N1s band on deconvolution showed peak at 396.8 eV attributable to Si-N bonds, which confirm the assignment of silicon 2p photoelectrons. The peaks at 397.8 eV and 398.1 eV indicate Si-N (mostly  $\text{Si}_3\text{N}_4$ ) and BN bonds respectively. Based on this XPS analysis, the average Si to B ratio was observed to be 1:1.26. A more accurate analysis would

require sophisticated combustion analysis techniques but nonetheless it is clear that a good percentage of boron could be retained in the resulting ceramic shell. It would also be possible to tune the percentage of boron to higher or lower levels by controlling the amounts of tri-methyl borate in the starting polymer. The elemental composition and empirical formula based on XPS data is shown in Table 2-1.

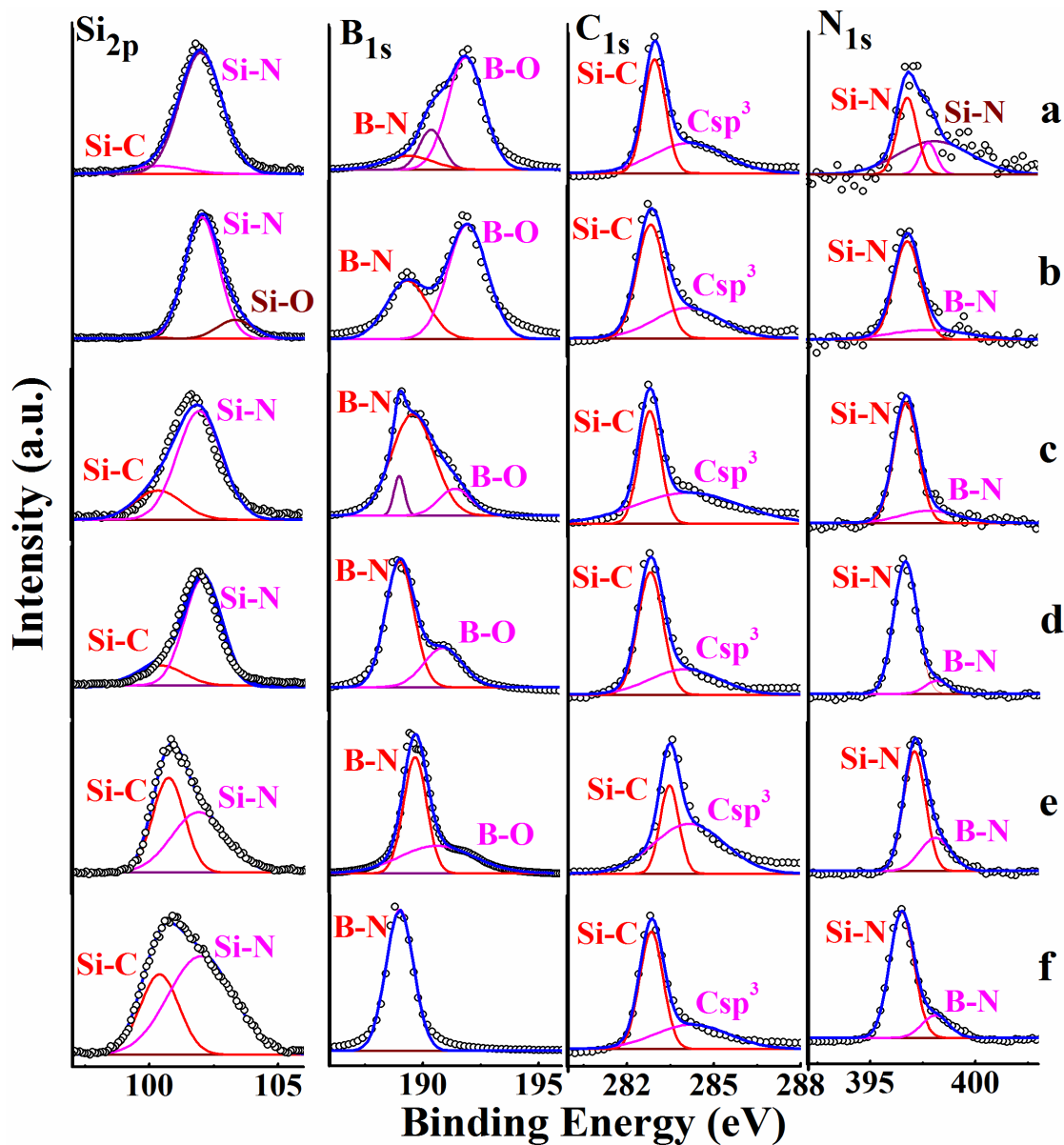


**Figure 2-7:** (a to f) Core level elemental XPS spectra of Si(B)CN-MWCNT synthesized 800 °C, 1100 °C, 1200 °C, 1300 °C, 1400 °C and 1500 °C, respectively.

**Table 2-1:** XPS Chemical composition of SiBCN-MWCNT nanowires for varying pyrolysis temperatures ( $T_{\text{pyrolysis}}$ ). Hydrogen content is assumed to be less than 1 wt % and is neglected in analysis.

$T_{\text{pyrolysis}}$ (°C)	Si (wt%)	B (wt%)	C (wt%)	N (wt%)	O (wt%)	Empirical formula
800	13.8	18.26	37.09	17.83	13.02	$\text{SiB}_{3.43}\text{C}_{6.27}\text{N}_{2.58}\text{O}_{1.65}$
1000	9.93	6.49	52.89	2.95	27.74	$\text{SiB}_{1.69}\text{C}_{12.43}\text{N}_{0.59}\text{O}_{4.89}$
1100	5	3.45	69.39	2.56	19.6	$\text{SiB}_{1.79}\text{C}_{32.38}\text{N}_{1.02}\text{O}_{6.86}$
1300	5.81	7.86	61.67	7.19	17.46	$\text{SiB}_{3.51}\text{C}_{24.77}\text{N}_{2.48}\text{O}_{5.26}$
1400	7.17	10.98	56.31	9.12	16.29	$\text{SiB}_{3.97}\text{C}_{18.33}\text{N}_{2.54}\text{O}_{3.98}$
1500	7.93	17.69	39.86	27.02	7.5	$\text{SiB}_{5.78}\text{C}_{11.73}\text{N}_{6.81}\text{O}_{1.66}$

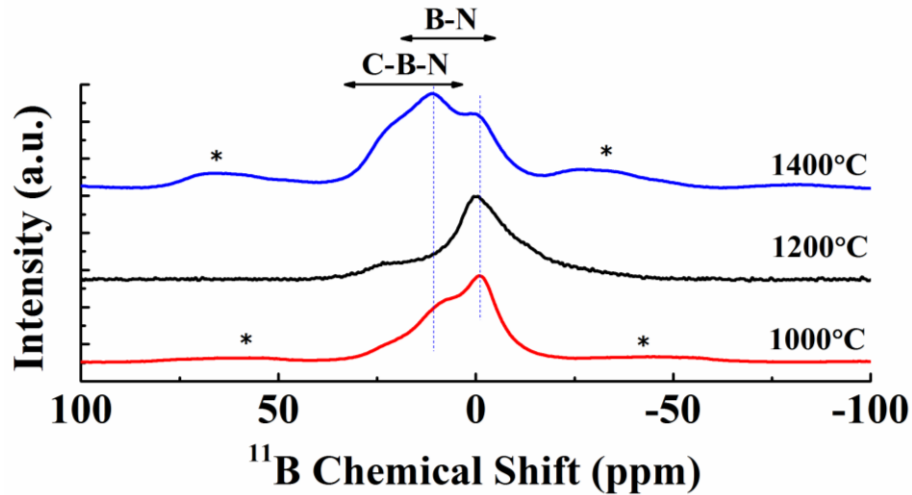


**Figure 2-8:** (a) Comparative experimental  $^{11}\text{B}$  SS-NMR spectra of the samples pyrolyzed at 1000 °C, 1200 °C and 1400 °C shows the B-N type bond formation (preferred at higher temperatures) than B-O at lower processing temperatures. These spectra were collected by finely crushing the sample using mortar and pestle.

The solid-state  $^{11}\text{B}$  spectra were collected for samples pyrolyzed at 1000 °C, 1200 °C and 1400 °C only; based on XPS and XRD data, these specimens are likely to capture major boron chemical shifts. These three representative samples were compared as shown in Fig. 2-8, where the upfield peaks most closely resembles the  $\text{BN}_3$  and  $\text{BC}_2\text{N}$  [44], and the downfield peaks

resemble more electronegative  $BC_3$  [45]. This analysis suggests that the ceramic boron possesses different magnetic environments among which the B-N type bonds dominate at higher pyrolysis temperatures (also confirmed by the XPS results).

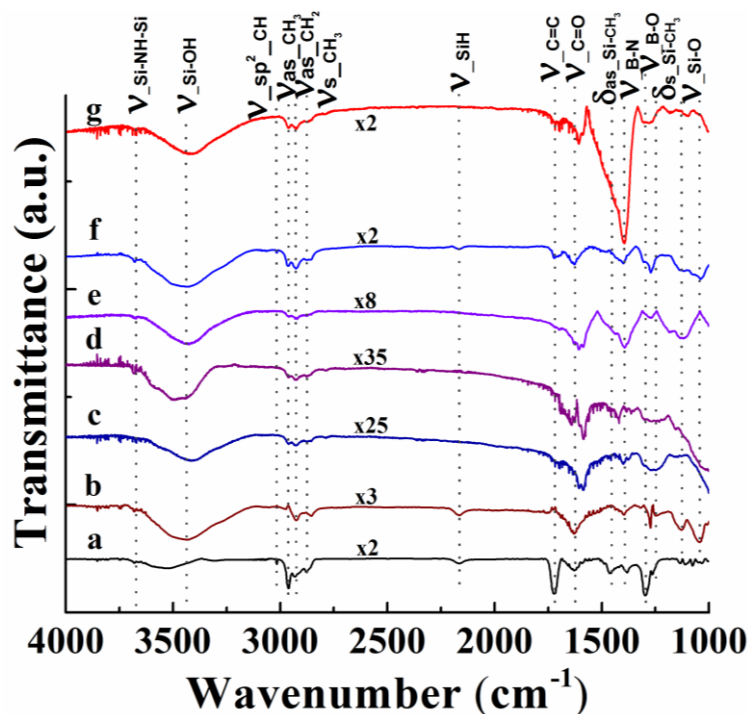


**Figure 2-9:** (a-g) Diffuse Reflectance Infrared Fourier Transform (DRIFT) spectra of samples pyrolyzed at 800, 1000, 1100, 1200, 1300, 1400 and 1500 °C. ( $\nu$ : stretching vibration mode and  $\delta$ : bending vibration mode).

The characteristic band at  $1715\text{ cm}^{-1}$  was an obvious assignment, due to C=C stretching vibrations in the CNT. Small peak at  $1629\text{ cm}^{-1}$  is characteristic of C=O stretching in N-Disubstituted amides (in the urea group in ceramic precursor) which typically appears at  $1680\text{ cm}^{-1}$ - $1630\text{ cm}^{-1}$  for solids [46]. The Ketone groups which usually stretches at  $1715\text{ cm}^{-1}$  wavenumber, have a modified frequency due to the mesomeric effects causing the  $\pi$  electron delocalization and resulting in a weaker C=O bond. The  $-CH_3$  asymmetric (weak at  $1475\text{ cm}^{-1}$ - $1450\text{ cm}^{-1}$ ) and symmetric deformations (typically at  $1280\text{ cm}^{-1}$ - $1255\text{ cm}^{-1}$ ) were responsible for

the weak and medium intensity bands at 1476 and 1265  $\text{cm}^{-1}$  corresponding to Si-CH<sub>3</sub> group. The medium-to-strong peaks at 1396  $\text{cm}^{-1}$  could be assigned to hexagonal B-N stretching modes that are strongly absorbed at 1465  $\text{cm}^{-1}$ -1330  $\text{cm}^{-1}$  [47, 48]. The strong absorption at 1301  $\text{cm}^{-1}$  could be due to B-O stretching (typically 1350  $\text{cm}^{-1}$ -1310  $\text{cm}^{-1}$ ) in B(OCH<sub>3</sub>)<sub>3</sub> [49, 50]. Peaks at 1124  $\text{cm}^{-1}$  and 1044  $\text{cm}^{-1}$  could be assigned to Si-O-Si stretching vibrations, which were characteristic bands of siloxane chains, and typically appeared as strong bands at 1130  $\text{cm}^{-1}$ -1000  $\text{cm}^{-1}$ . Small peaks at 904  $\text{cm}^{-1}$  and 808  $\text{cm}^{-1}$  could be assigned to C-H out-of-plane bending vibrations (typically at 990-910  $\text{cm}^{-1}$ ) and to Si-H bending vibration mode (usually 960  $\text{cm}^{-1}$ -800  $\text{cm}^{-1}$ ) respectively.

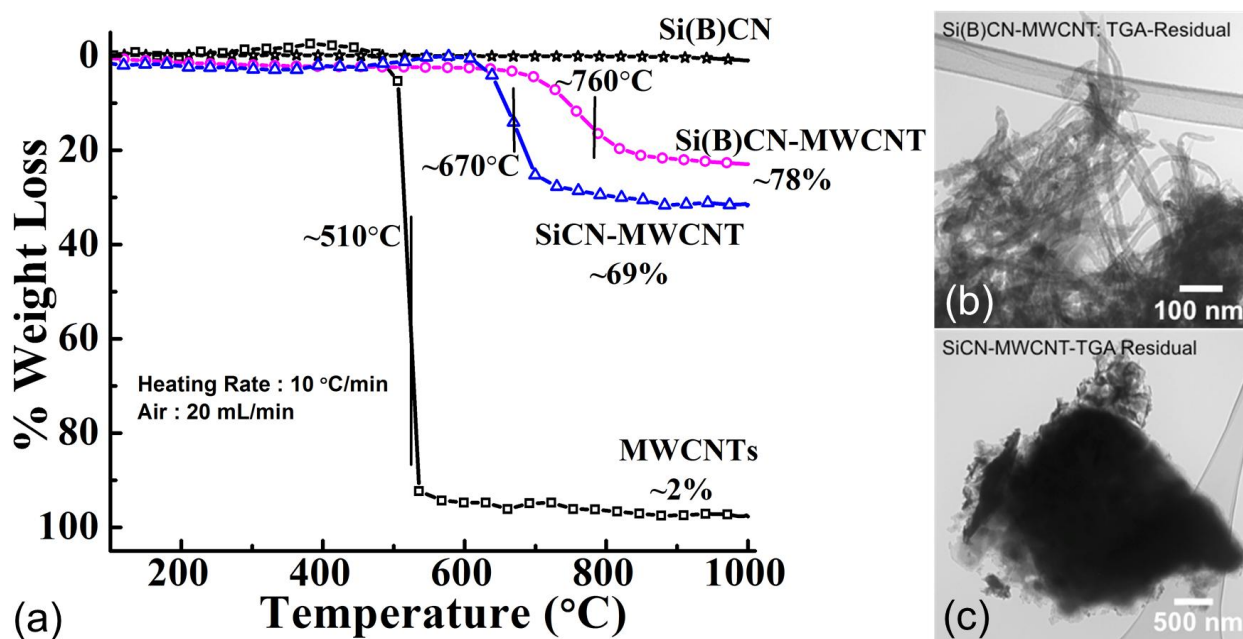


**Figure 2-10:** (a) TGA plots showing the weight loss (%) and oxidation temperature (°C) for Si(B)CN, MWCNTs, Si(B)CN-MWCNTs and SiCN-MWCNTs performed in flowing air. (b) and (c) TEM micrographs showing residual TGA Si(B)CN-MWCNT and SiCN-MWCNT respectively. MWCNTs could be seen in the Si(B)CN-MWCNTs TGA residual while for SiCN-MWCNTs, the material turned white indicating severe oxidation and burning of the CNT core.

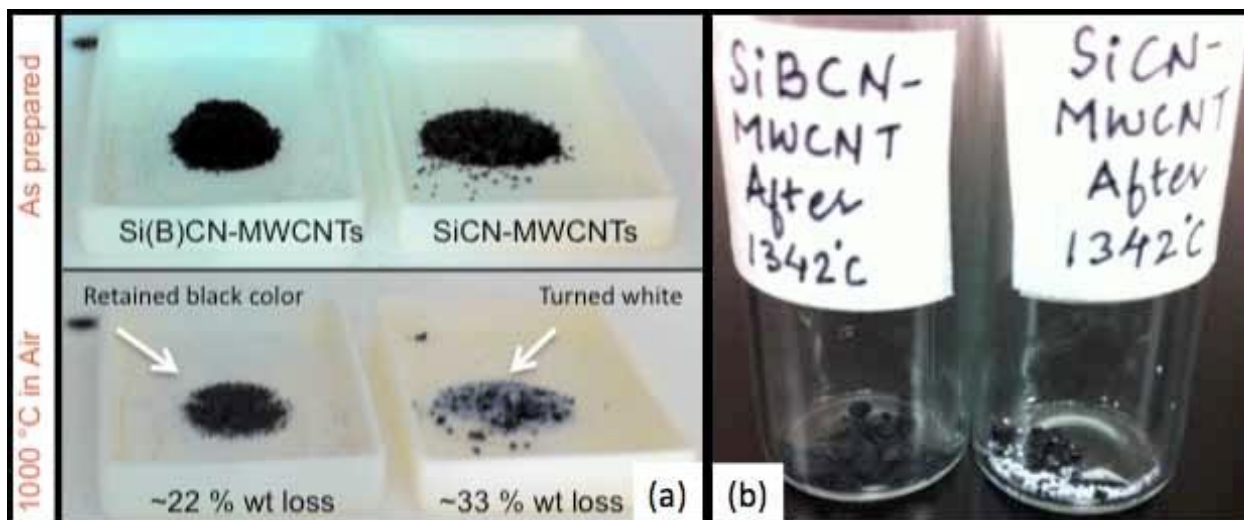


**Figure 2-11:** Comparison of bulk SiCN/CNT and Si(B)CN/CNT nanowires heated in air up to (a) 1000 °C (b) 1340 °C in air.

Thermogravimetric analysis was performed for Si(B)CN-MWCNT as well as pristine MWCNTs for comparing their high temperature behavior. As shown in Fig. 2-10, the Si(B)CN-MWCNT specimen had a linear relationship between residual mass and the oxidation temperature, which was observed to be about  $750 \pm 10$  °C. After the weight loss at about 750 °C, the composite nanowire specimen showed stability in their weight and consequently their physical structure. The oxidation/threshold temperature did not seem to depend much on nanowire processing temperature. TGA residual weight was 77 % for the Si(B)CN specimen processed at 1100 °C. The residual mass consisted of composite nanowires along with some “clusters” of the ceramic material. The Si(B)CN-MWCNT TGA residual was later on observed under the TEM. The walls and core structure remained intact, at least for thicker nanotubes (diameter > 50 nm). TGA performed on as-obtained MWCNTs showed 98 % weight loss at ~510 °C. The narrow weight loss range of pristine nanotubes suggested that they were formed of homogenous material whereas an extended weight loss range for the composite nanowire sample implies a larger range of oxidation temperature with lesser weight loss of a comparatively non-homogenous amorphous



ceramic. The (25 to 30) % weight loss for Si(B)CN-MWCNT composite nanowires could be attributed to the combustion of small diameter, defective or non-uniformly coated nanotubes. This was further confirmed from the fact that mostly larger diameter nanowires were observed in TGA residual. Also, as thermal annealing have been shown to increase the stability of MWCNTs [52], this increase in the oxidation resistance of Si(B)CN-MWCNTs could be credited collectively to the protective ceramic shield and defect elimination in CNTs during the pyrolysis process.

We also compared TGA of Si(B)CN-MWCNT with SiCN-MWCNT processed under identical conditions (same wt % of CNTs). Si(B)CN-MWCNT TGA residual retained its original appearance (black in color) while the SiCN-MWCNT turned into white chunks @1000 °C in flowing air (instrument limited to 1000 °C). No nanotubes could be seen in SiCN-MWCNT TGA residual (Fig. 2-10c). In another set of experiments, SiCN-MWCNT and Si(B)CN-MWCNT specimen were heated in a box furnace up to 1350 °C (Fig. 2-11). Here also Si(B)CN-MWCNT retained its characteristic black while SiCN-MWCNT turned into white particles, indicating superior oxidation resistance of Si(B)CN-MWCNT nanowires. To further confirm the survival of MWCNTs in Si(B)CN-MWCNT-TGA residual, we performed Raman spectroscopy for all specimens starting with “as-obtained” MWCNTs. Characteristic CNT peaks could be seen in the Raman spectrum of Si(B)CN-MWCNT TGA residual (Fig. 2-12). The high temperature stability of Si(B)CN could be explained based on previous work by Riedel and Co-workers [7, 51], where the B/C/N turbostratic phase acted as a barrier for the diffusing oxygen atoms, inhibiting structural reorganizations and retarding the related decomposition reactions in the ceramic. Study of high temperature oxidation resistant for selected Si(B)CN specimens is shown in Fig. 2-13.

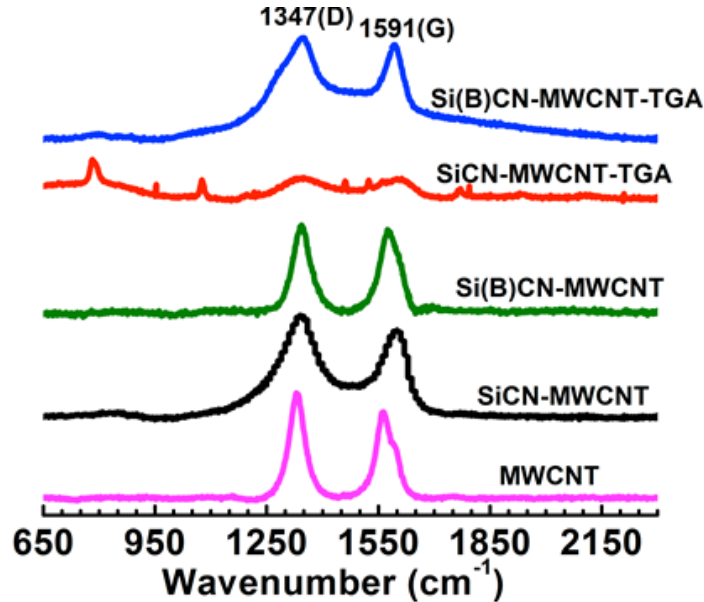


**Figure 2-12:** Raman spectra for various specimens prepared in this study. Raman plot of Si(B)CN-MWCNT TGA residual confirms presence of D ( $\sim 1350\text{ cm}^{-1}$ ) and G ( $\sim 1600\text{ cm}^{-1}$ ) bands (peaks) that are characteristic of CNT similar to that observed in “as-obtained” MWCNTs specimen. As expected, SiCN-MWCNT TGA residual did not show distinct D and G peaks indicating burning of MWCNTs in this specimen (correlating TEM observations in Fig. 2-10).

Eventually, at high temperatures the retention of ceramic shell on nanotubes is critical and may depend on the ceramic and CNT thermal expansion coefficients (CTE). The thermal expansion phenomenon for CNTs is rather complex and has been studied the least. CTE for CNTs can vary anywhere from  $-1 \times 10^{-6}\text{ }^{\circ}\text{C}^{-1}$  to  $9 \times 10^{-6}\text{ }^{\circ}\text{C}^{-1}$  depending upon the type of nanotube (SWCNT or MWCNT), its diameter and the number of walls etc [53, 54, 55]. In general, SWCNTs have lower CTE than MWCNTs while graphene has a CTE of  $\sim 2.5 \times 10^{-6}\text{ }^{\circ}\text{C}^{-1}$  at  $\sim 1000\text{ }^{\circ}\text{C}$  [54]. For Si(B)CN is it approximately  $3\text{ to }4 \times 10^{-6}\text{ }^{\circ}\text{C}^{-1}$ , which falls within the range specified for CNTs and graphitic carbon [56]. Our TEM results show survival of the coating and NT core @  $1000\text{ }^{\circ}\text{C}$  (in air), we surmise that the Si(B)CN-CNT interface is stable at high temperatures.

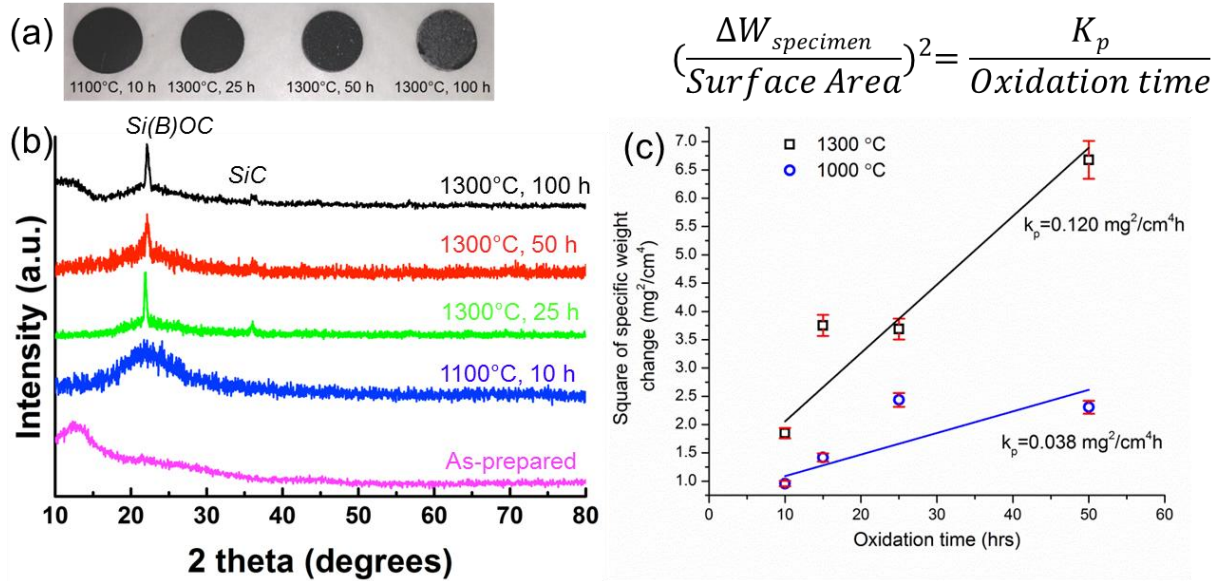


**Figure 2-13:** (a) Digital photograph of the pellets prepared at different pyrolysis conditions (1100, 1300 °C) and oxidation times (10, 25, 50 and 100 hours) (b) Corresponding powder XRD spectra of the as-prepared, 1100 °C-10 h, 1300 °C-25 h, 1300 °C-50 h, 1300 °C-100 h pellet specimens (c) Square of specific weight change versus oxidation time to determine the oxidation rate constant ( $K_p$ ) for the 1000 °C and the 1300 °C pellet specimens.

Based on the information regarding the bond formation obtained from spectroscopy results carried out at several processing stages (from polymer to ceramic), we propose the molecular structural evolution of the Si(B)CN from polyborosilazane precursor as shown in the Fig. 2-14. Boron occupies the side groups in the Si-N backbone at the nitrogen sites forming a linear or a branched chain. Whereas, the vinyl groups help in rearrangement of crosslinked network, with low boron concentrations.

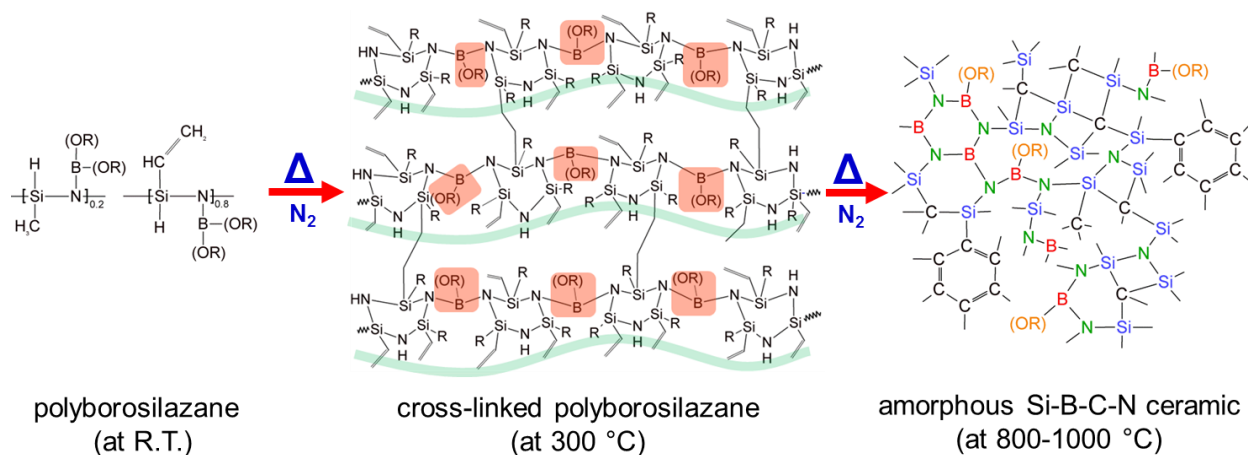


**Figure 2-14:** Proposed structural evolution of Si(B)CN ceramic from polyborosilazane polymer precursor via cross-linked infusible mass.

## 2.4 Conclusion

We have demonstrated successful introduction of boron in a polysilazane polymer precursor following a single-step process. This was achieved through a reaction of trimethyl borate with polyureasilazane under atmospheric conditions. The boron-modified polymer, which is liquid at room temperature was then interfaced with carbon nanotube surfaces to form Si(B)CN/MWCNT shell/core nanowires. SEM images confirmed high nanowire yield, while TEM validated the amorphous nature of the ceramic shell with thicknesses of approximately (5 to 10) nm. Detailed spectroscopy studies reveal that B-O type bonds are preferred at lower processing temperatures (800 to 1200) °C while B-N type bonds are dominant for samples processed at or above 1300 °C. Almost all of the boron could be retained in the final ceramic, with Si:B ratio of 1:1 or higher. The overall ceramic yield ranged (50 to 55) %. TEM of TGA residual revealed that Si(B)CN ceramic shell protected the nanotube core at 1000 °C in flowing air, while SiCN-MWCNTs did not survive under identical conditions and formed white chunks. This method of boron doping offers a rapid and more efficient alternative to the conventional sophisticated methods and can be

utilized to produce bulk Si(B)CN components as well. The ease of polymer synthesis presents greater flexibility in tailoring the chemistry and structure of the final ceramic.

## 2.5 References

1. S.S. Fan, M.G. Chapline, N.R. Franklin, T.W. Tomblor, A.M. Cassell and H.J. Dai. "Self-oriented regular arrays of carbon nanotubes and their field emission properties," *Science*, **283**, 512-514 (1999).
2. R.S. Ruoff and D.C. Lorents. "Mechanical and Thermal-Properties of Carbon Nanotubes," *Carbon*, **33**, 925-930 (1995).
3. S.B. Sinnott and R. Andrews. "Carbon nanotubes: Synthesis, properties, and applications," *Critical Reviews in Solid State and Materials Sciences*, **26**, 145-249 (2001).
4. M.F. Yu, B.S. Files, S. Arepalli and R.S. Ruoff. "Tensile loading of ropes of single wall carbon nanotubes and their mechanical properties," *Phys. Rev. Lett.*, **84**, 5552-5555 (2000).
5. Y. Gogotsi, "High-Temperature Rubber Made from Carbon Nanotubes," *Science*, **330**, 1332-1333 (2010).
6. R. Riedel, G. Passing, H. Schonfelder and R.J. Brook. "Synthesis of Dense Silicon-Based Ceramics at Low-Temperatures," *Nature*, **355**, 714-717 (1992).
7. R. Riedel, A. Kienzle, W. Dressler, L. Ruwisch, J. Bill and F. Aldinger. "A silicoboron carbonitride ceramic stable to 2,000 degrees C," *Nature*, **382**, 796-798 (1996).
8. K. Terauds, P.E. Sanchez-Jimenez, R. Raj, C. Vakifahmetoglu and P. Colombo. "Giant piezoresistivity of polymer-derived ceramics at high temperatures," *Journal of the European Ceramic Society*, **30**, 2203-2207 (2010).
9. Z.C. Wang, F. Aldinger and R. Riedel. "Novel silicon-boron-carbon-nitrogen materials thermally stable up to 2200 degrees C," *Journal of American Ceramic Society*, **84**, 2179-2183 (2001).
10. P. Greil, "Polymer derived engineering ceramics," *Advanced Engineering Materials*, **2**, 339-348 (2000).

11. S.R. Shah and R. Raj. "Mechanical properties of a fully dense polymer derived ceramic made by a novel pressure casting process," *Acta Materialia*, **50**, 4093-4103 (2002).
12. S. Trassl, M. Puchinger, E. Rossler and G. Ziegler. "Electrical properties of amorphous Si<sub>x</sub>C<sub>x</sub>N<sub>y</sub>H<sub>z</sub>-ceramics derived from polyvinylsilazane," *Journal of the European Ceramic Society*, **23**, 781-789 (2003).
13. A. Saha, R. Raj and D.L. Williamson. "Characterization of nanodomains in polymer-derived SiCN ceramics employing multiple techniques," *Journal of American Ceramic Society*, **88**, 232-234 (2005).
14. I. Menapace, G. Mera, R. Riedel, E. Erdem, R. A. Eichel, A. Pauletti and G. A. Appleby. "Luminescence of heat-treated silicon-based polymers: promising materials for LED applications," *Journal of Material Science*, **43**, 5790-5796 (2008).
15. P. Colombo, G. Mera, R. Riedel and G.D. Soraru. "Polymer-Derived Ceramics: 40 Years of Research and Innovation in Advanced Ceramics," *Journal of American Ceramic Society*, **93**, 1805-1837 (2010).
16. M. Karmarkar, G. Singh, S. Shah, R.L. Mahajan and S. Priya. "Large piezoresistivity phenomenon in SiCN-(La,Sr)MnO(3) composites," *Applied Physics Letters*, **94**, 072902 (2009).
17. R.G. Duan and A.K. Mukherjee. "Synthesis of SiCNO nanowires through heat-treatment of polymer-functionalized single-walled carbon nanotubes," *Advanced Materials*, **16**, 1106, (2004).
18. L. N. An, W. X. Xu, S. Rajagopalan, C. M. Wang, H. Wang, Y. Fan, L. G. Zhang, D. P. Jiang, J. Kapat, L. Chow, B. H. Guo, J. Liang and R. Vaidyanathan. "Carbon-nanotube-reinforced polymer-derived ceramic composites," *Advanced Materials*, **16**, 2036 (2004).

19. S.R. Shah and R. Raj. "Nanodevices that explore the synergies between PDCs and carbon nanotubes," *Journal of the European Ceramic Society*, **25**, 243-249 (2005).
20. J.H. Lehman, K.E. Hurst, G. Singh, E. Mansfield, J.D. Perkins and C.L. Cromer. "Core-shell composite of SiCN and multiwalled carbon nanotubes from toluene dispersion," *Journal of Material Science*, **45**, 4251-4254 (2010).
21. S. Bernard, M. Weinmann, P. Gerstel, P. Miele and F. Aldinger. "Boron-modified polysilazane as a novel single-source precursor for SiBCN ceramic fibers: synthesis melt-sinning, curing and ceramic conversion," *Journal of Materials Chemistry*, **15**, 289-299 (2005).
22. A. M. Hermann, Y. T. Wang, P. A. Ramakrishnan, D. Balzar, L. N. An, C. Haluschka, and R. Riedel. "Structure and electronic transport properties of Si-(B)-C-N ceramics," *Journal of American Ceramic Society*, **84**, 2260-2264 (2001).
23. R. Riedel, J. Bill and A. Kienzle. "Boron-modified inorganic polymers - Precursors for the synthesis of multicomponent ceramics," *Applied Organometallic Chemistry*, **10**, 241-256 (1996).
24. Z.C. Wang, F. Aldinger and R. Riedel. "Novel silicon-boron-carbon-nitrogen materials thermally stable up to 2200 degrees C," *Journal of American Ceramic Society*, **84**, 2179-2183 (2001).
25. M.A. Schiavon, C. Gervais, F. Babonneau and G.D. Soraru. "Crystallization behavior of novel silicon boron oxycarbide glasses," *Journal of American Ceramic Society*, **87**, 203-208 (2004).



26. M.A. Schiavon, G.D. Soraru and I.V.P. Yoshida. "Poly(borosilazanes) as precursors of Si-B-C-N glasses: synthesis and high temperatures properties," *Journal of Non-Crystalline Solids*, **348**, 156-161 (2004).
27. Z. Zhang, F. Zeng, J. Han, Y. Luo and C. Xu. "Synthesis and characterization of a new liquid polymer precursor for Si-B-C-N ceramics," *Journal of Material Science*, **46**, 5940-5947 (2011).
28. Ishida Y, Donnadiou B., Bertrand G., "Stable Four- $\pi$ -Electron, Four-Membered Heterocyclic Cations and Carbenes," *Proceedings of the National Academy of Sciences*, **103**, 37, 13585-13588(2006).
29. N. Janes and E. Oldfield. "Prediction of Si-29 Nuclear Magnetic-Resonance Chemical-Shifts using a Group Electronegativity Approach - Applications to Silicate and Aluminosilicate Structures," *Journal of American Chemical Society*, **107**, 6769-6775 (1985).
30. Y. Kim and R.J. Kirkpatrick. "B-11 NMR investigation of boron interaction with mineral surfaces: Results for boehmite, silica gel and illite," *Geochimica et Cosmochimica Acta*, **70**, 3231-3238 (2006).
31. W.D. Phillips, H.C. Miller and E.L. Muetterties. "B11 Magnetic Resonance Study of Boron Compounds," *Journal of American Chemical Society*, **81**, 4496-4500 (1959).
32. H.C. Brown, T.E. Cole, M. Srebnik and K.W. Kim. "Hydroboration .79. Preparation and Properties of Methylborane and Dimethylborane and their Characteristics as Hydroborating Agents - Synthesis of Tertiary Alcohols Containing Methyl-Groups Via Hydroboration," *Journal of Organic Chemistry*, **51**, 4925-4930 (1986).
33. E. Framery and M. Vaultier. "Efficient synthesis and NMR data of N- or B-substituted borazines," *Heteroatom Chemistry*, **11**, 218-225 (2000).

34. F. Guilhon, B. Bonnetot, D. Cornu and H. Mongeot. "Conversion of tris(isopropylamino)borane to polyborazines. Thermal degradation to boron nitride," *Polyhedron*, **15**, 851-859 (1996).
35. L.J. Malone and R.W. Parry. "Preparation and Properties of Boranocarbonates," *Inorganic Chemistry*, **6**, 817 (1967).
36. J.A. Perdigon-Melon, A. Auroux, D. Cornu, P. Miele, B. Toury and B. Bonnetot. "Porous boron nitride supports obtained from molecular precursors. Influence of the precursor formulation and of the thermal treatment on the properties of the BN ceramic," *Journal of Organometallic Chemistry*, **657**, 98-106 (2002).
37. B. Toury and P. Miele. "A new polyborazine-based route to boron nitride fibres," *Journal of Materials Chemistry*, **14**, 2609-2611 (2004).
38. S.Y. Kang, K. Yoshizawa, T. Yamabe, A. Naka and M. Ishikawa. "An ab initio study on the structure and reactivity of 1,4-disilabenzene," *Journal of Organometallic Chemistry*, **611**, 280-287 (2000).
39. E. Leonova, J. Grins, M. Shariatgorji, L.L. Ilag and M. Eden. "Solid-state NMR investigations of Si-29 and N-15 enriched silicon nitride," *Solid State Nuclear Magnetic Resonance*, **36**, 11 (2009).
40. "NIST X-ray Photoelectron Spectroscopy Database NIST Standard Reference" Database no.20, Version 3.4.
41. D. Hegemann, R. Riedel and C. Oehr. "PACVD-derived thin films in the system Si-B-C-N," *Chemical Vapor Deposition*, **5**, 61 (1999).

42. N. Janakiraman, M. Weinmann, J. Schuhmacher, K. Muller, J. Bill, F. Aldinger and P. Singh. "Thermal stability, phase evolution, and crystallization in Si-B-C-N ceramics derived from a polyborosilazane precursor," *Journal of American Ceramic Society*, **85**, 1807-1814 (2002).
43. J.T. Titantah and D. Lamoen. "sp(3)/sp(2) characterization of carbon materials from first-principles calculations: X-ray photoelectron versus high energy electron energy-loss spectroscopy techniques," *Carbon*, **43**, 1311-1316 (2005).
44. C. Gervais, F. Babonneau, L. Ruwisch, R. Hauser and R. Riedel. "Solid-state NMR investigations of the polymer route to SiBCN ceramics," *Canadian Journal of Chemistry- Revue Canadienne De Chimie*, **81**, 1359-1369 (2003).
45. A.L. Smith, "Infrared Spectra-Structure Correlations for Organosilicon Compounds," *Spectrochimica Acta*, **16**, 87-105 (1960).
46. R.E. Richards and H.W. Thompson. "Spectroscopic Studies of the Amide Linkage," *Journal of the Chemical Society*, 1248-1260 (1947).
47. K. Niedenzu and J.W. Dawson. "Boron Nitrogen Compounds .1. Syntheses of B-Aminoborazines," *Journal of American Chemical Society*, **81**, 3561-3564 (1959).
48. K. Niedenzu and J.W. Dawson. "Boron Nitrogen Compounds .2. Aminoboranes .1. the Preparation of Organic Substituted Aminoboranes through a Grignard Reaction," *Journal of American Chemical Society*, **81**, 5553-5555 (1959).
49. L.J. Bellamy, W. Gerrard, M.F. Lappert and R.L. Williams. "Infrared Spectra of Boron Compounds," *Journal of the Chemical Society*, 2412-2415 (1958).
50. D.E. Bethell and N. Sheppard. "The Infra-Red Spectrum and Structure of Boric Acid," *Transactions of the Faraday Society*, **51**, 9-15 (1955).

51. M. Weinmann, R. Haug, J. Bill, M. de Guire and F. Aldinger. "Boron-modified polysilylcarbodi-imides as precursors for Si-B-C-N ceramics: Synthesis, plastic-forming and high-temperature behavior," *Applied Organometallic Chemistry*, **12**, 725-734 (1998).
52. D. Bom, R. Andrews, D. Jacques, J. Anthony, B. L. Chen, M.S. Meier and J.P. Selegue. "Thermogravimetric analysis of the oxidation of multiwalled carbon nanotubes: Evidence for the role of defect sites in carbon nanotube chemistry," *Nano Letters*, **2**, 615-619 (2002).
53. Y.C. Zhang and X. Wang. "Thermal effects on interfacial stress transfer characteristics of carbon nanotubes/polymer composites," *International Journal of Solids Structures*, **42**, 5399-5412 (2005).
54. H. Jiang, B. Liu, Y. Huang and K. C. Hwang. "Thermal Expansion of Single Wall Carbon Nanotubes", *Journal of Engineering Materials and Technology*, **126**, 265 (2004)
55. J.T. Han, J.S. Kim, H.D. Jeong, H.J. Jeong, S.Y. Jeong, and G.W. Lee. "Modulating conductivity, environmental stability of transparent conducting nanotube films on flexible substrates by interfacial engineering, " **4**, 8, 4551–4558 (2010).
56. Z.H. Yang, Y. Zhou, D.C. Ha and Q.C. Meng. "Microstructures and properties of SiB<sub>0.5</sub>C<sub>1.5</sub>N<sub>0.5</sub> ceramics consolidated by mechanical alloying and hot pressing," *Materials Science and Engineering A-Structural Materials Properties Microstructure and Processing*, **489**, 187-192 (2008).

## **Chapter 3 - Synthesis of Polymer-derived Ceramic Si(B)CN-Carbon**

### **Nanotube Composite by Microwave Induced Interfacial**

#### **Polarization**

##### **Abstract**

In this chapter we demonstrate our findings on synthesis of a PDC-MWCNT composite using microwave irradiation at 2.45 GHz. The process takes about 10 minutes of microwave irradiation for the polymer-to-ceramic conversion. The successful conversion of polymer coated carbon nanotubes to ceramic composite is chemically ascertained by Fourier transform-infrared and X-ray photoelectron spectroscopy and physically by thermogravimetric analysis and transmission electron microscopy characterization. Frequency dependent dielectric measurements in the S-Band (300 MHz to 3 GHz) were studied to quantify the extent of microwave-CNT interaction and the degree of selective heating available at the MWCNT-polymer interface. Experimentally obtained return loss of the incident microwaves in the specimen explains the reason for heat generation. The temperature dependent permittivity of polar molecules further strengthens the argument of internal heat generation.

---

Reprinted with permission from (R. Bhandavat, W. Kuhn, E. Mansfield, J. Lehman, and G. Singh, "Synthesis of Polymer-derived Ceramic Si(B)CN-Carbon Nanotube Composite by Microwave Induced Interfacial Polarization," ACS Applied Materials and Interfaces, **4**, 1, 11-16). Copyright (2012) American Chemical Society

### 3.1 Introduction

Carbon nanotubes (CNT) are known to possess high microwave absorbance characteristics at specific frequencies, because they couple strongly with both the electric and magnetic components of the applied external field. Temperatures as high as 2000 °C along with light emission and specimen out-gassing have been reported [1]. Capitalizing on the ability of CNTs to absorb microwaves, several researchers have demonstrated (a) nanotube purification and functionalization, (b) polymer curing, (c) synthesis of monolayer graphene, and (d) electromagnetic shielding, among other applications [2-9].

Based on their broad application potential, CNT behavior has intrigued researchers to propose various microwave-CNT interaction mechanisms. Several contrasting theories have been proposed to explain the high microwave absorbance mechanism in CNTs. Wadhawan *et al.* [1] demonstrated that the presence of ferromagnetic catalytic impurities in CNTs are responsible for microwave absorption and also ruled out possibility of any gas adsorption and density for the microwave CNT heating. On the other hand, Walton *et al.* [10] have shown that nanoparticles have minimal interaction with microwave at low frequencies. Further, Guo *et al.* proposed the relative telescopic motion between the CNT resonating tubes as the cause of heat generation [11]. Wu *et al.* experimentally concluded that the electromagnetic response of CNTs to microwaves is primarily due to dielectric properties, because they possess very weak magnetism, and the dielectric properties are collectively or individually due to the motion of conducting electrons, relaxation, and resonance [12]. Several researchers have advanced these observations and employed CNTs as internal heat source for synthesis of CNT-polymer composites [6,7,9,13-16].

Polymer-derived ceramics (PDCs) of the type Si-C-N or Si-B-C-N are of interest to us because of their rheological properties in the polymer phase, ultra-high temperature stability, and

resistance to oxidation [17-19]. The final ceramic's chemical and physical properties are known to depend on the initial molecular arrangement of the polymer precursor and processing conditions. Moreover, boron doping of PDCs results in enhanced electrical conductivity and thermoelectric power [20]. PDCs are amorphous ceramics prepared by controlled heating of polysilazane (SiCN) or polysiloxane (SiOC) based liquid polymeric precursors. Typically, a liquid precursor is heated to about 400 °C for cross-linking, which results in formation of an infusible polymer; followed by crushing and thermal decomposition of the infusible mass by heating it to high temperatures (~800 °C to 1100 °C) in inert atmospheres to yield the resulting ceramic. This method has also been utilized to prepare CNT-PDC ceramic matrix composites by either physical mixing or soaking the carbon nanotubes in liquid polymer followed by heating to convert polymer into ceramic [21-24]. The MWCNT-Si(B)CN ceramic composite prepared by a novel and single step *ab-initio* polymer MWCNT synthesis method is also described elsewhere [25]. This route is multistep and typically consumes several hours. In this chapter, we propose an alternate approach that involves microwave irradiation of polymer (boron-doped polysilazane)-coated MWCNTs. The heat generated at the polymer-CNT interface causes thermal degradation and transformation of the polymer into Si(B)CN ceramic shell that protects the nanotube core in flowing air up to at least 1000 °C.

## **3.2 Experimental Procedure**

### **3.2.1 Materials and Methods**

Two sets of experiments were performed. For the first set involving microwave irradiation experiments, specimens containing equal proportions of polymeric precursor and carbon nanotubes were prepared. Briefly, the specimen preparation involved dispersion of 1 g MWCNTs (Bayer MaterialScience AG, North America) in 125 mL of toluene and sonication for

30 min, followed by drop-wise addition of 5 g Si(B)CN polymeric precursor (boron-modified polyureamethylvinylsilazane) with stirring for 24 h and drying in an inert atmosphere [25]. The dried polymer-nanotube mix (~200 mg) was sealed in a quartz tube and exposed to full magnetron power of 900 W at 2.45 GHz (domestic microwave) for 5 min, 10 min and 15 min (a total of 3 samples). Fig. 3-1 is the schematic showing the major steps involved in this process and its comparison with conventional processing of PDC composites. The other set of experiments involved dielectric measurements with vector network analyzer (VNA). For these experiments, MWCNTs (about 5 wt %) were dispersed in the polymeric precursor to obtain a polymer-CNT gel.

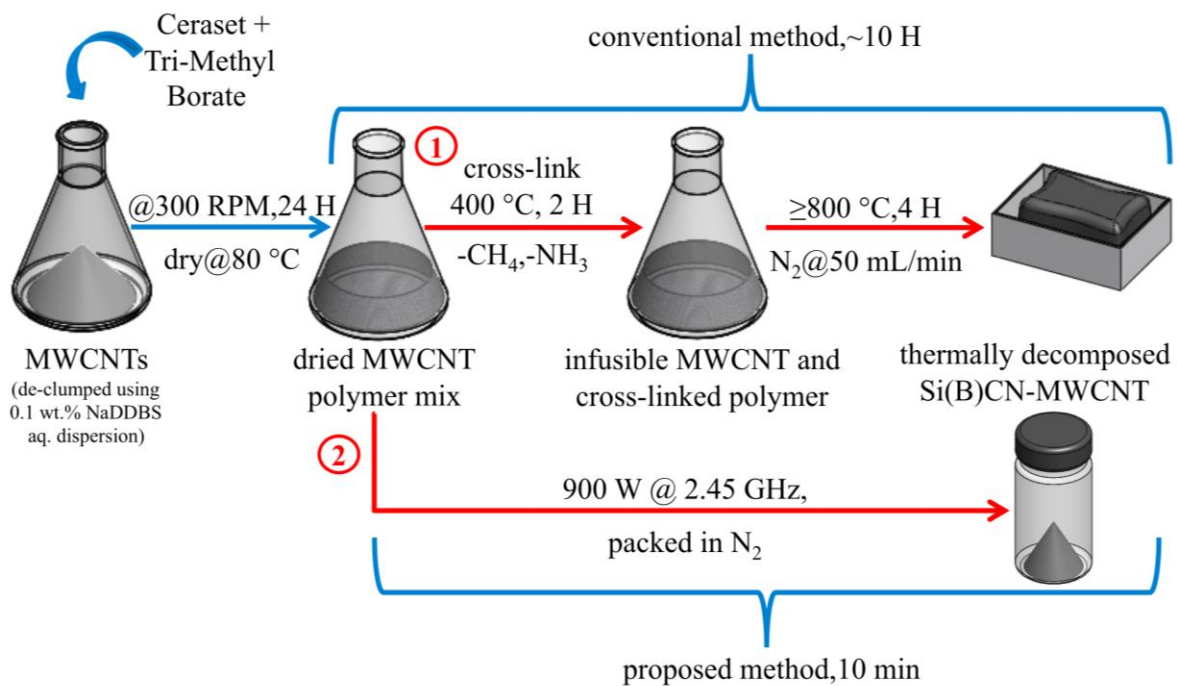


**Figure 3-1:** Experimental procedure for the synthesis of polymer-derived ceramic coated MWCNTs by (1) conventional heating method and (2) proposed method.

To ascertain the polymer to ceramic conversion, the molecular structure and bond formation of the composite was studied with X-ray photoelectron and Fourier transform infrared spectroscopy



(FTIR), and results were compared with our previous work on Si(B)CN-MWCNTs composite prepared by conventional heating [25]. Transmission electron microscopy (TEM) was performed by use of a CM 100 microscope (Philips/FEI Corporation, Eindhoven, Holland) and Tecnai F20 XT microscope (FEI Corporation, Hillsboro, USA). X-ray photoelectron spectra were collected with a PHI Quantera SXM (ULVAC-PHI, Inc) to study the surface chemistry of the nanocomposite by using monochromatic Al K $\alpha$  X-radiation with beam size <9  $\mu$ m. Following a survey scan, a 15 minute high resolution scan was performed at the major elemental peaks energy window. The FTIR spectra were collected on the Thermo-Nicolet Nexus 870FT-IR from the specimen prepared by mixing approximately 1 wt % of the finely powdered specimen with FTIR grade KBr powder. TGA was performed using a T.A. Instruments Q5000IR. The initial specimen weight of approximately 5 mg was heated at a rate of 10  $^{\circ}$ C/min in air flowing (25 mL/min) until the weight loss stopped and the specimen weight stabilized.

### **3.2.2 Dielectric Measurement Setup**

The impedance measurements were collected from a Hewlett Packard (HP) 8753C VNA used in combination with HP85046A for the S-Band (300 MHz to 3 GHz) at room temperature with coaxial cable (Fig. 3-2). The connector (sensor) translates the variations in the permittivity of the material with the change in frequency into changes in the input impedance. The reflected line scattering parameters were then calculated from the impedance measurements obtained on the VNA over the desired frequency range.

To quantify the microwave interaction properties of MWCNT-polymer mix, we measured the impedance and thereby calculated the complex permittivity of the nanocomposite from 100 MHz to 3 GHz frequency. The permittivity measurement test setup consisted of a HP 8753C VNA connected to the sample through a 50  $\Omega$  nominal impedance NTC195 Flexco coaxial test cable

terminated with a 20 mm length female-female SMA adapter (Outer diameter of center-conductor = 5 mm; Inner diameter of outer-conductor = 4.064 mm). This setup allows accurate measurement over a broad frequency range, because transmission-line theory can be used to address parasitic capacitances and inductances inherent in the non-negligible sample size at the higher frequencies applied. An  $S_{11}$  one-port calibration was performed prior to measurements by attaching short, open, and load standards at the end of an unmodified SMA adapter. During measurements, an identical female-female adapter was employed, but with 6 mm of its Teflon insulation removed as shown in the Fig. 3-2 to allow the test sample material to be inserted.

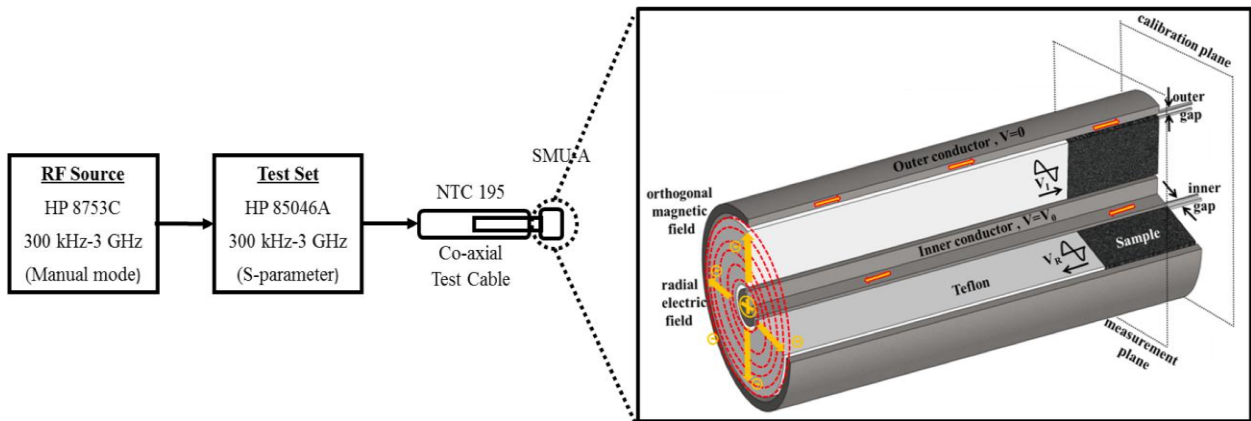


**Figure 3-2:** Block diagram of the experimental setup used for measuring the impedance at different resonant frequencies and the expanded view of field lines in the TEM mode in the co-axial connector with specimen sandwiched between conductors.

The test sample was thus placed so that it constituted a part of the transmission line, and the coaxial line operated in the TEM mode and did not support propagation of higher-order modes. During sample insertion, it was ensured that no air gap exists between the coaxial conductors and the sample to prevent measurement inaccuracies. Since the calibration and measurement plane are not identical, the reflection coefficient measurements are mathematically adjusted to the new reference plane before extraction of the material's permittivity from the measured impedances.

### 3.3 Results and Discussion

#### 3.3.1 Irradiation experiments and carbon nanotube functionalization mechanism

As expected, a large volume of outgassing was observed within a few seconds of microwave exposure, and hence a relatively small amount of material was used in large vials to avoid overpressure in the container [1]. Some sparks from the metal catalyst particles (typically present in MWCNTs) were also observed during the microwave exposure. About 50 % weight loss was observed in the first five minutes of microwave exposure. The specimen did not lose weight thereafter (even after exposure to as much as 30 min). It is worth mentioning that a 30 % to 40 % weight loss is typical of PDCs prepared by conventional heating techniques. The increased weight loss in microwave-synthesized specimens could be collectively due to decomposition of the polymer into ceramic as well as burning of uncoated MWCNTs.

We propose a noncovalent sidewall functionalization of MWCNTs by the polymeric precursor, as shown in Fig. 3-3. It is well known that the chemical reactivity in CNTs is primarily due to the  $\pi$  orbital misalignment that exists between the adjacent carbon atoms oriented at an angle to the tube circumference [26]. Therefore, a strong van der Waals interaction between the aromatic group from toluene and the  $\pi$ - $\pi$  stacking of the MWCNT sidewalls is very likely. This assists the immobilization of the polymer precursors on nanotube surfaces. Thus, a noncovalent interaction results between amine domains from the hydrophobic polymer backbone and the MWCNT sidewalls, where the former becomes the binding site. Microwave irradiation leads to selective heating of the nanotube core, resulting in thermal degradation of polymer into ceramic and thereby forming a protective coating on the nanotube surfaces. Moreover, the molecular dynamics simulations described in the literature also suggest that the concave outer surfaces of

CNTs are more submissive to covalent functionalization than the inner surfaces, and hence ceramic exoskeleton is favored on the CNT surface [26].

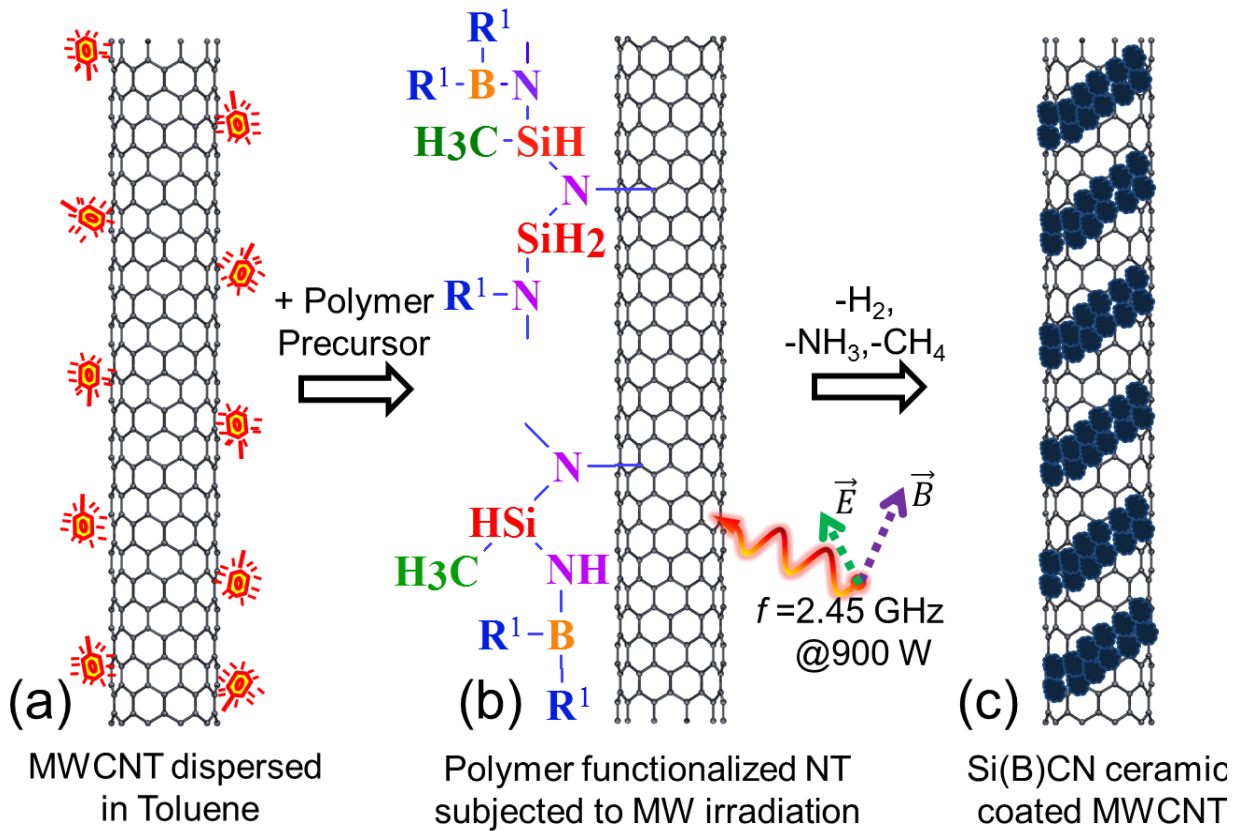


**Figure 3-3:** Symbolic illustration explaining the mechanism of non-covalent exohedral sequential sidewall functionalization of MWCNT with: (a) solvent (toluene), (b) boron-modified polysilazane polymeric precursor and (c) pyrolyzed Si(B)CN ceramic following microwave irradiation.

### 3.3.2 Material Characterization

#### *Electron Microscopy*

Structural characterization was carried out with TEM to observe: (a) polymer distribution on nanotube surfaces before microwave exposure and (b) polymer and/or carbon nanotube decomposition (if any) after microwave irradiation was complete. After microwave exposure, the

specimens showed considerable change; a more uniform amorphous coating on carbon nanotubes could be seen in the high-resolution TEM and high angle annular dark field (HAADF) images (Fig. 3-4), possibly indicating polymer decomposition and ceramic formation.

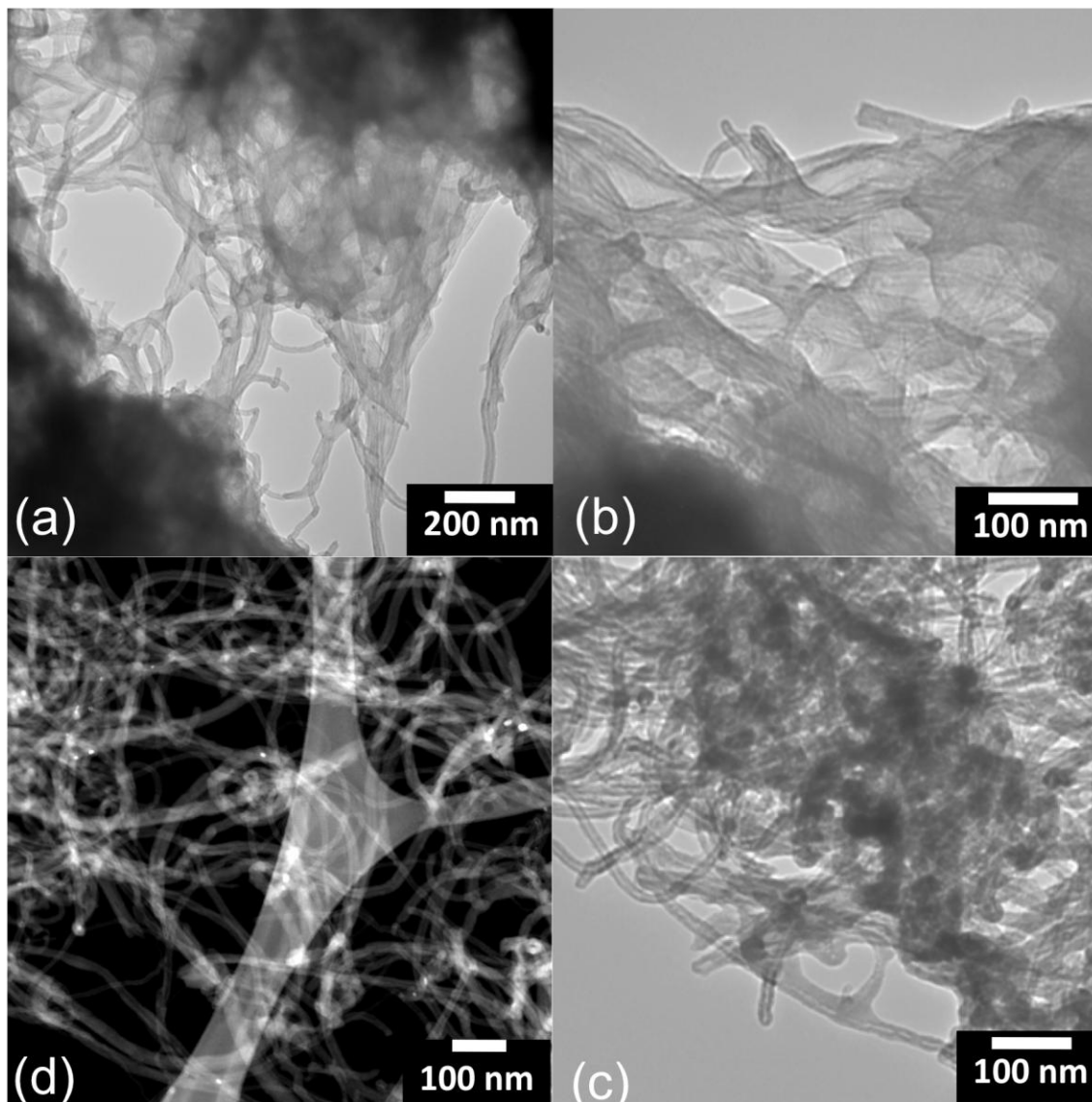


**Figure 3-4:** (a) and (b) are TEM images showing untreated polymer-MWCNT mix. (c) and (d) are the conventional TEM and high angle annular dark field (HAADF) images of Si(B)CN-MWCNTs synthesized by microwave irradiation, respectively. Note that elements with higher atomic weight (i.e., Si) appears bright in HAADF mode.

The structure of the ceramic-coated CNT, including the shells and the core, was intact even for higher microwave exposure times. This is both remarkable and conclusive as the CNTs usually burn when exposed to microwave irradiation. Because both the starting polymer and resulting ceramic are amorphous (typical of PDCs), we further resorted to spectroscopic and thermogravimetric analysis to confirm the formation of Si(B)CN ceramic.

### *X-Ray Photoelectron Spectroscopy (XPS)*

XPS provides deterministic information about the nature of bond formation and the percentage of elements constituting a compound. We utilized XPS for comparing microwave irradiated specimens with those prepared by conventional heating. Comparison of the survey scans of specimens pyrolyzed at 800 °C and specimens irradiated with microwaves for 10 minutes consistently showed the existence of Si, B, C and N elemental peaks arising from the valence energy levels for the respective atoms (Fig. 3-5).

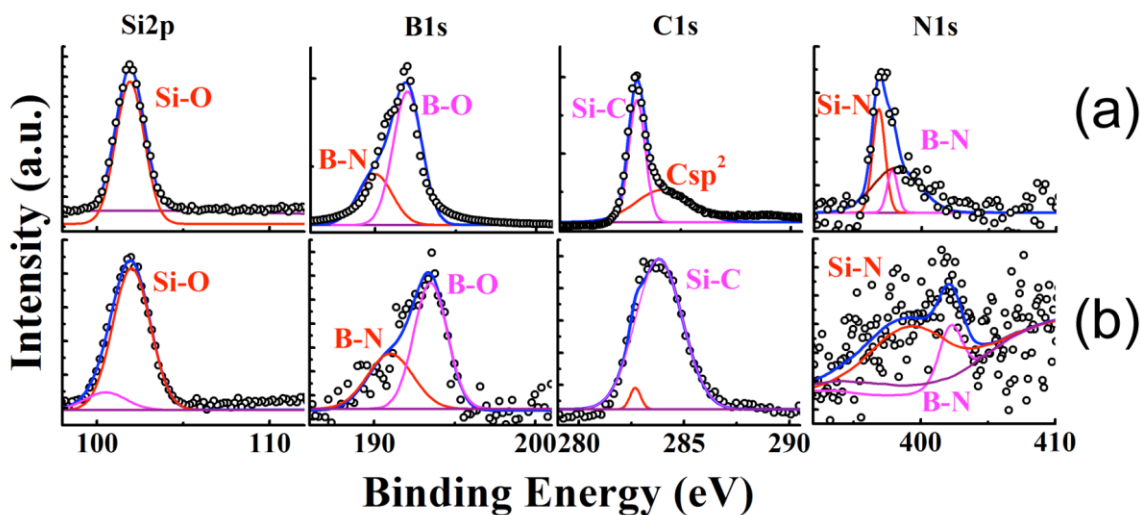


**Figure 3-5:** Core level elemental XPS spectra of Si(B)CN-MWCNT processed (a) at 800 °C for 4 hours and (b) exposed to microwave for 10 min.

The resolution of each elemental peak determined the corresponding phases and their proportion in the final compound, as shown in Fig. 3-5. The thermal degradation of the polymer and subsequent transformation to ceramic results in complementary changes in the elemental phases. Hence, XPS is critical in determining the extent of polymer conversion into ceramic. A single broad peak fitted at 102 eV observed in both specimens which is due to Si-O bonds, implying the ceraset and trimethyl borate reaction and the cleavage of the methyl group from the latter. Small broad peak at lower energy at 192.5 eV is due to B-N type bond, whereas the large peak at higher energy at 195 eV is clearly due to more electronegative B-O bond as in B<sub>2</sub>O<sub>3</sub>. The sharp intense peak in the pyrolyzed specimen at 283 eV and the broad peak at 283.8 eV in the microwave irradiated specimen are due to Si-C, whereas the higher energy carbon peak at 284.18 eV is due to sp<sup>2</sup> bonded carbon. Nitrogen peaks were not very noticeable due its small fraction in the total composition; however, the Si-N bond present in the polymer backbone emerged as a prominent peak. To sum up, the XPS comparison of microwave irradiated and conventional heated specimens strongly suggests conversion of polymer precursor into ceramic by microwave irradiation.

**Table 3-1:** XPS elemental and phase analysis comparison of the specimen synthesized by microwave exposure for 10 min and pyrolysis at 800 °C for 4 hours.

Specimen	Elemental Ratios			Estimated Bonding Character				
				Si bonds			B bonds	
	Si/N	Si/B	B/O	SiO <sub>2</sub>	SiC	Si <sub>3</sub> N <sub>4</sub>	B <sub>2</sub> O <sub>3</sub>	BN
Microwave, 10 min	4.75	1.91	0.18	15.7	81.49	2.81	58.1	41.9
Pyrolyzed, 800 °C	0.77	0.75	1.4	81.56	6.08	12.37	57.44	42.56

As shown in Table 3-1, comparative analysis of chemical composition by XPS also revealed certain drawbacks associated with microwave assisted heating: (a) low ceramic yield (~50 %) compared to that of conventional pyrolysis process (~65 %), (b) lesser boron is retained in the

final ceramic, probably due to high initial weight loss of the polymer and (c) relatively high surface oxygen content in the microwave specimens. We believe that these drawbacks could be reduced or eliminated by optimizing the microwave irradiation power and exposure times as well as composition of the starting polymer.

### ***Fourier Transform Infrared Spectroscopy (FTIR)***

Fig. 3-6 is the comparison between the FTIR spectrum obtained from liquid polymer precursor, SiBCN-MWCNT synthesized by microwaves and the specimen synthesized by conventional pyrolysis at 800 °C. For the precursor, peaks from 2950  $\text{cm}^{-1}$  to 2850  $\text{cm}^{-1}$  and 2127  $\text{cm}^{-1}$  correspond to C-H stretching vibration and Si-H type bond, respectively. The decrease in intensity of both these bonds in microwave irradiated specimen and the pyrolyzed specimen indicates decomposition of the polymer and subsequent ceramic formation typically observed in Si/C/N systems [27]. Moreover, the retention of B-O and B-N peaks at 1480  $\text{cm}^{-1}$  and 1380  $\text{cm}^{-1}$ , respectively, in the processed specimens indicates retention of boron in the final ceramic (also observed in XPS analysis, Fig. 3-5). Additional peaks at 1603  $\text{cm}^{-1}$  and 1457  $\text{cm}^{-1}$  are due to C=C bonds in MWCNT. Close resemblance between the microwave irradiated and conventionally pyrolyzed specimens suggests successful ceramization as a result of heat generation due to MWCNT-microwave interactions. Additionally, the following peaks were correspondingly assigned for the Diffuse Reflectance Infrared (DRIFT) spectra collected for all the specimens: 3680  $\text{cm}^{-1}$ : free  $\nu\text{OH}$ ; 3480-3400  $\text{cm}^{-1}$ : bonded  $\nu\text{OH}$  in Si-OH; 3420-3390  $\text{cm}^{-1}$ :  $\nu\text{Si-NH-Si}$ ; 3030  $\text{cm}^{-1}$ : terminal vinyl group on silicon,  $\nu\text{C-H}$ ; 2960  $\text{cm}^{-1}$ :  $\nu\text{as-CH}_3$ ; 2930  $\text{cm}^{-1}$ :  $\nu\text{as-CH}_2$ ; 2865  $\text{cm}^{-1}$ :  $\nu\text{s-CH}_3$ ; 2850  $\text{cm}^{-1}$ :  $\nu\text{s-CH}_2$ ; 2160  $\text{cm}^{-1}$ :  $\nu\text{Si-H}$ ; 1715  $\text{cm}^{-1}$ : terminal  $\nu\text{C=O}$ ; 1629  $\text{cm}^{-1}$ :  $\nu\text{C=O}$  [N-Disubstituted amides] 1476  $\text{cm}^{-1}$ :  $\delta\text{as-CH}_3$ ; 1265  $\text{cm}^{-1}$ :  $\delta\text{s-CH}_3$  [Si-CH<sub>3</sub>]; 1396  $\text{cm}^{-1}$ :  $\nu\text{h-}$



B-N ; 1301  $\text{cm}^{-1}$ :  $\nu$ B-O [ $\text{B}(\text{OCH}_3)_3$ ] ; 1124, 1044  $\text{cm}^{-1}$  :  $\nu$ Si-O-Si ; 904  $\text{cm}^{-1}$ :  $\delta$ C-H out-of-plane ;808  $\text{cm}^{-1}$ :  $\delta$ Si-H ( $\nu$ : stretching vibration mode,  $\delta$ : bending vibration mode).

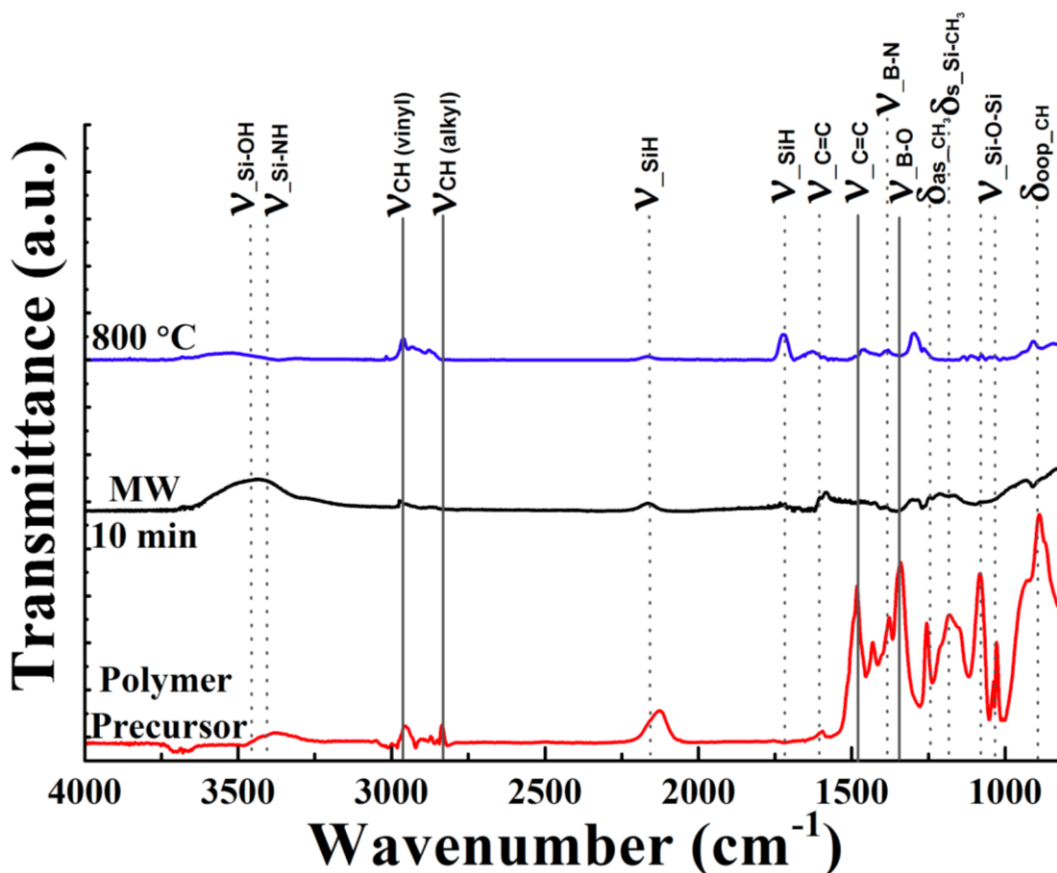


**Figure 3-6:** Diffuse reflectance spectrum of Si(B)CN-MWCNT microwave (MW) specimen, Si(B)CN-MWCNT specimen pyrolyzed at 800 °C and the starting polymeric precursor ( $\nu$ : stretching vibration mode and  $\delta$ : bending vibration mode).

### *Thermogravimetric Analysis (TGA)*

TGA was employed to compare the high temperature stability of microwave-synthesized nanowires with those prepared through the conventional pyrolysis route. The TGA for PDC specimens processed by conventional heating route typically follows three phases: a low temperature weight loss due to solvent evaporation, followed by the oxidation of non-ceramic coated nanotubes and other organic impurities at higher temperatures, and lastly the weight

stabilization phase (Fig. 3-7(a)). The weight loss curves for the microwave-synthesized specimen should resemble similar transitions if successful ceramization occurred during microwave exposure. As shown in the comparison plot, Fig. 3-7 (a), the specimen pyrolyzed at 800 °C and the specimen synthesized by microwave exposure for ten minutes most closely resemble one another. Remarkably, the microwave specimen showed less weight loss ( $25.5\pm 3.3$  %) compared to the pyrolyzed specimen ( $37.9\pm 2.8$  %). The oxidation temperatures of both specimens were in the same temperature range. The TGA residual maintained its characteristic black color indicating survival of the nanotube core, which was later confirmed by TEM of the residual mass, Fig. 3-7 (b), (c) and (d). TGA analysis clearly suggests that the microwave-synthesized Si(B)CN-MWCNTs are as robust as those prepared by conventional pyrolysis methods.

The high-temperature stability of Si(B)CN-MWCNT specimens is further highlighted by comparing the TGA data with that of 'as obtained' MWCNT and MWCNT-polymer mix. As shown in Fig. 3-7 (a), the MWCNTs experienced ~98 % weight loss at ~536 °C. The weight loss profile of non-microwave specimens (*i.e.*, specimen consisting of polymer-nanotube mix) showed weight loss typical of a polysilazane precursor: (a) ~23 % weight loss at ~100 °C (attributed to atmospheric absorbed moisture), (b) ~14 % weight loss in 380 °C to 480 °C temperature range due to the release of oligomers and NH<sub>3</sub>, and (c) a maximum weight loss of ~37 % at  $623.9\pm 0.6$  °C, most likely due to burning the non-polymer coated MWCNTs. Further weight loss could be due to release of CH<sub>4</sub> and H<sub>2</sub>, typical of silazane-based polymers [28].

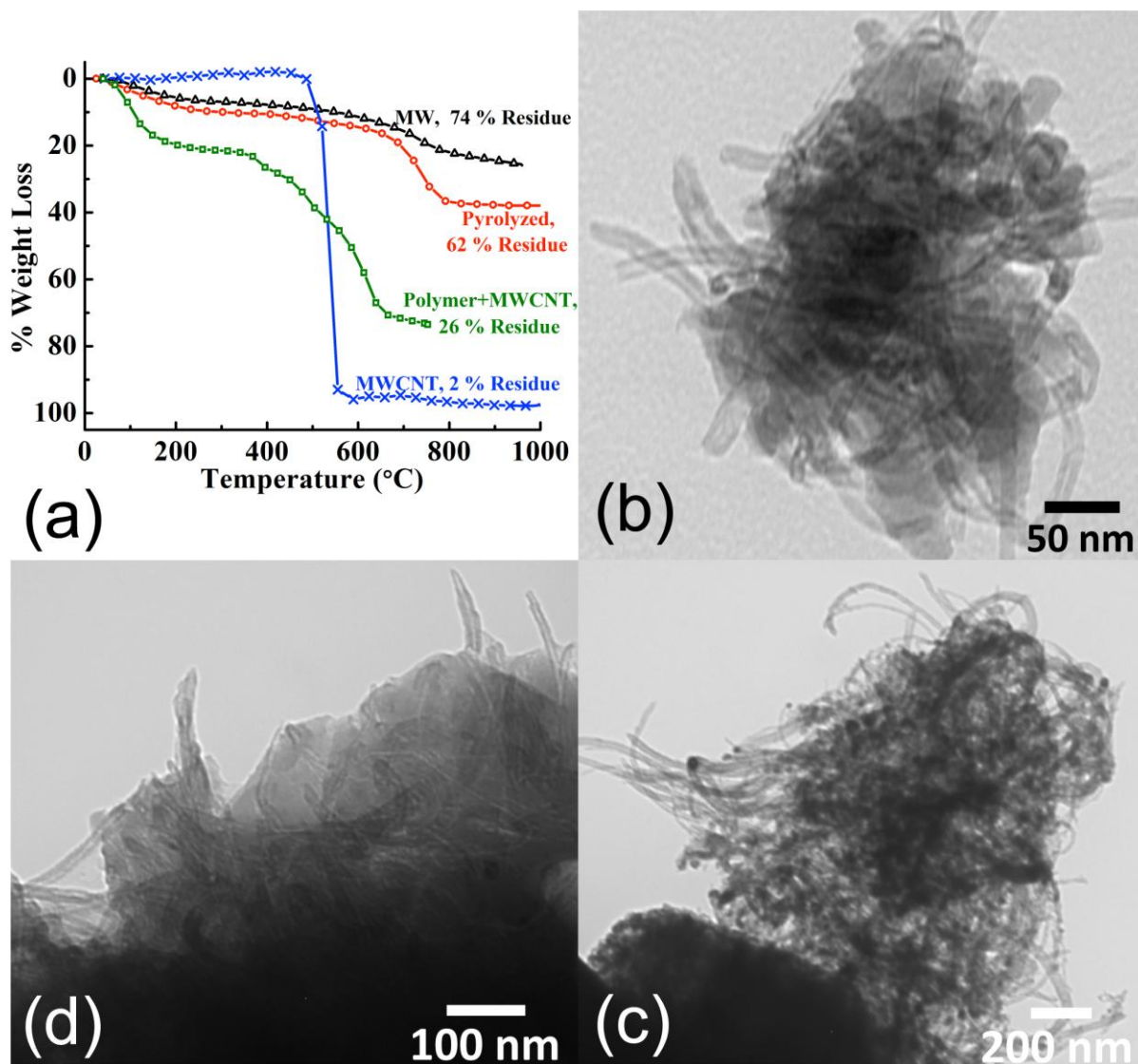


**Figure 3-7:** (a) TGA plots showing the comparative weight loss (%) for Si(B)CN-MWCNT composites synthesized by 10 minute microwave irradiation (black) and conventional pyrolysis at 800 °C (red). Labels indicate respective residual weight percentages. Weight loss for ‘as obtained’ MWCNTs (blue) and ‘untreated’ polymer-MWCNT mix (green) has also been included for comparison. TGA was performed in flowing air @ 25 mL/min. (b)-(d) TEM micrographs of TGA residual corresponding to Si(B)CN-MWCNT composite synthesized by microwave irradiation.

As shown in Table 3-2, due to an insignificant difference observed between the specimens processed at increasing microwave exposure times it was concluded that (a) the polymer to ceramic conversion occurs initially within the first few minutes of microwave exposure and (b) after the initial ceramic transformation, CNT oscillation are possibly damped by the surrounding ceramic matrix.

**Table 3-2:** Summary of oxidation temperatures and residual weight obtained from TGA analysis of various specimens used in this study.

Specimen	Oxidation Temperature (°C)	Total Weight Loss (%)
MWCNT	536.3	97.7±0.1
Polymer-MWCNT	100.8±2.0, 380.4±1.8, 479.7±1.4, 623.9±0.6	73.6±1.2
Si(B)CN-MWCNT 800 °C	730.0±0.3	37.9±2.8
Si(B)CN-MWCNT 5 min	736.8±0.5	20.5±3.6
Si(B)CN-MWCNT 10 min	736.2±0.4	25.5±3.3
Si(B)CN-MWCNT 15 min	723.7±0.4	24.9±3.4

### 3.4 Dielectric Measurements

#### *Permittivity Calculations*

The reflection coefficient  $\Gamma$  measured by the VNA is a function of load impedance  $Z_L$  seen at the adjusted measurement plane. Following standard transmission-line theory, and  $Z_L$  are related by

$$\Gamma = \frac{Z_L - Z_0}{Z_L + Z_0} \quad (3-1)$$

The load  $Z_L$  is composed of an open-circuited 6 mm transmission line formed from the coaxial metal conductors and the sample material, which acts as the dielectric. In general,  $Z_L$  is a

function of both this dielectric material and the length of coaxial line, and cycles through capacitive and inductive values repeatedly as the frequency of excitation is increased. However, for a sufficiently short length of line (electrical length less than one-half wavelength) such as the 6 mm length used, there is a one-to-one mapping between the impedance  $Z_L$  and the sample's real and complex permittivity. This mapping is defined by basic transmission-line theory and can be determined either analytically or through simulation. Thus, once  $Z_L$  is known, the permittivity can be accurately extracted.

In this work, the mapping was done by simulating a 6 mm coaxial line with Agilent's ADS software with different values of permittivity until the measured  $Z_L$  was obtained at each frequency.

As shown in Fig. 3-8(a) and 8(b), the permittivity plots for the specimen displayed a diminishing response with increasing frequency at room temperature. This behavior of permittivity corresponds to the Debye ( $\beta$ ) relaxation phase, caused by reduced molecular polarization at the MWCNT polymer interface with increasing microwave frequency. This secondary ( $\beta$ ) relaxation rate is temperature dependent given by the Arrhenius relationship:

$$R(T) = R_{\infty} \exp\left(\frac{-E_A}{k_B T}\right) \quad (3-2)$$

where  $R_{\infty}$  is the relaxation rate in the high temperature limit,  $k_B$  is the Boltzmann constant and  $E_A$  is the activation energy [29]. Alternatively, the Eyring relationship also gives an inverse relationship between temperature and relaxation time as,

$$\tau(T) = \frac{h}{kT} \exp\left(\frac{\Delta H}{RT}\right) \exp\left(-\frac{\Delta S}{R}\right) \quad (3-3)$$

where  $h$  and  $k$  are Planck and Boltzmann constants, respectively, and  $\Delta H$  and  $\Delta S$  are the change in enthalpy and entropy, respectively [30].

We consider the MWCNT-polymer composite as a heterogenous mix containing a small amount of conducting MWCNTs in a nonconducting polymer matrix. Under the influence of an external electromagnetic field, the charge buildup occurs at the MWCNT-polymer interface. This interfacial polarization is the cause of heat loss in the composite specimen. The MWCNT-polymer dielectric specimen, after an initial absorption of microwave energy (shown as low permittivity at room temperature in Fig. 3-8(b)), experiences a temperature rise by Joule heating. This further leads to an increase in phonon vibrations, inducing dielectric and ionic conduction losses by electric carrier-phonon interactions resulting further increase in effective permittivity,  $\epsilon''$ . Moreover for the heterogenous dielectric material in conducting medium, the effective permittivity loss exponentially increases with temperature as given by

$$\epsilon''(\omega) = B(T) \epsilon_0 \omega^{n(T)-1} \quad (3-4)$$

where  $B(T)$  is a temperature-dependent function at a given frequency ' $\omega$ ' [31]. Hence, the progressively increasing permittivity leads to higher temperatures, also known as thermal runaway. Moreover, at room temperature the induced dipole moments partially cancels out; but at higher temperatures (*i.e.*, higher thermal energy) the molecules have greater degree of freedom and decreases the dipole cancelling effect, resulting in high permittivity [29]. This explains the reason for high heat generation at the nanotube polymer interface sites. As shown in Fig. 3-8(d), the return loss of dispersed MWCNT in polymer is 5.6 dB at 2.45 GHz. This implies that 72.5 % of incident power was dissipated as heat by the significantly lossy specimen.

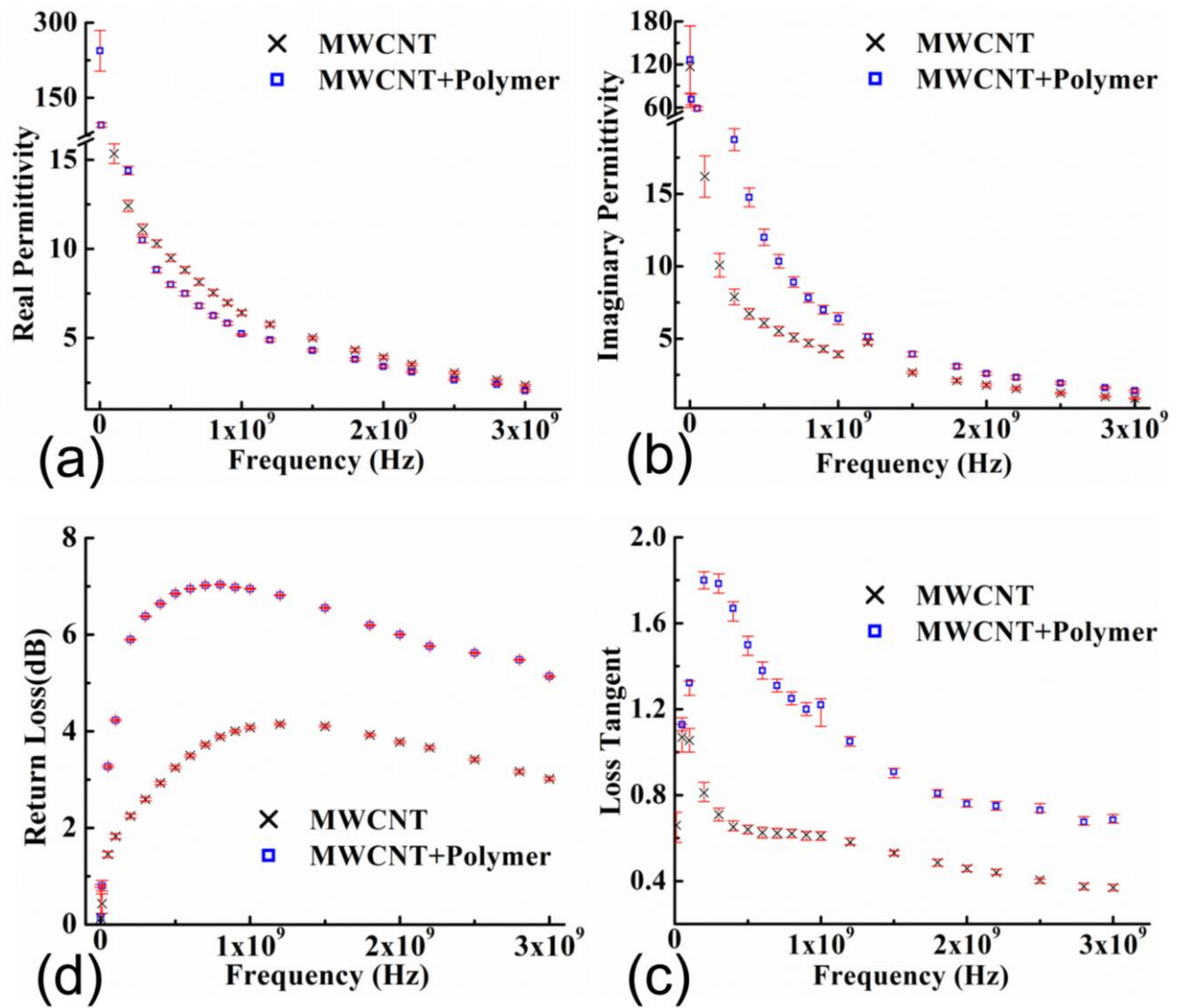


**Figure 3-8:** Dielectric properties calculated from impedance measurements: (a) Real permittivity quantifies the electrical energy the dielectric can retain; (b) imaginary permittivity determines the effectiveness to absorb microwave energy; and (c) loss tangent represents the ability to effectively convert the electromagnetic energy into heat energy, and (d) return loss is a measure of effectiveness of the power delivered from the transmission line to the load for the dispersed MWCNT in polymer and agglomerated MWCNT specimens measured in the microwave frequency range from 100 MHz to 3 GHz.

As observed in Fig. 3-8, the dispersed MWCNTs (5 wt %) in polymer showed slightly higher imaginary permittivity than the ‘as obtained’ nondispersed MWCNTs. In an alternating electric field, the acquired dipole of the CNT is directed towards its length [32], and hence the CNTs dispersed in polymer may have better microwave absorption than the agglomerated CNTs. The loss tangent and return loss (Fig. 3-8(c) and 3-8(d)) showed a similar pattern because they possess high values at low microwave frequencies and starts decreasing after ~ 600 MHz. This behavior could be due to more time available to  $\pi$ - $\pi$  electron stacks at the CNT polymer interface to polarize at low frequency than at higher frequencies, where the period of electric field is significantly smaller than the relaxation time of the dipoles [12].

### **3.5 Conclusion**

Synthesis of PDC-MWCNT composites by microwave irradiation (in a domestic microwave oven) has been demonstrated. The most effective polymer-to-ceramic conversion occurs during the first few minutes of microwave exposure. The proposed process takes a fraction of the time required by the conventional process and hence offers an energy, time, and cost effective alternative. The XPS surface analysis and FTIR spectral analysis of microwave specimen presents the dominance of Si-O, Si-C, B-O and B-N bonds, analogous to that found in Si(B)CN ceramics processed at 800 °C following conventional routes. Furthermore, the high temperature oxidation resistance of the microwave specimen is comparable to or better than that of Si(B)CN-MWCNT composites prepared by conventional routes, as revealed by the TGA. TEM of residual TGA showed that the MWCNT structure stayed intact within the ceramic shell, further asserting the successful polymer-to-ceramic transformation.



Dielectric measurements at room temperature showed an exponentially decaying dielectric response, suggesting it to be a  $\beta$ -relaxation phase due to interfacial polarization. Low permittivity at 2.45 GHz suggests low energy retention, but the return loss analysis shows that about 70 % of incident microwave energy on the specimen is effectively converted into heat at the polymer-nanotube interface, revealing the cause of high heat generation that leads to polymer to ceramic conversion. A similar methodology could be implemented to synthesize carbon-nanotube-based multifunctional nanocomposites with reduced processing times thereby saving energy-related costs.

### 3.6 References

1. T.J. Imholt, C.A. Dyke, B. Hasslacher, *et al.* "Nanotubes in microwave fields: Light emission, intense heat, outgassing, and reconstruction," *Chemistry of Materials*, **15**, 3969-3970 (2003).
2. W. Lin, K.S. Moon, S.J. Zhang, *et al.* "Microwave Makes Carbon Nanotubes Less Defective," *ACS Nano*, **4**, 1716-1722 (2010).
3. Y.H. Chen, Z. Iqbal and S. Mitra. "Microwave-induced controlled purification of single-walled carbon nanotubes without sidewall functionalization," *Advanced Functional Materials*, **17**, 3946-3951 (2007).
4. Y.H. Chen and S. Mitra. "Fast Microwave-Assisted Purification, Functionalization and Dispersion of Multi-Walled Carbon Nanotubes," *Journal of Nanoscience and Nanotechnology*, **8**, 5770-5775 (2008).
5. W.S. Kim, S.Y. Moon, N.H. Park, H. Huh, K.B. Shim and H. Ham. "Electrical and Structural Feature of Monolayer Graphene Produced by Pulse Current Unzipping and Microwave Exfoliation of Carbon Nanotubes," *Chemistry of Materials*, **23**, 940-944 (2011).
6. A.L. Higginbotham, P.G. Moloney, M.C. Waid, *et al.* "Carbon nanotube composite curing through absorption of microwave radiation," *Composites Science and Technology*, **68**, 3087-3092 (2008).
7. Y.B. Wang, Z. Iqbal and S. Mitra. "Microwave-induced rapid chemical functionalization of single-walled carbon nanotubes," *Carbon*, **43**, 1015-1020 (2005).
8. C.J. Gannon, P. Cherukuri, B.I. Yakobson, *et al.* "Carbon nanotube-enhanced thermal destruction of cancer cells in a noninvasive radiofrequency field," *Cancer*, **110**, 2654-2665 (2007).

9. J.A. Roberts, T. Imholt, Z. Ye, C.A. Dyke, D.W. Price and J.M. Tour. "Electromagnetic wave properties of polymer blends of single wall carbon nanotubes using a resonant microwave cavity as a probe," *Journal of Applied Physics*, **95**, 4352-4356 (2004).
10. D. Walton, H. Boehnel and D.J. Dunlop. "Response of magnetic nanoparticles to microwaves," *Applied Physics Letters*, **85**, 5367-5369 (2004).
11. W.L. Guo and Y.F. Guo. "Giant axial electrostrictive deformation in carbon nanotubes," *Physics Review Letters*, **91**, 115501 (2003).
12. J.H. Wu and L.B. Kong. "High microwave permittivity of multiwalled carbon nanotube composites," *Applied Physics Letters*, **84**, 4956-4958 (2004).
13. S. Shi and J. Liang. "The effect of multi-wall carbon nanotubes on electromagnetic interference shielding of ceramic composites," *Nanotechnology*, **19**, 255707 (2008).
14. W.L. Song, M.S. Cao, Z.L. Hou, J. Yuan and X.Y. Fang. "High-temperature microwave absorption and evolutionary behavior of multiwalled carbon nanotube nanocomposite," *Scripta Materialia*, **61**, 201-204 (2009).
15. R. Benitez, A. Fuentes and K. Lozano. "Effects of microwave assisted heating of carbon nanofiber reinforced high density polyethylene," *Journal of Materials Processing Technology*, **190**, 324-331 (2007).
16. N. Li, Y. Huang, F. Du, *et al.* "Electromagnetic interference (EMI) shielding of single-walled carbon nanotube epoxy composites," *Nano Letters*, **6**, 1141-1145 (2006).
17. P. Greil, "Polymer derived engineering ceramics," *Advanced Engineering Materials*, **2**, 339-348 (2000).

18. L. A. An, R. Riedel, C. Konetschny, H.J. Kleebe, and Raj, R. Newtonian viscosity of amorphous silicon carbonitride at high temperature *Journal of American Ceramic Society* **1998**, 81, 1349.
19. R. Riedel, A. Kienzle, W. Dressler, L. Ruwisch, J. Bill and F. Aldinger. "A silicoboron carbonitride ceramic stable to 2,000 degrees C," *Nature*, **382**, 796-798 (1996).
20. A.M. Hermann, Y.T. Wang, P.A. Ramakrishnan, *et al.* "Structure and electronic transport properties of Si-(B)-C-N ceramics," *Journal of American Ceramic Society*, **84**, 2260-2264 (2001).
21. S.R. Shah and R. Raj. "Nanodevices that explore the synergies between PDCs and carbon nanotubes," *Journal of the European Ceramic Society*, **25**, 243-249 (2005).
22. J.H. Lehman, K.E. Hurst, G. Singh, E. Mansfield, J.D. Perkins and C.L. Cromer. "Core-shell composite of SiCN and multiwalled carbon nanotubes from toluene dispersion," *Journal of Material Science*, **45**, 4251-4254 (2010).
23. L.N. An, W.X. Xu, S. Rajagopalan, *et al.* "Carbon-nanotube-reinforced polymer-derived ceramic composites," *Advanced Material*, **16**, 2036 (2004).
24. A. Francis and R. Riedel. "Unusual magnetic behavior of SiCN/multiwalled carbon nanotubes nanocomposites," *Journal of Applied Physics*, **105**, 07A318 (2009).
25. R. Bhandavat, G. Singh, "Synthesis, Characterization and High Temperature Stability of Si(B)CN Coated Carbon Nanotubes Using a Boron-modified Poly(ureamethylvinyl)silazane Chemistry," *Journal of American Ceramic Society*, **95**, 5, 1536-1543 (2012).
26. A. Hirsch, "Functionalization of single-walled carbon nanotubes," *Angewandte Chemie-International Edition*, **41**, 1853-1859 (2002).

27. S.R. Shah and R. Raj. "Mechanical properties of a fully dense polymer derived ceramic made by a novel pressure casting process," *Acta Materialia*, **50**, 4093-4103 (2002).
28. R. Riedel and A.O. Gabriel. "Synthesis of polycrystalline silicon carbide by a liquid-phase process," *Advanced Material*, **11**, 207 (1999).
29. F. Kremer and A. Schönhal. *Broadband Dielectric Spectroscopy*, Springer: Heidelberg, 2002.
30. N.T. Correia and J.J.M. Ramos. "On the cooperativity of the beta-relaxation: A discussion based on dielectric relaxation and thermally stimulated depolarisation currents data," *Physical Chemistry Chemical Physics*, **2**, 5712-5715 (2000).
31. A. Metaxas, R. Meredith, *Industrial Microwave Heating*. In IEEE Power Engineering Series 4. Peter Peregrinus Ltd: London, 1983.
32. L.X. Benedict, S.G. Louie and M.L. Cohen. "Static Polarizabilities of Single-Wall Carbon Nanotubes," *Physical Review B*, **52**, 8541-8549 (1995).

## Chapter 4 - Very High Laser-Damage Threshold of Polymer-derived Si(B)CN- Carbon Nanotube Composite Coatings

### Abstract

We study the laser irradiance behavior and resulting structural evolution of polymer-derived silicon-boron-carbonitride (Si(B)CN) functionalized multiwall carbon nanotube (MWCNT) coatings. We report a damage threshold value of  $15 \text{ kWcm}^{-2}$  and an optical absorbance of 0.97 after irradiation. This is an order of magnitude improvement over MWCNT ( $1.4 \text{ kWcm}^{-2}$ , 0.76), SWCNT ( $0.8 \text{ kWcm}^{-2}$ , 0.65) and carbon paint ( $0.1 \text{ kWcm}^{-2}$ , 0.87) tested at 2.5 kW CO<sub>2</sub> laser at 10.6  $\mu\text{m}$  exposure. Further, ex-situ measurement of the reflected power at 10.6  $\mu\text{m}$  from the laser irradiated spots show absorption efficiency in excess of 97.5 %. Electron microscopy, Raman spectroscopy, and X-ray photoelectron spectroscopy suggests partial oxidation of Si-B-C-N forming a stable protective SiO<sub>2</sub> phase upon irradiation at  $15 \text{ kWcm}^{-2}$  for 10 seconds. Based on these experimental results, the coating's high optical absorbance is attributed to the presence of carbon nanotubes, while the unprecedented damage threshold performance is attributed to stable Si(B)CN ceramic chemical structure.

---

Submitted as

Bhandavat, R., Feldman, A., Cromer, C., Lehman, J. & Singh, G. (2013). Very High Laser-Damage Threshold of Polymer-derived Si(B)CN- Carbon Nanotube Composite Coatings, *ACS Applied Materials & Interfaces*.

## 4.1 Introduction

Copper cone-type thermal calorimeters (or thermal detectors) are commonly used as measurement standards for calibration of high-power infrared lasers used by the military and laser-based manufacturing companies. The inside surface of the copper cone is coated with a radiation-absorbent material to convert the incident radiation energy into thermal energy (conduction). An optimal coating material is desired to possess several functional properties for accuracy and proper working of the detector, which includes: (a) high thermal conductivity for effective transmission of absorbed heat to the substrate, [1, 2], (b) absolute zero reflectivity in the visible to infrared spectrum for accurate response and to prevent coating damage due to radiation attenuation [3], (c) low thermal mass of the coating for higher responsivity [3,4] , and (d) high visual damage threshold (mainly for high power lasers) [1]. Additionally, physical properties such as (a) forming a uniform and optimum coating thickness on the desired surface, (b) adhering and forming a stable coating against adverse handling and test conditions, [2] and (c) morphology that allows maximum surface area contact with the substrate are also desired [5-8].

To this end, a variety of coating materials have been investigated including carbon paint and black metallic coatings (such as the gold black), because of absorption over a broad wavelength range (up to 40 micrometers) [9-14]. In spite of having low thermal mass, these coating materials are not suitable for high-power laser radiometry because of their poor laser damage threshold (or low oxidation resistance) [19-20]. In addition, these materials exhibit non-uniform spectral response with reflectance reaching as high as (10 to 20) % [15]. For the same, better performance using single and multiwalled carbon nanotubes (MWCNT) coatings have been reported previously [1,15-20]. MWCNTs are the most promising, because of their broad and uniform spectral absorbance from visible to IR wavelengths, high thermal conductivity and a laser damage threshold of approximately  $15 \text{ kWcm}^{-2}$  at  $1.06 \mu\text{m}$  exposure ( $7.1 \text{ kWcm}^{-2}$  for SWCNTs)

[20]. Unfortunately, MWCNT coatings experienced greater damage at 10.6  $\mu\text{m}$  exposure with a reduced damaged threshold value of 1.4  $\text{kWcm}^{-2}$  and 76 % absorption efficiency [20].

One way to improve the laser damage resistance of MWCNTs (at 10.6  $\mu\text{m}$  exposure) would be to functionalize their surfaces with a high oxidation resistant material such as the polymer-derived Si(B)CN ceramic [22]. Polymer-derived Si(B)CN, which is produced by controlled thermal decomposition (pyrolysis) of liquid polymer (such as boron modified polysilazane) is chemically stable up to as high as 1500°C [23]. Polymeric precursor can be readily interfaced with CNTs to yield a core/shell type structure upon pyrolysis. Apart from improved oxidation resistance, the core/shell composite is likely to exhibit high thermal conductivity and optical absorbance contributed by both the nanotube core and graphene like carbon inherently present in Si(B)CN ceramic shell [24-28]. Also, the one pot-synthesis of Si(B)CN-nanotube composite will make it relatively easy to be prepared in large quantities (gram levels), which makes it feasible for laminating any desired substrate of large area using simple spray coating techniques, including the surface of a laser thermal detector. Therefore, we had good reason to prepare and test spray-coatings of Si(B)CN-MWCNT composite for potential application in high-power radiometry, particularly at 10.6  $\mu\text{m}$  exposure.

## **4.2 Experimental Procedure**

### **4.2.1 Composite material and coating preparation**

Coating material was prepared by dispersing 1.0 g of MWCNTs (Bayer Material Science) in 125 mL of toluene by sonication (Branson 2510) for 30 min. This was followed by drop-wise addition of 10.0 g boron-modified polymeric precursor (prepared by use of commercially available polyurea(methylvinyl) silazane (Cerset<sup>TM</sup>, KiON Specialty Polymers, Charlotte, NC) and tri-methyl borate (Alfa Aesar)) with stirring for 24 hours followed by slow drying it at 80



°C in an inert atmosphere. On pyrolysis at 1100 °C, this resulted in a core-shell structured, Si(B)CN-MWCNT composite. Detailed step-by-step synthesis is described in our recent work [22, 29]. The composite material was gently crushed using mortar-pestle to obtain a fine powder. It was then dispersed in toluene (ACS reagent) and sonicated for 1 hour to obtain a homogenous dispersion. As shown in the Fig. 4-1, the dispersion was carefully sprayed on copper substrates by use of an airbrush (Model: Paasche-H#1) at 15 psi of nitrogen gas. The spraying was done with longitudinal passes while the substrate surface temperature was raised to 80 °C. Frequent stops between the passes allowed the solvent to evaporate and thereby form a uniform compact coating. Spray coating was carried out until the appropriate dark black coating thickness was visually realized with an approximate thickness of 10  $\mu\text{m}$ . The coated copper test specimens were then maintained at 100 °C on a hot plate for 12 hours to ensure removal of volatile entities.

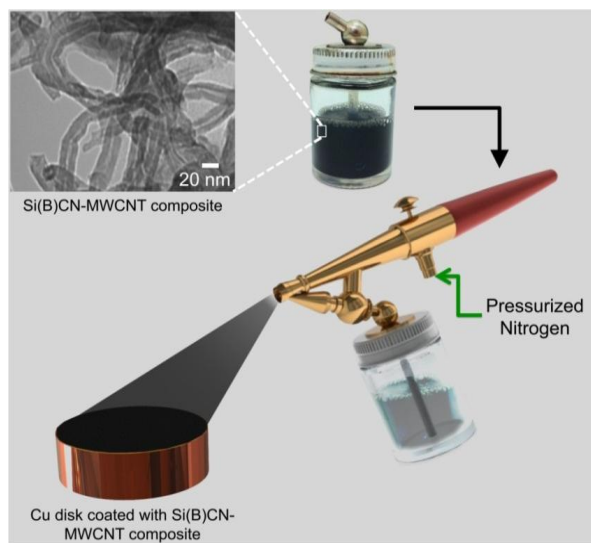


**Figure 4-1:** Schematic representation of the spray coating process (Inset is the TEM image showing shell/core structure of the Si(B)CN-MWCNT composite). Uniformly dispersed Si(B)CN-MWCNT nanowires in toluene solution were spray coated using an air brush technique. The coated specimen were then baked overnight at 100 °C for curing.

#### **4.2.2 Tape test for measuring the composite coating adhesion on the copper substrate**

Si(B)CN-CNT coating's adhesion on the copper plate specimen was tested in accordance with the ASTM D3359-09-'Test Method B' (Standard Test Methods for Measuring Adhesion by Tape Test). The procedure involved following steps:

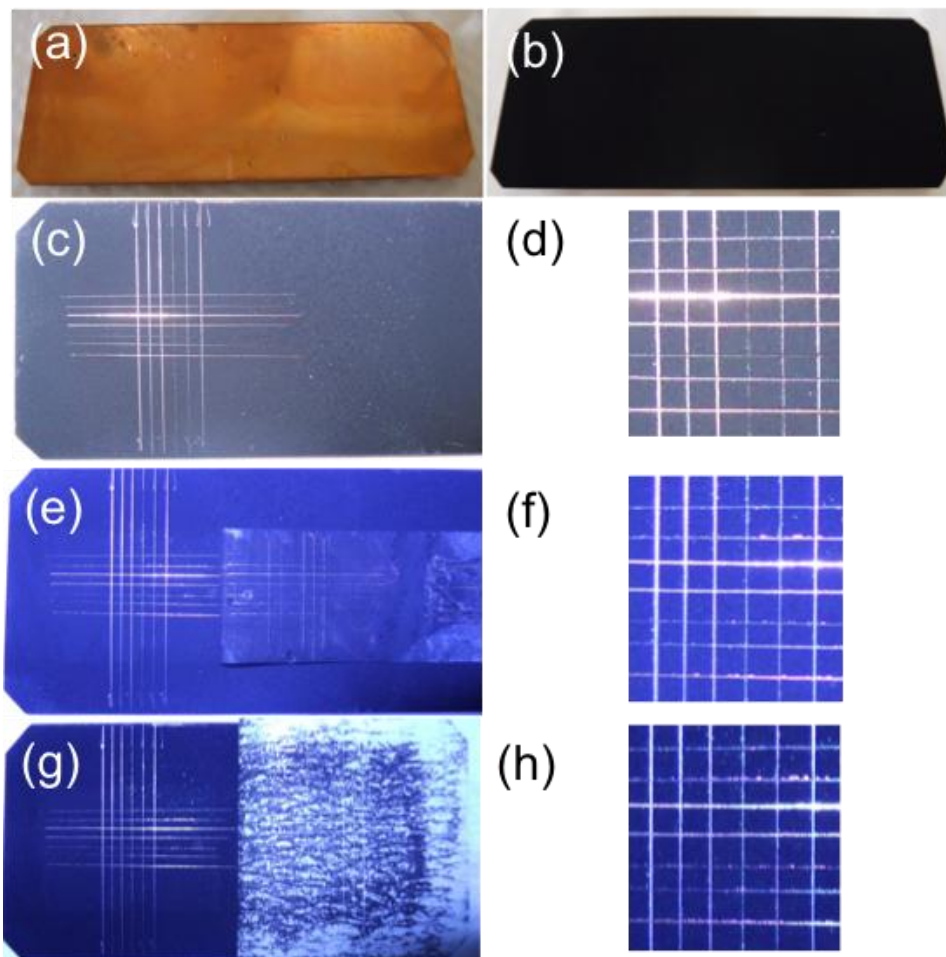
1. Make 13 incisions (20 mm long, spaced 1 mm) through the coating on the substrate using a diamond point pen and a foot rule as a guide in a steady motion using just sufficient pressure to have the cutting edge reach the substrate. The foot rule was kept on the uncut surface while making incisions.
2. Incision depth in the coating was ensured by reflection of light from the cuts on the substrate.
3. Carefully cleaned the coating substrate before applying the tape.
4. Apply the pressure-sensitive tape (with known adhesion properties) of about 50 mm length on the coating in the direction of X marks.
5. Ensured the uniform adhesion of the tape on the coating by pressing it with fingers and rubbing firmly with the eraser on pencil's end.
6. In about 30 seconds, peel off the tape uniformly at 180 ° from the coating.
7. Visual inspection (illuminated magnifying glass) of the X marked area on the coating and comparing it with the scale mentioned in the standard, can qualitatively determine the coating's adhesion on the substrate.

Following two tapes were used in this test:

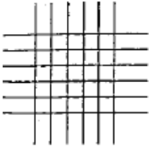
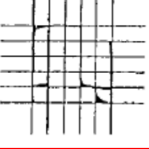


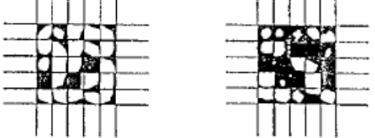
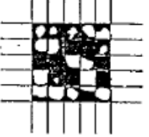
Tape 1: 3M<sup>TM</sup> Removable Repositionable 665 Clear Tape (5 oz/in)

Tape 2: Scotch® General Purpose Masking Tape 234 (34 oz/in)

Results: The results shown in Fig. 4-2, correspond to class '4B' (area removed: less than 5 %) in the 'Classification of Adhesion Test Results' of the ASTM Standard (Fig. 4-3), when tested with Tape 2.



**Figure 4-2:** Digital image of the (a) bare copper test slide, (b) copper test slide coated with Si(B)CN-CNT composite, (c)-(d) copper test slide with incisions made on coating, (e)-(f) results of the Tape test using 3MTM Removable Repositionable 665 Clear Tape, and (g)-(h) Results of the Tape test using Scotch® General Purpose Masking Tape 234.

CLASSIFICATION OF ADHESION TEST RESULTS		
CLASSIFICATION	PERCENT AREA REMOVED	SURFACE OF CROSS-CUT AREA FROM WHICH FLAKING HAS OCCURRED FOR SIX PARALLEL CUTS AND ADHESION RANGE BY PERCENT
5B	0% None	
4B	Less than 5%	
3B	5 - 15%	
2B	15 - 35%	
1B	35 - 65%	
0B	Greater than 65%	

**Figure 4-3:** Table classifying the adhesion test results and highlighted class ‘4B’ (in red) corresponds to the flaking undergone by the composite coating when tested with Tape 2 [31].

"Reprinted, with permission, from ASTM D3359-09e2 Standard Test Methods for Measuring Adhesion by Tape Test, copyright ASTM International, 100 Barr Harbor Drive, West Conshohocken, PA 19428."

### 4.2.3 Experimental Setup

The coated copper test specimens were used for studying thermal damage threshold at constant wavelength of  $10.6 \mu\text{m}$  produced by  $\text{CO}_2$  laser at increasing power densities of  $4 \text{ kWcm}^{-2}$ ,  $8 \text{ kWcm}^{-2}$ ,  $12 \text{ kWcm}^{-2}$  and  $15 \text{ kWcm}^{-2}$ . Details on the laser experimental set-up are available in reference [19]. Disk specimens received 10 seconds exposure, while copper plate specimens were exposed for 2 seconds. Typically, a laser thermal detector test setup has a flowing-water jacket to absorb the heat transferred from laser to copper substrate via the coating material. This flowing water also acts as an infinite sink for the heat transferred. This set-up is rather complex and is not feasible for small-scale damage-threshold-testing; hence we utilized a copper disk with large mass (as a heat sink) as a closest representation of the actual calorimeter cone. Additionally, coatings on copper plates (with lesser heat dissipation) will test the coating material more severely, as they neither have the thermal mass nor did they receive any cooling.

The coatings were prepared on two different substrate types: (a) a copper circular disk (weighing 600 grams) with 76 mm diameter and 13.6 mm thickness and, (b) a rectangular copper plate with dimensions 24 mm x 62 mm and 0.75 mm thickness.

The exposed and unexposed areas of the coatings were analyzed and compared by use of scanning electron microscopy (SEM), Raman and X-ray photoelectron spectroscopy (XPS). SEM analysis of the irradiate areas was done by use of Carl Zeiss EVO low vacuum SEM operating at 5 kV with 25 mm (low resolution) and 10 mm (high resolution) working distance. Specular reflectance of the material was measured from the exposed and unexposed areas (disk specimen) by use of a NIST customized test setup. Briefly, a  $10.6 \mu\text{m}$   $\text{CO}_2$  laser with a 3 mm diameter beam measured at 1.137 W incident power was reflected at approximately  $45^\circ$  from the specimen surface. The power of the reflected beam was detected by use of a thermopile

photodetector. To ensure the beam alignment, the beam was first reflected off of a molybdenum mirror, which was then replaced with the Si(B)CN-MWCNT coated disk specimen. This specimen was mounted on a translation stage in order to maintain the aligned angle as measurements at different spots were performed. Broadband reflectance measurements for the mid-IR range were carried out by use of Thermo Fisher Nicolet 6700 FT-IR Spectrometer in the ATR mode. Raman spectra were collected on HORIBA LabRAM ARMIS spectrometer using 17 mW HeNe laser source [632.8 nm wavelength (1.96 eV)]. The spectra were collected using a 100 X NIR objective lens (theoretical spot size: 842 nm), 200  $\mu\text{m}$  confocal hole, 150  $\mu\text{m}$  wide entrance slit, 600  $\text{gr. mm}^{-2}$  grating. The surface chemistry of the coating was studied by use of PHI Quantera SXM (ULVAC-PHI, Inc) and monochromatic Al  $K\alpha$  X-radiation with beam size  $<9 \mu\text{m}$ . Following a survey scan, a 15-minute high-resolution scan was performed in the major elemental peaks' energy window.

### **4.3 Results and Discussion**

#### ***Electron Microscopy***

The effect of incremental laser power on coating morphology can be observed in corresponding electron microscopy images. As the copper disk specimen has comparatively better heat dissipation (due to its large thermal mass) than the plate specimen, the coating on disk specimen is expected to withstand much higher power densities and longer periods without damage. Hence, the characterization data is presented in a manner to show incremental coating damage i.e., data from the disk specimen are presented first (Fig. 4-4 and 4-5) followed by a copper plate specimen (Fig. 4-6 and 4-7).

At low magnifications, the non-irradiated coating surface exhibited a structurally stable and porous morphology with interconnected particles (Fig. 4-5a). MWCNTs are believed to provide

the reinforcement to the composite coating by holding porous ceramic on to the copper substrate under harsh testing conditions (Fig. 4-2).

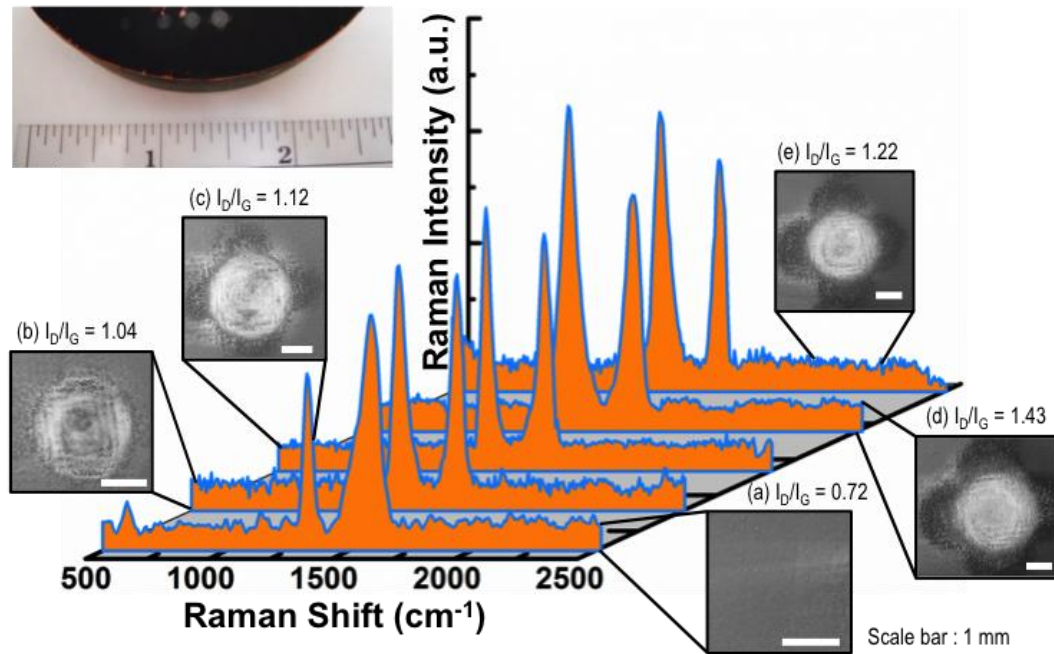


**Figure 4-4:** Normalized Raman spectra of Si(B)CN MWCNT coatings exposed to laser irradiance at (a)  $0 \text{ kWcm}^{-2}$  (unexposed), (b)  $4 \text{ kWcm}^{-2}$ , (c)  $8 \text{ kWcm}^{-2}$ , (d)  $12 \text{ kWcm}^{-2}$ , and (e)  $15 \text{ kWcm}^{-2}$  for 10 seconds respectively, along with the corresponding SEM micrographs. Scale bar (image b to e) is 1 mm. Insert (top left) is the digital camera image of the specimen.

The laser-irradiated region of the coating appeared as a bright spot (SEM image charging) while the unexposed areas were relatively dark in both the disk (Fig. 4-4) and plate (Fig. 4-6) specimens. For the disk specimen, the transition from non-irradiated to irradiated spot was prominently noticeable (Fig. 4-4a through 4-4e). This observation suggests partial oxidation of the ceramic (either  $\text{Si}_3\text{N}_4$  /  $\text{SiC}$  in the coating transforming to  $\text{SiO}_2$ ) or burning of partially coated MWCNTs when compared to the ‘as-prepared’ coating, shown in Fig. 4-5a and 4-5b. For the  $4 \text{ kWcm}^{-2}$ , 10 second irradiance (Fig. 4-5c), as much as 70 % of the spot appeared bright. The

irradiated spots with  $8 \text{ kWcm}^{-2}$  and  $12 \text{ kWcm}^{-2}$  exposure showed extension of the bright area to about 95 percent. At higher magnifications, Fig. 4-5d and 4-5e, these darker areas showed presence of ceramic-coated MWCNT mesh like morphology. Spot at  $15 \text{ kWcm}^{-2}$  (Fig. 4-5f) appeared similar to that of  $12 \text{ kWcm}^{-2}$  and no new changes could be observed in the coating's morphology.

**Table 4-1:** Dependence of D-peak position and  $I_D/I_G$  (Intensity ratio of D and G peak) as observed in the Raman spectra for the disk specimen, on the incident laser irradiation power density.

Irradiance ( $\text{kWcm}^{-2}$ )	D-Peak		G-Peak		$I_D/I_G$
	Position ( $\text{cm}^{-1}$ )	FWHM	Position ( $\text{cm}^{-1}$ )	FWHM	
Unexposed	1333	40.2	1584.9	86.4	0.72
4	1351.2	58.5	1585.2	56.9	1.04
8	1351.5	47.3	1587.4	59.3	1.12
12	1334.5	81.5	1593	71.7	1.43
15	1356.2	69.8	1592.1	51.4	1.22

SEM images from the copper plate specimen are compared in Fig. 4-6 and 4-7. The 'as-prepared' coating looked similar to the one on disk specimen (Fig. 4-5a). The irradiated spot at  $4 \text{ kWcm}^{-2}$  (Fig. 4-6b and 4-7a) revealed bright areas, with some discontinuities. The surface of these discontinuities (gaps) appeared uniform and smooth with intermittent mesh of interconnected ceramic-coated MWCNTs. These gaps are believed to originate from volume changes induced in the composite material due to an abrupt and intense heat generation on coating top surface during continuous laser exposure. As a result, the top layer experienced cracks and increased discontinuities due to increased volume change compared to the inner layer or bottom regions, thereby forming two layers with distinct appearance. We believe that this



issue of differential heating could be addressed by optimizing composite coating thickness, which can be a subject of future research.

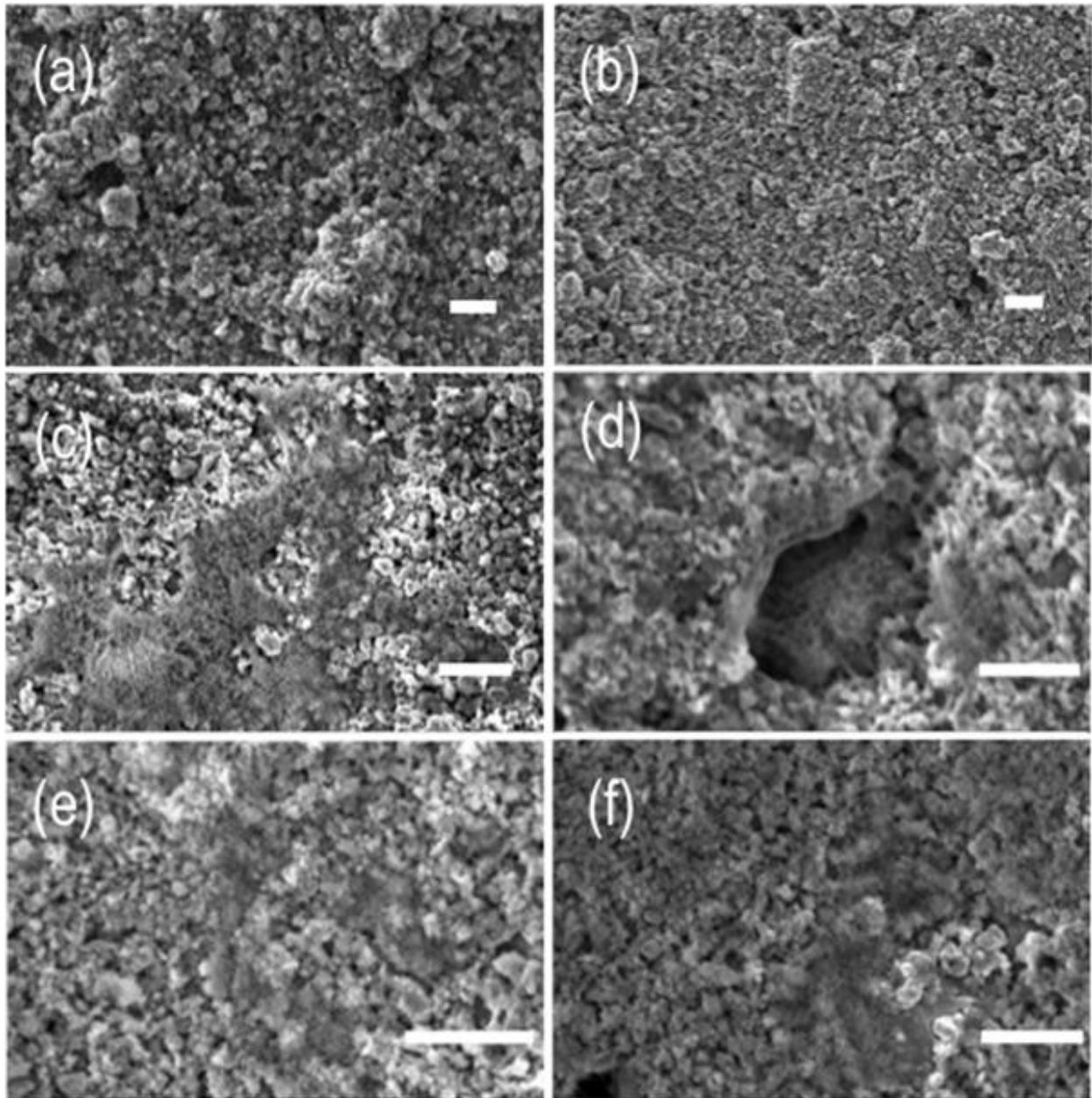


**Figure 4-5:** (a)-(b) SEM images of the ‘as-prepared’ coating on copper disk specimen. While (c) through (f) are SEM images from the coating area irradiated at 4, 8, 12, and 15 kWcm<sup>-2</sup> for 10 seconds, respectively. Image (d) seems out of focus because of the coating height difference. Scale bar is 5 micrometer in all images.

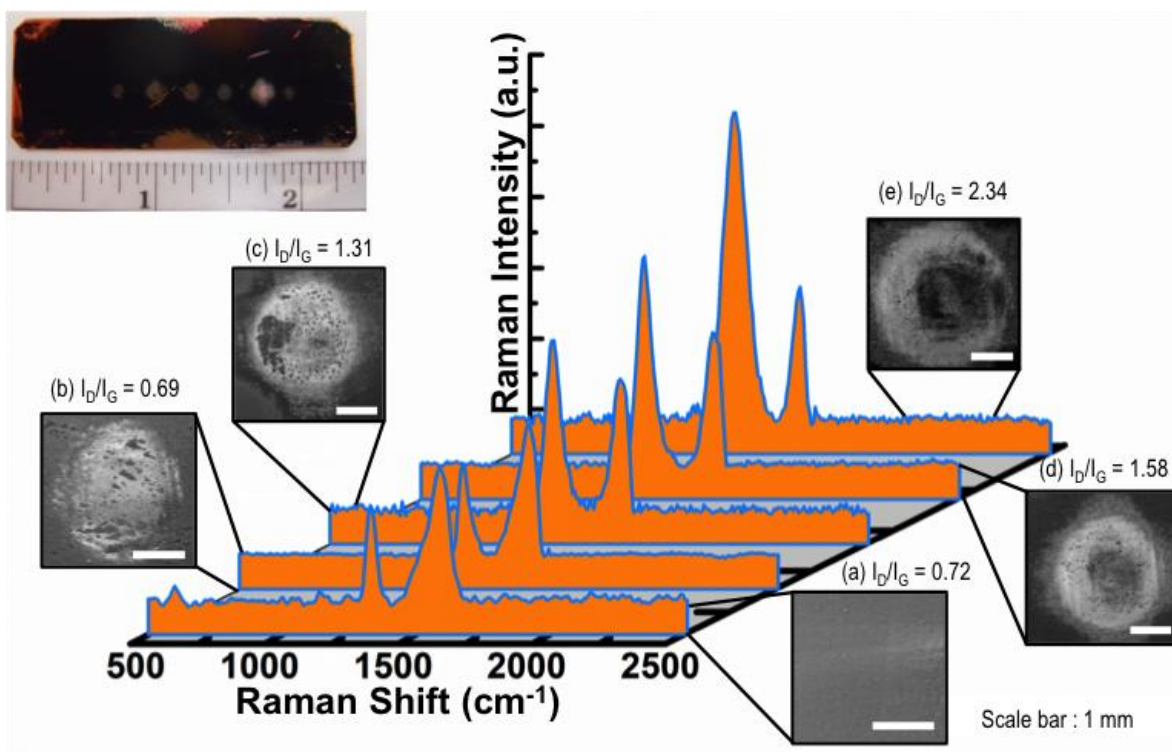


**Figure 4-6:** Normalized Raman spectra of Si(B)CN-MWCNT coatings exposed to laser irradiance at (a)  $0 \text{ kWcm}^{-2}$  (unexposed), (b)  $4 \text{ kWcm}^{-2}$ , (c)  $8 \text{ kWcm}^{-2}$ , (d)  $12 \text{ kWcm}^{-2}$ , and (e)  $15 \text{ kWcm}^{-2}$  for 2 seconds, respectively with the corresponding low-magnification SEM micrographs. Scale bar (image b to e) is 1 mm. Insert (top left) is the digital camera image of the plate specimen.

SEM images also showed round and isolated particles (size less than  $1 \mu\text{m}$ ) that are most likely to be the hard ceramic phase. The area irradiated at higher laser density of  $8 \text{ kWcm}^{-2}$  (Fig. 4-7b) exhibited major transition in the discontinuity regions. Unlike smooth gaps observed for lower laser power densities, this spot showed fused-in/solidified liquid-type of morphology. Further, at  $12 \text{ kWcm}^{-2}$  exposure (Fig. 4-7c), large isolated gaps ( $10$  to  $20 \mu\text{m}$ ) in the coating with solidified liquid-like texture were observed. While at the  $15 \text{ kWcm}^{-2}$  (Fig. 4-7d) exposure, these gaps

appeared more uniform. Remarkably, still under these conditions the coating was found to be relatively stable and intact on the substrate. The bright appearing spots realized as either SiO<sub>2</sub> or burned nanotubes appeared more pronounced. These observations confirm that composite coatings on the test copper plate specimen suffered more severe damage due to low thermal mass of the substrate and insufficient cooling.

**Table 4-2:** Dependence of D-peak position and I<sub>D</sub>/I<sub>G</sub> as observed in the Raman spectra for the plate specimen, on the incident laser irradiation power density.

Irradiance (kWcm <sup>-2</sup> )	D-Peak		G-Peak		I <sub>D</sub> /I <sub>G</sub>
	Position (cm <sup>-1</sup> )	FWHM	Position (cm <sup>-1</sup> )	FWHM	
Unexposed	1331.7	42.7	1588.8	94.7	0.72
4	1335.2	48.1	1581.7	78.2	0.69
8	1335.2	71.8	1588.8	65.4	1.31
12	1333.5	64.8	1594.1	64	1.58
15	1338.8	97	1580	49.1	2.34

### *Raman Spectroscopy*

Raman spectroscopy is a sensitive, nondestructive and non-invasive technique and hence qualifies for studying the evolution of carbon structure (sp<sup>3</sup>- and sp<sup>2</sup>-type carbon) in the irradiated area. The characteristic “D” and “G” peaks signify the presence of sp<sup>3</sup>- and sp<sup>2</sup> type carbon bonds in composite coatings, respectively. Hence, the origin of D-peak collectively corresponds to stretching of Si-C and defect sites in MWCNTs, whereas the G-peak corresponds to C=C (graphitic) bonds in the coating material. As shown in Fig. 4-4 and Fig. 4-6, existence of D-peak (1330-1356 cm<sup>-1</sup>) and G-peak (1580-1595 cm<sup>-1</sup>) are invariably observed for all exposures. For the disk specimen, the I<sub>D</sub>/I<sub>G</sub> ratio increased from 0.72 from the unexposed area to 1.43 from 12 kWcm<sup>-2</sup> and 1.22 from the 15 kWcm<sup>-2</sup>, 10 seconds irradiated spot. And for the plate specimen, I<sub>D</sub>/I<sub>G</sub> ratio was 2.34 from the spot that received 15 kWcm<sup>-2</sup>, 2 seconds exposure.

Hence, almost a linear effect of increasing laser power density on Raman  $I_D/I_G$  ratio was observed, suggesting increased defects in  $sp^2$  bonded graphitic carbon with irradiated power. These results also suggest that even under the influence of high irradiance, the graphitic (free) carbon in Si(B)CN is preserved and MWCNTs in the coatings are protected.

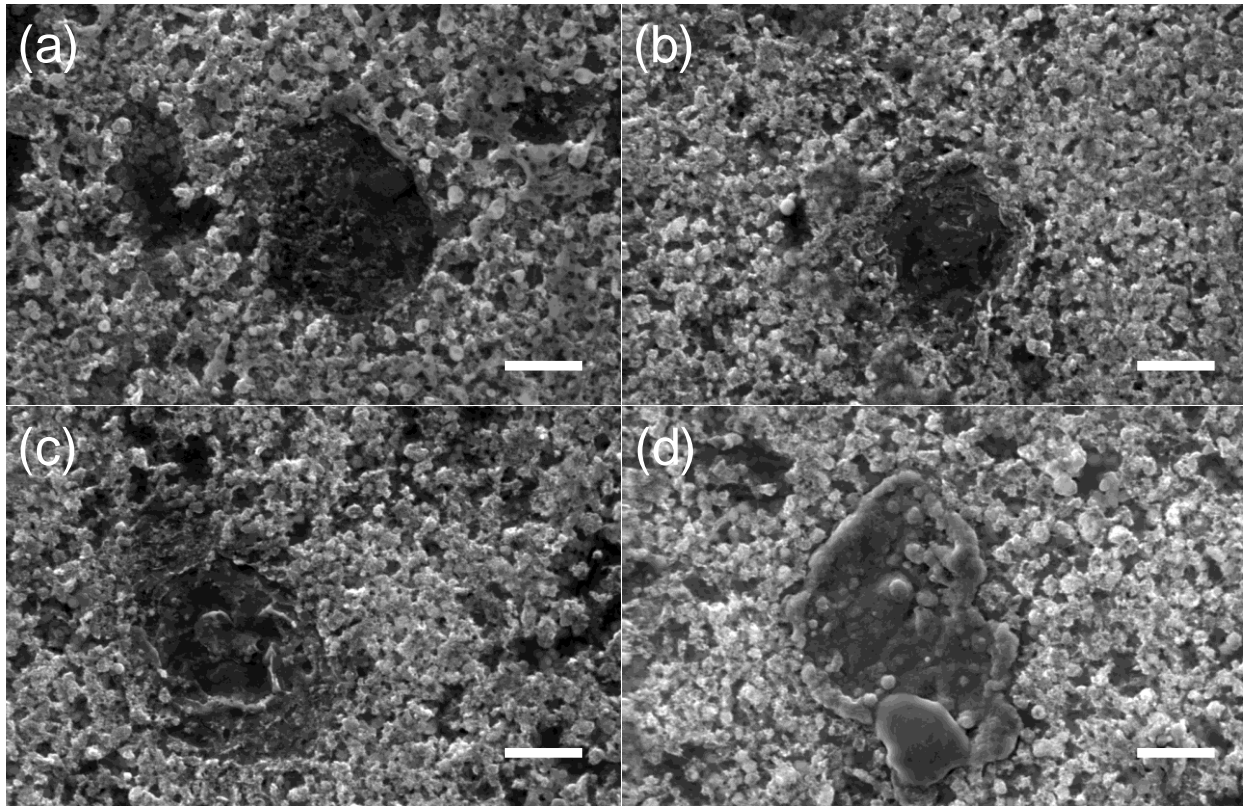


**Figure 4-7:** SEM micrographs showing laser-irradiated areas of the coating for copper plate specimen at (a)  $4 \text{ kWcm}^{-2}$ , (b)  $8 \text{ kWcm}^{-2}$ , (c)  $12 \text{ kWcm}^{-2}$ , and (d)  $15 \text{ kWcm}^{-2}$  for 2 seconds exposure. Scale bar is 5 micrometer in all images.

Detailed analysis and comparison of the spectrum collected for laser-irradiated spots and as-prepared coatings provided further understanding of structural changes in the carbon structure. As shown in Table 4-1 for the copper disk specimen, G-band (or peaks) experienced a blue shift from  $\sim 1584 \text{ cm}^{-1}$  to  $\sim 1593 \text{ cm}^{-1}$ , suggesting that the graphitic carbon or the MWCNTs experienced compressive stresses, probably due to change in volume of the surrounding ceramic

matrix upon irradiation (also observed in SEM images). [24,26] The calculated ratios of  $I_D/I_G$  (summarized in Table 4-1 and 4-2) for the irradiated spots showed a linear increase with increasing laser-power density, suggesting increasing defect sites in  $sp^2$ -bonded graphitic carbon in the coatings. The 2-D band in the spectra was not analyzed, due to their weak intensities.

### *Reflectance measurements*

The measured reflected power with reference to the incident power of 1.137 W laser (15 second pulse) is plotted against time in Fig. 4-8a. The reflectance from the as-prepared Si(B)CN-MWCNT coatings was  $1.3E-3 \pm 2.5E-6$  W, implying high optical absorption (99.87 %) at  $10.6 \mu\text{m}$  wavelength. As anticipated, increasing magnitude of reflected power is observed from areas that were exposed to higher laser irradiance. Reflected power remained unchanged for  $4 \text{ kWcm}^{-2}$  and  $8 \text{ kWcm}^{-2}$  irradiated spots, while for the  $12 \text{ kWcm}^{-2}$  and  $15 \text{ kWcm}^{-2}$  irradiated spots showed close to 98 % absorption.

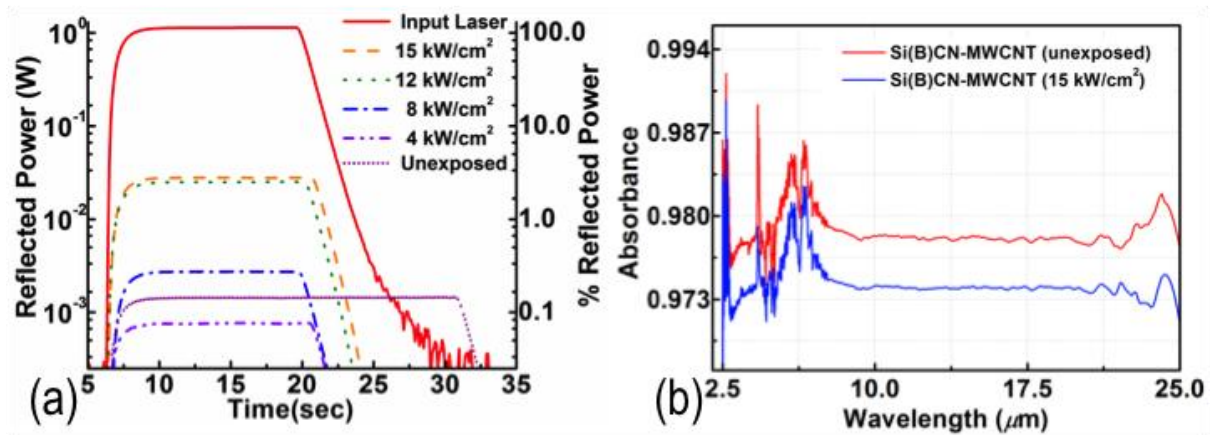


**Figure 4-8:** (a) Measured reflected power profiles for the incident laser of 1.137 W at  $10.6 \mu\text{m}$  wavelength from various irradiated areas on the coating for the copper disk specimen. Peak power measurements made with less than 0.5% variance. (b) Mid-IR range spectral absorption response of Si(B)CN-MWCNT coating before and after irradiation at  $15 \text{ kWcm}^{-2}$  for 10 seconds.

Further, the adaptability of the composite coatings for longer-wavelength (mid-IR) range was studied by spectral absorption measurements. Comparison of spectral absorption signal from the as-prepared and irradiated areas (Fig. 4-8b) showed high absorption even at longer-wavelengths. Strikingly, even after the damage inflicted by high laser irradiance ( $15 \text{ kWcm}^{-2}$ ), the coating maintained a spectral absorption at about 0.97. Change in the chemical structure of ceramic (oxidation) may have contributed to the minute reduction in spectral response observed from the irradiated spot. None-the-less, for a broad wavelength range the absorption remained uniform, implying that the composite material preserved its ability to generate a reliable response signal. [20,21]

### ***X-Ray Photoelectron Spectroscopy***

Surface characterization consistently revealed showed Si, B and C elemental peaks from the laser-irradiated areas. The high-resolution peaks were curve-fitted by use of Gaussian-Lorentzian (70:30) mix function and are plotted in Fig. 4-9. The total area under each peak provided an approximation of the respective elemental and phase composition, as summarized in Table 4-3. The deconvolution of Si2p elemental peak from the non-irradiated area showed a sharp peak corresponding to Si-N type bond (due to  $\text{Si}_3\text{N}_4$  at  $\sim 102 \text{ eV}$ ) and a smaller peak at a higher energy of  $\sim 103 \text{ eV}$  due to Si-O bond. The XPS peaks from laser-irradiated spots exhibited higher electronegativity shift in Si peak from Si-N to Si-O type bonds. The B1s valence elemental peak in the non-irradiated and irradiated spots showed mixed existence of both B-N and B-O type bonds at  $\sim 192.1 \text{ eV}$  and  $\sim 193.1 \text{ eV}$ , respectively.

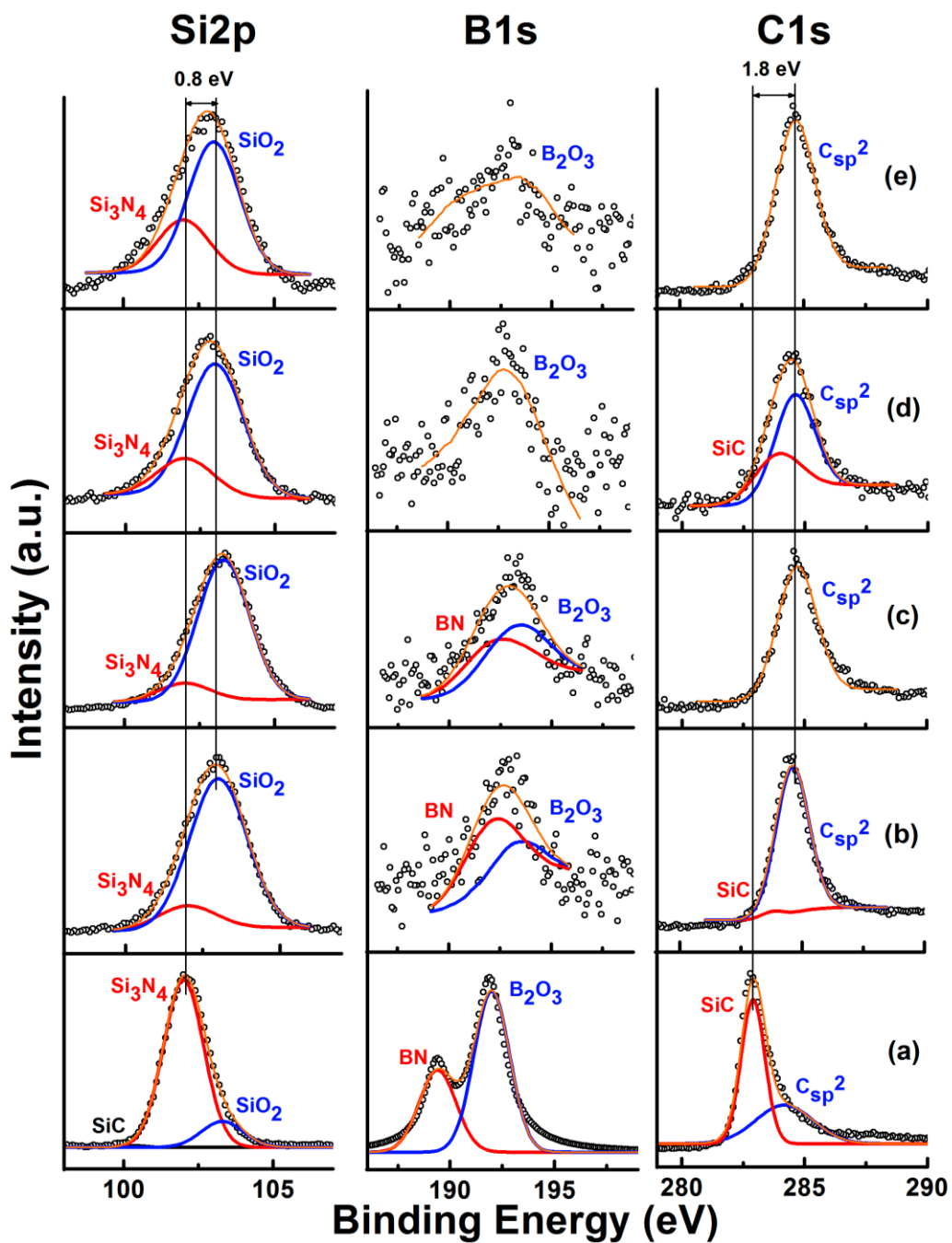


**Figure 4-9:** Elemental X-ray photoelectron spectra of Si(B)CN-MWCNT coatings on copper plate specimen exposed to laser irradiance at (a)  $0 \text{ kWcm}^{-2}$  (unexposed), (b)  $4 \text{ kWcm}^{-2}$ , (c)  $8 \text{ kWcm}^{-2}$ , (d)  $12 \text{ kWcm}^{-2}$ , and (e)  $15 \text{ kWcm}^{-2}$  for 2 seconds, respectively.

The boron peaks in laser-irradiated spots were not clearly recognized, suggesting a decrease in the amount of surface boron. The binding energy of C1s photoelectrons (as a strong and narrow peak) at ~283.8 eV confirmed the Si-C bond assignment in the non-irradiated specimen. The XPS spectrum from the laser-irradiated areas suggests a diminishing Si-C peak and an emerging sp<sup>2</sup> free-carbon peak (at higher binding energy of ~284.6 eV) [30]. In summary, the XPS analysis confirmed that coating's composition transformed from a Si-C rich phase into a Si-O type phase upon increasing laser irradiance, while the graphitic carbon could still be observed in the coating.

**Table 4-3:** Atomic composition of Si(B)CN-MWCNT coating for unexposed and irradiated coating areas (2 seconds exposure) for copper plate specimen obtained through XPS.

Irradiance [kWcm <sup>-2</sup> ]	Atomic Percentage					Elemental Ratio		
	Si	B	C	N	O	Si/B	Si/C	Si/O
Unexposed	13.3	6.5	37.8	2.9	39.3	2	0.3	0.3
4	17.8	2.7	40.5	--	39	6.6	0.4	0.5
8	24.6	2	17.5	--	55.8	12.3	1.4	0.4
12	25.4	1.8	17.9	--	54.9	14.1	1.4	0.5
15	20.1	1.6	39	--	39.3	12.6	0.5	0.5



## 4.4 Conclusion

In conclusion, we have demonstrated preparation of spray coatings composed of core shell Si(B)CN-MWCNT composite that sustain laser irradiation up to  $15 \text{ kWcm}^{-2}$  at  $10.6 \mu\text{m}$  for 10 seconds. Unlike some of the other coating materials reported in literature, this composite material shows both the high optical absorbance and an order-of-magnitude higher damage tolerance. The coatings exposed to incremental laser power density and exposure times were analyzed following various spectroscopic and imaging techniques. Electron microscopy revealed no major destruction (i.e., burning, delamination and deformation) for the disk specimen, other than some isolated surface discontinuities. Raman spectroscopy suggests the survival of graphitic carbon (and carbon nanotubes) in the coating. Direct dependence of irradiation power density on  $I_D/I_G$  ratio, suggests systematic evolution of  $sp^3$  carbon from  $sp^2$ -bonded-graphitic carbon. XPS results indicate partial oxidation of  $\text{Si}_3\text{N}_4$  /SiC ceramic shell into stable  $\text{SiO}_2$  phases and suggest its adaptable nature. Ex-situ power reflectance measurements confirmed the high optical absorbance of the coating, 99.87 % for the unexposed area and 97.54 % for the area that received  $15 \text{ kWcm}^{-2}$  exposure. Coating material's high damage tolerance and uniform absorbance can be collectively attributed to the presence of carbon nanotubes and high oxidation resistance of Si(B)CN ceramic structure.

## 4.5 References

1. C.L. Cromer, K.E. Hurst, X. Li and J.H. Lehman. "Black optical coating for high-power laser measurements from carbon nanotubes and silicate," *Optics Letters*, **34**, 193-195 (2009).
2. J. Lehman and A. Dillon. "Carbon-nanotube coatings promise better thermal detectors," *Laser Focus World*, **41**, 81-87 (2005).
3. J.H. Lehman, B. Lee and E.N. Grossman. "Far infrared thermal detectors for laser radiometry using a carbon nanotube array," *Applied Optics*, **50**, 4099-4104 (2011).
4. E. Theocharous, C. Engtrakul, A.C. Dillon and J. Lehman. "Infrared responsivity of a pyroelectric detector with a single-wall carbon nanotube coating," *Applied Optics*, **47**, 3999-4003 (2008).
5. J.H. Lehman, C. Engtrakul, T. Gennett and A.C. Dillon. "Single-wall carbon nanotube coating on a pyroelectric detector," *Applied Optics*, **44**, 483-488 (2005).
6. J. Lehman, A. Sanders, L. Hanssen, B. Wilthan, J. Zeng and C. Jensen. "Very Black Infrared Detector from Vertically Aligned Carbon Nanotubes and Electric-Field Poling of Lithium Tantalate," *Nano Letters*, **10**, 3261-3266 (2010).
7. J.H. Lehman, K.E. Hurst, A.M. Radojevic, A.C. Dillon and R.M. Osgood Jr. "Multiwall carbon nanotube absorber on a thin-film lithium niobate pyroelectric detector," *Optics Letters*, **32**, 772-774 (2007).
8. E. Theocharous and J. Lehman. "The evaluation of a pyroelectric detector with a sprayed carbon multi-wall nanotube black coating in the infrared," *Infrared Physics and Technology*, **54**, 34-38 (2011).
9. D.J. Advena, V.T. Bly and J.T. Cox. "Deposition and Characterization of Far-Infrared Absorbing Gold Black Films," *Applied Optics*, **32**, 1136-1144 (1993).

10. W.R. Blevin and J. Geist. "Infrared Reflectometry with a Cavity-Shaped Pyroelectric Detector," *Applied Optics*, **13**, 2212-2217 (1974).
11. W.R. Blevin and J. Geist. "Influence of Black Coatings on Pyroelectric Detectors," *Applied Optics*, **13**, 1171-1178 (1974).
12. J. Lehman, E. Theocharous, G. Eppeldauer and C. Pannell. "Gold-black coatings for freestanding pyroelectric detectors," *Measurement Science and Technology*, **14**, 916-922 (2003).
13. D.B. Betts, F.J.J. Clarke, L.J. Cox and J.A. Larkin. "Infrared Reflection Properties of 5 Types of Black Coating for Radiometric Detectors," *Journal of Physics E-Scientific Instruments*, **18**, 689-696 (1985).
14. N. Nelms and J. Dowson. "Goldblack coating for thermal infrared detectors," *Sensors and Actuators A-Physical*, **120**, 403-407 (2005).
15. J.H. Lehman, K.E. Hurst, L.K. Roberson, K. Nield and J.D. Hamlin. "Inverted spectra of single-wall carbon nanotube films," *Journal of Physical Chemistry C*, **112**, 11776-11778 (2008).
16. C. J. Chunnillall, J. H. Lehman, E. Theocharous and A. Sanders, "Infrared hemispherical reflectance of carbon nanotube mats and arrays in the 5–50  $\mu\text{m}$  wavelength region," *Carbon*, **50**, 14, 5348-5350, (2012).
17. K.E. Hurst, A.C. Dillon, S. Yang and J.H. Lehman. "Purification of Single Wall Carbon Nanotubes As a Function of UV Wavelength, Atmosphere, and Temperature," *Journal of Physical Chemistry C*, **112**, 16296-16300 (2008).
18. K. Ramadurai, C.L. Cromer, X. Li, R.L. Mahajan and J.H. Lehman. "Foam-based optical absorber for high-power laser radiometry," *Applied Optics*, **46**, 8268-8271 (2007).

19. K. Ramadurai, C.L. Cromer, A.C. Dillon, R.L. Mahajan and J.H. Lehman. "Raman and electron microscopy analysis of carbon nanotubes exposed to high power laser irradiance," *Journal of Applied Physics*, **105**, 093106 (2009).
20. K. Ramadurai, C.L. Cromer, L.A. Lewis, *et al.* "High-performance carbon nanotube coatings for high-power laser radiometry," *Journal of Applied Physics*, **103**, 013103 (2008).
21. E. Theocharous, R. Deshpande, A.C. Dillon and J. Lehman. "Evaluation of a pyroelectric detector with a carbon multiwalled nanotube black coating in the infrared," *Appl. Opt.*, **45**, 1093-1097 (2006).
22. R. Bhandavat, G. Singh, "Synthesis, Characterization and High Temperature Stability of Si(B)CN Coated Carbon Nanotubes Using a Boron-modified Poly(ureamethylvinyl)silazane Chemistry," *Journal of American Ceramic Society*, **95**, 5, 1536-1543 (2012).
23. Z.C. Wang, F. Aldinger and R. Riedel. "Novel silicon-boron-carbon-nitrogen materials thermally stable up to 2200 degrees C," *Journal of American Ceramic Society*, **84**, 2179-2183 (2001).
24. R. Riedel, A. Kienzle, W. Dressler, L. Ruwisch, J. Bill and F. Aldinger. "A silicoboron carbonitride ceramic stable to 2,000 degrees C," *Nature*, **382**, 796-798 (1996).
25. L.N. An, W.X. Xu, S. Rajagopalan, *et al.* "Carbon-nanotube-reinforced polymer-derived ceramic composites," *Advanced Material*, **16**, 2036-2040 (2004).
26. S.R. Shah and R. Raj. "Nanodevices that explore the synergies between PDCs and carbon nanotubes," *Journal of European Ceramic Society*, **25**, 243-249 (2005).

27. J. Bill and F. Aldinger. "Precursor-Derived Covalent Ceramics," *Advanced Material*, **7**, 775-787 (1995).
28. B. Papendorf, K. Nonnenmacher, E. Ionescu, H. Kleebe and R. Riedel. "Strong Influence of Polymer Architecture on the Microstructural Evolution of Hafnium-Alkoxide-Modified Silazanes upon Ceramization," *Small*, **7**, 970-978 (2011).
29. R. Bhandavat, W. Kuhn, E. Mansfield, G. Singh, *ACS Applied Material and Interfaces*, **4**, 11-16 (2012).
30. T. Tharigen, G. Lippold, V. Riede, *et al.* "Hard amorphous CSixNy thin films deposited by RF nitrogen plasma assisted pulsed laser ablation of mixed graphite/Si3N4-targets," *Thin Solid Films*, **348**, 103-113 (1999).
31. ASTM D3359-09<sup>E2</sup>: Standard Test Methods for Measuring Adhesion by Tape Test.

## **Chapter 5 - Improved Electrochemical Capacity of Precursor-Derived Si(B)CN-Carbon Nanotube Composite as Li-ion Battery Anode**

### **Abstract**

In this chapter we study the electrochemical behavior of precursor-derived Si(B)CN ceramic and Si(B)CN-MWCNT nanowires as a lithium-ion battery anode. Reversible capacity of Si(B)CN was observed to be 138 mAh/g after 30 cycles, which is four times that of SiCN (~25 mAh/g) processed under similar conditions, while the Si(B)CN-CNT composite showed further enhancement demonstrating 412 mAh/g after 30 cycles. Improved performance of Si(B)CN is attributed to the presence of boron that is known to modify SiCN's nanodomain structure resulting in improved chemical stability and electronic conductivity. Post cycling microscopy and chemical analysis of the anode revealed formation of a stable passivating layer, which resulted in stable cycling.

---

Reprinted with permission from (R. Bhandavat and G. Singh, "Improved Electrochemical Capacity of Precursor-Derived Si(B)CN-Carbon Nanotube Composite as Li-Ion Battery Anode," *ACS Applied Materials & Interfaces*, **4**, 10, 5092-5097). Copyright (2012) American Chemical Society

## 5.1 Introduction

Lithium-based secondary batteries such as the Li-ion battery (LIB) are currently being studied because of their ability to deliver high power and energy densities, longer cycle and shelf life [1-3]. Development of efficient and durable LIB mainly includes designing and testing of electrode and electrolyte materials with desired energy storage properties, rate capability, and synchronized performance. Ideally, a negative electrode material (anode) is expected to possess (a) high lithium ion intercalation ability, (b) ability to retain its physical and chemical structure, (c) high ionic and electronic conductivity, and (d) maintain intimate contact with the current collector. Performance of conventionally used graphite anode in LIB mainly has a practical limitation of low capacity at higher operating current rates (e.g., reversible capacity of ~50 mAh/g when operating at 100 mA/g) [4]. Several different materials and structures are being explored to address these requirements. The silicon based nanostructures have received the most attention, because of silicon's high Li alloyability (theoretical capacity exceeding 4000 mAh/g) and its low discharge potential that translates to a high power density [5]. But silicon's high electrochemical capacity comes at the cost of increased volume changes (as much as 400 %) that occur upon lithiation. Subsequently, the delithiation can cause several operational issues including pulverization, delamination, and poor capacity retention especially for large-size battery anodes, making them incompetent for practical applications [5]. Although several solutions have been suggested, convincing results are yet to be seen [6].

Silicon-based precursor-derived ceramics (PDCs) have been known for their unique amorphous structure that results in their high-temperature stability and mechanical strength, which in turn depends upon the starting precursor chemistry and processing conditions [7,8]. Recent studies on amorphous PDCs have highlighted their ability to store lithium in a reversible manner. These

materials seem to outperform conventionally used graphite in terms of useful capacity and high rate performance [4,9-17]. In addition, composites made by blending PDCs with nano-structured materials like carbon nanotubes and graphene have also been explored for battery applications [18-21].

The purpose of this work was to explore and measure the lithium cycling ability of Si(B)CN-CNT composite material. In our recent work we demonstrated synthesis of a boron-modified polymer that can be effectively utilized to synthesize Si(B)CN-CNT composite [22]. This composite offers improved oxidation resistance (stable in air up to 1000°C) over SiCN-CNT composite [22]. Also, previous studies have shown four orders of increase in temperature dependent conductivity for SiCN ceramics when doped with boron [23]. Improved performance of boron-doped SiCN is generally attributed to the nanoscale changes happening in its structure, like formation of graphene like chains and/or B(C)N domains [23,24]. Here, it is expected that the open nanodomain structure of amorphous Si(B)CN shell will contribute in effective Li-ion diffusion and storage, while the nanotube core will improve the availability of electrons at intercalation sites. Additionally, carbon nanotubes are expected to improve the mechanical toughness or long-term cycleability of the electrode.

In order to test this hypothesis of enhanced Li-ion cycling in PDCs by boron-doping and changing pyrolysis temperatures, we studied and compared the lithium cycling behavior of SiCN (1100°C), Si(B)CN (800, 1100 and 1500 °C) and Si(B)CN-CNT composites (800, 1100 and 1500°C) anodes. Si(B)CN-CNT anodes processed at 1100°C demonstrated a stable cycling performance with the highest reversible capacity and least first cycle loss.



## 5.2 Experimental Procedure

### 5.2.1 Material Preparation

Polymer-derived Si(B)CN ceramic and Si(B)CN-CNT composites were prepared through controlled pyrolysis of a boron-modified polyborosilazane precursor reported in our earlier works [22,25]. In brief, commercially available polyureamethyl vinylsilazane (commercial name: Ceraset™, Clariant) was modified using trimethyl borate reagent (Sigma Aldrich, 99.9 %) to obtain a polyborosilazane precursor. It was then homogeneously mixed with approximately 15 wt. % CNTs (Bayer AG) followed by crosslinking at 400°C for 2 hours and pyrolysis at various temperatures (~800, ~1100 or ~1500°C) for 4 hours in flowing nitrogen that resulted in formation of Si(B)CN-CNT shell/core morphology. Polymer-derived SiCN ceramic was prepared by cross-linking and pyrolysis of commercially available polyureasilazane (Ceraset™) precursor at 400°C and 1100°C, respectively [26-28].

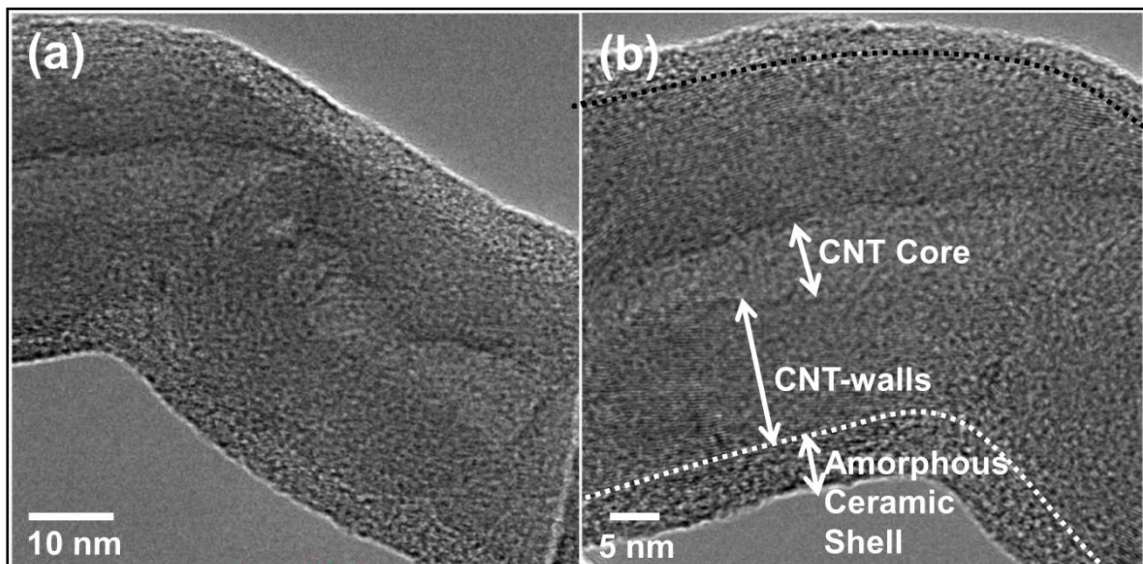


**Figure 5-1:** (a)-(b) High-resolution TEM images of the Si(B)CN-CNT-1100 composite showing the shell/core morphology.

### **5.2.2 Instrumentation**

Structural characterization of the synthesized ceramics, composites and anode surfaces was performed using 10 kV Carl Zeiss EVO Low-Vacuum SEM (Peabody, MA). Chemical composition of the specimen's surface was analyzed by X-ray photoelectron spectroscopy using PHI Quantera SXM (Physical Electronics Inc. Chanhassen, MN) with monochromatic Al K $\alpha$  X-radiation. Electrical conductivity measurements were carried out by use of a customized four-point probe setup and Keithley 2636A (Cleveland, OH) dual channel sourcemeter in the ohmic region. Electrochemical cycling of the assembled cells was carried out using multichannel Battery Test Equipment (Arbin-BT2000, Austin, TX) at atmospheric conditions.

### **5.2.3 Half-cell assembly and testing**

The working electrodes were prepared by mixing fine powdered active material (Si(B)CN or SiCN or Si(B)CN-CNT) with acetylene black, and polyvinyl difluoride binder (1-methyl-2-pyrrolidinone) in the weight ratios of 8:1:1. Approximately 1 to 2 mg/cm<sup>2</sup> of the active material was then applied on the copper current collector foil by use of a doctor's blade and a film applicator. The coatings were then dried at 100°C for 12 hours in an inert environment before using it as an electrode. Pure lithium metal acted as both the counter and reference electrode. The 2032 type cells were assembled crimped and closed in a Argon filled glovebox. A 24  $\mu$ m thick monolayer insulating membrane (Celgard) acted as the separator and approximately 1 mL electrolyte solution of 1M LiPF<sub>6</sub> (Alfa Aesar) dissolved in (1:1 v/v) dimethyl carbonate: ethylene carbonate was used as the electrolyte. The cells were tested in the voltage range of 10 mV to 2.5 V or 3 V at either 50 or 100 mA/g during both discharge and charge half cycles. For post-test

characterization the cells were disassembled in the glovebox and the electrodes were washed several times with dimethyl carbonate to get rid of excess electrolyte.

## 5.3 Results and Discussion

### 5.3.1 Electrochemical cycling results

Fig. 5-2a represents the first two-chronopotentiometric intercalation and deintercalation cycles of SiCN-1100 ceramic (complete polymer to ceramic conversion does not take place until 1000°C and hence 1100°C was the temperature of choice). The first cycle discharge and charge capacities were 99.4 mAh/g and 13.2 mAh/g that dropped to 25.9 mAh/g and 16.5 mAh/g, respectively in the second cycle. This drop in electrochemical capacity is typical of SiCN prepared from the polyureasilazane (Ceraset™) precursor [4]. Thus, resulting in a very high first cycle loss (ICL) of 86.6 % with a voltage hysteresis of 0.77 V. While the Si(B)CN-1100 ceramic specimen synthesized and cycled under similar conditions (Fig. 5-2c), showed a higher first discharge (241.9 mAh/g) and charge (98.5 mAh/g) capacities with a lower first cycle loss of 59.3 %. The Si(B)CN-CNT-1100 composite electrode showed further enhancement in the electrochemical capacity as compared with Si(B)CN and SiCN processed under similar conditions (Fig. 5-2e). A high reversible capacity (312.1 mAh/g) and relatively low first cycle loss (45.5 %) were observed.

The results were also the best when compared with other Si(B)CN-CNT specimen i.e., those processed at 800°C and 1500°C (Fig. 5-3). The dependence of electrochemical capacity on specimen pyrolysis temperature is similar to and is in agreement with recent electrochemical studies on SiCN and SiOC ceramics [4,14,16,29]. Moreover the electrochemical performance of Si(B)CN-CNT data showed enhanced reversible capacity and capacity retention after cycling as

compared to the SiCN and SiOC polymer derived ceramics and their composites reported earlier [20,21,29]. The initial cycle capacity values and other critical evaluation parameters like first cycle loss and capacity retention for SiCN and Si(B)CN electrodes are summarized in Table 5-1.

**Table 5-1:** Summary of electrochemical cycling data for various specimens. Error in the measurements is  $\pm 0.1$  %.

specimen	1 <sup>st</sup> discharge capacity (mAh/g)	1 <sup>st</sup> charge capacity (mAh/g)	first cycle loss (%)	charge capacity at (n <sup>th</sup> cycle)
SiCN-1100	99.4	13.2	86.6	24.8 (30)
Si(B)CN-800	52.8	19.5	63.1	20.7 (20)
Si(B)CN-1100	241.9	98.5	59.3	138.2 (30)
Si(B)CN-1500	48.1	16.5	65.7	20.2 (20)
Si(B)CN-CNT-800	815.4	314	61.5	237.3 (20)
Si(B)CN-CNT-1100	573.4	312.1	45.5	412.1 (30)
Si(B)CN-CNT-1500	613.5	212.4	65.4	190.7 (20)

Differentiated capacity with respect to voltage (dQ/dV) plots for SiCN, Si(B)CN and various Si(B)CN-CNT specimen are plotted in Figs. 5-1 (b, d, e) and Figs. 5-2(b and d). A dQ/dV peak position signifies the amount of Li-ions diffusing in or out of the host material at a given voltage. For SiCN electrode first cycle (Fig. 5-2b), major reduction peaks at  $\sim 50$  mV and  $\sim 0.28$  V suggests Li-ion intercalation in SiCN pores and free or graphitic carbon entities in SiCN ceramics, respectively [14,15]. The weak peak at 50 mV reappears in the second cycle. A small oxidation peak at  $\sim 0.39$  V was also observed for both first and second cycles. While for Si(B)CN

electrode (Fig. 5-2d), one strong reduction peak at ~30 mV indicate single reduction energy state for both first and second intercalation cycles.

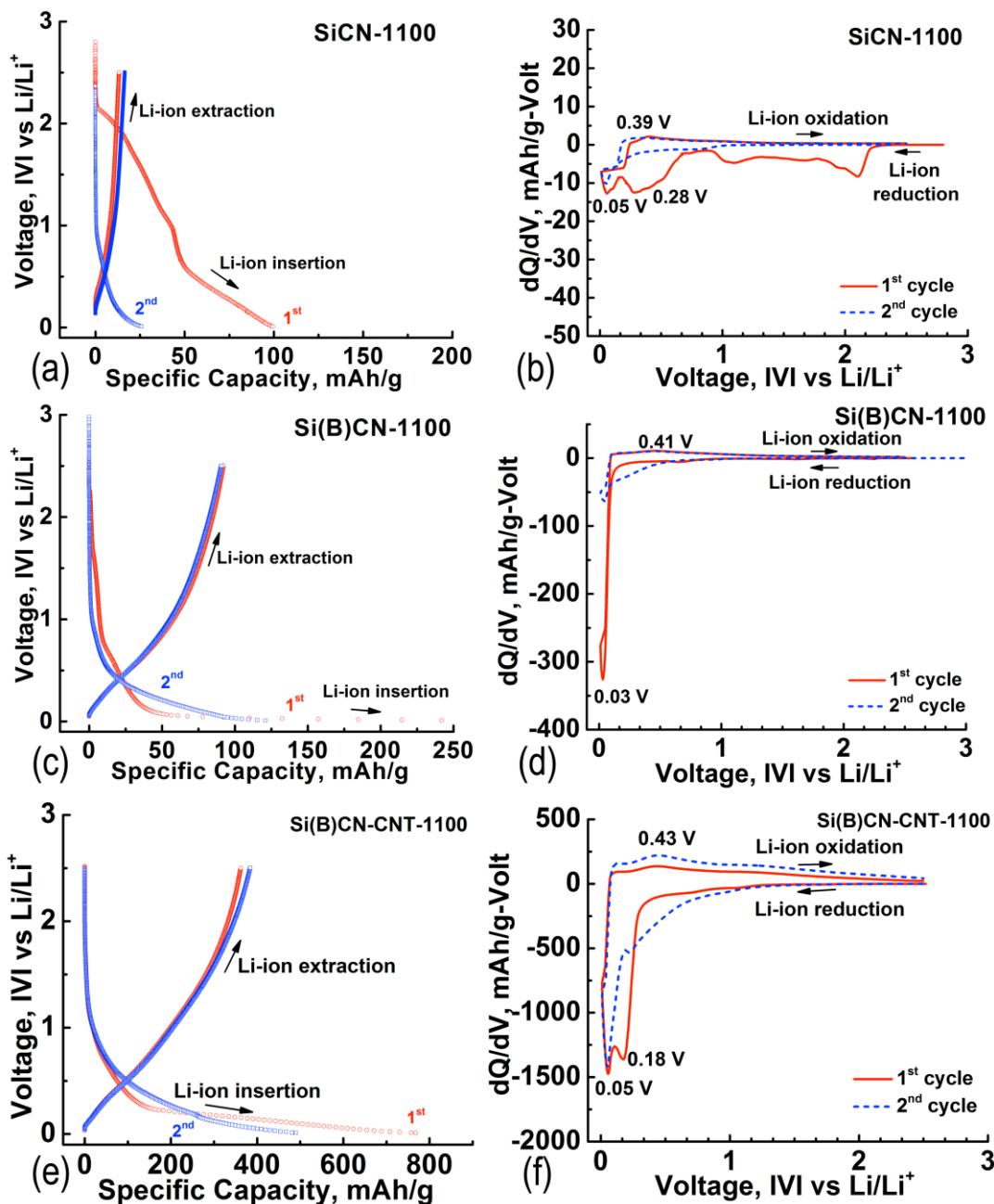


**Figure 5-2:** First and second electrochemical intercalation and deintercalation cycles and corresponding dQ/dV plots for (a)-(b) SiCN-1100, (c)-(d) Si(B)CN-1100, and (e)-(f) Si(B)CN-CNT-1100.

For all Si(B)CN-CNT specimens, dQ/dV plot showed multiple Li-ion reduction peaks majorly at ~50 mV, ~0.45 V and ~0.8 V (Fig. 5-2f and Fig. 5-3b, d). As observed in Fig. 5-2d, the reduction peak at ~50 mV is attributed to Si(B)CN ceramic, whereas the peaks at 0.45 V and 0.8 V suggests existence of multiple intercalation phases [5,30]. The additional peak observed for 800°C and 1500°C specimens at ~1.45 V, could have originated due to the presence of hydrogen (800°C) or crystalline nature (1500°C) of the specimen [4,15]. Broad peaks suggest availability of multiple Li-ion intercalation phases in the ceramic host material.

The variation in electrochemical cycling with changing pyrolysis temperature (Fig. 5-2e and Figs. 5-2 (a, c)), implies its dependence on molecular arrangement of ceramic constituents. This is not surprising since chemical co-ordinations in PDCs have been known to depend on the pyrolysis temperature of the precursor. Pyrolysis at 800°C have been known to result in a mix of organic and inorganic compounds along with the presence of excess hydrocarbons [31]. While, pyrolysis in the temperature range of (1000 to 1400) °C results in the formation of quaternary silicon possessing mixed bonds tetrahedral (Si-C-N), sp<sup>2</sup> bonded carbon chains and turbostratic B(C)N domains [23]. The electrochemical performance can thus be correlated with the carbon structure in the specimens. The presence of soft, disordered or hydrogenated carbon could be responsible for lithium ion irreversibility for the specimen synthesized at 800°C [13,20]. While for the specimen pyrolyzed at 1500°C or higher temperatures, Si(B)CN starts to undergo phase separation forming crystalline domains of Si<sub>3</sub>N<sub>4</sub>, SiC and BN that are inactive to lithium cycling (Fig. 5-7). Additionally, the abundance of dangling Si bonds for 800°C specimen as compared to the 1100°C specimens results in higher first cycle discharge capacity and higher irreversibility [16]. Hence, the 800 °C specimen (mostly disordered carbon) or crystalline nature of 1500°C

specimen (with turbostratic carbon or B(C)N) results in lower reversible electrochemical capacity and performance than the 1100°C specimen.

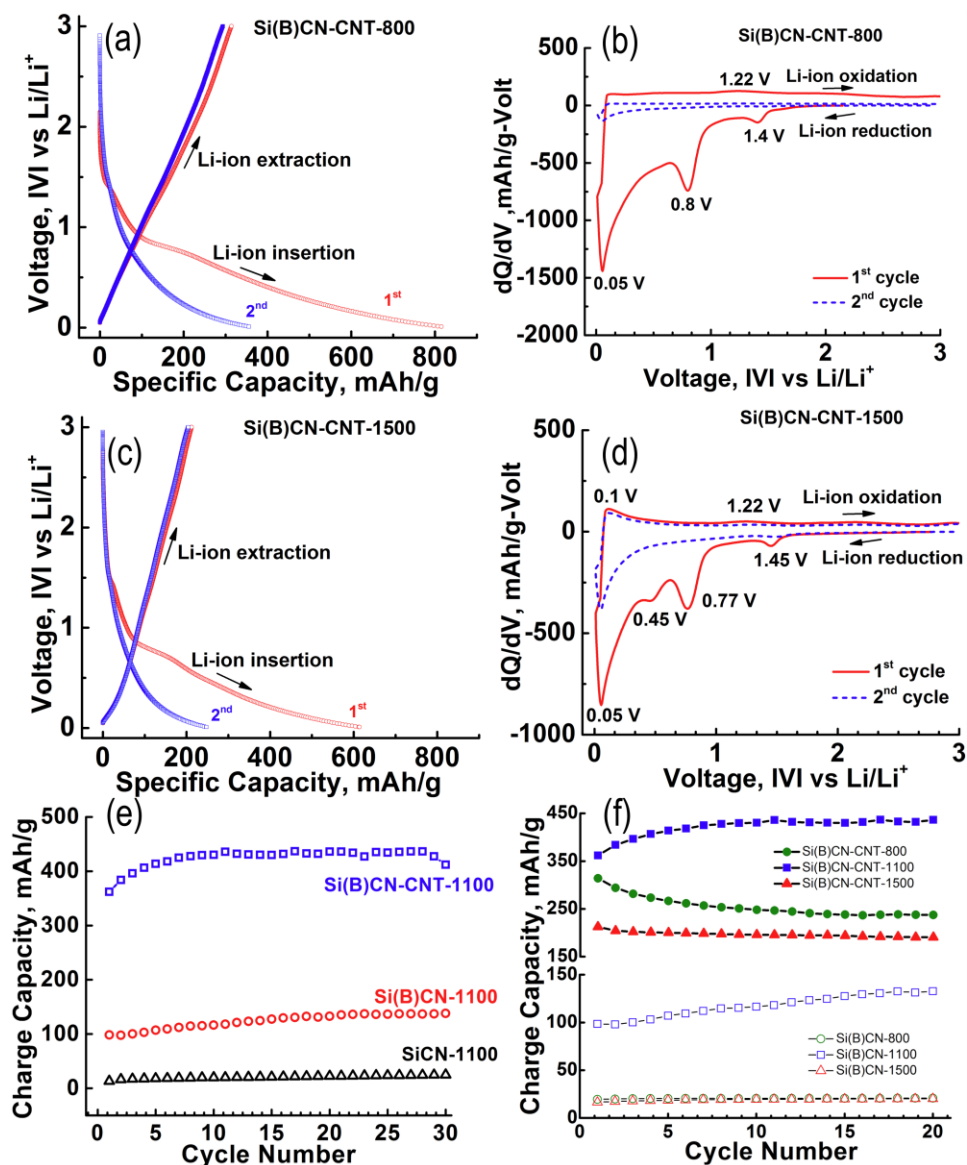


**Figure 5-3:** First two electrochemical voltage profiles and corresponding differentiated capacity with respect to the voltage for (a-b) Si(B)CN-CNT-800, (c-d) Si(B)CN-CNT-1500. Comparison of charge (reversible) capacity versus the cycle number for: (e) for SiCN-1100, Si(B)CN-1100 and Si(B)CN-CNT-1100 electrodes, and (f) various Si(B)CN electrodes showing the effect of pyrolysis temperature (20 cycles only).

The comparison of Li-ion reversible capacities of SiCN-1100, Si(B)CN-1100 and Si(B)CN-CNT-1100 specimens tested for 30 cycles are shown in Fig. 5-3e. Although the capacities for SiCN-1100 and Si(B)CN-1100 specimens are low, they retained the initial reversible capacity even after 30 cycles with more than 90 % cyclic efficiency. The electrochemical performance of MWCNT electrode (prepared and tested under same conditions) was studied (Fig. 5-4), verifying its low reversible capacity. It suggests that the enhanced electrochemical performance in the composite is a result of electrode architecture.

The effect of pyrolysis temperature on the long-term cycling performance of Si(B)CN-CNT specimens is presented in Fig. 5-3f (Please note that data for the 1100 °C specimens is repeated here for ease of comparison). It is apparent that inclusion of boron in SiCN ceramic results in both higher reversible capacity and better capacity retention. Further, the ab-initio approach of blending CNTs with ceramic precursor to form a core shell structure (Fig. 5-1) results in better performance on all critical performance parameters.

Galvanostatic Intermittent Titration Technique (GITT) performed to approximately determine and compare the solid state Li-ion diffusion coefficient ( $D_{Li}$ ) for the specimens and gain better understanding of higher capacity.  $D_{Li}$  for Si(B)CN-CNT-1100 specimen varied between  $2.3 \times 10^{-9}$  m<sup>2</sup>/sec to  $5.7 \times 10^{-8}$  m<sup>2</sup>/sec during delithiation and it varied between  $1.5 \times 10^{-8}$  m<sup>2</sup>/sec to  $4.9 \times 10^{-7}$  m<sup>2</sup>/sec during lithiation (Fig. 5-5). These values are about three orders of magnitude higher than those reported for other polymer derived ceramics (SiOC) materials ( $10^{-12}$  to  $10^{-14}$  m<sup>2</sup>/sec) [32]. Whereas for silicon,  $D_{Li}$  lies in the range of  $10^{-17}$  to  $10^{-14}$  m<sup>2</sup>/sec [5,33].



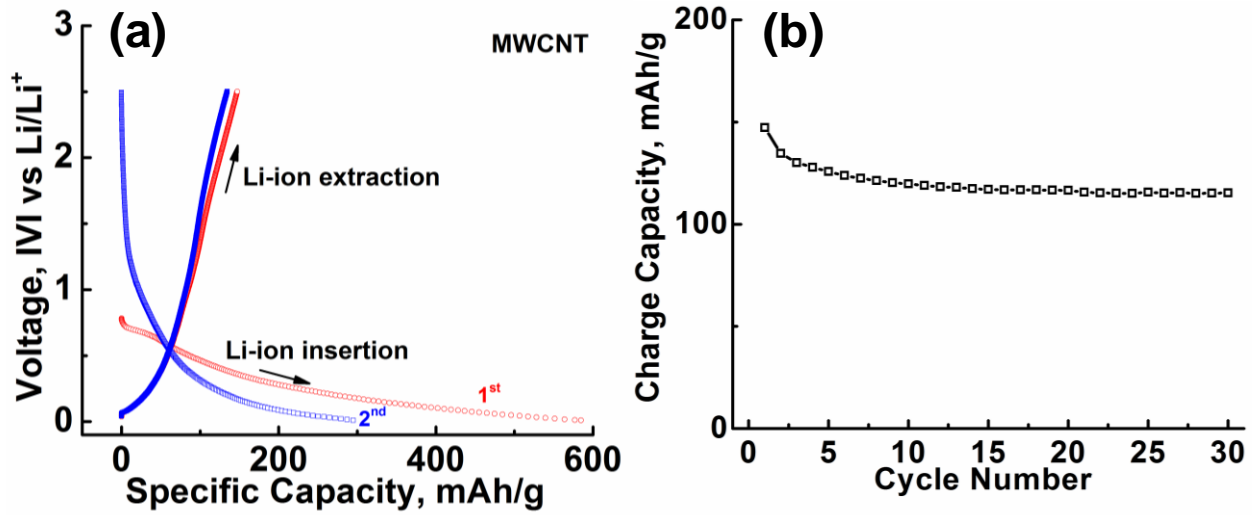


**Figure 5-4:** (a) First and second charge/discharge cycles for the MWCNT electrode, cycled at 100 mA/g, and (b) Charge capacity for the first 30 cycles for MWCNT electrode.

For the galvanostatic intermittent titration technique (GITT) Experiment, the solid-state lithium ion diffusion coefficients were determined using

$$D_{\text{Li}} = \frac{4}{\pi} \left( \frac{m_{\text{B}} V_{\text{M}}}{M_{\text{B}} S} \right)^2 \left( \frac{\Delta E_{\text{S}}}{\Delta E_{\text{t}}} \right)^2 \quad (5-1)$$

Where  $m_{\text{B}}$ ,  $V_{\text{M}}$ ,  $M_{\text{B}}$  and  $S$  are electrode mass, molar volume, molecular weight and surface area respectively and  $\Delta E_{\text{S}}$  and  $\Delta E_{\text{t}}$  are voltage steps as shown in Figure 5-5a.

GITT experiment was carried out on the best performing electrode i.e. Si(B)CN-CNT-1100. A current pulse of  $100 \text{ mA g}^{-1}$  for 15 min followed by a 4 hour of relaxation between pulses (until equilibrium is realized) was applied to the electrode for both during delithiation and lithiation. The diffusion coefficient ( $D_{\text{Li}}$ ) was thus calculated using the composite properties like weight of active material on electrode (2.5 mg), molecular weight (147.8 g/mol), molecular volume (64.2  $\text{cm}^3/\text{mol}$ ), surface area (1.6  $\text{cm}^2$ ) and voltages.

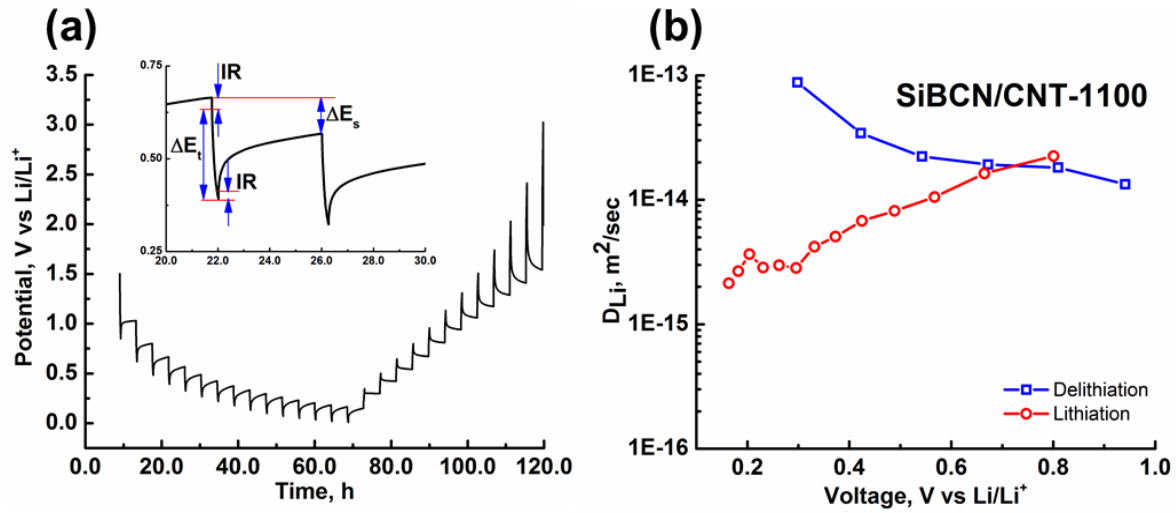


**Figure 5-5:** GITT Data: (a) Charge and discharge cycles with 15 min of current pulse at 100 mA/g followed by 4 h of relaxation for Si(B)CN-CNT- 1100 specimen and (b) calculated diffusion coefficient based on the relaxation steps at the corresponding voltages.

#### *Procedure for Measuring Electrical Resistivity of the Pellets*

Van der Pauw's Four Point Resistivity Measurement Method [36]: The specimen pellets used for these measurements were formed by cold pressing (4 ksi) the specimen powder for 30 seconds without using binder, conducting agent or other additives. The measurements were recorded in the ohmic region.

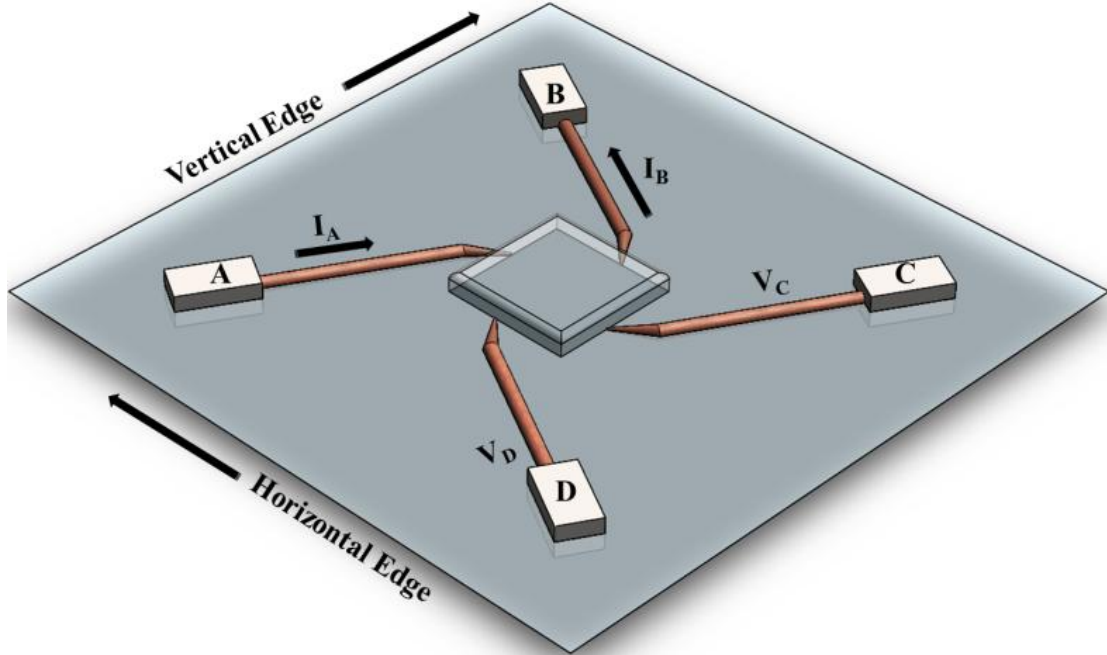


**Figure 5-6:** 4-point resistivity measurement test setup.

Step 1: Primary measurement

$R_{AB,CD}$  was defined as the resistance measured with current supplied between points A and B and consequently measuring the potential across points C and D. According to the Ohm's law

$R_{AB,CD}$  was found to be;

$$R_{AB,CD} = V_D - V_C / i_{AB} \quad (5-2)$$

$$\text{Similarly, } R_{BC,DA} = V_A - V_D / i_{BC} \quad (5-3)$$

Step 2: Reciprocal measurements

Ideally as  $R_{AB,CD} = R_{CD,AB}$ , the resistances measured along the edges of the samples were averaged for higher accuracy.

$$\text{Hence, } R_{\text{edge1}} = (R_{AB,CD} + R_{CD,AB}) / 2 \quad (5-4)$$

$$\text{and } R_{\text{edge2}} = (R_{BC,DA} + R_{DA,BC}) / 2 \quad (5-5)$$

Step 3: Reverse polarity measurements

For attaining higher precise measurements, the polarity at each points were reversed both at the current source and voltage measurement terminals.

$$\text{Hence, } R_{\text{edge1}} = (R_{\text{AB,CD}} + R_{\text{BA,DC}} + R_{\text{CD,AB}} + R_{\text{DC,BA}}) / 4 \quad (5-6)$$

$$\text{and } R_{\text{edge2}} = (R_{\text{BC,DA}} + R_{\text{CB,AD}} + R_{\text{DA,BC}} + R_{\text{AD,CB}}) / 4 \quad (5-7)$$

Finally, for the known thickness of the sample  $d$ , the resistivity was defined as;

$$\rho = \left( \frac{\pi d}{\ln 2} \right) \frac{R_{\text{edge1}} + R_{\text{edge2}}}{2} .f \quad (5-8)$$

Where  $f$  was defined as the function of the measured resistances.

Electrical conductivity measured using four point setup (Fig. 5-6), for the Si(B)CN pellets specimens synthesized at 800°C, 1100°C and 1500°C were  $1 \times 10^{-4}$  S/cm,  $8.7 \times 10^{-4}$  S/cm and  $1.3 \times 10^{-2}$  S/cm, respectively. Increased conductivity was observed for Si(B)CN-CNT powdered specimens synthesized at 800°C, 1100°C and 1500°C, which were  $7.6 \times 10^{-3}$  S/cm,  $2.3 \times 10^{-2}$  S/cm and  $1.2 \times 10^{-1}$  S/cm, respectively. Whereas the measuring instrument was found insensitive to insulating SiCN pellet specimen, but reasonable room temperature conductivities ( $\sim 10^{-7}$  to  $10^{-12}$  S/cm) reported elsewhere can be used for comparison [23]. For the dispersed (and dried) MWCNT powder specimen the electrical conductivity was approximately 0.25 S/cm. Thus, the increased electrical conductivity seems to influence the enhanced performance of Si(B)CN-CNT than Si(B)CN and SiCN, as easier flow of electrons in the electrode microstructure is desirable for easier and efficient Li-ion electrode cycling.

### ***X-Ray Diffraction Data (XRD)***

To characterize the crystalline nature of the specimens processed at higher temperature Bruker powder X-ray diffractometer (Madison, WI) using Cu-K $\alpha$  radiation and nickel filter was employed.

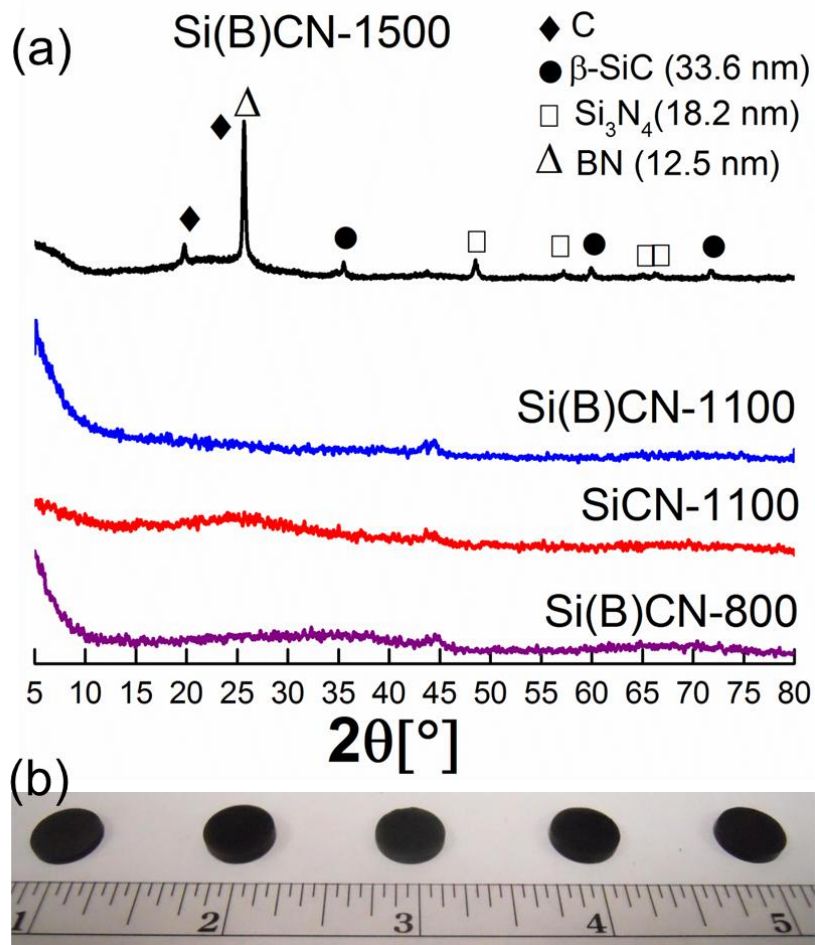


**Figure 5-7:** X-ray diffraction data for various Si(B)CN and SiCN pellet specimen, confirming the amorphous nature of the precursor-derived Si(B)CN ceramic for temperatures below 1500 °C.

### 5.3.2 Post-electrochemical cycling characterization

The cycled cells were disassembled and the electrodes were recovered for post electrochemical cycling analysis. SEM imaging was performed for SiCN, Si(B)CN and Si(B)CN-CNT electrodes and their surface morphology was compared with their respective precycled electrodes (Fig. 5-3). Precycled SiCN and Si(B)CN electrodes exhibited a particle (size <500 nm) like morphology. Interconnected particles with sponge like (fluffy) carbon black were also observed. The Si(B)CN-CNT electrodes were porous with a matrix like appearance.

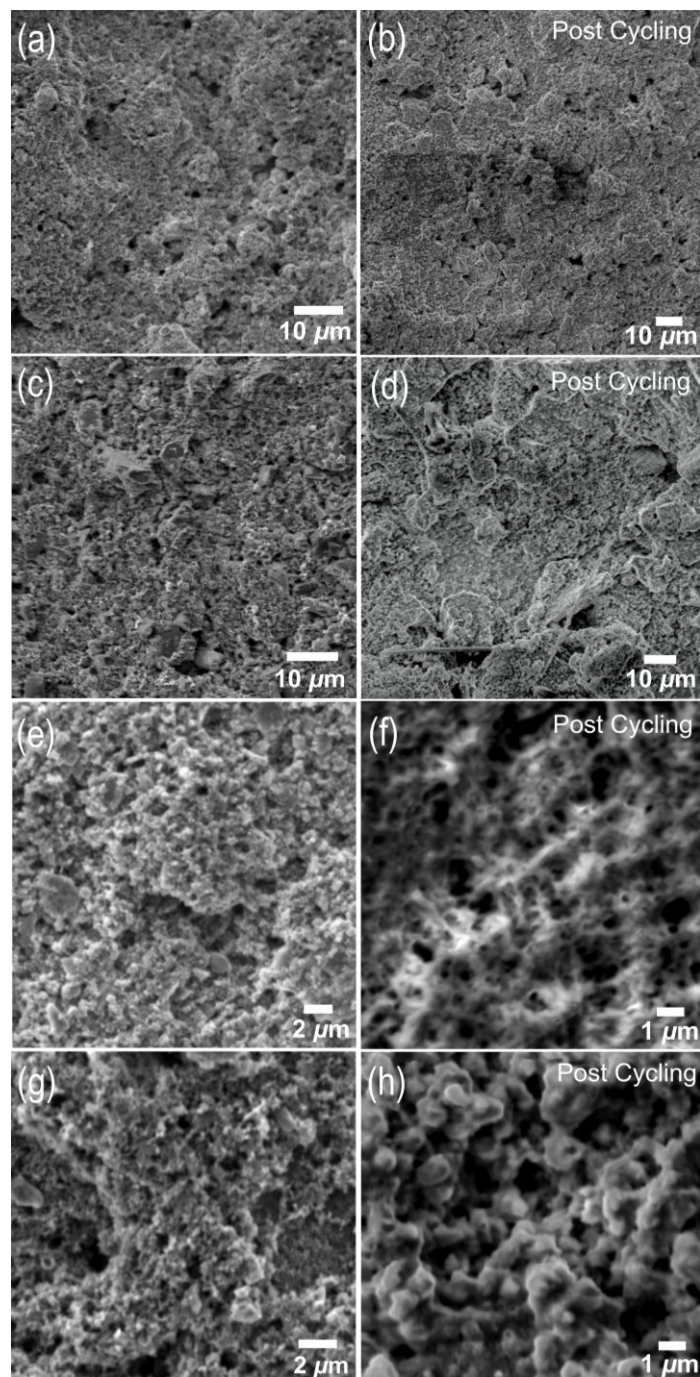


**Figure 5-8:** Comparison of SEM images of “as-prepared” electrodes with the cycled electrodes (disassembled in delithiated state) for (a, b) SiCN-1100 (after 30 cycles), (c, d) Si(B)CN-1100 (after 30 cycles), (e, f) Si(B)CN-CNT-800 (after 20 cycles), (g, h) Si(B)CN-CNT-1100 (after 30 cycles), and (i, j) Si(B)CN-CNT-1500 (after 30 cycles).

Remarkably, all cycled electrodes were largely intact with no obvious signs of delamination or pulverization. Unlike bulk silicon or thin films, where lithium cycling results in surface cracks due to volume expansion, absence of surface cracks in these electrodes suggested very stable cycling with minimal structural changes [5]. The cycled Si(B)CN-CNT-800, exhibited amorphous (soft) porous coating, whereas the cycled Si(B)CN-CNT-1500 specimen showed the formation of a few surface cracks. The Si(B)CN-CNT-1100 specimen showed the firmly integrated structure corroborating the best electrochemical performance results shown earlier. Presence of SEI (solid electrolyte interphase) layer looked more prominent on the Si(B)CN-CNT electrode surface than on either SiCN or Si(B)CN electrodes, as could be seen in the post-cycling SEM images.

### *X-Ray Photoelectron Spectroscopy*

Chemical composition on the surface of the specimens was analyzed by X-ray photoelectron spectroscopy using PHI Quantera SXM (Physical Electronics Inc. Chanhassen, MN) with monochromatic Al K $\alpha$  X-radiation (beam size <9  $\mu$ m).

**Table 5-2:** Summary of surface elemental composition of various specimen (atomic percent) used in this study all atomic percentage measurements are accurate up to approximately 15%

specimen	Si	B	C	N	O
Si(B)CN-800	24.9	4.6	32.4	19.8	18.4
Si(B)CN-1100	24.4	6.1	24.6	19.5	25.4
Si(B)CN-1500	23.2	5.5	19.7	14.3	37.4
Si(B)CN-CNT-800	13.8	18.2	37.1	17.8	13
Si(B)CN-CNT-1100	9.9	6.5	52.9	2.9	27.7
Si(B)CN-CNT-1500	7.9	17.7	39.9	27	7.5

*XPS: Post-electrochemical testing*

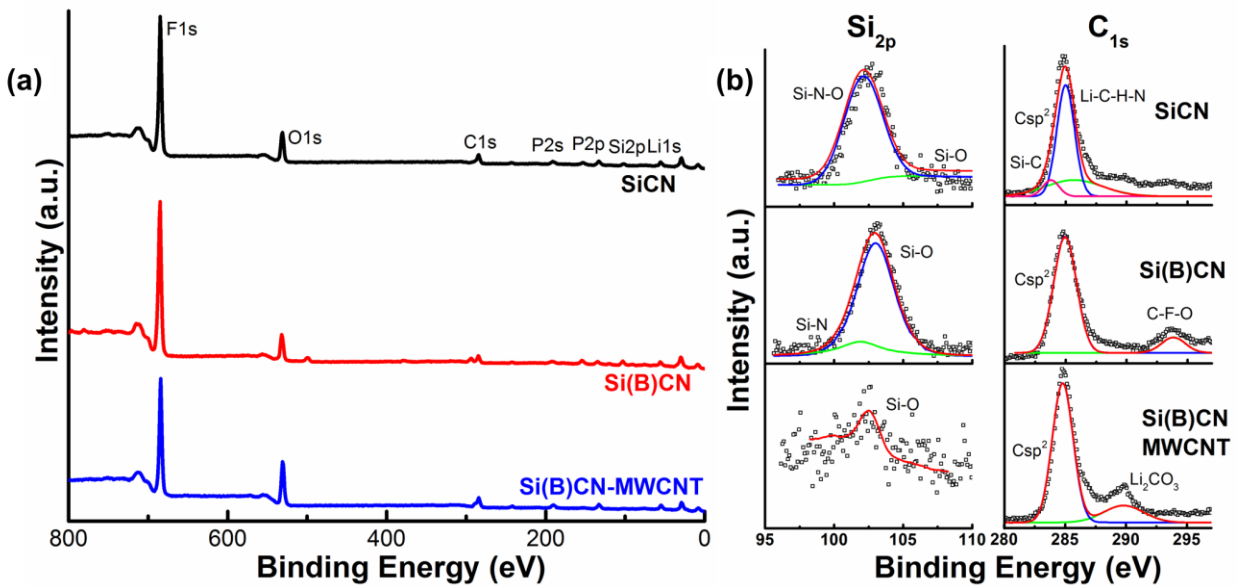


**Figure 5-9:** (a) Elemental survey (top) and (b) high-resolution scan (bottom) for SiCN-1100, Si(B)CN-1100, and Si(B)CN-CNT cycled electrode specimens.

XPS survey scan performed on disassembled SiCN-1100, Si(B)CN-1100 and Si(B)CN-CNT-800 electrodes, revealed presence of Si, C, Li, O, F and P elements (Fig. 5-9). As shown in Fig. 5-9, for the SiCN electrode, the Si<sub>2p</sub> elemental peak observed at ~102.5 eV can be deconvoluted into peaks at 103.2 eV and 102.1 eV due to Si-O and Si-N-O type bonds, respectively [34]. The C<sub>1s</sub> peak at ~285 eV can be assigned to peaks at 285.7 eV, 285 eV and 283.8 eV due to sp<sup>2</sup> carbon, Li-C-H-N, and Si-C, respectively. For the Si(B)CN electrode, the sharp peak at ~102.5 eV can be fitted by two peaks at 103 eV (Si-O) and 101.9 eV (Si-N). While the lower energy peak in C<sub>1s</sub> scan at ~284.9 eV is assigned to sp<sup>2</sup> bonded carbon and the higher energy peak at 293.7 eV is most likely due to the C-F-O bonds from the SEI layer [35]. The Si<sub>2p</sub> elemental scan for the Si(B)CN-CNT electrode showed a less intense peak at ~102.5 eV which can originate from Si-O-N type bonds. The lower energy peak in the C<sub>1s</sub> scan at ~284.8 eV is assigned to sp<sup>2</sup> bonded



carbon whereas the higher energy peak at ~289.8 eV is due to  $\text{Li}_2\text{CO}_3$  most likely from SEI layer that gets formed on the electrode's surface.

## **5.4 Conclusion**

Si(B)CN ceramic derived from controlled thermal decomposition (pyrolysis) of boron-modified polyureasilazane showed improved Li-ion storage ability and sustained capacity when utilized as battery electrode. Further, nanocomposites prepared by inclusion of CNTs in liquid phase polymeric precursor resulted in core-shell Si(B)CN-CNT morphology, which further enhanced the electrochemical capacity by four folds. This improved behavior is attributed to the structurally porous and thermodynamically stable Si(B)CN shell and electrically conducting CNT core.

## 5.5 References

1. P.V. Kamat, "Electrochemistry in the Driver's Seat," *Journal of Physical Chemistry Letters*, **1**, 2220-2221 (2010).
2. P.V. Kamat, "Graphene-Based Nanoassemblies for Energy Conversion," *Journal of Physical Chemistry Letters*, **2**, 242-251 (2011).
3. A. Manthiram, "Materials Challenges and Opportunities of Lithium Ion Batteries," *Journal of Physical Chemistry Letters*, **2**, 176-184 (2011).
4. D. Ahn and R. Raj. "Cyclic stability and C-rate performance of amorphous silicon and carbon based anodes for electrochemical storage of lithium," *Journal of Power Sources*, **196**, 2179-2186 (2011).
5. R. Ruffo, S.S. Hong, C.K. Chan, R.A. Huggins and Y. Cui. "Impedance Analysis of Silicon Nanowire Lithium Ion Battery Anodes," *Journal of Physical Chemistry C*, **113**, 11390-11398 (2009).
6. J. Luo, X. Zhao, J. Wu, H. Jang, H. Kung and J. Huang. "Crumpled Graphene-Encapsulated Si Nanoparticles for Lithium Ion Battery Anodes," *Journal of Physical Chemistry Letters* **3**, 1824-1829 (2012).
7. J. Bill and F. Aldinger. "Precursor-Derived Covalent Ceramics," *Advanced Materials*, **7**, 775-787 (1995).
8. M. Weinmann, J. Schuhmacher, H. Kummer, S. Prinz, J. Peng, H. Seifert, K. Mueller, J. Bill and F. Aldinger, "Synthesis and thermal behavior of novel Si-B-C-N ceramic precursors," *Chemistry of Materials*, **12**, 623-632 (2000).
9. D. Ahn and R. Raj. "Thermodynamic measurements pertaining to the hysteretic intercalation of lithium in polymer-derived silicon oxycarbide," *Journal of Power Sources*, **195**, 3900-3906 (2010).

10. Y. Feng, "Electrochemical properties of heat-treated polymer-derived SiCN anode for lithium ion batteries," *Electrochimica Acta*, **55**, 5860-5866 (2010).
11. H. Fukui, N. Nakata, K. Dokko, B. Takemura, H. Ohsuka, T. Hino and K. Kanamura, "Lithiation and Delithiation of Silicon Oxycarbide Single Particles with a Unique Microstructure," *ACS Applied Materials & Interfaces*, **3**, 2318-2322 (2011).
12. H. Fukui, H. Ohsuka, T. Hino and K. Kanamura. "Polysilane/Acenaphthylene Blends Toward Si-O-C Composite Anodes for Rechargeable Lithium-Ion Batteries," *Journal of Electrochemical Society*, **158**, A550-A555 (2011).
13. M. Graczyk-Zajac, G. Mera, J. Kaspar and R. Riedel. "Electrochemical studies of carbon-rich polymer-derived SiCN ceramics as anode materials for lithium-ion batteries," *Journal of the European Ceramic Society*, **30**, 3235-3243 (2010).
14. J. Kaspar, G. Mera, A.P. Nowak, M. Graczyk-Zajac and R. Riedel. "Electrochemical study of lithium insertion into carbon-rich polymer-derived silicon carbonitride ceramics," *Electrochim. Acta*, **56**, 174-182 (2010).
15. V. Liebau-Kunzmann, C. Fasel, R. Kolb and R. Riedel. "Lithium containing silazanes as precursors for SiCN : Li ceramics - A potential material for electrochemical applications," *Journal of the European Ceramic Society*, **26**, 3897-3901 (2006).
16. D. Su, Y. Li, Y. Feng and J. Jin. "Electrochemical Properties of Polymer-Derived SiCN Materials as the Anode in Lithium Ion Batteries," *Journal of American Ceramic Society*, **92**, 2962-2968 (2009).
17. H. Tamai, H. Sugahara and H. Yasuda. "Preparation of carbons from pitch containing polysilane and their anode properties for lithium-ion batteries," *Journal of Material Science Letters*, **19**, 53-56 (2000).

18. Y. Feng, G. Du, X. Zhao and E. Yang. "Preparation and electrochemical performance of SiCN-CNTs composite anode material for lithium ion batteries," *Journal of Applied Electrochemistry*, **41**, 999-1002 (2011).
19. Y. Feng, N. Feng and G. Du. "Preparation and Electrochemical Performance of Polymer-derived SiCN-graphite Composite as Anode Material for Lithium Ion Batteries," *International Journal of Electrochemical Science*, **7**, 3135-3140 (2012).
20. M. Graczyk-Zajac, C. Fasel and R. Riedel. "Polymer-derived-SiCN ceramic/graphite composite as anode material with enhanced rate capability for lithium ion batteries," *Journal of Power Sources*, **196**, 6412-6418 (2011).
21. R. Kolb, C. Fasel, V. Liebau-Kunzmann and R. Riedel. "SiCN/C-ceramic composite as anode material for lithium ion batteries," *Journal of the European Ceramic Society*, **26**, 3903-3908 (2006).
22. R. Bhandavat and G. Singh, "Synthesis, Characterization and High Temperature Stability of Si(B)CN Coated Carbon Nanotubes Using a Boron-modified Poly(ureamethylvinyl)silazane Chemistry," *Journal of American Ceramic Society*, **95**, 5, 1536-1543 (2012).
23. A.M. Hermann, Y.T. Wang, P.A. Ramakrishnan, D. Balzar, L. An, C. Haluschka and R.Riedel, "Structure and electronic transport properties of Si-(B)-C-N ceramics," *Journal of American Ceramic Society*, **84**, 2260-2264 (2001).
24. S. Sarkar, Z. Gan, L. An and L. Zhai. "Structural Evolution of Polymer-Derived Amorphous SiBCN Ceramics at High Temperature," *Journal of Physical Chemistry C*, **115**, 24993–25000 (2011)

25. R. Bhandavat, W. Kuhn, E. Mansfield, J. Lehman and G. Singh, "Synthesis of Polymer-derived Ceramic Si(B)CN-Carbon Nanotube Composite by Microwave Induced Interfacial Polarization," *ACS Applied Materials and Interfaces*, **4**, 1, 11-16. (2012).
26. J.H. Lehman, K.E. Hurst, G. Singh, E. Mansfield, J.D. Perkins and C.L. Cromer. "Core-shell composite of SiCN and multiwalled carbon nanotubes from toluene dispersion," *Journal of Material Science*, **45**, 4251-4254 (2010).
27. S.R. Shah and R. Raj. "Nanodevices that explore the synergies between PDCs and carbon nanotubes," *Journal of the European Ceramic Society*, **25**, 243-249 (2005).
28. G. Singh, S. Priya, M.R. Hossu, S.R. Shah, S. Grover, A. R. Koymen and R.L. Mahajan, "Synthesis, electrical and magnetic characterization of core-shell silicon carbo-nitride coated carbon nanotubes," *Materials Letters*, **63**, 2435-2438 (2009).
29. P. Dibandjo, M. Graczyk-Zajac, R. Riedel, V.S. Pradeep and G.D. Soraru. "Lithium insertion into dense and porous carbon-rich polymer-derived SiOC ceramics," *Journal of the European Ceramic Society*, **32**, 2495-2503 (2012).
30. B.J. Landi, R.A. Dileo, C.M. Schauerman, C.D. Cress, M.J. Ganter and R.P. Raffaele. "Multi-Walled Carbon Nanotube Paper Anodes for Lithium Ion Batteries," *Journal of Nanoscience and Nanotechnology*, **9**, 3406-3410 (2009).
31. P. Greil, "Polymer derived engineering ceramics," *Advanced Engineering Materials*, **2**, 339-348 (2000).
32. D. Ahn, Electrochemical Insertion of Lithium into Polymer Derived Silicon Oxycarbide and Oxycarbonitride Ceramics. Ph.D. Thesis, University of Colorado at Boulder, 2010

33. T.L. Kulova, A.M. Skundin, Y.V. Pleskov, E.I. Terukov and O.I. Kon'kov. "Lithium insertion into amorphous silicon thin-film electrodes," *Journal of Electroanalytical Chemistry*, **600**, 217-225 (2007).
34. C.D. Wagner, A.V. Naumkin, A.V. Vass, J.W. Allison, C.J. Powell and R. J. Rumble, NIST X-ray Photoelectron Spectroscopy Database [Online], August 27, 2007. <http://srdata.nist.gov/xps/> (accessed June 06, 2012).
35. K. Tasaki and S.J. Harris. "Computational Study on the Solubility of Lithium Salts Formed on Lithium Ion Battery Negative Electrode in Organic Solvents," *Journal of Physical Chemistry C*, **114**, 8076-8083 (2010).
36. Pauw V.D., L.J. *Philips Res. Repts.*, **13**, 1, 1-9 (1958).

## Chapter 6 - Stable and Efficient Li-ion Battery Anodes Prepared From Polymer-Derived Silicon Oxycarbide-Carbon Nanotube Shell/Core Composites

### Abstract

We demonstrate synthesis and electrochemical performance of polymer-derived silicon oxycarbide-carbon nanotube (SiOC-CNT) composites as a stable lithium intercalation material for secondary battery applications. Composite synthesis was achieved through controlled thermal decomposition of 1,3,5,7-tetramethyl 1,3,5,7-tetravinyl cyclotetrasiloxane (TTCS) precursor on carbon nanotubes surfaces that resulted in formation of shell/core type ceramic SiOC-CNT architecture. Li-ion battery electrode (prepared at a loading of  $\sim 1.0 \text{ mgcm}^{-2}$ ) showed stable charge capacity of  $686 \text{ mAhg}^{-1}$  even after 40 cycles. The average coulombic efficiency (excluding the first cycle loss) was 99.6 %. Further, the post electrochemical imaging of the disassembled cells showed no apparent damage to the electrode surface, highlighting improved chemical and mechanical stability of these composites. Similar trend was observed in the rate capability tests, where the SiOC-CNT electrode (with 5 wt.% loading in TTCS) again showed stable performance, completely recovering the first cycle capacity of  $\sim 750 \text{ mAhg}^{-1}$  when the current density was brought back to  $50 \text{ mAhg}^{-1}$  after cycling at higher current densities.

---

Submitted as

Bhandavat, R. & Singh, G. (2013). Stable Li-ion Battery Anodes Prepared From Polymer-Derived Silicon Oxycarbide-Carbon Nanotube Shell/Core Composites, *Journal of Physical Chemistry C*.

## 6.1 Introduction

A variety of silicon-based composites are currently being explored as negative electrode materials for lithium ion secondary batteries due to silicon's high lithium alloyability [1-4]. However, one major issue or limiting factor with silicon-based electrodes is the large amount of volume changes associated with insertion and extraction of lithium-ions as the battery is charged/discharged. This results in pulverization (amorphization), cracking (exposing new silicon surface to solvent ions, resulting in formation of an unstable passivating film) and eventual failure of the electrode (due to loss of electrical contact between active material and current collector). To mitigate these effects, several unique hybrid chemistries (that include Si/graphene and Si/carbon nanocomposites) and novel anode architectures (vertically aligned nanowires and core/shell structures) have been proposed that have improved electrochemical cycling in these materials for up to hundreds of cycles [5-9]. Nonetheless, these nanocomposite anodes (or batteries) usually have low absolute capacities as the amount of active material in the anode has been low (approximately  $0.02$  to  $0.1 \text{ mgcm}^{-2}$ ) and therefore may not be suitable for powering hybrid vehicles or other large devices that require more power and energy (in other words, applications requiring thicker anode) [10-11].

High temperature glass ceramics prepared from thermal decomposition of certain organosilicon polymers (such as polysiloxanes, polysilazanes etc.) have been shown to possess many functional properties including their high temperature thermal and chemical stability [12-16]. A more interesting and recently discovered behavior is their ability to cycle lithium at potentials ranging from 0 to 3 V (versus Li/Li+). Recent reports suggest that this behavior could be due to their "open" amorphous structure which predominantly consists of  $\sim(1 \text{ to } 2)$  nm size domains of silica wrapped by graphitic carbon chains [16]. Presence of nanovoids along with silicon and carbon dangling bonds could also provide ample sites for Li-insertion [17-18]. Unfortunately, the



Si/O/C family of polymer-derived ceramics (PDCs) that shows high Li-intercalation capacity is also the one that is electrically insulating, which ultimately results in poor charge transfer characteristics and voltage hysteresis [17-21].

One way to improve the electrochemical performance of Si-O-C based anodes would be to interface the starting polymeric precursor with conducting fillers such as carbon nanotubes (CNTs), which up on pyrolysis would result in electrical conducting and mechanically robust ceramic-CNT shell/core composite, thereby improving rate capability and resistance to fatigue associated with repeated cycling of Li-ions (particularly for thicker electrodes), respectively. Moreover, introduction of CNTs (weight density  $\sim 2.3 \text{ g cm}^{-3}$ ) in to SiOC is not likely to affect the overall density of the composite since SiOC weight density also lies in the same range ( $\sim 1.8$  to  $2.3 \text{ g cm}^{-3}$ ), thanks to its “open” amorphous structure [22]. Hence, in order to test this hypothesis we synthesized core-shell SiOC-CNT composite structure (with varying shell thickness) and studied its electrochemical performance as an active electrode material in a Li-ion half-cell. Determination of appropriate amount of CNTs in the composite was important as excess amounts of CNTs can result in undesirably high irreversibility, which is typically associated with trapping of Li-ions in-between the concentric CNT walls [23-24].

## **6.2 Experimental Procedure**

### **6.2.1 Material Preparation**

Synthesis of SiOC-CNT composite was performed in a manner similar to other PDC-CNT composites described in our recent work [25-27]. Briefly, the ‘as-obtained’ 1 gram of MWCNTs (C150 HP, Bayer AG) were dispersed in 1 gram L 1 sodium dodecyl benzene sulfonic acid (NaDDBS) (Sigma Aldrich) aqueous solution, followed by sonication for 1 h to remove any unwanted agglomerations. The dispersed nanotubes were then washed repeatedly with DI water

to eliminate any excess NaDDBS or related impurities, followed by slow drying that yielded a dry CNT mass.

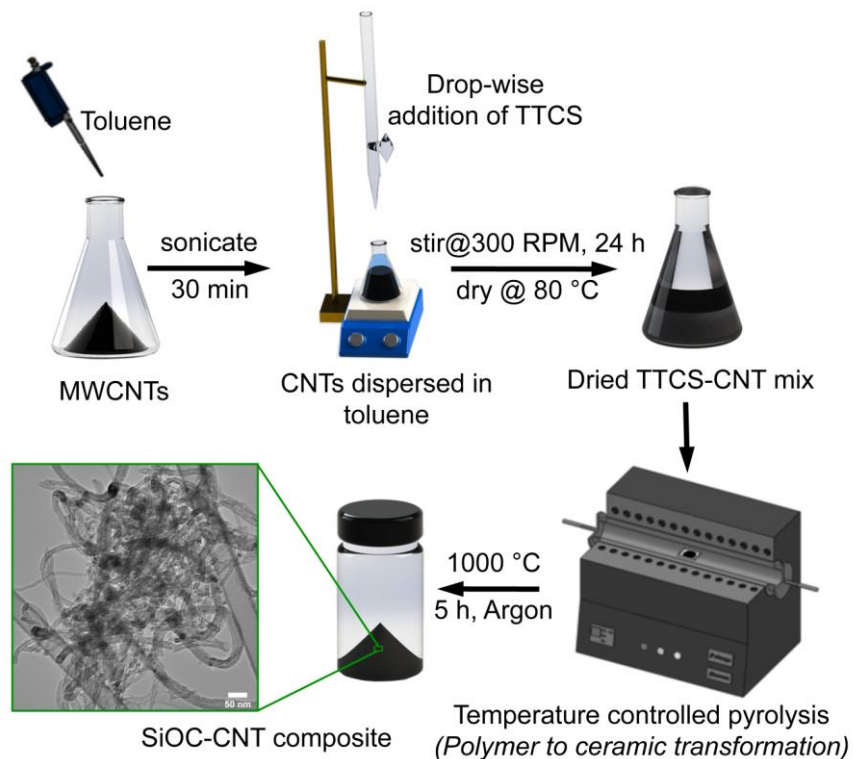


**Figure 6-1:** Schematic displaying the stepwise procedure for synthesis of SiOC (shell)-CNT (core) composite. TTCS is the polymeric precursor for SiOC ceramic.

These dried nanotubes (approximately 1 g) were then dispersed in toluene (125 mL) for further functionalization with the SiOC polymeric precursor. A mix of commercially sourced 1,3,5,7-tetramethyl 1,3,5,7-tetravinyl cyclotetrasiloxane (TTCS) (Gelest) with 1 wt. % dicumyl peroxide (Sigma Aldrich) was then slowly added (predetermined based on MWCNT to TTCS ratio) and stirred in the CNT-toluene dispersion (shown with the help of a schematic in Fig. 6-1). After stirring the mix for approximately 24 h, it was dried in inert atmosphere at 80 °C. The dried mix was then transferred to a tube furnace where it was heated to 400 °C for 4 h for cross-linking of

the precursor, followed by a pyrolysis at 1000 °C for 5 h in argon atmosphere at 5 °C min<sup>-1</sup> heating and cooling rates to yield SiOC-CNT composite (Fig. 6-1). Three specimens with 5, 8 and 10 wt. % of CNTs in TTCS were prepared; these specimens are labeled as SiOC-CNT-5, SiOC-CNT-8, and SiOC-CNT-10, respectively.

While the SiOC powder specimen was prepared following standard procedures described in the literature [16]. Briefly, liquid TTCS was cross-linked in a vertical tube furnace at approximately 300 °C in argon for 4 h resulting in an infusible mass, which was ball milled for 2 h and pyrolyzed at 1000 °C for 5 h in Ar resulting in a fine black SiOC powder.

### **6.2.2 Instrumentation**

Scanning electron microscopy (SEM) imaging of SiOC-CNT composite bulk and electrode specimens was performed by use of a 10 kV Carl Zeiss EVO Low-Vacuum SEM. Transmission electron microscopy (TEM) was carried out using 100 kV Philips CM 100. Fourier Transform Infrared (FT-IR) spectra were collected using liquid nitrogen cooled Thermo-Nicolet Nexus 870 FT-IR spectrometer in the diffuse reflectance mode. The crushed powder specimens were mixed with KBr powder, prior to collecting spectra. X-ray diffraction (XRD) was performed by use of Bruker D8 Advance powder X-ray diffractometer operating at room temperature, with Cu K $\alpha$  radiation and nickel filter. The pyrolyzed samples were finely crushed with mortar and pestle for analysis. Thermogravimetric analysis (TGA) was performed by use of Shimadzu 50 TGA (limited to 1000 °C). Sample weighing, approximately 5 mg, was heated in a platinum pan at a rate of 10 °C min<sup>-1</sup> in air flowing at 20 mLmin<sup>-1</sup>. Electrochemical characterization of the assembled coin cells was carried out using multichannel Battery Test setup (Arbin-BT2000) at atmospheric conditions.

### **6.2.3 Half-cell assembly and testing**

The synthesized composites were crushed (hand crushed or ball milled) to obtain a fine powder followed by mixing with acetylene black and polyacrylic acid as binder in the ratio of 8:1:1 by weight and about the same volume of 1-methyl 2-pyrrolidinone for providing the appropriate viscosity to the slurry. 127  $\mu\text{m}$  stepped applicator blade was then used to spread the slurry on to a 15  $\mu\text{m}$  thick copper foil (current collector). The film was then dried at approximately 80  $^{\circ}\text{C}$  overnight in inert conditions. Circles of 9/16" diameter were punched and weight of the active material in the film was measured. The 2032 sized coin-cells were then assembled in a argon filled glovebox. Composite coated on copper foil (punched circle) acted as the electrode (i.e., negative or working electrode) while pure lithium metal acted as the cathode (i.e., reference/counter electrode). A monolayer polypropylene membrane (Celgard) soaked in electrolyte acted as the separator between the two electrodes. The electrolyte consisted of 1M LiPF<sub>6</sub> (Alfa Aesar) lithium salt in (1:1 v/v) dimethyl carbonate (DMC): ethylene carbonate (EC) solvent. The assembled batteries were tested in the voltage range of 10 mV to 2.5 V at constant currents both during discharge (insertion) and charge (extraction) half cycles. The specific capacities mentioned are calculated based on the weight of active material only. Since these ceramics are mostly amorphous and have several energy levels available for Li-insertion/extraction, 'C-rate' here is defined (such that it gives time required to insert or extract the charge at a given value of the current) as the ratio of applied current (constant for both charge/discharge) to the observed electrochemical capacity.

### **6.3 Results and Discussion**

The SEM (Fig. 6-2 a, d, g) and TEM (Fig. 6-2 b ,e ,h) imaging revealed formation of a shell/core composite nanowire structure with thicker nanowires being formed at lower CNT loading in the

polymeric precursor (statistical variation in nanowire diameter is shown in Fig. 6-2 c, f, i). For the SiOC-CNT-5 specimen, some agglomerated SiOC particles along with SiOC coated CNTs were observed (Fig. 6-2a). While the nanotube core was more evident in SiOC-CNT-8 and SiOC-CNT-10 specimens, where the polymeric precursor was perhaps just sufficient to form a monolayer thick SiOC shell on the CNT sidewalls.

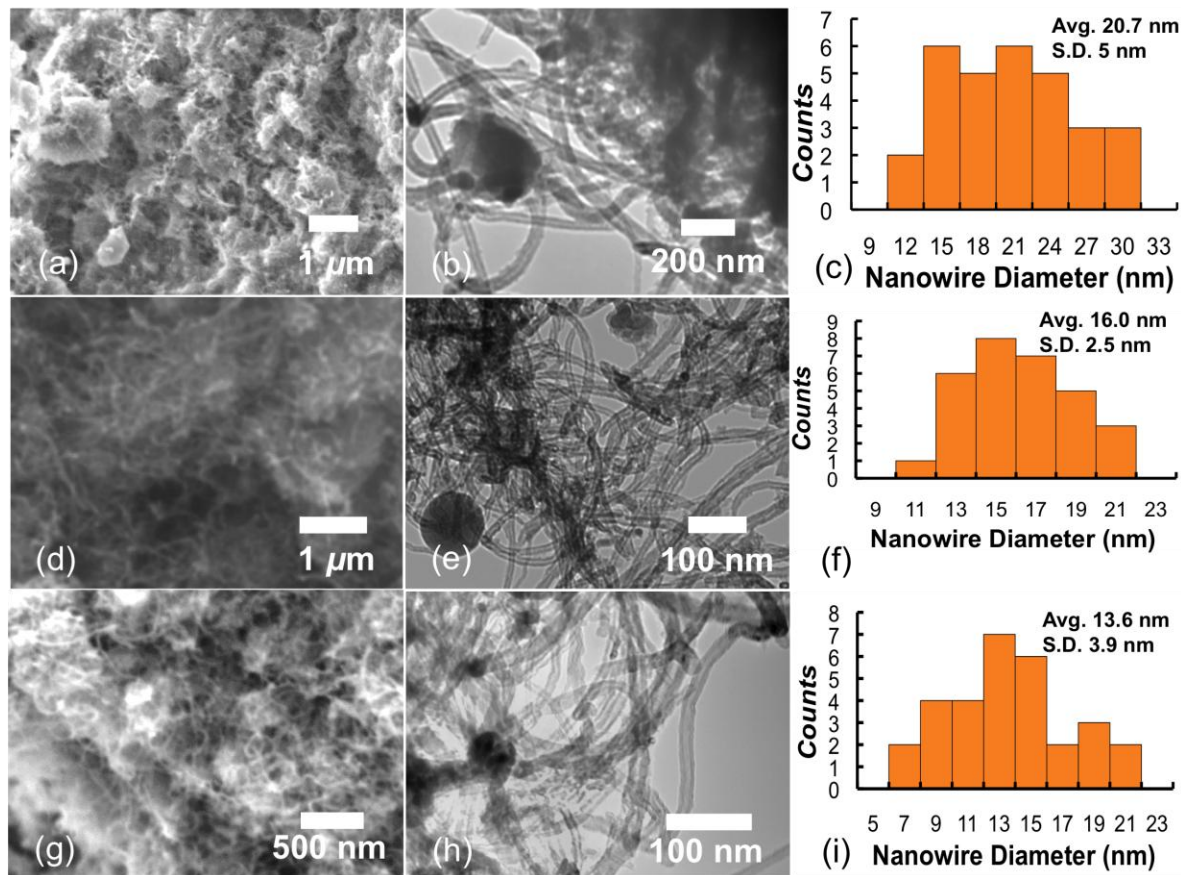


**Figure 6-2:** SEM, TEM image and Histogram (size distribution) of various SiOC/CNT composites prepared in this study: (a, b, c) SiOC/CNT-5, (d, e, f) SiOC/CNT-8 and (g, h, i) SiOC/CNT-10, respectively. Thicker composite nanowires were observed for composites with lower CNT loading.

This increasing amount of nanotubes in the ceramic composite became even more prominent when imaged at higher magnifications in a TEM (Fig. 6-2b, e, h). The polymer to ceramic transformation on the surface of a carbon nanotube is shown with the help of a schematic in Fig. 6-3a. Further, XRD results confirmed that the ceramic was indeed amorphous when processed at 1000 °C, which is one of the hallmarks of PDCs (Fig. 6-3b).

The FT-IR spectroscopy of SiOC and SiOC-CNT specimens (Fig. 6-3c) showed stretching of Si-O ( $3423\text{ cm}^{-1}$ ), Si-H ( $2314\text{ cm}^{-1}$ ), Si-O-Si ( $1384\text{ cm}^{-1}$ ), and C-H ( $2917\text{ cm}^{-1}$  to  $2877\text{ cm}^{-1}$ ) and bending of Si-CH<sub>3</sub> ( $1607\text{ cm}^{-1}$ ,  $1585\text{ cm}^{-1}$  and  $1420\text{ cm}^{-1}$ ) bonds. The polymer to ceramic transformation involves breaking of Si-CH<sub>3</sub> and C-H bonds, and this effect is clearly captured in the FTIR spectrum with the decrease in the intensity of corresponding peaks. These results are also in agreement with other studies on bulk polymer-derived SiOC ceramics. Moreover, presence of CNTs in the composite could be observed as C=C stretching at  $1722\text{ cm}^{-1}$  (due to its pristine nature) and C-H stretching at  $2864\text{ cm}^{-1}$  (possibly due to defect sites). The chemical interaction of SiOC with CNT sidewall could not be confirmed with these techniques. However, based on present analysis physical adhesion of SiOC ceramic on CNT surface can be safely predicted.

Further, TGA measurements were performed (in flowing air) to ascertain the amount of ceramic present in the composite. As expected more ceramic was observed in SiOC-CNT-5 specimen than SiOC-CNT-10 (Fig. 6-3d). Moreover, all SiOC-CNT composite specimens showed higher oxidation resistance ( $\sim 700\text{ }^{\circ}\text{C}$ ) than pure MWCNTs ( $\sim 530\text{ }^{\circ}\text{C}$ ), which suggests protection of nanotube core by the ceramic shell. TGA data for pure SiOC has also been included for comparison.

Now, assuming that the SiOC polymeric precursor uniformly covers the entire CNT surface, ceramic shell thickness can be approximated using the following relationship [28]:

$$ML_{SiOC} = \frac{w_{SiOC}}{1 - w_{SiOC}} \times \frac{MW_{CNT}}{MW_{SiOC}} \times \left( \frac{\Omega_{SiOC}}{\Omega_{CNT}} \right)^{\frac{2}{3}} \quad (6-1)$$

Where  $ML_{SiOC}$  are the number of SiOC monolayers on CNT,  $w_{SiOC}$  is the weight fraction of SiOC in the composite determined experimentally by TGA to be 84, 76 and 68 (for SiOC-CNT-5, SiOC-CNT-8 and SiOC-CNT-10 respectively, Table 6-1). Molecular weights  $MW_{CNT}$  and  $MW_{SiOC}$  are 12 and 56  $gmol^{-1}$  and  $\Omega$  is the ratio of molar volume/Avogadro's number for CNT and SiOC. TEM images seems to corroborate these results as the SiOC-CNT-5 specimen were observed to be considerably thicker than SiOC-CNT-8 and SiOC-CNT-10 specimens.

**Table 6-1:** Summary of the TGA data. Weight percent of CNTs in SiOC is calculated based on the residual weight. All weight values in the table are accurate up to 0.1 %.

specimen	wt. % of CNTs in TTCS	oxidation temperature	residual weight (%)	calculated wt. % of CNTs in SiOC	calculated monolayers of SiOC
MWCNTs	-	536.2	2.3	-	--
SiOC	-	746.8	97.2	-	--
SiOC-CNT-5	5	714.8	83.8	16.2	3.04
SiOC-CNT-8	8	704.1	76.3	23.7	1.89
SiOC-CNT-10	10	693.7	68.3	31.7	1.23

We studied the long-term electrochemical cycling of five specimen types including SiOC, MWCNTs and three SiOC-CNT composite specimens. The first and second cycle discharge and charge plots are shown in Fig. 6-4. Fig. 6-4a and 6-4c represents SiOC and MWCNT electrode, while Fig. 6-4 (e-i) are SiOC-CNT composite electrodes, respectively. The best performance was observed for SiOC-CNT-5 specimen, which showed a first cycle reversible capacity of 841.8  $mAhg^{-1}$  with a first cycle efficiency of 67.1 %.

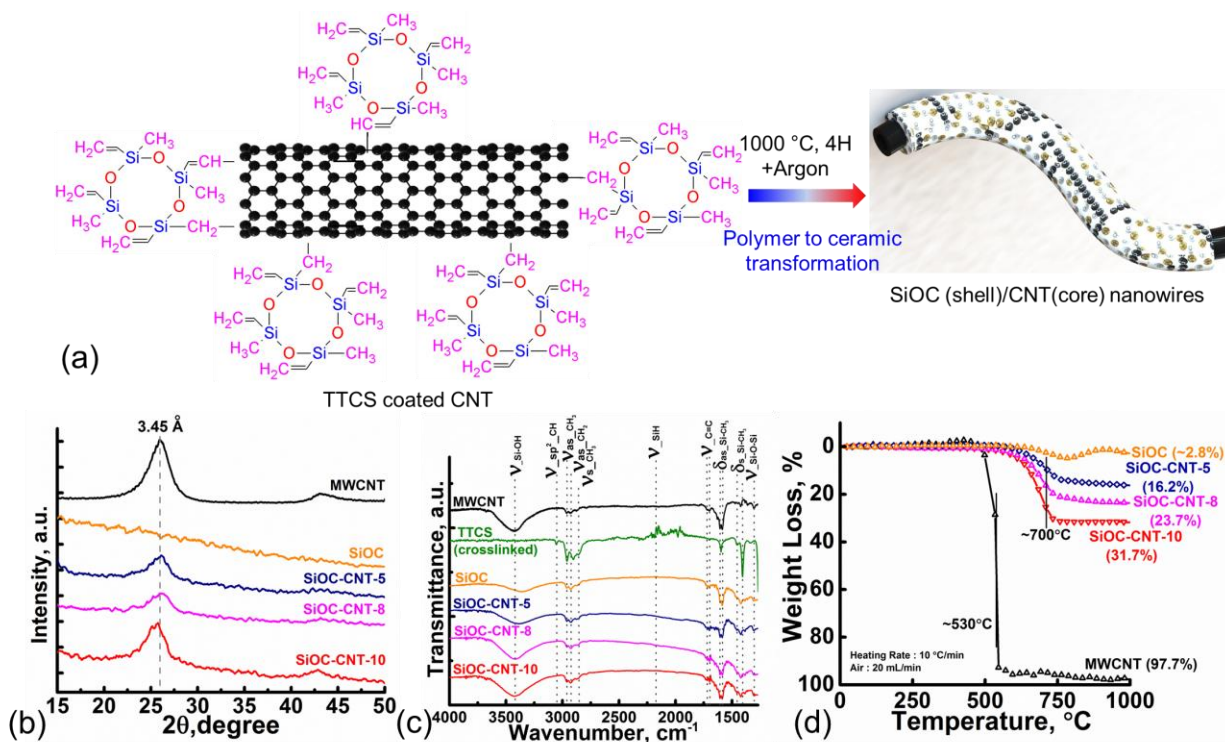


**Figure 6-3:** (a) Schematic representation of the molecular level interfacing of TTCS polymeric precursor with CNT sidewalls and resulting transformation to SiOC ceramic shell up on pyrolysis (the schematic is Not To Scale). (b) XRD data confirming the amorphous nature of polymer-derived SiOC ceramic (hallmark of these materials) and survival of carbon nanotubes in SiOC-CNT composites (peak at 26 degrees). (c) FTIR spectra showing chemical bond evolution for MWCNTs, cross-linked TTCS polymer, SiOC ceramic and various SiOC-CNT composite specimens. Polymer to ceramic conversion generally involves breaking of Si-H and Si-CH<sub>3</sub> bonds with release of hydrogen and other volatile species such as CO<sub>2</sub>, CH<sub>4</sub>, H<sub>2</sub>O etc., and (d) TGA data for determination of weight percent of CNTs in final composite.

The differentiated capacity curves (i.e.,  $dQdV^{-1}$  versus voltage) for the first two cycles for SiOC (Fig. 6-4b), MWCNTs (Fig. 6-4d) and various SiOC-CNT (Fig. 6-4f, h, j) electrodes are plotted next to their cycling plots. The reduction peaks are categorized as (I) at ~0.05 V, (II) between



~(0.25 V to 0.33) V, and (III) at ~0.7 V while oxidation peaks are categorized as (IV) ~0.1 V and (V) ~0.6 V. The reduction at ~0.05 V seems to originate from Li-intercalation in 'graphitic-carbon' which is present in both pristine SiOC ceramic and MWCNTs [18, 29]. While the reduction peak at ~0.3 V is most likely due to Li-intercalation in nanovoids or chemical bonding with dangling bonds present at Si and C sites in the ceramic [30]. One other reduction peak at ~(0.7 to 0.8) V was seen only in the first cycle for SiOC-CNT electrodes (absent in SiOC) and is characteristic of electrolyte decomposition (formation of passivating solid electrolyte interphase layer) for MWCNTs based electrodes with LiPF<sub>6</sub> based electrolytes [23, 24]. The Li-ion oxidation peaks at ~0.1 V corresponds to graphitic carbon present in SiOC and MWCNT [23, 31]. For these specimens, the dQdV<sup>-1</sup> plot in the second cycle showed an intense reduction peak-I (at 0.05 V), while a weaker oxidation peak-V (0.5 V) was observed for all the specimens. This implies that (a) multiple phases (energy levels) in SiOC-CNT seem to contribute toward lithium intercalation, and (b) Li-ion intercalation in SiOC ceramic phases start to dominate over the MWCNT after the first electrochemical cycle is over.

High first cycle irreversibility in MWCNTs is typical and is attributed to Li-trapping between their inter-tubular spacing (>56 %) [23, 24]. Thus increasing amounts of CNTs (5, 8 and 10 wt.%) in SiOC composites could be directly co-related to the increasing first cycle loss (ICL) of (32.9, 34.9 and 46.8 %) in the specimen performance. Additionally, as shown in Table 6-1, in SiOC-CNT-5 specimen the SiOC coating thickness on MWCNTs (~3 layers) can reduce the Li-ion diffusion in to the CNT core and there-by limit the entrapment of Li-ions inside nanotubes as compared to the SiOC-CNT-10 specimen (~1 layer of SiOC on CNT).

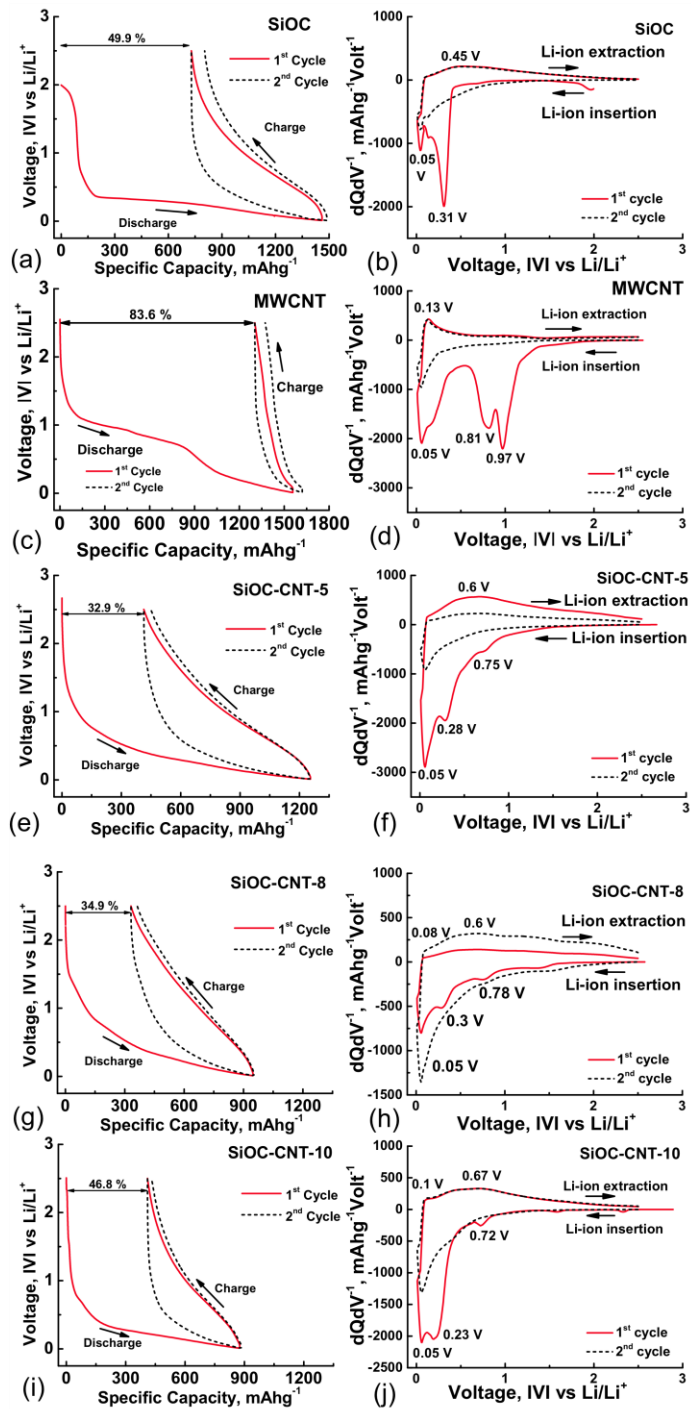


**Figure 6-4:** Electrochemical data for various SiOC electrodes used in this study: (a, c, e, g, i) first and second charge/discharge profiles for SiOC, MWCNT, SiOC/CNT-5, SiOC/CNT-8, and SiOC/CNT-10, respectively. (b, d, f, h, j) differentiated capacity versus voltage plot for SiOC, MWCNT, SiOC/CNT-5, SiOC/CNT-8, and SiOC/CNT-10, respectively.

Remarkably, the cycling efficiency in the SiOC-CNT specimens was observed to be consistently at 99 % or above, which can be collectively attributed to the stable SiOC ceramic shell that surrounds the conducting nanotube core resulting in efficient uptake and desorption of Li-ions. The reversible capacity and the first cycle efficiency of SiOC-CNT composites reported here (Table 6-2) are higher than that of some other PDC based electrodes [29, 32-34]. For example, porous-SiOC have been reported to have first cycle reversible (charge) capacity of  $\sim 272 \text{ mAhg}^{-1}$  (59 % efficiency) [20], SiCN at  $\sim 374 \text{ mAhg}^{-1}$  (74 % efficiency) [29], SiCN-graphite composite at  $\sim 474 \text{ mAhg}^{-1}$  (64.8 % efficiency) [33] and Si(B)CN-CNT at  $241.9 \text{ mAhg}^{-1}$  (41 % efficiency) [34].

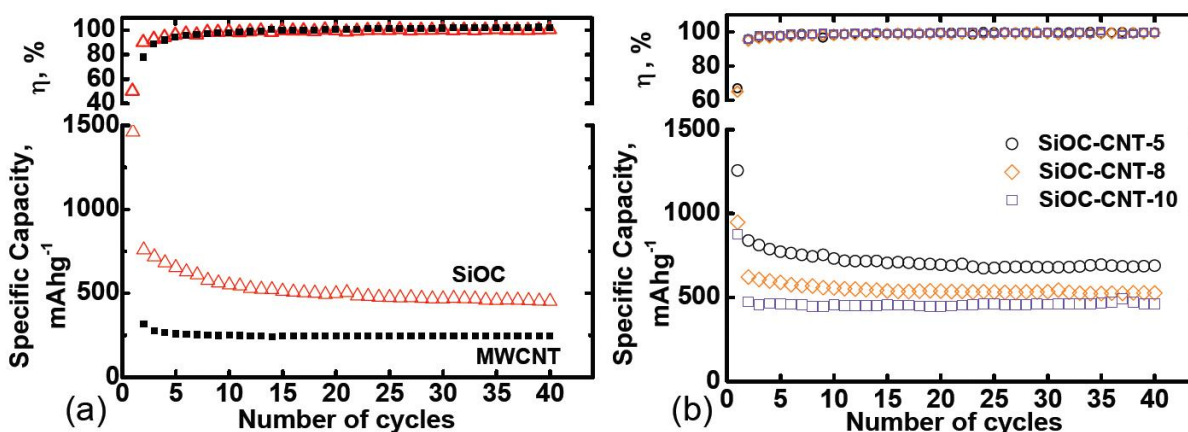


**Figure 6-5:** (a) Specific discharge capacity and efficiency of the SiOC particles and MWCNTs cycled for 40 cycles. (b) Specific discharge capacity and efficiency of SiOC/CNT electrode specimens cycled for 40 cycles at  $\sim C/10$ .

Long term cycling performance of SiOC and all SiOC-CNT specimens is plotted in Fig. 6-5a and b, respectively. High capacity retention in these electrodes is a good evidence of their chemical and structural stability induced by ceramic shell and nanotube core, respectively. For the SiOC electrode, the capacity dropped by approximately 44 % after 40 cycles. While SiOC-CNT specimens showed exceptional specific capacity retention with SiOC-CNT-10 leading with 98.6

% (at 459.6 mAhg<sup>-1</sup>) followed by SiOC-CNT-8 with 84.8 % (at 525.8 mAhg<sup>-1</sup>) and SiOC-CNT-5 with 81.5 % (at 686.3 mAhg<sup>-1</sup>) after 40 cycles. These results suggest improved mechanical toughness of the electrode due to inclusion of CNTs.

**Table 6-2:** Summary of the electrochemical data and comparison with results from literature.

(\*2nd cycle onwards)

specimen	first cycle charge capacity (mAhg <sup>-1</sup> )	first cycle loss (%)	first cycle coulombic efficiency (%)	charge capacity after 'n' cycles (mAhg <sup>-1</sup> )	% capacity retention after 'n' cycles	average coulombic efficiency (%) after 'n' cycles*
C-rich SiOC <sup>20</sup>	241	60.5	39.5	150 (30)	55.9 (30)	N/A
MWCNTs <sup>23</sup>	210	56.2	43.8	220 (20)	104.7 (20)	N/A
MWCNTs	255	83.6	16.3	250.6 (40)	101.7 (40)	99.2 (40)
SiOC	731.5	49.9	50.1	456.2 (40)	62.4 (40)	99.2 (40)
SiOC-CNT-5	841.8	32.9	67.1	686.3 (40)	81.5 (40)	99.6 (40)
SiOC-CNT-8	620.1	34.9	65.1	525.8 (40)	84.8 (40)	99.4 (40)
SiOC-CNT-10	465.9	46.8	53.2	459.6 (40)	98.6 (40)	99.6 (40)

In addition, we also note that the polysiloxane derived SiOC ceramics processed at 1000 °C are electrically insulating (<10-12 Scm<sup>-1</sup>) [19]. While pellets of SiOC-CNT composite powder prepared by cold pressing (approximately 4 kpsi) showed electrical conductivities in the range of 1.2 x 10<sup>-5</sup> Scm<sup>-1</sup> (SiOC-CNT-5) to 6.05 x 10<sup>-5</sup> Scm<sup>-1</sup> (SiOC-CNT-10). Thus, CNTs play an important role both in providing an electrical connection within the electrode and in binding the active SiOC particles as one unit.

Furthermore, a recent study on Si-O-C ceramic electrodes suggests formation of oxygen as well as carbon rich SixOyCz phases during Li-ion intercalation [35]. The dominant oxygen rich phases like SiO<sub>2</sub>C<sub>2</sub>, SiO<sub>3</sub>C and SiO<sub>4</sub> were observed to facilitate a reversible reaction with Li-ions, while carbon rich phases of SiOC<sub>3</sub> and SiC<sub>4</sub> were suggested to result in non-reversible reactions with lithium. It is likely that oxygen rich phases could be more dominant in SiOC-

CNT-5 specimen than others, resulting in lower first cycle loss. Nonetheless, further studies involving in-situ NMR could provide more insights into these composite materials and are currently beyond the scope of present work.

Later, post electrochemical imaging was carried out on disassembled electrodes to observe any signs of fatigue, crack formation, film delamination or pulverization that is typical in case of silicon based electrode when subjected to long-term electrochemical cycling. The process involved disassembling the batteries and recovering the electrode by repeated rinsing in DMC to clean the surface contaminants. The whole process was carried out in an argon-filled glovebox and the recovered electrodes were then instantly transferred to SEM for imaging. As seen in Fig. 6-6, all cycled electrodes except SiOC (Fig. 6-6 a, b), displayed uniform interconnected particle like appearance with uniform surface morphology and a stable coating. Crack-free SEI was observed on all SiOC-CNT electrode surfaces (Fig. 6-6, c through h). Degradation like delamination of active material and stress cracks due to volume expansion/contraction were also not seen. High magnification images of SiOC electrode showed that the particles were loosely held with a few micrometer size cracks being formed, which may be the reason for its reduced electrochemical capacity with increasing cycle number.

Lastly, the rate capability tests were performed (Fig. 6-7), where the electrodes were cycled for 5 cycles each at increasing current densities of 50, 100, 200, 400, 800 and 1600  $\text{mA g}^{-1}$  and then back at 50  $\text{mA g}^{-1}$ . Similar to previous observations, here also the SiOC-CNT electrodes showed better stability than bulk SiOC electrode. Among these, the SiOC-CNT-5 specimen showed highest specific capacity of  $\sim 750 \text{ mA h g}^{-1}$ , which was fully recovered when the current density was brought back to 50  $\text{mA g}^{-1}$ . In addition, we also cycled and compared the performance of SiOC-CNT-2.5 electrode specimen with SiOC and SiOC-CNT-5 specimen (Fig. 6-8). Here also

the SiCO-CNT-5 specimen (with specific capacity of  $\sim 260 \text{ mAhg}^{-1}$  at  $1600 \text{ mA}g^{-1}$ ) consistently outperformed SiOC-CNT-2.5 (specific capacity of  $\sim 46 \text{ mAhg}^{-1}$  at  $1600 \text{ mA}g^{-1}$ ), suggesting that 5 wt % loading of MWCNT in TTCS is necessary for achieving optimum performance in these composite nanowires.

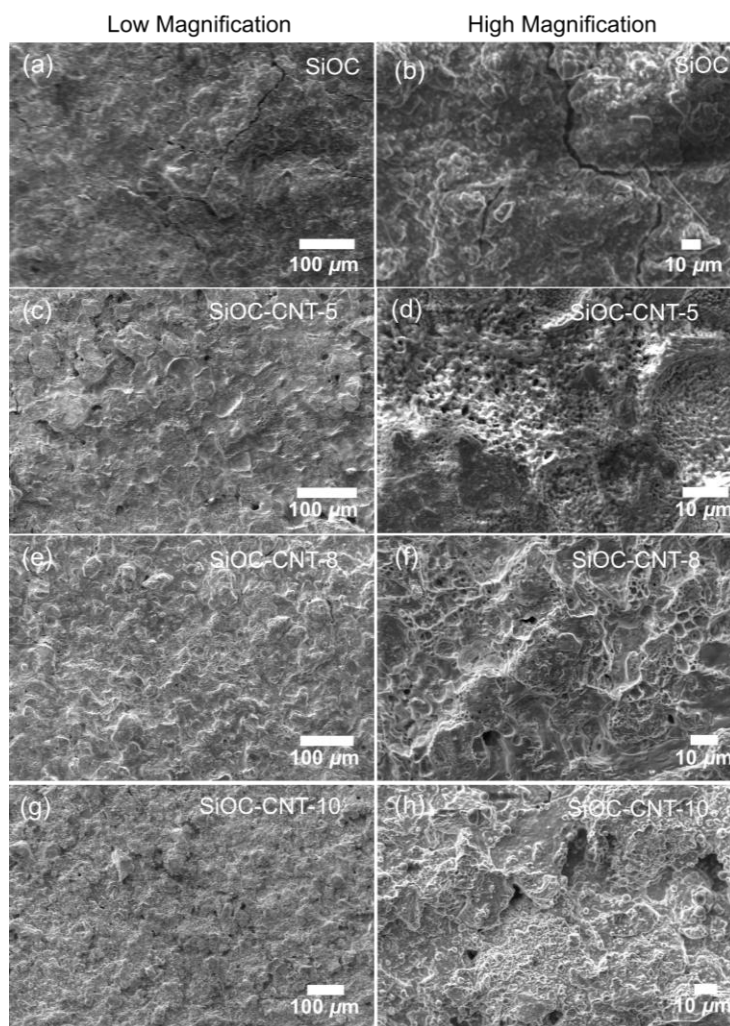


**Figure 6-6:** SEM micrographs (Left: low mag and Right: high mag) of various disassembled electrode specimen after testing for 40 cycles, (a, b) SiOC (active electrode weight :1.4 mg), (c, d) SiOC-CNT-5 (active electrode weight : 1.4 mg), (e, f) SiOC-CNT-8 (active electrode weight : 1.5 mg), and (g, h) SiOC-CNT-10 (active electrode weight : 1.6 mg). All electrodes were approximately  $127 \mu\text{m}$  thick.

Galvanostatic Intermittent Titration Technique (GITT) performed for quantitative comparison of Li-ion diffusion coefficients ( $D_{Li}$ ) for the cycled specimens and earlier published data. It can also enhance our understanding regarding specimen structure and performance interrelationship.  $D_{Li}$  for SiOC/CNT-5 specimen varied between  $1.3 \times 10^{-15} \text{ m}^2\text{sec}^{-1}$  to  $1.2 \times 10^{-14} \text{ m}^2\text{sec}^{-1}$  during lithiation of electrode and it varied between  $8.8 \times 10^{-15} \text{ m}^2\text{sec}^{-1}$  to  $7.4 \times 10^{-14} \text{ m}^2\text{sec}^{-1}$  during delithiation (Fig. 6-9). For SiOC specimen,  $D_{Li}$  lied between  $3.6 \times 10^{-16} \text{ m}^2\text{sec}^{-1}$  to  $1.6 \times 10^{-15} \text{ m}^2\text{sec}^{-1}$  during lithiation of electrode and it varied between  $1.2 \times 10^{-15} \text{ m}^2\text{sec}^{-1}$  to  $1.6 \times 10^{-14} \text{ m}^2\text{sec}^{-1}$  during delithiation. These calculations suggest an order of magnitude higher diffusion for SiOC/CNT-5 electrode than SiOC electrodes and are comparable to other PDC (SiOC) materials ( $10^{-12}$  to  $10^{-14} \text{ m}^2\text{sec}^{-1}$ ).

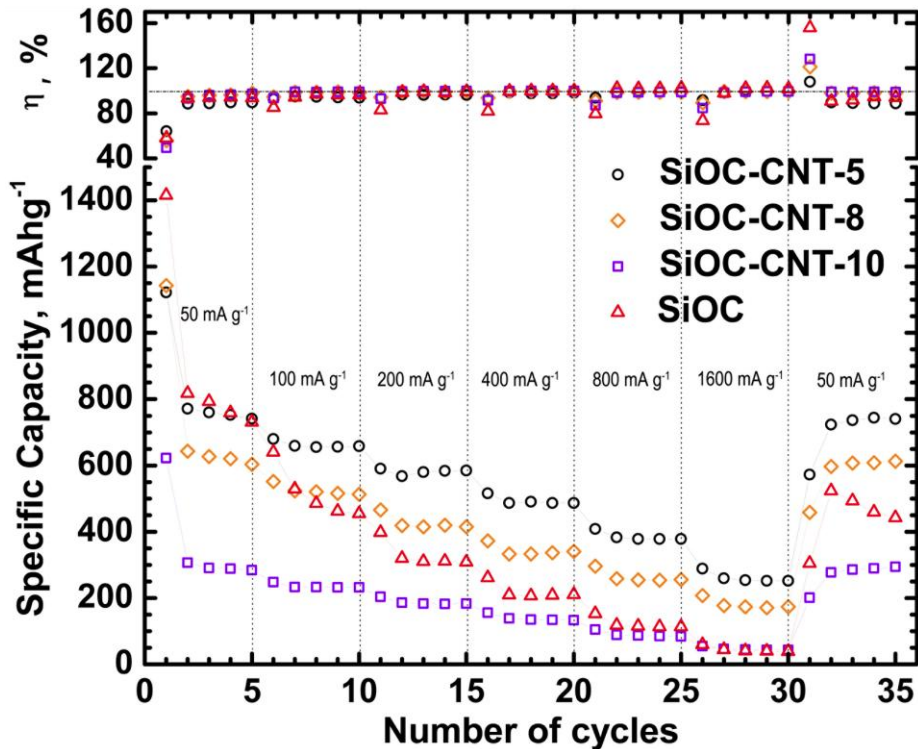


**Figure 6-7:** Rate capability test data for SiOC, SiOC-CNT-5, SiOC-CNT-8 and SiOC-CNT-10 electrode specimens showing specific discharge capacity and coulombic efficiency. All SiOC-CNT electrodes showed stable performance with SiOC-CNT-5 showing best overall cycleability.

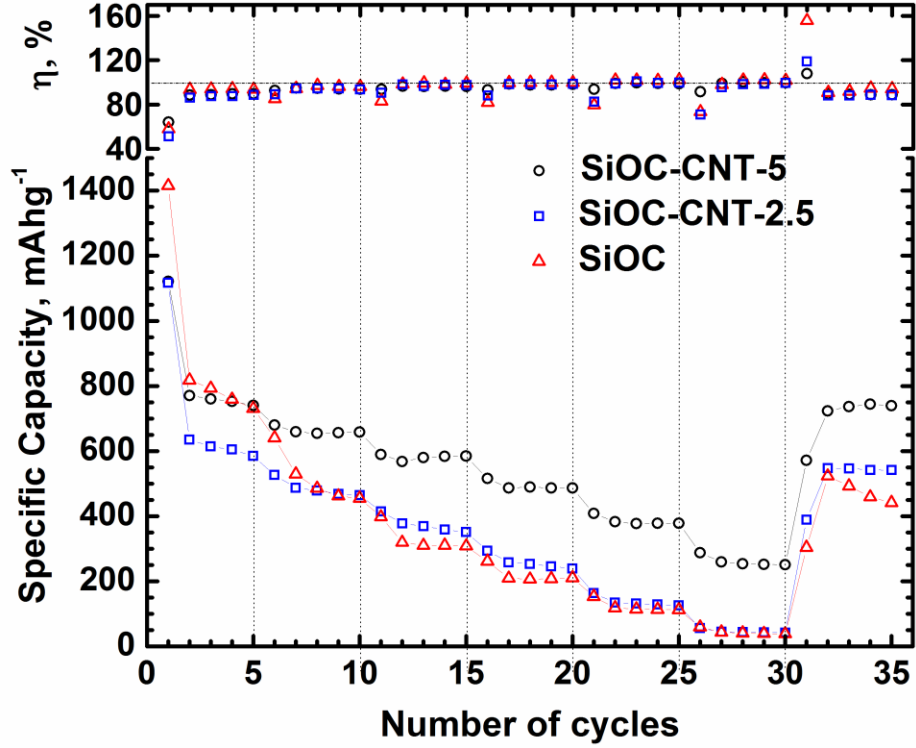


**Figure 6-8:** Rate capability test data for SiOC, SiOC-CNT-2.5 and SiOC-CNT-5 electrode specimens showing specific discharge capacity and columbic efficiency.

The solid-state lithium ion diffusion coefficients were determined using

$$D_{\text{Li}} = \frac{4}{\pi} \left( \frac{m_{\text{B}} V_{\text{M}}}{M_{\text{B}} S} \right)^2 \left( \frac{\Delta E_{\text{s}}}{\Delta E_{\text{t}}} \right)^2 \quad (6-1)$$

Where  $m_{\text{B}}$ ,  $V_{\text{M}}$ ,  $M_{\text{B}}$  and  $S$  are electrode mass, molar volume, molecular weight and surface area respectively and  $\Delta E_{\text{s}}$  and  $\Delta E_{\text{t}}$  are voltage steps as shown in Fig. 6-9.



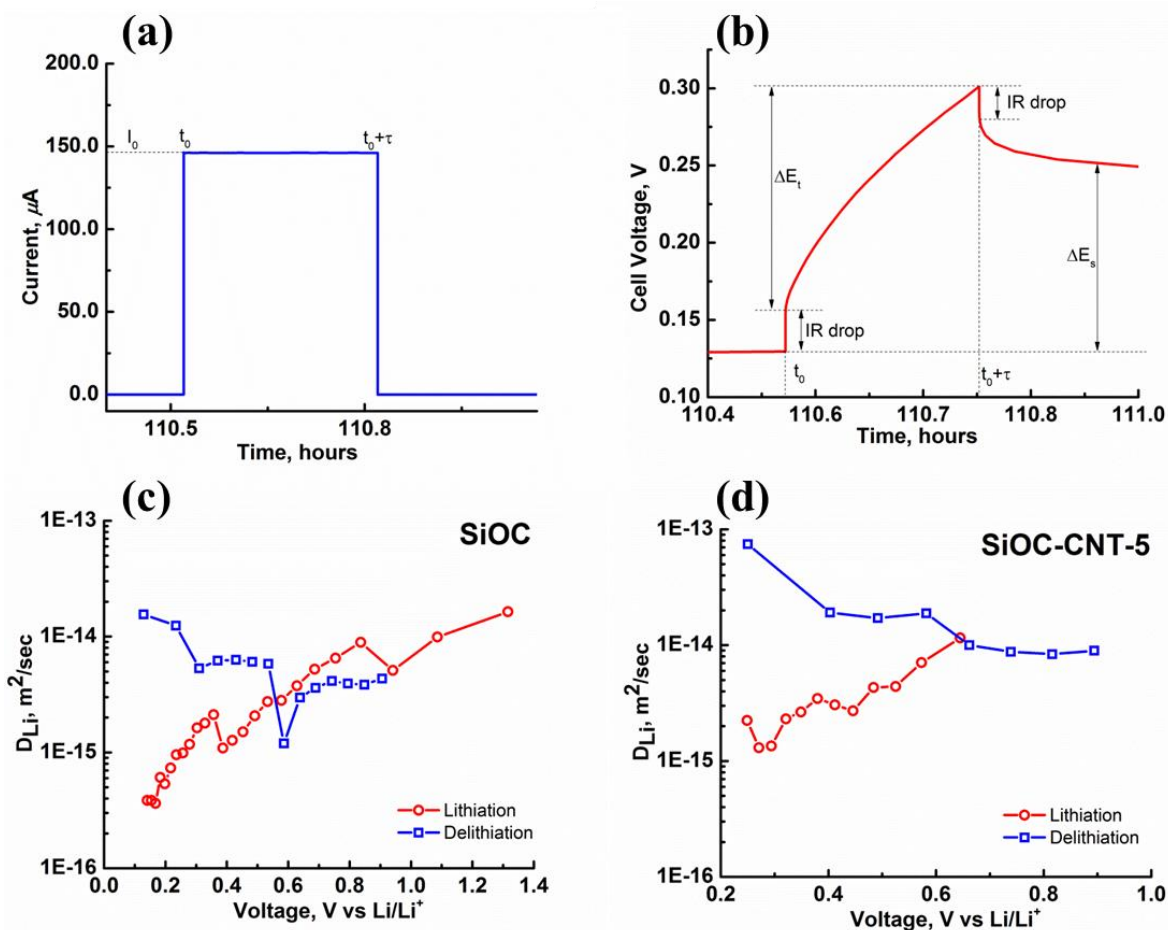


**Figure 6-9:** (a) 15 min of current pulse at  $100 \text{ mA/g}$  for SiOC/CNT-5 electrode specimen (b) Cell voltage response during the current pulse and relaxation for SiOC/CNT-5 electrode specimen (c)-(d) calculated diffusion coefficient based on the pulse and relaxation steps at the corresponding voltages during lithiation and delithiation.

GITT experiment was carried out on SiOC and SiOC/CNT-5 electrode specimens. A current pulse of  $100 \text{ mA g}^{-1}$  for 15 min followed by a 4 hour of relaxation between pulses (until equilibrium is realized) was applied to the electrode for both during delithiation and lithiation. The diffusion coefficient ( $D_{\text{Li}}$ ) was thus calculated using the composite properties like weight of active material on SiOC (1.46 mg) SiOC/CNT-5 (2.24 mg), molecular weight (50.39 g/mol);

assumed same for SiOC and SiOC/CNT-5 specimens), molecular volume ( $21.91 \text{ cm}^3/\text{mol}$ ), surface area ( $1.6 \text{ cm}^2$ ) and voltages.

## 6.4 Conclusion

We have demonstrated synthesis of polymer-derived SiOC-CNT composites with varying nanotube contents. Infrared spectroscopy revealed presence of Si-O, Si-O-Si, Si-H and C=C bonds from SiOC and C=C and C-H from CNTs suggesting conversion of TTCS polymer to ceramic on nanotube surfaces. These composites demonstrated stable performance and good rate capability with Li-ions when used as battery electrode. SiOC-CNT specimen prepared from pyrolysis of 5 wt.% CNTs in TTCS exhibited the best performance in terms of specific capacity ( $686.3 \text{ mAhg}^{-1}$ ) while capacity retention was 81.5 % after 40 cycles. More importantly, these electrodes reached coulombic efficiencies close to 99 % within the first few cycles. Further, the differentiated capacity curves ( $dQdV^{-1}$ ) revealed capacity contribution from  $\text{-sp}^2$  carbon in CNTs as well as SiOC ceramic (low voltage peak at  $\sim 0.05 \text{ V}$ ), while a separate peak between (0.2 to 0.3) V seem to emerge from lithiation at nanovoids or chemical bonding with silicon/carbon dangling bonds in SiOC ceramic. The post cycling imaging of the composite electrode surface revealed formation of a stable passivating film (improved chemical stability) with no signs of mechanical cracking or delamination (improved mechanical toughness).

## 6.5 References

1. X.H. Liu, L. Zhong, S. Huang, S.X. Mao, T. Zhu and J.Y. Huang. "Size-Dependent Fracture of Silicon Nanoparticles During Lithiation," *ACS Nano*, **6**, 1522-1531 (2012).
2. R. Krishnan, T. Lu and N. Koratkar. "Functionally Strain-Graded Nanoscoops for High Power Li-Ion Battery Anodes," *Nano Letters*, **11**, 377-384 (2011).
3. H. Kim and J. Cho. "Superior Lithium Electroactive Mesoporous Si@Carbon Core-Shell Nanowires for Lithium Battery Anode Material," *Nano Letters*, **8**, 3688-3691 (2008).
4. Y. Yao, M.T. McDowell, I. Ryu, *et al.* "Interconnected Silicon Hollow Nanospheres for Lithium-Ion Battery Anodes with Long Cycle Life," *Nano Letters*, **11**, 2949-2954 (2011).
5. J. Luo, X. Zhao, J. Wu, H. D. Jang, H. H. Kung and J. Huang, "Crumpled Graphene-Encapsulated Si Nanoparticles for Lithium Ion Battery Anodes," *Journal of Physical Chemistry Letters*, **3**, 1824–1829. (2012).
6. L. Cui, R. Ruffo, C.K. Chan, H. Peng and Y. Cui. "Crystalline-Amorphous Core-Shell Silicon Nanowires for High Capacity and High Current Battery Electrodes," *Nano Letters*, **9**, 491-495 (2009).
7. T.H. Hwang, Y.M. Lee, B. Kong, J. Seo and J.W. Choi. "Electrospun Core-Shell Fibers for Robust Silicon Nanoparticle-Based Lithium Ion Battery Anodes," *Nano Letters*, **12**, 802-807 (2012).
8. A. Magasinski, P. Dixon, B. Hertzberg, A. Kvit, J. Ayala and G. Yushin. "High-performance lithium-ion anodes using a hierarchical bottom-up approach," *Nature Materials*, **9**, 353-358 (2010).

9. B. Hertzberg, A. Alexeev and G. Yushin. "Deformations in Si-Li Anodes Upon Electrochemical Alloying in Nano-Confined Space," *Journal of American Chemical Society*, **132**, 8548-8549 (2010).
10. C.K. Chan, H. Peng, G. Liu, *et al.* "High-performance lithium battery anodes using silicon nanowires," *Nature Nanotechnology*, **3**, 31-35 (2008).
11. C.X. Xilin, X. Li, F. Ding, W. Xu, J. Xiao, Y. Cao, P. Meduri, J. Liu, G. Graff and J. Zhang, "Conductive Rigid Skeleton Supported Silicon as High-Performance Li-Ion Battery Anodes" *Nano Letters*, **12**, 4124-4130, 2012.
12. S. Sarkar, Z. Gan, L. An and L. Zhai. "Structural Evolution of Polymer-Derived Amorphous SiBCN Ceramics at High Temperature," *Journal of Physical Chemistry C*, **115**, 24993-25000 (2011).
13. R. Pena-Alonso, G. Mariotto, C. Gervais, F. Babonneau and G.D. Soraru. "New insights on the high-temperature nanostructure evolution of SiOC and B-doped SiBOC polymer-derived glasses," *Chemistry of Materials*, **19**, 5694-5702 (2007).
14. G.D. Soraru and D. Suttor. "High temperature stability of sol-gel-derived SiOC glasses," *J. Sol Gel Sci. Technol.*, **14**, 69-74 (1999).
15. S. Sarkar, J.H. Zou, J.H. Liu, C.Y. Xu, L.A. An and L. Zhai. "Polymer-Derived Ceramic Composite Fibers with Aligned Pristine Multiwalled Carbon Nanotubes," *ACS Applied Materials & Interfaces*, **2**, 1150-1156 (2010).
16. A. Saha, R. Raj and D.L. Williamson. "A model for the nanodomains in polymer-derived SiCO," *Journal of American Chemical Society*, **89**, 2188-2195 (2006).

17. H. Fukui, N. Nakata, K. Dokko, *et al.* "Lithiation and Delithiation of Silicon Oxycarbide Single Particles with a Unique Microstructure," *ACS Applied Materials & Interfaces*, **3**, 2318-2322 (2011).
18. J. Shen and R. Raj. "Silicon-oxycarbide based thin film anodes for lithium ion batteries," *J. Power Sources*, **196**, 5945-5950 (2011).
19. J. Cordelair and P. Greil. "Electrical conductivity measurements as a microprobe for structure transitions in polysiloxane derived Si-O-C ceramics," *Journal of the European Ceramic Society*, **20**, 1947-1957 (2000).
20. P. Dibandjo, M. Graczyk-Zajac, R. Riedel, V.S. Pradeep and G.D. Soraru. "Lithium insertion into dense and porous carbon-rich polymer-derived SiOC ceramics," *Journal of the European Ceramic Society*, **32**, 2495-2503 (2012).
21. W.B. Xing, A.M. Wilson, K. Eguchi, G. Zank and J.R. Dahn. "Pyrolyzed polysiloxanes for use as anode materials in lithium-ion batteries," *Journal of Electrochemical Society*, **144**, 2410-2416 (1997).
22. P. Colombo, G. Mera, R. Riedel and G.D. Soraru. "Polymer-Derived Ceramics: 40 Years of Research and Innovation in Advanced Ceramics," *Journal of American Ceramic Society*, **93**, 1805-1837 (2010).
23. B.J. Landi, M.J. Ganter, C.D. Cress, R.A. DiLeo and R.P. Raffaele. "Carbon nanotubes for lithium ion batteries," *Energy & Environmental Science*, **2**, 3406-3410 (2009).
24. E. Frackowiak, S. Gautier, H. Gaucher, S. Bonnamy and F. Beguin. "Electrochemical storage of lithium multiwalled carbon nanotubes," *Carbon*, **37**, 61-69 (1999).

25. R. Bhandavat, W. Kuhn, E. Mansfield, J Lehman, G. Singh, "Synthesis of Polymer-derived Ceramic Si(B)CN-Carbon Nanotube Composite by Microwave Induced Interfacial Polarization," ACS Applied Materials and Interfaces, **4**, 1, 11-16. (2012).
26. R. Bhandavat, G. Singh, "Synthesis, Characterization and High Temperature Stability of Si(B)CN Coated Carbon Nanotubes Using a Boron-modified Poly(ureamethylvinyl)silazane Chemistry," Journal of American Ceramic Society, **95**, 5, 1536-1543 (2012).
27. J.H. Lehman, K.E. Hurst, G. Singh, E. Mansfield, J.D. Perkins and C.L. Cromer. "Core-shell composite of SiCN and multiwalled carbon nanotubes from toluene dispersion," J. Mater. Sci., **45**, 4251-4254 (2010).
28. S.R. Shah and R. Raj. "Nanodevices that explore the synergies between PDCs and carbon nanotubes," Journal of the European Ceramic Society, **25**, 243-249 (2005).
29. M. Graczyk-Zajac, C. Fasel and R. Riedel. "Polymer-derived-SiCN ceramic/graphite composite as anode material with enhanced rate capability for lithium ion batteries," Journal of Power Sources, **196**, 6412-6418 (2011).
30. C.K. Chan, R. Ruffo, S.S. Hong, R.A. Huggins and Y. Cui. "Structural and electrochemical study of the reaction of lithium with silicon nanowires," Journal of Power Sources, **189**, 34-39 (2009).
31. M. Graczyk-Zajac, L. Toma, C. Fasel and R. Riedel. "Carbon-rich SiOC anodes for lithium-ion batteries: Part I. Influence of material UV-pre-treatment on high power properties," Solid State Ionics, **225**, 522-526 (2012).
32. Y. Feng, G. Du, X. Zhao and E. Yang. "Preparation and electrochemical performance of SiCN-CNTs composite anode material for lithium ion batteries," Journal of Applied Electrochemistry, **41**, 999-1002 (2011).

33. R. Kolb, C. Fasel, V. Liebau-Kunzmann and R. Riedel. "SiCN/C-ceramic composite as anode material for lithium ion batteries," *Journal of the European Ceramic Society*, **26**, 3903-3908 (2006).
34. Bhandavat, R. & Singh, G. Very High Laser-Damage Threshold of Polymer-derived Si(B)CN-Carbon Nanotube Composite Coatings, *ACS Applied Materials & Interfaces*, **4**, 10, 5092-5097 (2012).
35. X. Liu, M. Zheng and K. Xie. "Mechanism of lithium storage in Si-O-C composite anodes," *Journal of Power Sources*, **196**, 10667-10672 (2011).

## Chapter 7-Conclusion and Future Work

In this dissertation we have synthesized, characterized and tested the core-shell SiBCN/CNT and SiOC/CNT composite nanowires for two energy based applications (thermal absorber coatings and Li-ion battery anode). Chapter 1 gives a brief introduction about the need for a PDC-CNT and the potential multifunctional properties it could offer.

In chapter 2, we have shown successful introduction of boron in a polysilazane polymer precursor to synthesize a single source polyborosilazane precursor. The precursor was thermally transformed into SiBCN PDC through a one step process, under inert conditions. This boron doped precursor possesses both B-O and B-N bonds. Further, we also demonstrated the synthesis of core-shell SiBCN/MWCNT nanowire specimens pyrolysed between 800 and 1500 °C. Structural characterization suggested that a uniformly thick (5-10 nm) ceramic shell forms on the MWCNT core. Spectroscopy results revealed that the ceramic shell remained amorphous upto about 1300 °C and has high B/Si atomic ratio of greater than 1. These nanowires were also shown to exhibit high temperature stability (chemical and structural) and oxidation resistance in flowing air up to 1000 °C, which was confirmed by multiple characterization techniques.

Alternatively, in chapter 3, we have introduced a novel method to use microwaves at 900 W, 2.45 GHz for processing of SiBCN/CNT nanowires in about 10 minutes instead of 10 hours or more taken by conventional process, thus resulting in energy, time and cost savings. Moreover, the chemical structure, morphology and thermal stability of the nanowires prepared by this method are equally good when compared to the ones synthesized by the conventional route. Dielectric measurements suggests the conversion of polymer to ceramic on MWCNT surface results due to the heat generation as a result of interfacial polarization at MWCNT and polymer shell interface, during microwave exposure.



Coatings prepared by these multifunctional SiBCN/CNT nanowires were then tested for their damage tolerance against high power laser ( $15 \text{ kWcm}^{-2}$  at  $10.6 \mu\text{m}$  for up to 10 seconds) and the results are presented in Chapter 4. Unlike some of the other coating materials reported in literature, SiBCN/CNT shows both the high optical absorbance and an order-of-magnitude higher damage tolerance. The coating's response to incremental laser power density and exposure times were co-related to their structure and were further analyzed by spectroscopic and imaging techniques. Electron microscopy revealed no major destruction i.e., burning, delamination and deformation for the disk specimen other than some isolated surface discontinuities. Direct dependence of irradiation power density on  $I_D/I_G$  ratio, suggests systematic evolution of  $\text{sp}^3$  carbon from  $\text{sp}^2$  bonded-graphitic carbon. Ex-situ power reflectance measurements confirmed the high optical absorbance of the coating, 99.87 % for the unexposed area and 97.54 % for the area that received  $15 \text{ kWcm}^{-2}$  exposure. Coating material's high damage tolerance and uniform absorbance were understood to be due to the presence of carbon nanotubes and high oxidation resistance of Si(B)CN ceramic structure.

Secondly, the use of SiBCN/CNT nanowire coatings in lithium ion battery electrodes was explored and the results are presented in Chapter 5. When tested as battery electrode, Si(B)CN ceramic derived from boron-modified polyureasilazane showed improved Li-ion storage ability and sustained capacity as compared to the SiCN ceramic. Further, SiBCN/CNT core-shell nanowires enhanced the electrochemical capacity by four folds. This improved behavior is attributed to the structurally porous and thermodynamically stable Si(B)CN shell and electrically conducting CNT core.

In chapter 6, the practical limitation of low cyclic efficiency and reversible capacity experienced by SiBCN/CNT is overcome by replacing the PDC nanowire shell with SiOC. In order to study

the optimum performance parameters we synthesized polymer-derived SiOC/CNT composites with varying nanotube contents. SiOC/CNT specimen prepared from pyrolysis of 5 wt.% CNTs in TTCS exhibited the best performance in terms of specific capacity (686.3 mAh/g) while capacity retention was 81.5 % after 40 cycles. More importantly, these electrodes reached coulombic efficiencies close to 99 % within the first few cycles. Further, the differentiated capacity curves (dQ/dV) revealed capacity contribution from  $-sp^2$  carbon in CNTs as well as SiOC ceramic (low voltage peak at  $\sim 0.05$  V) while a separate peak between (0.2 to 0.3) V seem to emerge from lithiation at nanovoids or chemical bonding with silicon/carbon dangling bonds in SiOC ceramic. The post cycling imaging of the composite electrode surface revealed formation of a stable passivating film (improved chemical stability) with no signs of mechanical cracking or delamination (improved mechanical toughness).

Experimentation with core-shell nanowires and bulk ceramic specimens allowed us to suggest material modification and design recommendations which could show further enhancement in electrode performance.

1. Reducing the particle size of the active material can decrease the strains associated with non-uniform Li-ion diffusion. Hence, their cracking/pulverization could be prevented. Further, structurally stable nano-porous architectures like thin films (spin coated, layer by layer deposited) can facilitate easy Li-ion diffusion and hence deliver sustained capacities at higher current rates.
2. Volume expansion with cycling is known to break the physical and electrical contact between the active material, current collector and conducting additive resulting in capacity fading. Thus, use of composite materials with active component intercalating Li-ions and matrix component material providing the cushion for volume expansion can result in a more resilient structure and

hence stable cycling. The matrix component can act as an additional active material, further enhancing the specific capacity and electrode life.

3. Use of a customizable binder that can form a uniform and stable bond with the active material, this can result in reduced IRC losses. A binder with appropriate elasticity can accommodate volume changes during Li-ion cycling and still maintain the electronic and ionic conducting paths. Non-conducting polymer binders in the electrodes are known to contribute toward voltage hysteresis during cycling. Development of conducting binders can eliminate or reduce the hysteresis and enhance the anode's power density.